

4. SITE 1150¹

Shipboard Scientific Party²

BACKGROUND AND OBJECTIVES

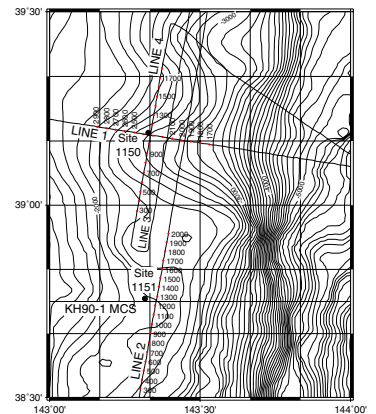
The two drilling sites of Leg 186 are located at the deep-sea terrace of the Japan Trench (Fig. F1). Although sharing similar geological goals of the previous Deep Sea Drilling Project (DSDP) Legs 57, 58, and 87 in this area (Scientific Party, 1980; Kagami, Karig, Coulbourn, et al., 1986), the main objective of this leg was to establish borehole geophysical observatories to monitor active processes in a plate subduction zone.

Site 1150 was drilled at common midpoint (CMP) 2337 on seismic line KH96-3, Line 1 (Fig. F2). We estimated that as much as 1400 m of drilling would be necessary to set the sensor strings, based on the seismic record and the core and logging data at Site 438. A compromise was made to drill to 1000 m, given the available length of time and space on the drillship. Site 438 results show that the *P*-wave velocity reached 2 km/s and the bulk density reached 1.8 g/cm³ at 920 meters below seafloor (mbsf) in the lower Miocene (Scientific Party, 1980). We estimated the reflectors at 5.0 and 5.3 s in two-way traveltime as Oligocene and Cretaceous boundaries found at Site 438, so the aimed depth of ~1000 m would be just above the Oligocene boundary.

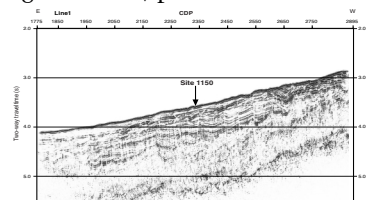
From a recent multichannel reflection seismic survey, the plate boundary immediately below Site 1150 is estimated to be at ~15 km depth from the sea surface and, therefore, only ~11 km beneath the sensor bottom (Tsuru et al., 1999). The distance to microearthquakes that occur within the hanging wall would be only ~5 km. This location provides probably the most favorable observatory site to study the plate subduction dynamics. The plate convergence rate is high here, and the seismic activity is high and relatively well coupled.

The geophysical observatory is designed to record strain, tilt, seismic signals, and temperature change. Little is known about how the dynamic sliding of the subducting plate occurs in relation to earthquakes on and off the plate boundary, since such data have been unavailable.

F1. Map of the Japan Trench area off northeast Japan, p. 69.



F2. Seismic reflection profile crossing Site 1150, p. 70.



¹Examples of how to reference the whole or part of this volume.

²Shipboard Scientific Party addresses.

Previous drilling results and seismic reflection surveys show that a tectonic erosion process is taking place in the Neogene at the Japan Trench region (Scientific Party, 1980; Kagami, Karig, Coulbourn, et al., 1986; von Huene et al., 1994). Further geological hard evidence to constrain the style of convergence and the forearc subsidence history will be sought. Analyses of faults and fractures in the cores will be compared with the present-day deformation as the observatory data become available.

The ash records from this site are expected to become an important reference section near Japan. A more detailed analysis of ash layers that are observed to increase from near the end of the upper Miocene into the lower Pliocene is expected to provide important information about eruptive processes, volcanic hazards, and aspects of climate such as response to wind, sand, and volcanogenic input of greenhouse and related gases.

OPERATIONS

Port Call

Leg 185 ended and Leg 186 officially began with the first line ashore at 2018 hr on Monday 14 June 1999 in Yokohama, Japan (all times are reported in local ship time, which is Universal Time Coordinated + 9 hr). Because of the large amount of casing to be used during Leg 186, the riser (casing) hold had to be emptied and rearranged. The following casing was loaded: 8 joints of 20-in casing (94 lb/ft; ~13.86 m/joint; total length = ~111 m), 83 joints of 16-in casing (75 lb/ft; ~12.70 m/joint; total length = ~1054 m), 156 joints of 10³/₄-in casing (40.5 lb/ft; ~12.98 m/joint; total length = ~2024 m), and 179 joints of 4¹/₂-in casing (10.5 lb/ft; ~11.64 m/joint; total length = ~2084 m).

Port call activities included a number of tours, which were managed by the Ocean Research Institute (ORI) and the Japan Marine Science and Technology Center (JAMSTEC), and a reception hosted the evening of 16 June by the ORI. All Ocean Drilling Program/Texas A&M University (ODP/TAMU) and Sedco employees plus scientists from Legs 185 and 186 were invited. The reception was attended by many dignitaries, including consulate personnel from various member countries and many Japanese scientists involved with the future of ocean drilling, particularly through the OD21 initiative. In the end, port call extended a day longer than anticipated owing in part to a strike by the Yokohama dock workers that fortunately extended only through the weekend. The extra time during the weekend was used to assemble the battery packs for the borehole instruments and to replace the aft crane boom on the port side of the ship.

Transit to Site 1150

The *JOIDES Resolution* departed Yokohama at 1145 hr on Monday 21 June. Traveling the 363-nmi transit at an average speed of 11.9 kt, we arrived at Site 1150 (JT-1C) at 1830 hr on 22 June and began drilling operations. The initial beacon deployed was released and recovered because it was not as close to the desired site location as we would have liked. A second beacon was released at 2047 hr and, because we would be spending a significant number of days at this site, a back-up beacon was deployed at 2145 hr.

Hole 1150A

Hole 1150A was spudded at 0530 hr on 23 June using the advanced hydraulic piston corer/extended core barrel (APC/XCB) coring system in a water depth of 2680.8 m (2692.2 meters below rig floor [mbrf]). Cores 3H through 12H were oriented using the Tensor tool. Three successful Adara temperature tool (Adara) measurements were taken on Core 3H at 26.7 mbsf, Core 6H at 55.2 mbsf, and Core 9H at 83.7 mbsf. An overpull of 60,000 lb after the third Adara run led us to cancel any further Adara measurements.

Biogenic methane was present throughout the APC-cored interval, which led us to cease APC coring. The gas content coupled with the tendency of the APC to pack material fully in the core liners resulted in the explosive ruptures of the core liners for Cores 10H and 11H. We believed rotary coring would alleviate some of the propensity of the liners to explode even if the gas remained present in the cores; therefore, APC coring was terminated before reaching any typical refusal point. Overpull at that point was running a mere 15,000–20,000 lb for non-Adara deployments.

XCB coring began with Core 13X and continued through Core 76X to a depth of 722.6 mbsf. Methane gas continued to be present in the cores at the same level; however, there was only a single exploding core liner incident with the XCB and this occurred before we removed the liner from the core barrel. The Davis-Villinger temperature probe (DVTP) was successfully run twice during the XCB-cored interval: once after Core 13X at 116.4 mbsf and again after Core 18X at 164.4 mbsf. The three Adara data points, two DVTP data points, and the single Adara mudline temperature measurement combined to define a very linear temperature gradient of 28.9°C/km. There were no hydrocarbon safety issues while drilling this hole. Biogenic methane was present for the entire section cored with head space data averaging around 3% methane and 1–2 ppm ethane.

Hole 1150A was cored to a total depth (TD) of 722.6 mbsf. The maximum drill string deployed was 3414.8 mbrf. A total of 566.40 m of core was recovered for an average of 78.4% of the section cored. Penetration rates varied from 99 m/hr in the surface sediments to just under 20 m/hr at TD. The entire XCB-cored section of 610.4 m was cored at an average rate of penetration (ROP) of 35.1 m/hr. Of the 112.2 m penetrated with the APC system, 118.25 m of core was recovered (105.4% recovery), and, of the 610.4 m penetrated with the XCB system, 448.15 m (73.4%) of core was recovered (Table T1, also available in [ASCII format](#)). The APC/XCB drilling assembly was pulled clear of the mudline at 1415 hr on Saturday 26 June 1999.

JET-IN TEST

The ship was offset ~20 m west of Hole 1150A and a jet-in test was conducted for the future emplacement of the reentry cone and 20-in casing string. The jet-in test was completed in 2.5 hr after washing without rotation to a depth of 67.0 mbsf. A hard layer was detected at 56.0 mbsf, though increased weight on the bit and circulation kept the drill bit advancing without any problem. The jet-in test was concluded at 1830 hr 26 June when the bit cleared the seafloor.

T1. Site 1150 coring summary, p. 176.

Hole 1150B

The APC/XCB core bit reached the rig floor at 2215 hr 26 June 1999 ending Hole 1150A and beginning Hole 1150B. The bit was found to be in excellent condition after accumulating a total of 23.2 rotating hr and 913.8 m of penetration.

Hole 1150B was spudded ~44 m east of Hole 1150A at 0415 hr on Sunday 27 June with the rotary core barrel (RCB) coring system in a water depth of 2680.8 m (2692.2 mbrf). The hole was drilled down to 703.3 mbsf before coring began. Drilling was briefly halted during this interval when a hydraulic line in the top drive umbilical ruptured. Extremely heavy rain and high wind hampered the repair effort, which took 1.5 hr. Overall, drilling and connection time was 19.75 hr, with an average ROP of 35.6 m/hr.

RCB coring was initiated about two cores above the XCB termination depth of 722.6 mbsf. We had originally planned to core to 1000 mbsf but continued deeper in search of more indurated sedimentary rock, which would be better suited for the borehole instruments planned for installation in Hole 1150C. In addition, we wanted to get deep enough to log through the rock units directly below and at the depth at which the borehole instruments were to reside. Coring ceased at 1181.6 mbsf on 1 July, when it was deemed that the lithification and depth was sufficient to accomplish our goals. In all, we cored 478.3 m and recovered 269.4 m of sediment and sedimentary rock from 50 RCB cores, for an average recovery of 56.3% (Table T1).

No hydrocarbon problems were experienced in this hole. Methane gas continued to be present in the cores at an average of ~3%, slightly higher than the average of 1.5% seen in Hole 1150A. Ethane was present at ~10 ppm, and no higher hydrocarbons were identified.

In preparation for logging, we completed a wiper trip, circulated a 30-bbl sepiolite pill, released the bit, displaced the hole with 330 bbl of sepiolite logging mud, and pulled the bottom of the drill pipe up to ~114 mbsf. Though we encountered no apparent restrictions during the wiper trip, the first logging run encountered a tight interval at ~643 mbsf, which we were unable to get through. Logging with the triple combination logging tool (triple combo) string proceeded upward from 646 mbsf. The second logging run, using the Formation MicroScanner (FMS) tool string, encountered a second obstruction, this time at ~473 mbsf, and the hole was logged upward from this depth. After completing the first two logging runs, we lowered the drill string to 742 mbsf. No resistance was identified by the driller. This allowed three logging runs—the triple combo, FMS, and borehole televiewer (BHTV) runs—to reach to within 7 to 11 m of the bottom of the hole. Formation MicroScanner data indicated an elliptical hole with one axis diameter measuring 10 in, the other measuring 14 in.

The wireline logging tools and sheaves were rigged down by 0600 hr 3 July, and the drill string was pulled to a depth of ~3292 m (~600 mbsf). A 30-bbl cement plug (~96 m long) was set at that point to ensure that there would be no communication of seawater downhole and through a fracture network to the reentry installation. The drill string was pulled clear of the seafloor at 0900 hr 3 July, and the drill string was flushed with seawater to remove any remnant cement.

Hole 1150C

While recovering the drill string the drillship was offset ~80 m west, which was ~40 m west of Hole 1150A. The end of the drill string reached the rig floor at 1330 hr on 3 July 1999, ending Hole 1150B and beginning Hole 1150C.

Reentry Cone and 20-in Casing String Installation

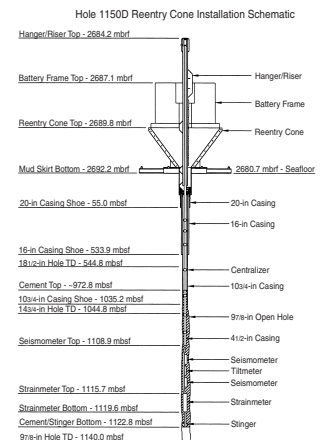
The upper guide horn was removed to assemble the 20-in casing string and reentry cone ensemble (Fig. F3). Assembly of the 20-in casing went exceptionally well, taking only 2.5 hr to join the shoe joint, three additional joints of casing, and the Dril-Quip running tool.

With the reentry cone positioned beneath the rotary table on the moonpool doors, we attempted to lower and latch the 20-in casing hanger into the reentry cone. The first sign of trouble occurred when the hanger landed at the base of the reentry cone panels rather than proceeding smoothly into the bore of the transition pipe. Even after jostling the cone around the hanger, the hanger continued to hang up sporadically in the transition pipe and would not move freely down to the landing shoulder. We decided that there must be a significant interference between the 20-in casing hanger body and the weld attaching the latch-ring body extension. To save time, the top joint of 20-in casing was laid out with the hanger attached. The next joint of 20-in casing was also laid out. The third and fourth joints of casing plus casing shoe were raised up into the derrick, allowing access to the reentry cone. The cone was then repositioned onto its side to allow a more detailed inspection. After inspecting the transition areas of both reentry cones aboard, it was apparent that the axial weld on the transition pipe and the weld attaching the transition pipe to the latch-ring body extension protruded far enough to prevent the casing hanger from traveling freely to the landing shoulder. Also, field measurements show that the uppermost ~1 in of the latch-ring body extension was incorrectly machined. Once the welds and the incorrectly machined portion of the latch ring were ground flush on the inside diameter, the casing string was once again assembled; this time the casing hanger latched into the proper position as designed. This incident resulted in 8.5 hr of lost time.

The casing string and reentry cone were lowered to a depth of 2654 m, and the subsea camera on the vibration-isolated television frame (referred to as VIT camera herein) was deployed during the pipe trip. Hole 1150D was spudded at 0930 hr on 4 July by jetting the casing into the seafloor. It took 4.25 hr to jet in the casing to a depth of 58.13 mbsf and land the reentry cone at the seafloor at a depth of 2692.2 m.

The pipe was tripped back to the rig floor, where the nozzles on the bit were replaced and the bottom-hole assembly (BHA) was assembled in preparation for drilling the 18.5-in diameter hole. The first reentry into the cone was made at 0245 hr on 5 July. By 0145 hr on 6 July, we had drilled the 18½-in hole down to a depth of 539.8 mbsf, for an average drilling rate of 27.5 m/hr. The hole was swept clean with two 50-bbl sepiolite pills and a wiper trip, displaced with 550 bbl of sepiolite, and the drill string pulled out of the hole, reaching the rig floor at 1245 hr.

F3. Schematic of equipment used in the borehole installation at Site 1150, p. 71.



Supply Boat Rendezvous

The 30-m-long seagoing tug *Fumi Maru #26* came alongside to discharge cargo and seven passengers at 0600 hr on 6 July. Arriving personnel included Masanao Shinohara from the Earthquake Research Institute of the University of Tokyo (shipboard participant), Kevin Sharp (cable-connector technician from Ocean Design), Andrew Green and Murray McGowan (seismometer technicians from Guralp Systems Ltd., United Kingdom), and Michael Acierno (computer specialist from Carnegie Institution). In addition, a two-man film crew (Satoru Ninomiya and Daisuke Yamada), hired by ORI, came aboard. The film crew and the two Guralp technicians departed the ship the following day at 1200 hr after their work was completed.

The 16-in Casing String

The rig crew ran the 42 joints (525.87 m) of 16-in casing, assembled the casing hanger, and engaged the Dril-Quip running tool in only 5.5 hr. The 16-in casing string was lowered to the seafloor, and the second reentry occurred at 0130 hr on 7 July. The casing began to show resistance almost immediately upon entry into the 20-in conductor pipe. The circulating head had to be installed, and the casing was circulated down to 137.8 mbsf. While running the casing into the bore hole, weights of 20–30 kilopounds (kips) were used to advance the casing string. By 0845 hr on 7 July, the casing hanger was landed. The casing was cemented using 30 bbl of cement, which should have resulted in cement reaching ~100 m up the exterior of the 16-in casing. The cementing dart was launched, and at 1015 hr the plug was landed at the cementing shoe and confirmed with 500-psi pump pressure. Within 15 min, the running tool was released and the drill string was then flushed with seawater to remove any residual cement in the drill string. The pipe was pulled out of the hole clearing the rotary table at 1600 hr on the same day.

After attaching a new 14³/₄-in drill bit, the drill string was lowered and the cone reentered at 2315 hr on 7 July. Because the bit was hanging up and not sliding smoothly into the transition pipe, the bit was pulled clear of the reentry cone at 2345 hr and the top drive was picked up to allow the pipe to be rotated. The reentry cone was reentered once again at 0030 hr on 8 July. The bit was “rolled” gently into the transition area. The 16-in cementing shoe was contacted at a depth of 527 mbsf, and we began drilling out the cementing shoe, wiper plug, and dart assembly.

Drilling had been in progress for 2.5 hr when, at 0640 hr, 60,000 lb of string weight was suddenly lost along with 300 psi of pump pressure. Calculations indicated that the drill string had parted at or near the seafloor. The VIT camera was deployed to verify the position of the fish (the part of the drill string in the hole) in relation to the reentry cone. The top of the fish was not visible. The camera showed, however, that the 5-in drill pipe had parted ~1 m below a tool joint in the area where the tube of the pipe had been rubbing the casing hanger during the cement-shoe drilling operation. Once the drill string was at the surface it was verified that the string did part in the 5-in drill pipe, 0.98 m below a box tool joint. The pipe showed signs of rubbing against the hanger or the transition pipe of the reentry cone during rotation but still measured a full 5 in in diameter. The pipe coating was worn away,

but no deep cuts or gouges were noted. The failure was a clean break with no metal extending over the diameter of the pipe.

To retrieve the fish, we used fishing tools consisting of a 8 $\frac{7}{8}$ -in diameter overshot with a 5-in basket grapple and an 8 $\frac{7}{8}$ -in diameter wall hook guide. The fish consisted of the BHA assembly plus 13 $\frac{2}{3}$ stands of 5-in drill pipe for a total length of 526.5 m. The top of the fish was calculated to be at 2693.3 m, which put it near the top of the 16-in casing hanger. The fishing assembly was made up and run into the top of the reentry cone. On the first two attempts to engage the fish, the overshot slid down beside the fish in the 15 $\frac{1}{8}$ -in inside diameter casing. On the third attempt, the guide passed over the top of the fish and the grapple engaged the 5-in drill-pipe tube. The fish was pulled to the surface and the broken joint was removed.

At 1045 hr on 8 July, Hole 1150C was reentered. As on the previous reentry, the bit once again hung on the lip of the reentry cone at the entrance to the transition pipe. This time, chain tongs were used to rotate the pipe and it eventually slipped into the throat of the reentry cone. The pipe was run to bottom, and at 1245 hr we once again began drilling operations. At 1400 hr on 10 July, we finished drilling the 14 $\frac{3}{4}$ -in hole for emplacement of the 10 $\frac{3}{4}$ -in casing string. It took 24.25 hr to drill the 510 m of 14 $\frac{3}{4}$ -in hole down to a depth of 1050.0 mbsf, an average rate of 21 m/hr. Sepiolite mud sweeps of 30 bbl every 40 m were pumped during the drilling process, and the hole was circulated with a 50-bbl sepiolite pill. The pipe was tripped to the rig floor at 0245 hr on 11 July.

The 10 $\frac{3}{4}$ -in Casing String

The 10 $\frac{3}{4}$ -in casing string, consisting of 82 joints of 10 $\frac{3}{4}$ -in casing plus the casing hanger, was assembled in just 8.75 hr. The casing string was lowered to the seafloor, and Hole 1150C was reentered at 1735 hr on 11 July.

An hour was spent attempting to advance the casing shoe through the throat of the reentry cone without success. The bit was pulled clear of the reentry cone at 1630 hr, and the top drive was picked up. The cone was reentered after 35 min of ship maneuvering, but the problem persisted. As the casing string was lowered, the casing shoe would catch and cause the casing string to bend or bow with as little as 5000–8000 lb of weight. We observed the deflection of the casing string with the subsea camera, which moved off center of the hole when weight was applied to the shoe. On previous reentries the same problem had occurred entering the transition pipe/casing hanger area but had been solved with rotation that allowed the bits to pass. Because the Dril-Quip running tool released with right-hand rotation, we planned left-hand rotation to work the casing shoe through the transition pipe/casing hanger area. The top drive torque limit was set at 150 A (~2000 ft-lb) to prevent overtorquing the running tool and to keep the reverse torque well below the make-up torque of the casing (4200 ft-lb). Very slow reverse rotation was initiated, and the pipe was worked in an attempt to pass. Because of the low torque limit setting, rotation stopped as soon as the casing shoe took weight and never approached the make-up torque of the casing. Rotation at the reentry cone matched the rotation at the surface. The casing string was worked with and without rotation with weights reaching 12,000 lb during vessel heaves. The vessel was also offset 20 m forward at this time to try to reposition the casing in relation to the cone.

At 1750 hr on 11 July, the string parted in a casing coupling 17 joints (~205 m) above the casing shoe. Part of the casing was observed falling down through the previously impassable transition pipe and into the hole (Fig. F4). The VIT camera was recovered and the remaining 67 joints of casing were pulled to the rig floor. Several days later when we returned to Hole 1150C to plug it with cement, we observed some of the lost joints lying on the seafloor.

After reviewing the operation, the failure of the casing coupling was attributed to the flexing and bending of the casing string. This may have been caused by flaws in the reentry cone. As noted earlier in the leg, when trying to land the 20-in casing hanger in the reentry base used on Hole 1150C, we observed that the landing-ring body extension welded to the transition pipe was machined improperly and that the welds inside the pipe were not dressed to specifications. When the same machined area on the reentry cone for Hole 1150D was ground flush, we noticed that the body extension was not welded properly, creating a serious weakness to the structure. If the same welding techniques were used on the base of the reentry cone for Hole 1150C, the weld could have failed, creating an opening between the casing hangers and the transition pipe welded to the bottom of the base. This could have been the cause of the difficulties getting the bits and casing shoes to pass through the transition pipe/hanger area. This also could have been the problem that led to the drill-pipe failure that occurred while we drilled out the 16-in casing shoe.

Considering the rapid rate at which the casing string dropped into the hole, there would have been a slim chance of removing the pile of metal that would have crashed at the base of the hole. There was also concern that even if we were able to fish the casing, we might not have been able to pull it through the flawed reentry cone. Thus, we abandoned operations on Hole 1150C and started over in Hole 1150D.

Hole 1150D

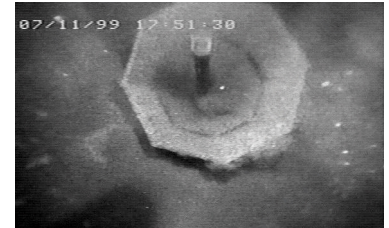
Operations at Hole 1150D began with a great deal of welding and grinding to bring the reentry cone up to required tolerance and strength specifications. A total of 14 hr was required before the reentry cone could be positioned in the center of the moonpool doors. In the meantime, the ship was offset 60 m south of Hole 1150A.

Reentry Cone and 20-in Casing String Installation

Four joints of 20-in casing (including the shoe joint) were assembled and attached to the 20-in casing hanger. The hanger was lowered into the reentry cone and engaged the reentry cone as designed without incident. Hole 1150D was spudded at 0545 hr on 13 July at a seafloor depth of 2692.2 m. The cone landed at the seafloor 11 hr later, positioning the 20-in casing shoe at a depth of 55.0 mbsf.

The drill string was pulled back to the ship, and we changed out the No. 16 jets with No. 24 jets in the 18½-in drill bit. The BHA was assembled and the drill string was run back to bottom. The first reentry was made into Hole 1150D at 0345 hr on 14 July after maneuvering the vessel for 45 min. This time the bit slid smoothly into the throat of the reentry cone and continued to the casing shoe with no resistance. We drilled the hole to a depth of 544.8 mbsf at an average penetration rate of 35.7 m/hr. Following bentonite mud sweeps, a wiper trip, and a hole

F4. The 10¾-in casing string falling into the reentry cone at Hole 1150C, p. 72.



displacement with sepiolite mud, we tripped the drill string to the rig floor.

The 16-in Casing String

By 1230 hr on 15 July, the drill crew had assembled 41 joints of 16-in casing. Reentry was made at 1700 hr on 15 July without requiring any time to reposition the vessel. The 16-in casing shoe went through the reentry cone transition with no problem, and the string was advanced to a depth of 278 m before the top drive was picked up. The remaining portion of the casing string was “washed” to bottom in the relatively tight hole. The 16-in casing shoe was landed at 533.9 mbsf at 0100 hr on 16 July and cemented into place with 30 bbl of cement 15.8 lb/gal (~1.92 g/cm³). The drill string was recovered to the rig floor by 0745 hr on 16 July.

After positioning the ship for 30 min, Hole 1150D was reentered at 1315 hr on 16 July with the 14³/₄-in drill bit. As before, the bit went straight through the reentry cone transition area and advanced to bottom, where the cementing shoe was tagged at a depth of 532.8 mbsf. By 0830 hr on 17 July, the hole was drilled to a depth of 1044.8 mbsf. Only 16 hr was required to drill the 500 m of hole at an average ROP of 31.3 m/hr. As before, the hole was circulated with a 50-bbl bentonite mud sweep, and a wiper trip was conducted up to the 16-in casing shoe.

The 10³/₄-in Casing String

It took ~7.5 hr to assemble 80 joints of 10³/₄-in and the casing hanger. The casing string was lowered, the VIT camera was deployed, and at 0800 hr on 18 July, after positioning the ship for 30 min, Hole 1150D was reentered for the fourth time. Unlike the difficulties we had at Hole 1150C, this time the 10³/₄-in casing shoe slipped through the throat of the reentry cone without resistance and we ran the string to 1044.8 mbsf and then cemented with 50 bbl of 15.8 lb/gal cement.

During this operation, we had been monitoring a storm system that was heading in our direction. To avoid the possibility of being caught in a storm while deploying the borehole instruments, we decided to delay the deployment and instead head to Yokohama to get additional casing and a reentry cone, which were needed for Site 1151 operations. The drill pipe was tripped to the surface, the rig floor was secured for transit, and the ship got under way at 2130 hr on 18 July.

Yokohama Port Call for Resupply

The 370-nmi distance to Yokohama was covered in 36.8 hr at an average rate of 10.3 kt. The pilot came aboard at 0750 hr, and we proceeded dockside with the first line ashore at 1000 hr on 20 July. Even though it was a Japanese holiday called “Day of the Oceans,” the resupply went exceptionally well. The shipping agent, Kiyooki Chiba of Sea Trade & Agency Inc., was able to arrange for a forklift and foreman to remain on duty to assist the ship’s crew with continued loading activities after normal holiday working hours had ended. In addition, loading was expedited by having the cargo predelivered dockside before our arrival. Cargo taken aboard included one reentry cone, 6 joints of 16-in casing, 48 joints of 10³/₄-in casing, and 32 joints of 4¹/₂-in casing. In addition, Michael Acierno and Kevin Sharp both departed the vessel since their work was completed. Dan Malone, Overseas Drilling Ltd., ware-

houseman replacement for the retiring Mick Malone (on the other crew), came aboard to spend the rest of the leg coordinating with Mike Cole, the warehouseman on the Leg 186 crew. All loading was completed by 1800 hr, although we were unable to depart right away because of harbor congestion associated with the holiday fireworks display. The delay provided a chance for all on the *JOIDES Resolution* to enjoy nearly 2 hr of fireworks and some much-needed entertainment along the dock. We eventually secured both pilots required for transit out of the port area and departed at 2145 hr on 20 July.

Return to Hole 1150D

The 364-nmi transit back to Site 1150 took 31 hr at an average rate of 11.7 kt. We acquired the positioning beacon at 0700 hr the morning of 22 July.

In exceptionally calm seas, we reentered Hole 1150D. Using a 9 $\frac{7}{8}$ -in tricone drill bit, we drilled through the cementing shoe at a depth of 1031.8 mbsf and began drilling the 9 $\frac{7}{8}$ -in diameter hole. Drilling in Hole 1150D was completed to a depth of 1140.0 mbsf. The final 95.2 m of hole took 5.5 hr to drill at a rate of 17.3 m/hr. We circulated the hole with a 50-bbl bentonite gel mud sweep and commenced the wiper trip back to the 10 $\frac{3}{4}$ -in casing shoe. We completed the trip back to the casing shoe without incident, though on the return back down we experienced 20–30 kips of drag almost from the start. Torquing and elevated pump pressure were also apparent. After we reamed the hole to bottom twice and circulated two additional sepiolite pills, the hole seemed to be clean.

Cementing Hole 1150C

At 1315 hr on 23 July, we began pulling out of the hole to the seafloor. We cleared the reentry cone at 1530 hr and offset the ship back to Hole 1150C to plug the open hole with cement. During the move between holes we identified a string of 10 $\frac{3}{4}$ -in casing resting on the seafloor near Hole 1150C. As discussed above, the 10 $\frac{3}{4}$ -in casing string at Hole 1150C apparently failed in more than one place, which allowed some casing to fall into the reentry cone and some to fall outside onto the seafloor. We were not able to accurately determine the quantity of casing outside the reentry cone.

At 1630 hr we reentered Hole 1150C and, as anticipated, had to rotate the drill bit with the top drive to pass through the cone transition area. Because we had made five flawless reentries into Hole 1150D, we can now definitively rule out environmental causes for the reentry problems experienced in Hole 1150C. Therefore, there must be a major structural problem or failure in the transition area of the Hole 1150C reentry cone. The pipe was advanced to a depth of 263.0 mbsf, and a 15-bbl plug of cement was pumped into the 16-in casing. This was to prevent flow between Hole 1150C and Hole 1150D, where the instrument string was to be emplaced. At 1845 hr, after displacing the cement plug, the pipe was pulled clear of the Hole 1150C reentry cone. The pipe cleared the rotary table at 2230 hr, and preparations began for deployment of the instrument package in Hole 1150D.

Installation of the Borehole Instruments in Hole 1150D

The ship was offset back to Hole 1150D as the rig floor was prepared for handling the instruments. The instrument string was assembled by its various parts, of which the lowest is a stinger pipe, a tube that allows cement to be pumped below the instruments (Fig. F3). The stinger is bolted to a overlying strainmeter. Above this is a deployment frame with two seismometers and a tiltmeter. This part of the instrument package was lowered into the moonpool area below the rig floor where the four $\frac{3}{4}$ -in diameter instrument cables were connected to the respective instruments. The rest of the instrument string consisted of $4\frac{1}{2}$ -in casing, a circulating sub, and a riser/casing hanger. Ninety-five joints (~1107.1 m) of $4\frac{1}{2}$ -in casing were run while strapping and taping the instrument cables with tie wraps and duct tape. In addition, casing centralizers were installed ~7.0 m apart along the casing. After deploying 40 joints of casing, the circulating sub, which allows the drill string to be flushed after the instruments are cemented in place, was installed. Then the other 55 joints of $4\frac{1}{2}$ -in casing were assembled with cables being attached in the same manner. The last two joints were not taped because this portion of cable was to be removed later to allow the watertight connectors to be installed in the subsea shop.

After running all of the $4\frac{1}{2}$ -in casing, the J-slot running tool was assembled, and the riser and casing hanger were picked up and connected to the top joint of $4\frac{1}{2}$ -in casing. The assembly was then lowered into the moonpool area, where the instrument cables were measured and cut to length. The riser was pulled back up to the rig floor while the cable ends were fed into the subsea shop for installation of the watertight connectors, a process referred to as cable termination.

The cable termination began at 1945 hr on 24 July and extended until 1030 hr on 25 July. By 1200 hr the multiple-access expandable gateway (MEG) had been installed into the specially designed riser carrier, and the four cables and their new connectors were plugged into the MEG. The MEG is composed of a combiner/repeater module, analog-digital converter modules, strainmeter interface module, and power conditioning/distribution module, all of which acquire signals from the sensors, convert analog signals to digital data, and send out the converted digital data to recorders via a single serial link. By 1300 hr, the final instrument checks had been completed. Once the riser/hanger was lowered beneath the ship, the VIT camera was deployed over the running tool/riser/casing hanger assembly to ensure that there was no interference. The VIT was recovered after the successful test, and we commenced tripping the drill string to seafloor.

After positioning the ship for 1 hr, we reentered Hole 1150D at 1730 hr on 25 July. The reentry drill string was spaced out so as to allow the entire 16-m instrument package to be inserted completely into the throat of the reentry cone with the top of the instruments below the $10\frac{3}{4}$ -in casing hanger. The bottom of the instrument string was then lowered to a depth of 1032 mbsf, where the top drive was picked up in preparation for inserting the instrument package into the borehole. Slow circulation was maintained as the package was lowered into the open $9\frac{7}{8}$ -in hole so that we would know immediately if the end of the stinger began to plug. Resistance was met almost immediately after entering the open hole. Washing continued for 3.5 hr as the package was advanced to a depth of 1101.8 mbsf, or 23.4 m short of landing the riser/casing hanger in the reentry cone. Throughout the insertion

period we experienced 10–20 kips overpull or drag and pressures of as much as 1500 psi. When making connections with each new pipe joint, the hole would close around (pack off) the stinger or the stinger would become plugged. Casing advance proved impossible until pump pressures returned to normal. Several times the casing had to be picked up and worked back down again. This frequently failed to lower the pressure, indicating the stinger pipe was probably still plugged. Our efforts to emplace the instrument package were further aggravated by a leak path that was apparently coming from the J-type running tool. This made it difficult to determine how much circulation was going out the stinger and how much was leaking past the running tool. Mud sweeps did not improve the situation. At 2400 hr on 25 July, we elected to pull the instrument string back inside the casing shoe. At this point, the stinger was completely plugged, and increasing the pump pressure did not unplug it.

It was obvious that we needed to reenter the hole with a drilling assembly and ream out the ~100 m of open hole before we had any chance of successfully inserting the instrument package. Fortunately the stinger unplugged itself during the pipe trip, eliminating another potentially serious problem. The final step was to check the status of the instruments once the riser was pulled into the moonpool area. To our relief, all of the instruments were functioning. Given their multiple trips up and down the tight part of the open hole and their trip through the casing and reentry cone, the instruments and cables proved to be quite robust.

We decided to attempt to hang off the intact instrument string from the ceiling above the moonpool rather than undertake the enormous job of re-spooling the cables, removing the tape, tie wraps, and centralizers, breaking down the 4½-in casing string, and disassembling the stinger/strainmeter/seismometer/tilt meter instrument package. We were able to attempt this nonstandard operation because of very calm weather and sea conditions and because the hang-off loads were relatively low at ~20 T. To allow hanging off the instrument string we had to make some modifications to the riser/hanger stabilizer fins. These were cut back ~18 cm (~7 in) to install the 10¾-in casing elevators with the 10¾-in casing slips installed below. We then disengaged the running tool and set it aside for inspection and repair. Four 1½-in-diameter wire slings were attached to the 10¾-in elevators and connected to the blocks. As the blocks were lowered, the load was slowly transferred from the lowering slings to the hang-off slings. This allowed the ~1130-m-long instrument string to swing slightly forward in the moonpool where it was secured with a tugger line (Fig. F5). The transfer was completed in 5 hr (including riser/hanger modifications), and the rig floor was then clear for pipe handling/drilling operations to continue. In addition to the hang-off activities, the wash pipe in the running tool was welded at the top end to eliminate a circulation leak path within the J-type running tool.

A 9⅞-in tricone drill bit was assembled with two stands of drill collars and the normal 5½-in transition pipe. We lowered the pipe to bottom and reentered Hole 1150D at 1730 hr on 26 July. We reamed out the hole by making several passes through tight spots and circulated several 30-bbl sepiolite mud sweeps. This was followed by a wiper trip, circulating 5 m of fill from the hole, and then displacing the hole with 40 bbl of sepiolite mud.

We pulled out of the hole clearing the reentry cone at 0515 hr on 27 July and proceeded pulling pipe until clearing the rotary table at 0900

F5. Instrument string configuration hanging in the moonpool area, p. 73.



hr. Within 2 hr, the instrument string was transferred back to the running tool and a final instrument check was performed. The pipe was then run to bottom, and Hole 1150D was reentered for the eighth and final time at 1630 hr on 27 July.

This time the string entered the open hole with little resistance; however, after three pipe joint connections the drag and elevated pump pressure once again became our nemesis. As before, when a connection was made the string would pack off and high pump pressure was required to initiate circulation. Despite the repairs made to the running tool, we were faced with a circulation leak. We worked the pipe and unplugged the stinger multiple times, and after 3 hr we successfully landed the riser and casing hanger in the reentry cone, placing the end of the instrument string stinger at 1122.8 mbsf.

We pumped 80 bbl of 15.8 lb/gal cement, displacing it with the rig pumps. The cementing dart landed in the circulating sub located ~455 m above the instrument package and the sleeve sheared as designed at ~1500 psi. This opened up circulation ports to the annulus and allowed the drill string to be thoroughly circulated (two times capacity) to remove any remaining cement. The VIT camera was recovered, and at 0045 hr on 28 July we began to rig up for assembling the battery frame halves on the moonpool doors.

Battery Pack Installation

The battery frame halves were bolted together around the pipe on the moonpool doors. Final deployment rigging and release bridles with dual acoustic release systems were attached. We waited until daylight to deploy the assembly through the moonpool because of the intricate rigging required and the poor visibility at night within the moonpool. We did not want to risk snagging a deployment cable on the guide horn. After waiting until 0430 hr (~45 min) we began to lower the platform through the moonpool. This intricate operation was completed quite well, partly because of the relatively calm sea state, although there was some surge within the moonpool.

The battery platform was lowered at ~3500 ft/hr using the logging line, and, at 0830 hr, the assembly landed in the reentry cone. Within 10 min, a portable command unit was used to send a 10-kHz acoustic signal to the release system. After recovering the logging line and the remaining deployment bridle equipped with acoustic releases, the VIT camera was deployed. At 1145 hr we verified that the battery platform had indeed been placed exactly in position as planned (Fig. F6). All cables and surface gear appeared to be in good condition, undamaged by the deployment process.

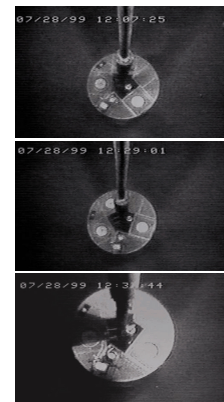
It took ~1 hr to actually release the J-type running tool from the riser, keeping the entire drill crew and science party on edge. At 1245 hr on 28 July, while working the tool through the neutral point and with ~200 A torque, the running tool abruptly released from the riser/hanger. This completed the instrument installation for Hole 1150D.

During the pipe trip to the rig floor, both positioning beacons were released and recovered aboard, the rig floor was secured for transit, and at 1900 hr on 28 July the ship got under way for Site 1151.

Weather

The weather was quite variable during operations in Hole 1150B. At no time was the operation halted because of weather, though condi-

F6. The successfully installed battery frame at Hole 1150D, p. 74.



tions did deteriorate markedly during the passage of a low-pressure cell northwest of the drilling location. We began to experience the effects of one low-pressure cell on the afternoon of 30 June, which continued through midday on 1 July. At its worst this gale brought sustained winds of 42 kt gusting to 56 kt, 28-ft seas on 7-s periods, and 30-ft swells on 7- to 8-s periods. The maximum roll, pitch, and heave experienced was 5°, 4°, and 9 ft, respectively.

Weather while drilling Hole 1150C was moderate and did not influence operations. The climate was characterized by frequent fog, overcast skies, frequent rain showers, and cool temperatures.

Weather and sea state were both excellent during operations at Site 1150D. The concern that a tropical depression was going to cross the site before installation of the instrument string influenced us to head to port earlier than would have been ideal. The storm appeared to dissipate as it neared the site, though we have no idea what its final effect on the site was since we were in Yokohama then.

LITHOSTRATIGRAPHY

Introduction

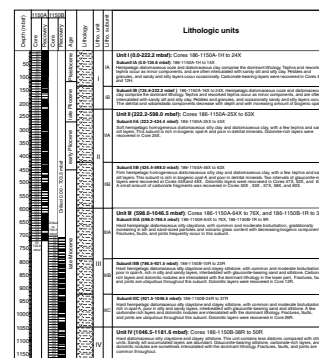
A 1181.6-m-thick sedimentary section of Holocene to middle Miocene age was cored from Holes 1150A and 1150B (Fig. F7). The major lithology of the recovered sediments predominantly consists of homogeneous diatomaceous silty clay and diatomaceous clay and its lithified equivalents, which are variable mixtures of biogenic siliceous microfossils, siliciclastic grains, and volcanoclastic grains (Figs. F8, F9).

Primary and reworked ash, and pumice layers are intercalated with the dominant lithology. Rounded to subangular heterogeneous pebbles and granules are locally distributed, and reworked sand and silt-sized grains and layers are disseminated and intercalated in the section (see “Minor Lithologies,” p. 21). These minor components are common in the upper and lower parts of the sedimentary section. Dolomitic layers and concretions are present in a few intervals. Authigenic and reworked glauconitic sand and silt-sized grains are also found in the middle to lower parts of the section.

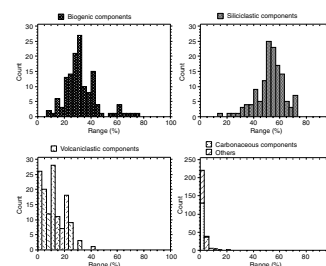
Lithologic Units

The sedimentary section at Site 1150 was divided into four lithologic units with subunits (Fig. F7). The unit and subunit boundaries are not sharp because major and minor components of the sediments change gradually with depth. We subdivide units and subunits mainly based on the composition of the major lithology, determined by visual observation of smear slides (see “Site 1150 Smear Slides,” p. 124), bulk mineralogy from X-ray diffraction (XRD) analysis (Table T2, also available in ASCII format), amount and composition of minor lithologies (Tables T3, T4, both also available in ASCII format), variations in color reflectance spectrophotometry, and degree of lithification. In addition, magnetic susceptibility, natural gamma radiation (NGR), and gamma-ray attenuation (GRA) bulk density data from multisensor track (MST) measurements were also used to help in the division of units. Even though the color reflectance spectrophotometry data contain an error (see “Lithostratigraphy,” p. 3, in the “Explanatory Notes” chapter), they proved useful for identifying lithologic changes. Occurrences of minor

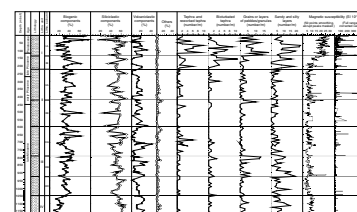
F7. Lithologic units and color reflectance, p. 75.



F8. Histogram of the three major sediment types and other components, p. 77.



F9. Downhole variations of major sediments, other components from smear-slide observations, and minor lithologies, p. 78.



T2. XRD data, p. 179.

T3. Number of ash layers, p. 180.

T4. Number of pebbles, granules, and sand/silt grains and accumulations, p. 182.

lithologies such as ash layers, fractures, and silty layers are referred to as sparse or low (<0.4 occurrences/m), common or intermediate (<1 occurrence/m), and abundant or high (>1 occurrence/m). Lithification of the sediments is based on visual core description (VCD) and resistivity logging data from downhole measurements.

Lithologic Unit I

Interval: Cores 186-1150A-1H through 24X

Depth: 0–222.2 mbsf

Age: Holocene to late Pliocene

Description: Hemipelagic diatomaceous ooze and hemipelagic diatomaceous clay, with tephra and reworked tephra as minor components typically intercalated with sandy silt and silty clay. Pebbles and granules and sandy and silty layers are common.

Subunit IA

Interval: Cores 186-1150A-1H through 15X

Depth: 0–135.6 mbsf

Age: Holocene to latest Pleistocene

Description: Hemipelagic diatomaceous ooze and diatomaceous clay, with tephra and reworked tephra as minor components often intercalated with sandy silt and silty clay. Pebbles and granules and sandy and silty layers are common. Carbonate-bearing layers were recovered in Cores 5H and 12H.

Subunit IB

Interval: Cores 186-1150A-16X through 24X

Depth: 135.6–222.2 mbsf

Age: late Pliocene

Description: Hemipelagic diatomaceous ooze and diatomaceous clay, with tephra and reworked tephra as minor components often intercalated with sandy silt and silty clay. Pebbles and granules, and sandy and silty layers are common. The detrital and volcanoclastic components decrease with depth and with increasing amount of biogenic opal-A.

Unit I consists primarily of homogeneous diatomaceous ooze, diatomaceous clay, and silty clay with rare bioturbation. The color of the sediments in Unit I is dominantly dark olive gray and olive gray. Unit I is also characterized by volcanic grains and discrete layers such as pumice, primary and reworked ash, and bioturbated ash, typically intercalated with the dominant diatomaceous sediments (Fig. F9). Single grains or layers of rounded to subangular pebbles and granules interpreted to be reworked or, less likely, ice-rafted grains of volcanic origin are also commonly disseminated within the unit. Sandy and silty intervals and layers are abundant. These minor lithologies result in abrupt peaks and background variation of magnetic susceptibility (Fig. F9). Pyrite is often disseminated in cores, and authigenic framboidal pyrite with siliceous microfossils is always observed in smear slides.

The basal boundary of Unit I is taken at the interval where ash and sand layers decrease to the background level as constrained by VCD and by magnetic susceptibility, NGR activity, and resistivity data. Unit I is divided into two subunits. The boundary between Subunits IA and IB is determined at the interval where opal-A begins to increase and quartz

and clay minerals start to decrease downhole, as documented by XRD intensities and magnetic susceptibility variations.

Subunit IA is characterized by intercalation of hemipelagic diatomaceous ooze and diatomaceous clay. Tephra and reworked tephra are commonly intercalated with sandy silt and silty clay. Pebbles and granules, and sand- and silt-rich layers are common in the cores. Biogenic siliceous components at the top and base of Subunit IA are relatively high compared with the middle part due to the increased siliciclastic components. Calcareous microfossils account for a small part of the biogenic components, but foraminifers are relatively common in the upper and lower parts of the unit and nannofossils are common in the middle part of the unit. High-amplitude variations of biogenic and detrital components correspond to intercalation of large amounts of biogenic and siliciclastic components.

Subunit IB also consists of hemipelagic diatomaceous ooze and diatomaceous clay. However, detrital and volcanic minor lithologies decrease with depth and with increasing amount of biogenic opal-A. There is a downhole trend in Subunit IB toward reddish and slightly yellowish color (based on color reflectance data), though the dominant color throughout the section is olive green. There is also an increase of biogenic silica, a decrease of siliciclastic components, and decreasing ash and sand/silt accumulations.

Lithologic Unit II

Interval: Cores 186-1150A-25X through 63X

Depth: 222.2–598.0 mbsf

Age: late Pliocene to early Pliocene

Description: Soft and firm hemipelagic diatomaceous silty clay and clay, with a few tephra and sandy silt layers.

Subunit IIA

Interval: Cores 186-1150A-25X through 45X

Depth: 222.2–424.4 mbsf

Age: late Pliocene to early Pliocene

Description: Soft hemipelagic homogeneous diatomaceous silty clay and diatomaceous clay, with a few tephra and sandy silt layers. The unit is rich in biogenic opal-A and poor in detrital minerals. Dolomite-rich layers were recovered in Core 25X.

Subunit IIB

Intervals: Cores 186-1150A-46X through 63X

Depth: 424.4–598.0 mbsf

Age: early Pliocene

Description: Firm hemipelagic homogeneous diatomaceous silty clay and diatomaceous clay, with a few tephra and sandy silt layers. The unit is rich in biogenic opal-A and poor in detrital minerals. Two intervals with glauconite-rich layers were recovered in Cores 45X and 46X. Dolomitic layers were recovered in Cores 47X, 52X, and 63X. Carbonate fragments were recovered at low recovery in Cores 50X, 53X, 57X, 58X, and 60X.

Unit II consists of homogeneous diatomaceous clay and diatomaceous silty clay, characterized by an abundance of biogenic components and a paucity of siliciclastic components. Biogenic components increase from the top of Subunit IIA with little variation, attaining the highest value in

the entire section at the lower part of Subunit IIA. Biogenic components are also high at the bottom of Subunit IIB. The division of subunits in Unit II is based on the degree of lithification of the major lithology, which increases from soft to firm. The “coring biscuits” are obviously induced by XCB coring in this unit (Fig. F10). Visual core descriptions of recovered sediments focus on the firm biscuits, not on interbiscuit soft slurry mud. Ash and pebbles are rare in this unit. The basal boundary of Unit II is drawn at the interval where enrichment of sand and silt begins and biogenic opal starts to decrease. Lithofacies are generally homogeneous in Unit II, and the intensity of bioturbation becomes rare to moderate in Subunit IIB. Based on L^* , a^* , and b^* data, respectively, the dominantly dark olive sediments become quantitatively darker and have more light reddish and bright yellowish color than other lithologic units (Fig. F7).

Dolomitic layers are intercalated in intervals 186-1150A-47X-2, 42–59 cm (436.02–436.61 mbsf), and 63X-CC, 22–26 cm (589.85–589.89 mbsf), in Subunit IIB. Dolomitic angular or subangular fragments are recovered at the top of Core 52X (482.3 mbsf), identified by peaks in XRD measurements (Table T2) and peaks in the resistivity and bulk density data from downhole measurements (Table T3). Other carbonate fragments are recovered with pumice grains and volcanic fragments at the tops of Cores 50X (462.9 mbsf), 53X (492 mbsf), 57X (530.6–540.3 mbsf), 58X (540.3–549.9 mbsf), and 60X (559.5–569.1 mbsf), which are all low-recovery cores. The concentration of these fragments at the top of the cores is an artifact of drilling. Glauconite-rich layers are present in intervals 186-1150A-45X-4, 102 cm, to 45X-5, 100 cm (420.32–421.8 mbsf), and in Core 46X (424.4–434.1 mbsf).

Lithologic Unit III

Intervals: Cores 186-1150A-64X through 76X and 186-1150B-1R through 37R

Depth: 598.0–1046.5 mbsf

Age: early Pliocene to late Miocene

Description: Hard hemipelagic diatomaceous silty claystone and clayey siltstone, rich in silt and sand accumulated layers, with common and moderate bioturbation, and with interbedded glauconite-bearing sand and siltstone.

Subunit IIIA

Intervals: Cores 186-1150A-64X through 76X and 186-1150B-1R through 9R

Depth: 598.0–786.5 mbsf

Age: early Pliocene to late Miocene

Description: Hard hemipelagic diatomaceous silty claystone with common and moderate bioturbation gradually increasing in silt- and sand-sized particles and volcanic glass content with decreasing biogenic components. Open fractures, faults, and joints are abundant.

Subunit IIIB

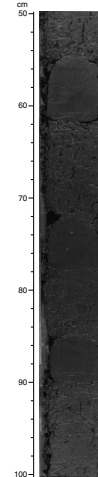
Interval: Cores 186-1150B-10R through 23R

Depth: 786.5–918.0 mbsf

Age: late Miocene

Description: Hard hemipelagic diatomaceous silty claystone and clayey siltstone, with common and moderate bioturbation, poor

F10. Photograph of typical “coring biscuits” by XCB coring, p. 79.



in opal-A, rich in silty and sandy layers, interbedded with glauconite-bearing sand and siltstone. Carbonate-rich layers and dolomitic nodules are intercalated with the dominant lithology in the lower part. Fractures, faults, and joints are ubiquitous throughout the cores. Dolomitic layers were recovered in Core 12R.

Subunit III C

Interval: Cores 186-1150B-24R through 37R

Depth: 918.0–1046.5 mbsf

Age: late Miocene

Description: Hard hemipelagic diatomaceous silty claystone and clayey siltstone, with common and moderate bioturbation, rich in opal-A, poor in silty and sandy layers, interbedded with glauconite-bearing sand and siltstone. A few carbonate-rich layers and dolomitic nodules are intercalated with the dominant lithology. Fractures, faults, and joints are ubiquitous throughout the cores. Dolomitic layers were recovered in Core 26R.

Unit III is composed of hard hemipelagic diatomaceous silty claystone and clayey siltstone with moderate to common bioturbation. Ichnofossils are dominated by *Planolites* (Fig. F11A), *Chondrites* (Fig. F11B), and *Zoophycos* (Fig. F11C). Primary and bioturbated ash layers, pumice grains, and pumice layers are sometimes interbedded in the dominant lithology, as are silt- and sand-sized accumulations and layers and glauconite-bearing sand and siltstone. Glauconite-rich layers are especially common in interval 186-1150A-64X-2, 0–150 cm (599.5–601 mbsf). Carbonate fragments are recovered from the tops of Cores 186-1150A-64X, 65X, 75X, and 76X. Fractures, faults, and joints frequently disturb the sedimentary sequence (see “**Structural Geology**,” p. 60). Dolomitic layers were recovered from the top part of each subunit. White sponge spicule aggregates occur very often throughout the unit.

Subunit IIIA is characterized by a gradual increase in silt- and sand-sized particles with decreasing biogenic components. Intensity of bioturbation varies over short intervals from rare to common.

Subunit IIIB is characterized by a paucity of biogenic silica and an abundance of silt and sand accumulations and layers. A few carbonate-rich layers and dolomitic nodules are intercalated with the dominant lithology, as are pumice grains and layers and primary and bioturbated ash layers and patches. Disseminated pyrite and pyrite patches are common. Bioturbation is moderate to common throughout the subunit.

Subunit IIIC is rich in opal-A and poor in silt and sand accumulations and layers. Bioturbation is moderate to common throughout the subunit. A few carbonate-rich layers and dolomitic nodules are intercalated with the dominant lithology, as are pumice grains and layers. Primary and bioturbated ash layers and patches are also common.

Lithologic Unit IV

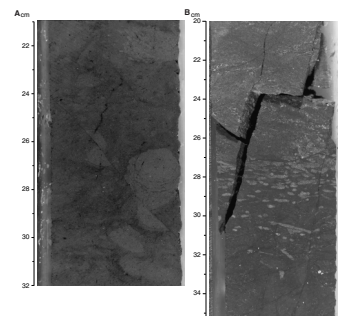
Interval: Cores 186-1150B-38R through 50R

Depth: 1046.5–1181.6 mbsf

Age: late Miocene

Description: Hard diatomaceous silty claystone and clayey siltstone. This unit contains fewer diatoms than the other units. Sandy silt accumulated layers are abundant. Glauconite-bearing siltstone, carbonate-rich layers, and dolomitic nodules are some-

F11. Photograph of ichnofossils *Planolites*, *Chondrites*, and *Zoophycos*, p. 80.



times intercalated with the dominant lithology. Open fractures, faults, and joints are common throughout the cores.

Unit IV is characterized by hard diatomaceous silty claystone and clayey siltstone. The boundary between Units III and IV is marked by a distinct downhole increase in resistivity. Within Unit IV, biogenic tests of diatoms are rare, but the ratio of opal-CT to opal-A is high. All of the detrital minerals are common, and sand and silt accumulations and layers are rich in glauconite. Thick, coarse sand turbidites occur in interval 186-1150B-38R-1, 93–120 cm (1057.23 –1057.50 mbsf). Pumice grains, ash layers, and bioturbated patches are commonly intercalated with the dominant lithology. Bioturbation is moderate to common and is dominated by *Planolites*, *Chondrites*, and *Zoophycos*. Fractures, faults, and joints are common throughout the unit.

Major Lithology

Key factors used to subdivide the recovered sedimentary section are compositional variations of major components and the degree of diagenetic lithification.

Variation of Components

The recovered sediments at Site 1150 consist of biogenic, siliciclastic, and volcanoclastic components determined from smear slides (Figs. F8, F9; see “Site 1150 Smear Slides,” p. 124). Siliciclastic material typically is the dominant component, but with variable composition with depth (Fig. F9).

The biogenic component varies from 8% to 75% with an average of 32%. The biogenic component is dominated by siliceous microfossils (mainly diatoms), siliceous sponge spicules, and a small number of radiolarians and silicoflagellates (Fig. F12). The biogenic component is high in the upper part of Units I and II and lower in the middle part of Units I, III, and IV. Calcareous biogenic components such as foraminifers and nannofossils are generally few to rare, though they are abundant in a few short intervals in Units I, III, and IV (Fig. F12).

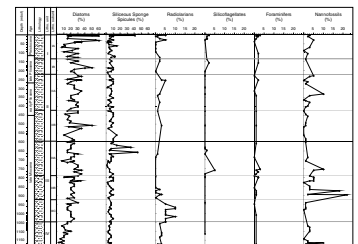
Siliciclastic components mainly consist of clay minerals and sand-, silt-, and clay-sized quartz and feldspar grains with small amounts of mica, glauconite, hornblende, and clinopyroxene grains (Fig. F12). The siliciclastic components range from 15% to 71%, with an average of 52%. Grains of feldspar and hornblende are often extremely common in thin silty or sandy layers. The siliciclastic components are high in Unit I, Subunit IIIC, and Unit IV and poor in Unit II.

Volcanoclastic components in the major lithology are almost constant, with an average of 11%, but increase slightly below 650 mbsf (Fig. F12). The components are predominantly volcanic glass. Other minor components such as authigenic pyrite, hematite, volcanic and rock fragments, and carbonate grains are observed in the sediments.

Variation of Mineral Assemblages

Minerals in the dominant lithology, determined by XRD analysis, consist of opal-A, quartz, feldspar, hornblende, clay minerals, and calcite; this analysis is consistent with smear-slide observations (Fig. F13A). Opal-A input is predominantly from diatoms. Minor silt- and sand-rich layers have a tendency to be rich in feldspar and hornblende

F12. Downhole variations of each lithologic component, p. 82.



F13. X-ray diffractograms of the major lithology, a minor silt layer, and a dolomitic layer, p. 85.

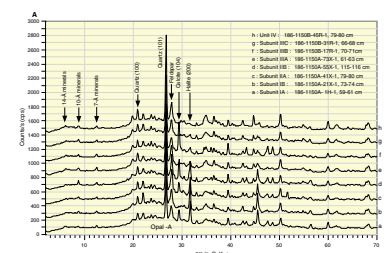


(Fig. F13B). Carbonate-rich layers and concretions consist mainly of dolomite (Fig. F13C). Halite, which is always observed, is precipitated from interstitial water during the drying procedure. Variations of these major minerals with depth are compiled as a series of XRD intensities of each mineral as counts per second (cps) (Fig. F14). These results enable us to determine the semiquantitative variation of each mineral with depth.

The coupled variation of biogenic opal-A and detrital minerals is observed over the entire sedimentary section. The opal-A hump is high in the top 50 mbsf, decreasing down to 70 mbsf in Unit I and then increasing with broad peaks of variation at ~200, 400, and 550 mbsf in Unit II, with maximum values between 400 and 600 mbsf in Unit II. Below these intervals, opal-A generally decreases with depth, although it locally increases in Subunit IIIC and in the bottom of Unit IV.

Detrital minerals are mainly represented by quartz and by 14- and 7-Å minerals, where 14-Å minerals are smectite and mixed-layer clay minerals and 7-Å minerals are kaolinite and/or chlorite. Their variation downhole is roughly inverse to that of opal-A. Variation of 10-Å minerals, which consist of illite and/or glauconite, is similar to 14- and 7-Å minerals in Units I and IV and Subunits IIIA and IIIB but differs in Unit II and Subunit IIIC. Feldspar and hornblende are locally concentrated in the sand- and silt-rich intervals. Their variation with depth appears to be similar to that of the major detrital mineral.

Calcite variation seems to be independent of other components. Peaks in calcite occur at around 70, 220, 320, 400, 500, 750, 850, 950, and 1150 mbsf, where calcareous microfossils are rich or burrows are filled by light-colored calcareous material.

Compositional variations are consistent with variations of color reflectance, NGR, GRA bulk density, and magnetic susceptibility and with the downhole measurements, such as total gamma ray, potassium, and thorium, as well as the resistivity logs. The variation of opal-A at Site 1150 appears to be similar to that of the Leg 127 sites in Japan Sea, although postcruise studies are needed to confirm the correlation and investigate possible regional influences.

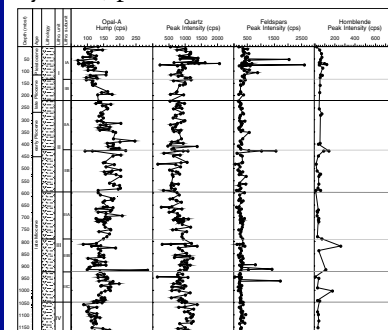
Cyclic Variations of Major Components

A weak 100-m cyclicity in the sediments may exist in the MST and downhole measurements data sets (Fig. F15). In addition, there are several meter- and dekameter-scale variations of biogenic opal-A and detrital minerals. The diatom-rich intervals correspond to slightly high a^* values (reddish), low resistivity, low NGR counts, and low density. In contrast, clay-rich intervals show slightly low a^* values (light reddish or light greenish), high resistivity, high NGR counts, and high density (Fig. F16).

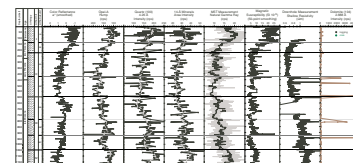
Lithification and Diagenesis

Induration of the sediments generally increases with depth (Fig. F17) and changes downhole from soft to firm at 424 mbsf. Below 598 mbsf, we described the lithology with the suffix “-stone” (see “**Descriptive Terminology**,” p. 8, in the “Explanatory Notes” chapter). Resistivity data from the downhole measurements show shifts at 424.4, 786.5, and 1046 mbsf with smaller shifts at 598 and 918 mbsf. The calculated ratio of opal-CT to opal-A shows increasing shifts at 786.5 and 1046 mbsf. A possible interpretation of these shifts is that opal-phase transformation

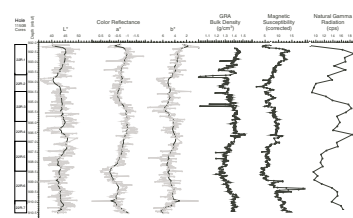
F14. Variations of major minerals by XRD, p. 88.



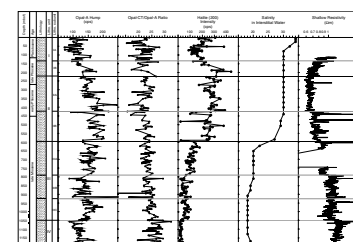
F15. Variations of color (a^*), opal-A, quartz, and 14-Å minerals, p. 91.



F16. Core-scale cyclic variations of color, GRA density, magnetic susceptibility, and NGR by MST measurement, p. 92.



F17. Lithification and diagenesis, p. 93.



from opal-A to opal-CT may start in Subunit IIIC and Unit IV; however, more detailed study is required to confirm this.

Sediment induration decreases downhole in some intervals. In general, the more indurated intervals are dolomite layers, which overlie less-indurated intervals with biogenic opal-A. Several of these intervals can be observed in the resistivity data because the dolomite layers have high resistivity relative to the biogenic-rich intervals. For example, the decreasing resistivity in the lower part of Unit I and upper part of Unit II (~100–220 mbsf) is very obvious (Figs. F15, F18; see “Downhole Measurements,” p. 49). The intervals in the uppermost part are resistive dolomite layers. The downhole decrease in resistivity below this can be explained by an increase of biogenic opal-A, which has high porosity, and by a decrease of detrital minerals.

Minor Lithologies

Ash

Volcaniclastic minor grains and layers are intercalated with the dominant lithology. At Site 1150, we classified four kinds of volcaniclastic layers: (1) pumice grains and layers, (2) primary ash layers, (3) reworked ash layers, and (4) bioturbated ash layers, which are represented by ash patches.

The pumice is intercalated as single grains or accumulations of grains with the dominant lithology. The grains have round, subangular, or angular shape and vesicular texture (Fig. F19).

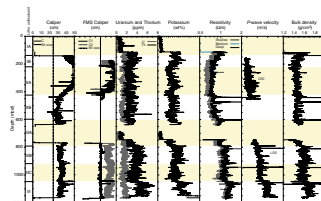
The primary ash layers typically consist of light gray to white fine-grained vitric ash (Fig. F20). The basal boundary of the ash layers is generally sharp with some scattered or mottled grains and patches in the dominant diatomaceous sediments below the basal boundary. The upper boundary, which is mostly diffuse or grades upward into diatomaceous sediments, is sometimes bioturbated.

The reworked ash layers consist of dark gray fine- to coarse-grained ash with sand-sized quartz, feldspar, hornblende, and other minerals (Fig. F21). The basal boundary of reworked layers is erosional. The upper boundary is typically irregular and grades upward to diatomaceous sediments that are sometimes bioturbated.

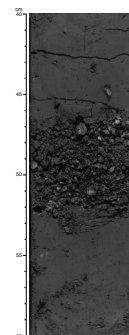
The bioturbated ash layers are laterally discontinuous and occur as discrete patches of primary and reworked ash layers as mentioned above. They show light- (Fig. F22) and dark-colored (Fig. F23) discrete and diffuse shapes. Some dark greenish patches are interpreted as altered ash.

The number of pumice and ash layers were counted in each core, and then the total was divided by recovered length in meters (Table T5; Fig. F9). We recorded two maxima in volcanism at Site 1150, one broad maximum during the late Pliocene to Pleistocene spanning Unit I, and another small maximum during the late Miocene at ~700 mbsf. The timing of these two maxima is similar to the volcanism of the ODP Leg 127 sites in the Japan Sea and the DSDP sites east of Japan (Tamaki, Pisciotto, Allan, et al., 1990; Scientific Party, 1980; Kagami, Karig, Coulbourn, et al., 1986), possibly representing volcanic activity that affected the whole area of the Japan Arc System. The timing of volcanism at Site 1150 also seems to be similar to that at DSDP Leg 86 Sites 578, 579, and 580 in the Western Pacific (Heath, Burckle, et al., 1985) and ODP Leg 132 Site 810 on the Shatsky Rise (Storms, Natland, et al., 1991), although the frequency of ash layers is lower at Site 810 than at Site 1150.

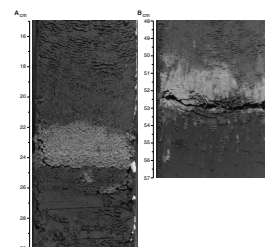
F18. Summary of logs at Hole 1150B compared with lithologic units, p. 94.



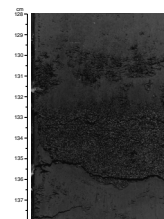
F19. Photograph of a typical pumice layer recovered at Site 1150, p. 95.



F20. Photographs of typical primary ash layers, p. 96.



F21. Photograph of typical reworked ash layers, p. 97.



However, more detailed age and compositional studies on individual ash layers are needed before an accurate tephrochronology can be determined.

Dolomite

The intervals of thin dolomitic layers (Fig. F24) in the recovered sediments and those interpreted as dolomitic layers from the downhole measurements (see “Downhole Measurements,” p. 49) are listed in Table T3 and plotted in Figures F14 and F15. Turbiditic dolomitic layers have low XRD peak intensities, and authigenic dolomitic layers or concretions are completely composed of dolomite. Both types mainly occur in intervals with high amounts of detrital minerals, low biogenic opal-A, and high NGR activity and resistivity.

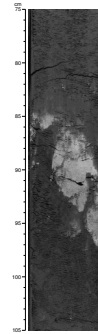
Pebbles and Granules, and Sand and Silt Accumulation

The major and mostly homogeneous lithology of diatomaceous silty clay is locally interbedded by rare coarser grained accumulations of sand/silt and pebbles/granules. These accumulations of variable thickness and diameter occur as layers with sharp, uncertain, or erosional lower boundaries and with gradational or diffuse upper boundaries; distributed grains over distances of varying scale; patches with sharp boundaries; and accumulations of different shapes and densities with diffuse boundaries. The sand/silt occurrences are mostly a mixture of dark and white grains in strongly varying proportions, which sometimes include considerable amounts of olive-green material.

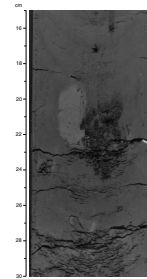
The pebbles/granules occur as single and/or several grains, accumulations, and layers and with rounded or subrounded to angular shapes. We recognize several kinds of pebbles and granules. The white pebbles are presumably pumice or carbonate. The symbol for pumice was added to the core descriptions only if a clear visible vesicular structure was present. The dark gray and black granules and pebbles are mostly lithoclasts of volcanic rocks. The dark gray and black sand and silt grains are interpreted to be dark volcanic glass, altered grains of volcanic glass, lithoclasts of volcanic rocks, or glauconite grains. Detrital grains of feldspar and hornblende are rich in sand and silt layers. The light-colored sand/silt grains were determined under the microscope to be quartz and volcanic glass. A close relationship exists between the presence of detrital glauconite grains and sand accumulations. Detrital glauconite usually occurs in aggregates of green to greenish black sand-sized grains. In most cases, the accumulations are small in vertical extent, but locally, the thickness increases to several tens of centimeters.

The occurrences of sand/silt and pebbles/granules in each core were counted, and then the total number was divided by recovered length in meters (Table T4, Fig. F9). The upper part of Hole 1150A (Unit I) has higher values in sand/silt than the lower part below 250 mbsf, and in pebbles/granules as well. Below 700 mbsf, it shows a pattern of pebbles/granules with higher numbers in the upper part, and lower numbers in the lower part, where the sand/silt number is highly variable. Increases in sand/silt layers correspond to increases in pebbles/granules between 700 and 950 mbsf and at ~430 mbsf. Between the seafloor and 320 mbsf, the peaks of pebbles/granules are offset downhole relative to the sand/silt peaks.

F22. Photograph of typical bioturbated ash “patches,” p. 98.

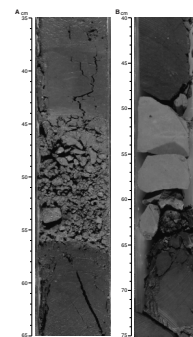


F23. Photograph of typical reworked ash layers, p. 99.



T5. Occurrences of dolomitic layers, p. 184.

F24. Photographs of a dolomite layer and a fragmented dolomite layer, p. 100.



BIOSTRATIGRAPHY

An apparently continuous sequence of upper Miocene through Pleistocene sediments and sedimentary rocks was recovered from Site 1150. The 1181-m-thick section consists mainly of diatomaceous silty clay and diatomaceous clay. Calcareous nannofossils are generally barren to abundant throughout, with variable preservation. Except for distinct ash and/or sand/silt layers, the sequence contains common to abundant diatoms throughout. Diatoms are moderately well preserved. Because the first occurrence (FO) of the diatom *Denticulopsis dimorpha* was not recognized, we interpret the base of the section to be younger than 9.9 Ma.

Calcareous Nannofossils

Calcareous nannofossils at this site were dated primarily from core-catcher samples. The sequence ranges from Quaternary to late Miocene in age. They are barren to abundant and poorly to well preserved in Holes 1150A and 1150B (Table T6).

The Pleistocene assemblage is marked by *Calcidiscus leptoporus*, *Coccolithus pelagicus*, *Emiliania huxleyi*, *Pseudoemiliania lacunosa*, the genus *Gephyrocapsa*, *Reticulofenestra*, and the rare genus *Helicosphaera*. The FO of *E. huxleyi*, which defines the boundary of the Zones CN15 and CN14b, was estimated to be in Core 186-1150A-6H by using an optical microscope, but this needs to be reexamined postcruise with a scanning electron microscope (SEM). Without the detail provided by an SEM, it is difficult to tell *E. huxleyi* from the small-sized *Gephyrocapsa*. Trace reworked *Discoaster brouweri* and *Calcidiscus macintyreii* were found in Sample 186-1150A-1H-1, 30 cm. Samples 186-1150A-6H-CC and 7H-CC were assigned to Subzone CN14b because neither *E. huxleyi* nor *P. lacunosa* was observed. Calcareous nannofossils are few to common, moderately preserved, and dominated by the genus *Gephyrocapsa* in these two samples. Samples 186-1150A-8H-CC, 9H-CC, and 10H-CC were assigned to Subzone CN14a because they contain both *P. lacunosa* and *Gephyrocapsa parallela*. Calcareous nannofossils are abundant and well preserved in these samples. Samples 186-1150A-11H-CC to 14X-CC were assigned to Subzone CN13b based on the rare occurrence of *Gephyrocapsa caribbeanica* in Sample 186-1150A-14X-CC. Calcareous nannofossils are rare and poorly preserved in these four core-catcher samples. Sample 186-1150A-15X-CC was assigned to Subzone CN13a because neither *Discoaster* nor *Gephyrocapsa caribbeanica* was present even though calcareous nannofossils are common and well preserved in this sample. The lower boundary of the Pleistocene was assigned between Sample 186-1150A-15X-CC and 16X-CC. The rare and scattered presence of *Helicosphaera inversa* makes it impossible to delimit its FO and last occurrence (LO). The LO of *C. macintyreii* occurs before the FO of the *Gephyrocapsa oceanica* and the FO of *G. caribbeanica* occurs in the same sample as the FO of *G. oceanica* (Sample 186-1150A-14X-CC), so only the FO of *G. oceanica* was used to estimate the age.

In the Pliocene and upper Miocene sediment, the assemblage is dominated by the genus *Reticulofenestra*, *C. leptopora*, *C. pelagicus*, and *C. macintyreii*. However, the genus *Discoaster*, which prefers warm water, consistently is only rare to few in abundance in the nonbarren samples, which makes determining the zonation difficult. The preservation is poorer downhole. Samples 186-1150A-16X-CC to 21X-CC were as-

T6. Stratigraphic occurrence and chronology of datum levels of calcareous nannofossils, p. 185.

signed to Subzone CN12d, the base of which is marked by the LO of *Discoaster pentaradiatus*. Because nannofossils are rare and are poorly preserved in the lower two samples, this boundary may need to be moved up. Samples 186-1150A-22X-CC to 26X-CC were assigned to Subzone CN12b-12c, the base of which is marked by the FO of *Discoaster tamalis*. *Discoaster surculus* was not observed. Samples 186-1150A-27X-CC to 37X-CC were assigned to Subzone CN12a because no *Reticulofenestra pseudoumbilicus* was observed. Nannofossils in these samples are usually poorly preserved and rare to common. A single well-preserved *Ceratolithus rugosus* in Sample 186-1150A-64X-CC indicates that this sample is in Subzone CN10c. The first datum in Hole 1150B is the LO of *Discoaster quinqueramus*, which defines the CN10/CN9 zonal boundary. The base of CN10 was put between Samples 186-1150B-11R-1, 10 cm, and 11R-3, 10 cm. A single well-preserved *Amaurolithus amplificus* in Sample 186-1150B-19R-CC puts the age of this sample between 5.993 and 6.840 Ma. From Samples 186-1150A-38X-CC to 76X-CC at the bottom of Hole 1150A, about one-third of the core-catcher samples (13 out of 38 samples) are barren or contain rare nannofossils. Nannofossils are rare or barren in about half (9 out of 19 samples) of the core-catcher samples from Sample 186-1150B-1R-CC to 19R-CC. Samples 186-1150B-20R-CC to 38R-CC were assigned to Zone CN9 because the FO of *Discoaster berggrenii* was identified, though 10 out of 19 core-catcher samples have rare abundances of nannofossils or are barren in this interval. Below this, no nannofossil datums were identified. The base of the section is probably in Zone CN8 based on diatoms. In Cores 186-1150B-48R, 49R, and 50R, *Catinaster coalitus* abundances are rare to common. The LO of *D. surculus*, LO and FO of *Amaurolithus* spp., *Ceratolithus acutus*, *Triquetrorhabdulus rugosus*, and FO of *Discoaster loeblichii* were not identified owing to the sparsity of these nannofossils.

Diatoms

Most of our observations come from core-catcher samples. For determination of zonal boundaries, additional smear slides were prepared from other core intervals. Diatoms are generally common to abundant and moderately well preserved throughout the Pleistocene through upper Miocene section recovered at Site 1150. In the upper Miocene section, however, abundance of diatoms slightly decreases because of the increase of clay content and probably because diagenetic alteration destroys diatoms as opal-A is converted to opal-CT. A range chart showing the distribution of the index species and other selected species is shown in Table T7 (also available in [ASCII format](#)). From the distribution of these species, 17 datum levels were identified (Table T8, also available in [ASCII format](#)).

The boundary between the upper Pleistocene *Neodenticula seminae* and *Proboscia curvirostris* Zones (North Pacific diatom [NPD] Zones 12/11) is indicated by the LO of *Proboscia curvirostris* (0.30 Ma) between Section 186-1150A-6H-CC and 7H-4. The continuous occurrence of *Thalassiosira jouseae*, the LO of which corresponds to 0.30–0.41 Ma, is observed near this depth. The warm-water species *Nitzschia reinholdii*, the LO of which corresponds to 0.62 Ma in the equatorial Pacific (Shackleton et al., 1995), is found in the lower part of this zone.

The last common occurrence (LCO) of *Actinocyclus oculatus* (1.01–1.46 Ma), which defines the boundary between the upper Pleistocene *P. curvirostris* Zone and the lower Pleistocene *A. oculatus* Zone (NPD 11/

T7. Distribution and relative abundance of selected diatom species, p. 186.

T8. Stratigraphic occurrence and chronology of datum levels of diatoms, p. 190.

10), is clearly identified between Sections 186-1150A-11H-CC and 12H-1. *Thalassiosira antiqua*, which has its LO from 1.52 to 1.8 Ma, is scarce in the lower part of this zone (Section 186-1150A-13X-3). The FO of *P. curvirostris* lies between Sections 186-1150A-14X-3 and 14X-5. According to Koizumi and Tanimura (1985), this datum is within the geomagnetic Chron C1r.2r (1.07–1.77 Ma). Furthermore, the warm-water species *Fragilariopsis* (= *Pseudoeunotia*) *doliolus*, the FO of which corresponds to 2.0 Ma, is observed in Section 186-1150A-13X-CC. The rare occurrence of *Neodenticula koizumii* (LO at 2.0 Ma) in Core 186-1150A-13X is, therefore, thought to be reworked specimens.

The base of the *A. oculus* Zone (NPD 10) and the top of the underlying *N. koizumii* Zone (NPD 9) is defined by the LO of *N. koizumii*. This uppermost Pliocene event occurs between Sections 186-1150A-14X-3 and 14X-5.

The LCO of *Neodenticula kamtschatica* (2.61–2.68 Ma) between Sections 186-1150A-21X-CC and 22X-3 marks the top of the *N. koizumii*–*N. kamtschatica* Zone (NPD 8). The FO of *N. seminae* is observed in Section 186-1150A-22X-3, which is concordant to the previous studies (e.g., Koizumi, 1992), suggesting that the FO of *N. seminae* falls immediately below the LCO of *N. kamtschatica*. Yanagisawa and Akiba (1998) reported, however, that this datum lies at the middle of NPD 9 and that this diachroneity was caused by a taxonomic problem because *N. seminae* and its ancestor *N. koizumii* are very similar in valve morphology. They also propose that these two species can be distinguished by the type of copula: *N. seminae* with a closed copula and *N. koizumii* with an open copula. In Section 186-1150A-22X-3, closed copula are rare but do exist; therefore, the discrepancy of the FO of *N. seminae* does not seem to be caused by the taxonomic problem mentioned above.

The FO of *N. koizumii* (3.53–3.95 Ma), which defines the boundary between the upper Pliocene *N. koizumii*–*N. kamtschatica* Zone and the lower Pliocene *Thalassiosira oestrupii* Zone (NPD 8/7B), is clearly identified between Sections 186-1150A-28X-CC and 29X-3. Within NPD 7B, the FO of *Thalassiosira latimarginata* (5.07 Ma) lies between Sections 186-1150A-45X-CC and 46X-CC.

The FO of *T. oestrupii* sensu lato defines the top of the upper Miocene *N. kamtschatica* Zone of Koizumi (1992). This datum exists between Sections 186-1150A-56X-CC and 57X-1. Though the abundance is very rare, *Rouxia californica* appears continuously in the lower part of this zone. It suggests that the boundary of NPD 7Ba and 7A (6.65 Ma), which divides the *N. kamtschatica* Zone, exists between Sections 186-1150B-20R-CC and 21R-3. The existence of the LO of *Cavitatus jouseanus* (6.7–6.8 Ma) between Sections 186-1150B-23R-CC and 24R-CC supports this zonal boundary. The FO of *Pyxidicula* (= *Thalassiosira*) *zabelinae* falls within NPD 7A of this zone, but its age has not been determined.

The upper Miocene *R. californica* Zone of Koizumi (1992) lies in the lower part of NPD 7A. The top of this zone is defined by the FO of *N. kamtschatica* (7.3–7.4 Ma). This datum is documented between Sections 186-1150B-28R-CC and 29R-3.

The LO of *Thalassionema schraderi* (7.6 Ma) between Sections 186-1150B-31R-CC and 32R-3 marks the top of the upper Miocene *T. schraderi* Zone (NPD 6B). *Actinocyclus ingens* appears continuously from this zone to the lowermost, but the age of its FO is uncertain.

Barron and Gladenkov (1995) defined the top of the upper Miocene *Denticulopsis katayamae* Zone (NPD 6A) by the LCO of *Denticulopsis simonsenii* (8.6 Ma), whereas Yanagisawa and Akiba (1998) defined it by

the LO of *Denticulopsis katayamae* (8.5 Ma). Since the former zonation was adopted in this volume (see “**Biostratigraphy**,” p. 10, in the “Explanatory Notes” chapter), the zonal boundary is determined by *D. simonsenii* as between Sections 186-1150B-40R-CC and 41R-1. On the other hand, the LO of *D. katayamae* occurs between Sections 186-1150B-39R-CC and 40R-CC. The bottom of NPD 6A is defined by the LO of *D. dimorpha* (9.16 Ma). This datum is recognized between Sections 186-1150B-43R-1 and 43R-3.

The underlying *D. dimorpha* Zone (NPD 5D) is the oldest zone in Site 1150. Within NPD 5D, the FO of *D. katayamae* (9.16 Ma) and the FO of *T. schraderi* (9.26 Ma) are between Sections 186-1150A-45R-CC and 46R-CC and between 186-1150A-46R-CC and 47R-CC, respectively. The base of this zone is defined by the FO of *D. dimorpha* (9.9 Ma). This datum is not identified at this site, so the age of the lowermost sediment is slightly younger than 9.9 Ma. Extrapolation of the 43 m/m.y. sedimentation rate (see “**Sedimentation Rates**,” p. 35) between the LCO of *D. simonsensii* (8.60 Ma) and LO of *D. dimorpha* (9.16 Ma) would give a much older age of 11.6 Ma for the sediments at the bottom of the hole and is, therefore, unacceptable.

Diatom assemblages from all samples consist almost entirely of oceanic species. They are mainly of the subarctic North Pacific Ocean, although such warm-water taxa as *N. reinholdii*, *Hemidiscus cuneiformis*, and *F. doliolus* are typically present throughout the section. Neritic species such as *Actinoptynchus senarius*, *Paralia sulcata*, and *Cocconeis* spp. vary in a small amount (from few to trace), but their presence is recognized in most samples. Freshwater species such as *Aulacoseira* spp. occur sporadically.

Resting spores of *Chaetoceros* spp. are mostly few to abundant between NPD 10 and 12 and rare to few in lower zones. At nearby Holes 438A and 584, however, the amount of these resting spores in the upper Miocene NPD 6B and 7A is one to three times as much as the total valves of usual diatoms (Akiba, 1986). Because resting spores frequently are present in nearshore sediments, Akiba (1986) suggests that this event is caused by the uplift of northeastern Honshu. The sedimentation rate also shows a significant difference between Site 1150 and the previously drilled sites. Two major episodes of low sedimentation rate, based mainly on diatom datums, were found at 9.16–8.6 and 2.0–0.41 Ma at Site 1150 (see “**Sedimentation Rates**,” p. 35), whereas in Holes 438A and 584 there are hiatuses at these ages. According to the distribution of Neogene basins off northern Honshu based on seismic data (Ishiwada and Ogawa, 1976), the basin around Site 1150 is distinguished from the basin around Sites 438 and 584: the Kitakami basin situated on ~38°–40°N (this site) and the Ishikari-Hidaka basin extends northward (Sites 438 and 584). Therefore, it appears that the depositional environment and history of this site is different from that of the previous sites. The basin including Site 1150 was probably deeper even in the uplift period; thus, valves of in situ oceanic diatoms have been deposited continuously in the basin since at least the late Miocene through the Pleistocene.

PALEOMAGNETISM

Summary

A large variety of paleomagnetic and rock magnetic experiments were conducted on discrete samples in addition to the standard remanence measurements on the archive halves. The most significant conclusions to be drawn from these combined observations are

1. All the sediments have a steep downward overprint induced by drilling. This overprint represents a larger percentage of the remanent magnetization in the APC cores than in the XCB or RCB cores, with the RCB cores being the least affected. In general, ~10 mT alternating field (AF) demagnetization removes the drill-string overprint but also reduces the magnetization by 30% to 80%.
2. Following demagnetization at 30 mT, the magnetization of sediments is $\sim 8 \times 10^{-4}$ to 8×10^{-3} A/m in the upper 70 mbsf and gradually decreases downhole to 150 mbsf. Below this depth the intensities are $\sim 3 \times 10^{-5}$ to 8×10^{-4} A/m. The lower intensities are at or near the noise level of the cryogenic magnetometer. Similarly, the magnetic susceptibility is about an order of magnitude smaller below 150 mbsf than above this depth.
3. Sediments from the upper 70 mbsf contain a stable remanent magnetization that most likely provides a record of the geomagnetic field at or near the time of deposition.
4. Below ~70 mbsf, reduction diagenesis likely results in the partial dissolution of iron oxides, particularly magnetite or titanomagnetites, and the formation of iron sulfide minerals such as pyrite, which is visible in all smear slides, pyrrhotite, and greigite. This process is likely responsible for the gradual reduction in the intensity of magnetization from 70 to 150 mbsf and the overall low values of both susceptibility and intensity of magnetization below 150 mbsf.
5. Besides drilling-induced and chemical overprints (e.g., reduction diagenesis), the sediments lower in the section have been subjected to increasing levels of mechanical overprints. Numerous microfaults and fractures are visible on the split-core surface of RCB cores (below 700 mbsf). Very likely, structural deformation affects sediments above, though to a lesser degree. The degree of deformation is more difficult to quantify in the intervals cored with the XCB system owing to the large amount of drilling disturbance.
6. The remanence from 70 mbsf down to ~850 mbsf is weak and is partially overprinted by a recent normal polarity field, of which the most likely candidate is the Brunhes field. XCB coring disturbance contributes an additional level of noise to the split-core data. This interval, however, also has a primary component. Resolving the primary component is difficult over most of the interval, and is impossible over part of the interval. Thus, no definitive magnetostratigraphy can be derived from the magnetic record, though a few reversal boundaries can be identified with confidence. The diatom datums provide the primary age constraints, with the few identified reversal boundaries aiding only in adjusting the ages between diatom datums (Table T9).

T9. Depths of prominent geomagnetic reversals, p. 191.

- The remanence below 850 mbsf is overprinted even more by a recent normal field than for the sediments above. In general, these sediments contain a single stable component following removal of a small drill-string overprint. The mean inclination of the sediments is 56° to 60° , which is consistent with the present-day geocentric axial dipole direction of 58.5° . The declination obtained from the RCB cores is likewise very stable and consistent within a continuous piece of core. Assuming the overprint is a recent normal polarity direction, the declination thus provides a means of reorienting the core and the structures present within it.

The details of the measurements and experiments upon which these conclusions are based are described below.

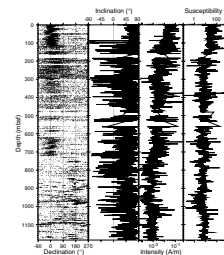
Split-Core and Whole-Core Measurements

The magnetic remanence of all archive halves of APC (0–112.2 mbsf), XCB (112.2–722.6 mbsf), and RCB (703.3–1181.6 mbsf) cores recovered at Site 1150 was measured at 2- or 5-cm intervals. Each section was also stepwise AF demagnetized at 0 (natural remanent magnetization [NRM]), 10, 20, and 30 mT. Two sections, 186-1150A-43X-4 and 186-1150B-23R-4, were demagnetized at 5-mT steps from 0 to 60 mT. Magnetic susceptibility was measured on whole-core sections every 2 cm (Fig. F25). Both remanence and susceptibility data for these sections are available from the ODP (Janus) database.

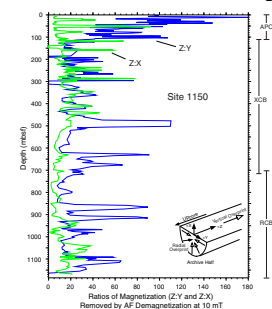
Before demagnetization, the inclinations displayed a very strong tendency toward large positive values ($\sim 60^\circ$ to 90°) over the entire cored interval, indicating the presence of a steep downward-directed drill-string overprint. In addition, the declinations are biased toward 0° in the interval cored with the APC and XCB systems or have a slight bias toward 180° in the interval cored with the RCB system. These biases in azimuthally unoriented cores indicate the presence of a radial overprint. The overprint is radially inward for the APC and XCB cores and radially outward for the RCB cores. Both the radial and vertical overprints are observed during most ODP legs and are artifacts of the drilling process.

We have further documented the presence of the drilling-related overprint by illustrating the amount of magnetization removed in the z direction (vertical component) relative to that in the x direction (horizontal component that is perpendicular to the archive-half split-core face) and y direction (horizontal component perpendicular to x-axis; see Fig. F7, p. 43, in the “Explanatory Notes” chapter) following AF demagnetization at 10 mT (Fig. F26). The thin dark line in Fig. F26 shows that 10 to 180 times more magnetization is removed in the z direction than in the y direction. Thus, the vertical component of the drill-string overprint clearly contributes a larger low coercivity component than do other secondary or primary horizontal components. The z:y ratio is about six to eight times larger in the APC-cored interval than in the XCB- and RCB-cored intervals, illustrating that the vertical drill-string overprint is largest in the APC cores. The z:x ratio (the thick shaded line in Fig. F26) is much smaller than the z:y ratio in the APC-cored interval and slightly smaller in the other intervals. This illustrates that the radial component, which contributes no net magnetization in the y direction owing to the orientation system used, contributes a significant low-coercivity component in the x direction. The size of this component is

F25. Split-core paleomagnetic results prior to AF demagnetization, p. 101.



F26. Ratio of magnetization removed from split cores after 10 mT AF demagnetization along the x-, y-, and z-axes of the core, p. 102.



still small relative to the vertical overprint as is evidenced by the ratio of removed magnetization (z:x in Fig. F26) being >5 and averaging ~15.

A large proportion of the initial magnetization is removed by AF demagnetization, even with peak fields of only 10 mT (Fig. F27). For most of the APC and XCB cores, <40% of the magnetization remains after 10 mT demagnetization, whereas the RCB cores retain ~50%–60% of their magnetization. From this and the above information, we conclude that ~40%–80% of the remanence is carried by very low coercivity magnetic minerals (those influenced by ≤10-mT magnetic fields), which are easily remagnetized by coring-induced magnetic fields.

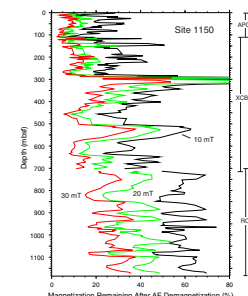
The magnetization remaining after demagnetization at 20 or 30 mT reflects the characteristic remanent magnetization (ChRM), a term we use to refer to the high coercivity or high unblocking temperature component that records the ancient magnetization of the sediments. In some cases the ChRM is not a primary magnetization that was acquired at or near the time of deposition but is instead a secondary magnetization probably acquired during subsequent chemical and mechanical remagnetization.

After 30 mT demagnetization, the bias that was present in the declination appears to be removed for the APC and RCB cores, but a bias remains for the XCB cores (Fig. F28). The declinations for each APC core cluster at different mean declinations, as expected for azimuthally unoriented cores. Reorientation of the APC cores (Cores 186-1150A-3H to 8H) using the Tensor-tool data brings the mean declination to near 0° (Fig. F29), as would be expected for the sediments of Brunhes age (<780,000 yr). Cores 186-1150A-9H and 12H are not included in Fig. F29 because they are partly or totally reversed polarity, and Cores 186-1150A-10H and 11H are not included because their core liners were shattered by gas expansion while the cores were still on the catwalk. The large standard deviation for the corrected declinations (52.9°) reflects the uncertainty in the Tensor-tool correction along with possible rotation of the core barrels as they were shot into the sediments. The standard deviation may also be inflated because of the relatively low number of oriented cores collected.

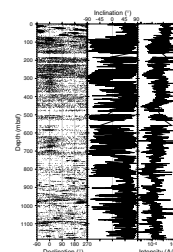
Examination of inclinations after 30 mT AF demagnetization (Fig. F28) illustrates that both normal and reversed polarities are recorded in at least the upper 850 m, though with a considerable amount of noise. Below 850 m, however, virtually the entire section has very stable positive inclinations, with mean inclinations of 56° to 60° (Fig. F28). This would indicate that the sediments are of normal polarity, with the exception of a few short intervals (e.g., from 940 to 950 mbsf). This conflicts with biostratigraphic information, which instead indicates that about half of the section should be reversed polarity. Given the abundance and good preservation of diatoms, and the resulting high quality of the biostratigraphy (see “Biostratigraphy,” p. 23), it seems unlikely that the sedimentary section below 850 mbsf has a primary remanence. Remagnetization appears to be required and is supported by other evidence. For example, middle Miocene sediments obtained from DSDP Site 584 in the Japan Trench were remagnetized as confirmed by a bedding-correction test (Niitsuma, 1986).

The remagnetization process that has replaced all or nearly all of the primary remanence in the lower 850 mbsf has probably also partially replaced the magnetization in the section above. The noise in the interval below ~70 mbsf we attribute to the low intensities and to partial remagnetization of the sedimentary section. Assuming that either chemical remagnetization, mechanical remagnetization, or both increase

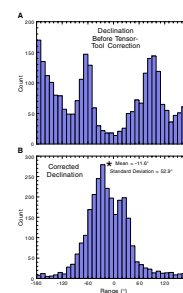
F27. Magnetization remaining after AF demagnetization of the split cores, p. 103.



F28. Split-core declination, inclination, and intensity of magnetization after AF demagnetization, p. 104.



F29. Histogram of declinations for Cores 186-1150A-3H to 8H before and after Tensor-tool orientation correction, p. 105.



progressively downhole, then it is not surprising that below 850 mbsf there is relatively little evidence of reversed polarity and that in the interval from 850 to 70 mbsf the reversed polarity intervals are more poorly resolved than the normal. Given that the field has had a normal polarity for the past 780,000 yr, there would be ample opportunity for the net bias of the sedimentary section to be in a normal-polarity direction. An additional source of noise for the sediments from 700 to 70 mbsf comes from drilling disturbance generated by XCB coring, which results in drilling biscuits (coherent pieces of core) surrounded by slurry.

In contrast, the sediments above 70 mbsf likely contain a primary magnetization acquired at or near the time of deposition. The magnetization of this interval appears to be unaffected by reduction diagenesis as evidenced by the intensity and susceptibility data, which again are about an order of magnitude higher than for sediment lower in the section. The presence of pyrite in the upper cores may indicate that some level of reduction takes place shortly after deposition, but not enough to consume completely magnetic minerals carrying a primary remanence. Unlike the lower part of the sedimentary section, there has been little time for mechanical deformation to remagnetize the sediment in the upper 70 mbsf, and evidence from ash layers and burrows suggests deformation is absent. Finally, inclinations and declinations within this interval are very stable and consistent with a Brunhes normal polarity direction (Fig. F30).

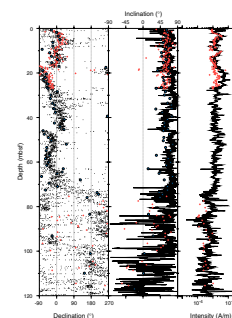
Discrete Samples

The remanent magnetization directions and intensities obtained from measurements on discrete samples (7-cm³ cubes) agree well with split-core results (Figs. F30, F31). The only small systematic differences observed in the inclinations are in the APC-cored intervals, where the split-core inclinations are steeper by ~8° to 13°. Because the inclinations from the discrete samples agree with the expected geocentric axial dipole inclination and because the discrete samples come from the center of the core and are unaffected by sediment shearing that distorts the outer part of the APC cores, the discrete samples more accurately represent the paleomagnetic inclination. The sediment shear effect has been shown to bias the inclination of APC cores to both shallower and steeper values but generally produces steeper values for an expected inclination of ~60° (Keigwin, Rio, Acton, et al., 1998).

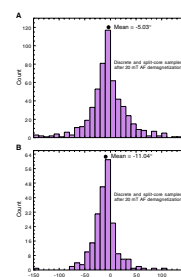
The demagnetization behavior of typical samples from the entire cored interval is illustrated in Figures F32, F33, F34, F35, F36, F37, F38, and F39. Thermal demagnetization of samples from the upper 6 mbsf (Figs. F32, F33) indicates that a large proportion (>60%) of the magnetization has unblocking temperatures of <210°C. By ~330°C, the samples had been demagnetized to the noise level of the cryogenic magnetometer. In comparison with AF demagnetization of samples in the same interval (Figs. F32, F33, F34), thermal demagnetization appears to be less effective at separating the steep drill-string overprint from the ChRM. Basically, the unblocking temperature spectrum for the overprint and the ChRM are similar, with both components being removed simultaneously during demagnetization.

For samples from the upper 70 mbsf (down to about the middle of Core 186-1150-8H), the ChRM direction can be resolved well with AF demagnetization (e.g., Fig. F34). In general, the steep drill-string overprint is removed by 8 to 10 mT, leaving a linear decay of the magnetiza-

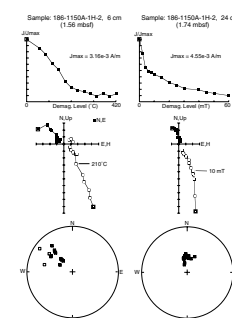
F30. Split-core and discrete declination, inclination, and intensity of magnetization after AF demagnetization at 20 mT, p. 106.



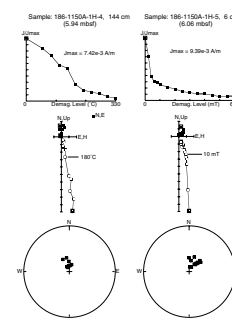
F31. Histograms of difference in discrete and split-core inclinations, p. 107.



F32. Demagnetization behavior of Samples 186-1150A-1H-2, 6 cm, and 186-1150A-1H-2, 24 cm, p. 108.



F33. Demagnetization behavior of Samples 186-1150A-1H-4, 144 cm, and 186-1150A-1H-5, 6 cm, p. 109.



tion toward the origin of the orthogonal plots (Figs. F32, F33, F34). In some cases, the sample does not decay directly to the origin, which might be caused by the samples picking up a small ARM during AF demagnetization, a viscous component of magnetization following each thermal demagnetization step (as the samples are carried for the magnetically shielded oven to the sample tray), and/or an induced component within the magnetometer.

Below 70 mbsf, the ChRM is more difficult to resolve because of the chemical and mechanical overprinting (discussed above) and the decreased intensity. In general, it is possible to determine at least the polarity of the sample. For example, Sample 186-1150A-10H-1, 20 cm (83.90 mbsf), is normal polarity and Sample 186-1150A-12H-2, 39 cm (104.59 mbsf), is reversed polarity, but both samples give very noisy demagnetization paths on the orthogonal plots (Fig. F35). In other intervals, the magnetic directions can be resolved well (to better than 5°), particularly for some RCB cores (see Figs. F37, F38, F39).

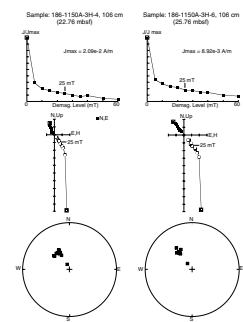
Measurements Made on the NP2 Spinner Magnetometer

Initially the noise level on the spinner magnetometer was high because of the continuous change in the ship's orientation. The noise in the electronics of the NP2 was reduced from 2 mV to 0.1 mV by placing a 3-layer μ -metal shield (35.5 cm outer diameter, 30.5 cm inner diameter, and 61 cm height) over the spinner magnetometer. After stacking repeat measurements 10 times, the noise level approached that of the cryogenic magnetometer (see "Paleomagnetism," p. 12, in the "Explanatory Notes" chapter). Demagnetization of the NRM and ARM was conducted up to 40 mT in 10-mT steps (Tables T10, T11, both also available in ASCII format). The ARM was applied in a peak AF of 40 mT with a 29- μ T direct current-biasing field (Table T10).

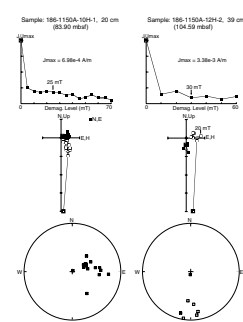
Measurements made by the NP2 agree well with those of discrete samples and split-core sections made by the cryogenic magnetometer. As noted above, for APC cores, the inclinations from discrete samples were on average 8° to 13° shallower than from the split-core sections. In addition, the inclinations from the NP2 are shallower than discrete samples measured by the cryogenic magnetometer by an insignificant $2.5^\circ \pm 3.4^\circ$ (95% confidence limit). Thus, similar conclusions to those discussed above can be drawn from the NP2 data.

Some additional insights, however, can be gained from the NP2 data because the NP2 provides measurements beyond those commonly obtained by the cryogenic magnetometer. In particular, demagnetization of the ARM shows an interesting contrast to the NRM demagnetization (Figs. F40, F41). The median destructive field (MDF)—the AF demagnetization field at which half of the magnetization is removed—for the NRM is typically <8 mT from 0 to 150 mbsf, whereas it averages 20 mT for the ARM. This illustrates two main points. First, there must be a significant proportion ($\geq 50\%$) of magnetic minerals in the samples that have coercivities greater than 20 mT as shown by the MDF for the ARMs. Second, the drill-string overprint, which applies an IRM, is very effective at magnetizing the sediments with coercivities <8 mT. On the other hand, the processes by which the sediments in the upper part of the sedimentary section acquire an ancient magnetization, presumably by a depositional remanent magnetization (DRM) or a postdeposition remanent magnetization (pDRM), must be fairly poor at orienting/magnetizing the minerals in the direction of the ambient field, at least poor relative to an ARM. Had the NRM been as effective as the ARM at mag-

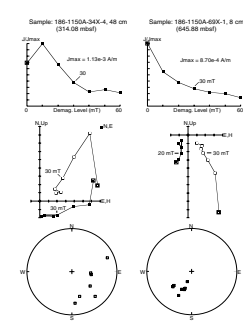
F34. Demagnetization behavior of Samples 186-1150A-3H-4, 106 cm, and 186-1150A-3H-6, 106 cm, p. 110.



F35. Demagnetization behavior of Samples 186-1150A-10H-1, 20 cm, and 186-1150A-12H-2, 39 cm, p. 111.



F36. Demagnetization behavior of Samples 186-1150A-34X-4, 48 cm, and 186-1150A-69X-1, 8 cm, p. 112.



netizing the magnetic minerals with coercivities greater than 8 mT, then the MDF for the NRM would have been similar to that for the ARM.

Below 150 mbsf, the MDF of the ARM and NRM are similar, both averaging ~20 mT, though the MDF for the NRM shows much greater variability. Below 650 mbsf, one-third of the samples have MDFs greater than 40 mT. Two primary processes contribute to the change in behavior with depth. First, the proportion of magnetic minerals with coercivities <~8 mT decreases below ~150 mbsf, a point that can also be drawn from the split-core data (e.g., Figs. F26, F27). Because larger magnetic grains commonly have lower coercivities, this indicates that there are more coarse-grained magnetic minerals above 150 mbsf than below. As discussed above, reduction diagenesis is likely responsible for the decrease in magnetization and in concentration of magnetic minerals as magnetite and titanomagnetite grains are converted to iron sulfide minerals. Second, the magnetic minerals with coercivities higher than ~10–20 mT are more effectively magnetized below ~150 mbsf. Thus, the magnetization imparted by the ARM is more similar to the NRM below 150 mbsf than above.

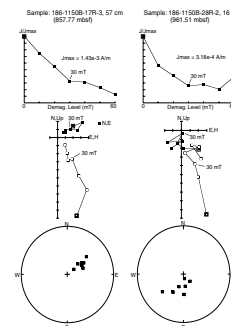
Rock Magnetic Experiments

The only direct evidence of the identity of magnetic minerals comes from visual examination of the cores and from smear-slide analyses. Both of these confirm the presence of iron sulfides in the form of pyrite patches on the surface of many split cores and pyrite framboids in the smear slides (see “Lithostratigraphy,” p. 14, and the “Core Descriptions” contents list). Pyrrhotite (e.g., Fe_7S_8) and greigite (Fe_3S_4) might also be expected to be present in the reducing environment in which the sediments have been deposited. Pyrite is paramagnetic and so carries no remanent signal, though pyrrhotite and greigite may contribute to the paleomagnetic signal (e.g., Chapter 3 of Opdyke and Channell, 1996). Other minerals common to marine sediments include magnetite (Fe_3O_4), titanomagnetite ($Fe_{2+x}Ti_{1-x}O_4$; $0 < x \leq 1$), maghemite ($\gamma-Fe_2O_3$), and hematite (Fe_2O_3).

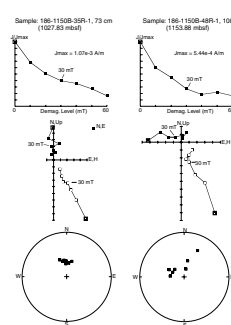
In an attempt to determine the identity of the magnetic minerals that are the most significant carriers of the remanent magnetization, we have conducted a variety of rock magnetic experiments. Each experiment provides only circumstantial evidence. Some of the characteristics we use include the unblocking temperature and coercivity spectra. Curie/Néel temperatures are 320°C for greigite, ~325°C for pyrrhotite, -150°C to 580°C for titanomagnetite, 580°C for magnetite, and 675°C for hematite. At temperatures >250°C maghemite inverts to hematite, and at a temperature >300°C iron sulfides oxidize to magnetite (e.g., Opdyke and Channell, 1996). The coercivities of these minerals are dependent on grain size and/or relative amount of titanium. In general, titanomagnetite’s coercivity < magnetite ~ maghemite ~ greigite < pyrrhotite < hematite (e.g., Opdyke and Channell, 1996).

From the thermal demagnetization of the NRM, we know that most of the unblocking temperatures of the NRM are <300°C (Figs. F32, F33, F42). However, we were prevented from looking at the higher end of the temperature spectrum because the samples demagnetize to the noise level of the magnetometer above ~300°C. We circumvented this problem by thermal demagnetization of a composite three-axis IRM using the method of Lowrie (1990). Four samples from normally magnetized zones in Hole 1150B were selected. IRMs of 1 T, 0.3 T, and 0.1 T,

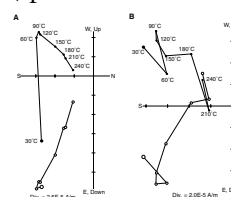
F37. Demagnetization behavior of Samples 186-1150B-17R-3, 57 cm, and 186-1150B-28R-2, 16 cm, p. 113.



F38. Demagnetization behavior of Samples 186-1150B-35R-1, 73 cm, and 186-1150B-48R-1, 108 cm, p. 114.



F39. Example of progressive thermal demagnetization of a discrete sample, p. 115.



T10. NRM and ARM results from the NP2 magnetometer before and after AF demagnetization, p. 192.

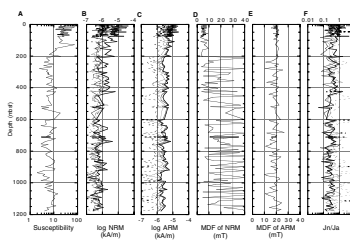
T11. NRM results from the NP2 magnetometer before and after AF demagnetization, p. 193.

respectively, were imparted along the three axes of each sample and then progressively demagnetized in 30°C steps. The results from all samples are similar (Fig. F43). First, demagnetization of the 1-T component (the high or “hard” coercivity component) can be separated into three segments: a 30° to 180°C segment with a gradual decay in magnetization, a 180° to 360°C segment with a sharp decrease, and a 360° to 600°C segment with a gradual decay of the remaining magnetization (~20%–25%). The 0.1-T (“soft”) and 0.3-T (“medium”) components showed similar behavior but were weak and difficult to monitor accurately. The retention of some magnetization for the hard component between 330° and 600°C indicates the presence of fine-grained magnetite and/or low-titanium titanomagnetite. Those minerals with unblocking temperatures <330°C could be pseudo-single or multidomain magnetite, titanomagnetite, maghemite, pyrrhotite, or greigite.

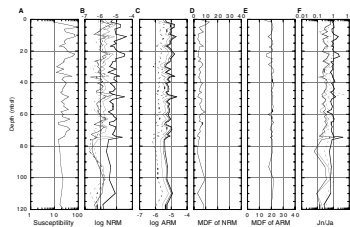
The sediments also contain a viscous remanent magnetization (VRM) component as shown by combined thermal and AF-demagnetization experiments (Fig. F39). In this experiment, samples were taken in stably magnetized intervals and then thermally demagnetized. After each thermal demagnetization step, a sample was measured in the cryogenic magnetometer (Fig. F39B) and then subjected to a weak AF demagnetization (5 mT) to remove soft coercivity components and remeasured (Fig. F39A). Soft components with intensities of $1\text{--}2 \times 10^{-5}$ A/m appeared after samples were heated in the furnace. This can be seen by comparing the data before and after AF demagnetization. Before AF demagnetization, the sample displays a variable decay of magnetization and changes in directions (a noisy signal) on the orthogonal plot, whereas after demagnetization the sample has a very linear decay of magnetization. The noise is attributed to a VRM that is acquired during the time the sample cools in the oven or in the time it takes to carry the sample from the oven to the sample tray. Because VRMs are commonly associated with coarse-grained minerals, we can conclude that part of the magnetic mineralogy includes a viscous coarse-grained assembly of minerals.

AF demagnetization of the NRM, ARM, and IRM, along with IRM acquisition experiments for the upper three cores (Fig. F44), indicate that coercivities are also consistent with magnetite or titanomagnetites being the dominant magnetic minerals. Some intervals appear to have an additional magnetic mineral that has a significant susceptibility but contributes little to the paleomagnetic intensity. Evidence for this comes from the relative paleointensity records, which can be derived by normalizing the NRM intensity after 30 mT demagnetization by the susceptibility (NRM/k), and by the ARM (NRM/ARM) and IRM (NRM/IRM), both also after 30 mT demagnetization (Fig. F45). The normalization removes the effect of variations in the concentration of the magnetic minerals, assuming that the minerals present are those that carry the remanent signal. All three records would then give similar relative paleointensities. The NRM/ARM and NRM/IRM records give similar results but the NRM/k record differs from the other two in a couple of intervals. The presence of iron sulfides could explain this observation because the iron sulfides have high susceptibilities but often do not carry a paleomagnetic signal (e.g., Chapter 3 of Thompson and Oldfield, 1986). Alternatively, a viscous coarse-grained titanomagnetite assembly could be responsible for the differences since the viscous assembly of grains would be represented in the susceptibility but could be remagnetized in the time it takes to carry the samples across the lab following application of the ARM or IRM.

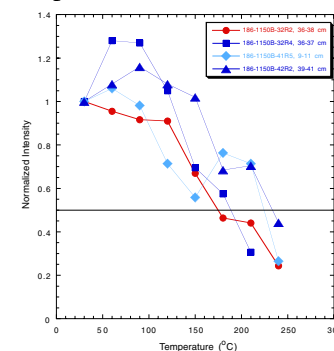
F40. Discrete sample results from the NP-2 spinner magnetometer, p. 116.



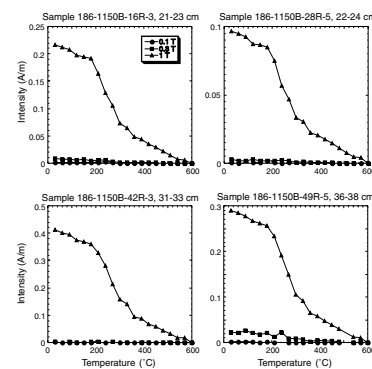
F41. Results from the NP-2 spinner magnetometer for discrete samples from the top 120 mbsf of Hole 1150A, p. 117.



F42. Normalized change in intensity during thermal demagnetization, p. 118.



F43. Thermal demagnetization of isothermal remanent magnetizations, p. 119.



From the above information, we suggest that magnetite and titanomagnetite are present in fine- to coarse-grain sizes and are the dominant magnetic minerals. The low coercivity and low unblocking temperature component, that which acquires the drill-string overprint, is likely carried by the coarser grain sizes (multidomain grains) and by high-titanium titanomagnetites. The ChRM or paleomagnetic signal is likely carried by the finer grain sizes (pseudo-single and single-domain grains) and by magnetite and low-titanium titanomagnetite. Pyrrhotite, greigite, and maghemite could also be present and could contribute significantly to the remanent signal, though their presence is not required based on the observations.

Chemical Treatments

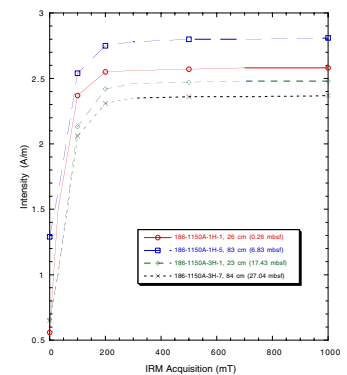
Chemical treatments of seven samples from XCB and RCB intervals illustrate that some of the magnetic minerals, particularly part of the fine-grained fraction, may be bound to organic matter (OM) and carbonate. This could explain why the demagnetization spectrum for the NRM and ARM differ, since both DRM and pDRM processes would be less effective at orienting the fine-grained fraction if it was bound to other material.

The seven samples were selected from the core catchers. Three samples were from diatom dominant intervals (Cores 186-1150A-21X, 41X, and 61X). Four samples were taken from cyclic changing intervals where diatom dominant (Cores 186-1150B-36R and 48R) or terrigenous-matter dominant (Cores 186-1150B-28R and 40R). They were remagnetized to the present geomagnetic field.

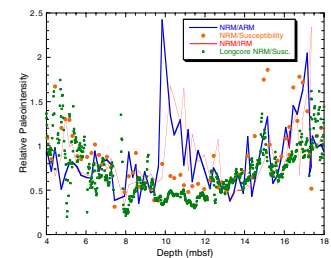
The chemical treatments were conducted as follows: the selected samples were ground into a loose sediment. The sediments were washed with water and centrifuged for 10–20 min at 4000 rpm. Each sample was then divided into two specimens, which were placed in plastic sample cubes (the French cube). The first specimen had its NRM measured and then was demagnetized at 5, 10, 20, 30, and 40 mT. These and other measurements were made by N. Niitsuma in the NP2 magnetometer. Next, the sample was given an ARM and then demagnetized as with the NRM. The second specimen was subjected to various reagents (using ~30 mL). First, the sediment was removed from the cube, soaked in 5% hydrogen peroxide (H₂O₂) for 1 hr, washed with water, centrifuged, and packed back into the cube, and then the remanence was measured before and after 5 mT AF demagnetization. Second, the sediment was removed from the cube, soaked in 0.03-M disodium ethylenediamine-tetraacetate (EDTA) for 6 hr, washed with water, centrifuged, and packed back into the cube, and then the remanence was measured before and after 5 mT AF demagnetization. Third, the sediment was removed from the cube, soaked in 2-N hydrochloric acid (HCl) for 1.5 hr, washed with water, centrifuged, and packed back into the cube, and then the remanence was measured before and after AF demagnetization at 5, 10, 20, 30, and 40 mT. The sample was given an ARM and then demagnetized again up to 40 mT. The results are given in Table T12, also available in [ASCII format](#).

Hydrogen peroxide breaks down OM. The overall magnetization showed a decrease only for Sample 186-1150A-21X-CC and increases for the three lowermost samples (Table T12). This is interpreted as an increase in the magnetic fraction, possibly by oxidation of iron or by a release of the magnetic fraction that was bound to OM. The released fraction would then be able to orient to the ambient field. In either case, the magnetic fraction released or created was most likely coarse

F44. IRM acquisition results from Hole 1150A APC cores, p. 120.



F45. Relative paleointensity for a short interval from the APC cores, p. 121.



T12. Results of chemical treatments, p. 194.

grained because the MDF decreased from 10–23 mT to 2.3–5.5 mT for the four shallowest samples. This is interpreted as an overall loss of the fine-grained fraction.

EDTA removes Ca and Mg ions and decomposes carbonates. The changes in the intensities of remanent magnetization after the EDTA treatment varied with samples, as shown in Table T12. This variation may be explained by depth-dependent releases of different grain size particles. For example, the samples from depths above the salinity cline, determined from the interstitial water (<400 mbsf), showed increases where carbonates with finer grained particles were deposited on the seafloor. Below this, the finer grained particles may have been dissolved. The intensity increase and larger MDFs above 400 mbsf may therefore have occurred as a result of releases of finer grains.

Most of the remanent magnetization was destroyed by the HCl treatment. However, the ARM measurements suggest that the remaining ARM carrier is different from that of NRM.

The results from above-described chemical experiments, together with other results, are expected to help relate intensity changes to different depths and infer their causes among decomposition of OM, dissolution of carbonates, or precipitation of the diagenesis. For example, although further verification is necessary, Figure F46 constructed from Table T12 suggests that the above processes seem to be depth dependent.

Magnetostratigraphy

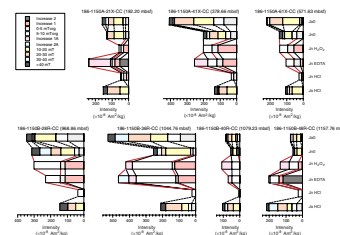
Magnetostratigraphic interpretation is hampered by the large amount of overprinting caused by drilling, reduction diagenesis, coring disturbance, and structural deformation. Even determining the location of the Brunhes/Matuyama reversal was difficult because gas expansion caused core deformation and resulted in the destruction of core liners for Cores 186-1150A-10H and 11H and the loss of their azimuthal orientation. Unfortunately, the Brunhes/Matuyama boundary probably occurs in this region of core deformation, probably near the top of Core 186-1150A-10H (~84.18 mbsf). Below this there are a few prominent reversals, but identifying the geomagnetic chron to which they belong is impossible without additional age information.

Diatom datums provide the main age control for the sediments at Site 1150. A magnetostratigraphy generated from the diatom age constraints (see “Biostratigraphy,” p. 10, in the “Explanatory Notes” chapter) predicts the location of some of the best resolved reversals observed in the paleomagnetic inclination data (Fig. F47; Table T9). Given the overall age constraints provided by the diatoms, the prominent reversals can be used to make slight adjustments to the age estimates for the sediments, particularly between diatom datums. None of the adjustments violate the diatom datums, and together the biostratigraphic and magnetostratigraphic data provide good constraints on the sedimentation rates (see “Sedimentation Rates,” p. 35).

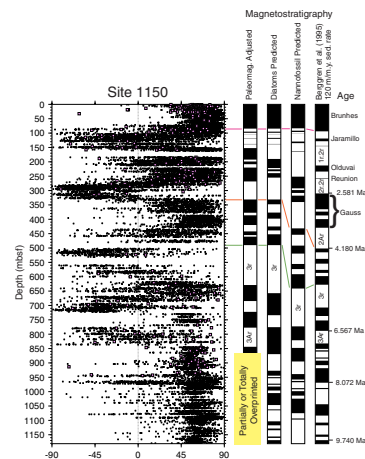
SEDIMENTATION RATES

Because the diatom and calcareous nannofossil datum levels used in this study have been tied to the geomagnetic polarity time scale (see “Biostratigraphy,” p. 10, in the “Explanatory Notes” chapter), Site 1150 sedimentation rates can be estimated by combination of bio-

F46. Magnetic properties changes caused by chemical treatments, p. 122.



F47. Magnetostratigraphic models, p. 123.



stratigraphy and magnetostratigraphy. This estimation is based primarily on datums of diatom zonal boundaries because diatom valves were well preserved and the datums were continuously recognized. The magnetostratigraphy is poorly constrained and at best provides a few reversal boundaries that can be used to adjust the age estimates predicted between diatom datums. A magnetostratigraphy derived from the diatom datums does, however, accurately predict several of the more prominent observed reversal boundaries, and so we consider the two to be in good agreement above ~850 mbsf. Below ~850 mbsf, however, the inclination indicates a long interval with normal polarity, which is interpreted as an overprint (see “Paleomagnetism,” p. 27).

As discussed in “Biostratigraphy,” p. 23, calcareous nannofossil datums indicate younger ages than those from diatom biostratigraphy between 150 and 900 mbsf. The age assignments based on calcareous nannofossils at Site 1150 are uncertain because there are few nannofossils and these occur discontinuously, the nannofossils have poor preservation, and the datum levels are possibly diachronous.

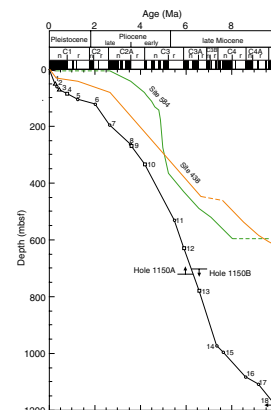
The control points for age assignment were thus chosen from eleven diatom datums, five geomagnetic chron boundaries above 800 mbsf, and two nannofossil datums above 80 mbsf (Table T13). Ages of diachronous events were averaged, but the age of the FO of *N. koizumii* (diatom) was defined as its youngest value (3.53 Ma) because the bottom of the Gauss Chron (C2An/C2Ar, 3.58 Ma) was recognized immediately below this datum. Since the FO of diatom *D. dimorpha* was not found, the lowermost depth (1180.23 mbsf) is slightly younger than 9.9 Ma. The average sedimentation rate is >119 m/m.y.

In general, the sedimentation rate of Site 1150 is high relative to nearby DSDP Sites 438 and 584 (Fig. F48), suggesting a much greater amount of biogenic and/or detrital input to the basin around this site. An age-depth plot for Holes 1150A and 1150B indicates that the upper 70 m has a relatively high sedimentation rate (108 to 205 m/m.y.), which may be related to lower compaction of the uppermost part (see “Physical Properties,” p. 41). There is an interval of significantly low sedimentation rates between 70 and 122 mbsf (24 to 42 m/m.y.). It is possible that there is a very short hiatus (<0.42 m.y.) between 120 and 122 mbsf because the FO of the Pleistocene diatom *P. curvirostris* is recognized in this interval, together with the LO of the late Pliocene fossil *N. koizumii* (see “Biostratigraphy,” p. 23). More detailed postcruise study will be necessary to confirm this. In the interval between 122 and 195 mbsf, the sedimentation rate increases to 114 m/m.y. Below this depth the rate decreases to 76 m/m.y., and then increases gradually until 530 mbsf. High sedimentation rates (>200 m/m.y.) occur between 530 and 971 mbsf, with the highest value of 248 m/m.y. in the interval of 529–629 mbsf. Below this the rate suddenly decreases, varying from 43 to 100 m/m.y.

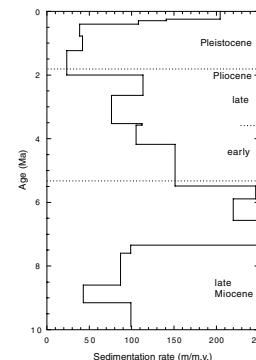
Though sedimentation rates at Site 1150 are high and hiatuses are absent or span a very short interval of time, there is a common trend of the sedimentation rate between Site 1150 and Sites 438 and 584. In particular, all three sites had high rates in the latest Miocene and early Pliocene and low rates before and after this (Fig. F49). On the other hand, two intervals of low rates correspond to the early late Miocene (prior to 7.35 Ma) and the early to mid-Pleistocene (2.0–0.41 Ma), respectively. In general, the intervals of high sedimentation rate during the latest Miocene to the early Pliocene (~7.5–3.0 Ma) correspond to higher content of opal-A (see “Lithostratigraphy,” p. 14). In addition, a higher concentration of terrigenous minerals occurs in the upper Mio-

T13. Age control points for datum events and sedimentation rates, p. 195.

F48. Age-depth relationship, p. 124.



F49. Sedimentation rate vs. age, p. 125.



cene (~7–6 Ma) and the upper Pleistocene, which also correspond to the higher sedimentation rates. Therefore, increasing siliceous biogenic and terrigenous siliciclastic inputs may both be related to the change of the sedimentation rate.

GEOCHEMISTRY

The shipboard geochemistry program at Site 1150 included (1) analyses of volatile hydrocarbons; (2) determinations of abundances of inorganic carbon, total carbon, total sulfur, and total nitrogen in sediments; and (3) measurements of salinity, alkalinity, pH, and concentrations of some dissolved anionic species in interstitial waters (for description of methods see “Geochemistry,” p. 15, in the “Explanatory Notes” chapter).

Volatile Hydrocarbons

Headspace Gas

Gas analyses at Site 1150 indicate that most hydrocarbon gases are below detection limits, with the exception of methane and ethane. Methane (C_1) concentrations range from 0.05% to 9%, whereas ethane (C_2) concentrations range from undetectable values to 26 ppmv, as measured from headspace gas analyses (Table T14, also available in ASCII format). C_1 and C_2 concentrations show a similar distribution with depth (Fig. F50). Both concentrations irregularly increase in the upper 120 m to reach values of ~5% for C_1 and 12 ppmv for C_2 . Concentrations then irregularly decrease to ~1% for C_1 and 2 ppmv for C_2 at 250 mbsf and remain at about these low values for ~300 m downhole. C_1 and C_2 concentrations steadily increase to reach maximum values of 9% for C_1 and 26 ppmv for C_2 at 1100 mbsf and then decrease to ~2% for C_1 and 9 ppmv for C_2 at the bottom of the borehole.

C_1/C_2 values abruptly decrease from 22,230 at the top to ~4200 at 60 mbsf because of the increase in ethane. Values then irregularly increase to ~6000 at ~500 mbsf. Below this depth, C_1/C_2 values tend to gradually decrease with depth to reach a minimum value of ~2800 at the bottom of the borehole (Fig. F50).

Free-Gas Samples

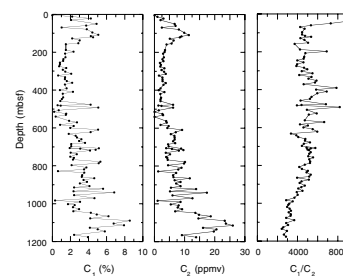
Free gases withdrawn from within core liners (for description of methods see “Geochemistry,” p. 15, in the “Explanatory Notes” chapter) show that C_1 and C_2 concentrations throughout the borehole are similar, ranging from 87% to 90% for C_1 and 79 to 7633 ppmv for C_2 (Table T15). Other hydrocarbon gases are below detection limits.

Carbonate Content

Carbonate abundances typically are of ~2–4 wt% and exhibit several excursions with values as high as 70 wt%. Most of these excursions, however, fall between 5 and 12 wt%. Values lower than 0.2 wt% are also observed in several intervals (Fig. F51). These low carbonate abundances are in agreement with few to trace occurrences of calcareous nannofossils in the sediments (see “Biostratigraphy,” p. 23).

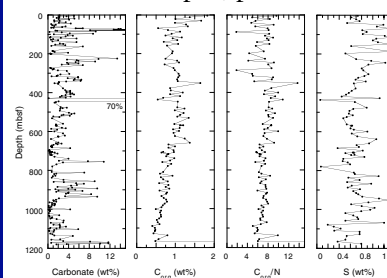
T14. Headspace concentrations of light hydrocarbons, p. 196.

F50. Distribution with depth of headspace concentrations of C_1 and C_2 , and C_1/C_2 ratios, p. 126.



T15. Results of gas pocket analyses, p. 197.

F51. Distribution of carbonate, C_{org} , C_{org}/N ratios, and S abundances with depth, p. 127.



Organic Carbon, Total Nitrogen, and Total Sulfur

Abundance of organic carbon (C_{org}) fluctuates between 0.5 and 1.8 wt%, with an average value of ~ 0.8 wt% (Fig. F51). C_{org} values tend to decrease in the upper 200 m from 1.8 wt% at the top to ~ 1 wt%. This value remains as the typical C_{org} abundance for ~ 450 m down in the borehole. Values then irregularly decrease to reach a minimum of 0.5 wt%. C_{org}/N ratios range from 2 to 13 with typical values of ~ 7 (Fig. F51). The distribution of C_{org}/N shows an irregular pattern in the upper 400 m with values fluctuating between 4 and 9. Below this depth, C_{org}/N values are more regular ranging from 6 to 9. Total sulfur abundances irregularly fluctuate between 0.5 and 1.35 wt% with an average value of 0.85 wt% (Fig. F51).

Interstitial Waters

A total of 39 whole-round samples from Holes 1150A and 1150B were analyzed for pH, alkalinity, salinity, chlorinity, sodium, potassium, magnesium, calcium, sulfate, ammonium, lithium, and strontium. Results are summarized in Table T16 (also available in [ASCII format](#)).

Salinity and Chlorinity

Salinity and chlorinity exhibit in general a similar trend with depth (Fig. F52). Values gradually decrease with depth from ~ 34 for salinity and 550 mM for chlorinity at the top of the borehole to 30 and 500 mM at ~ 100 mbsf. Salinity remains constant at 30 for 350 m down in the borehole. Chlorinity concentrations remain constant for ~ 200 m down in the borehole and gradually increase from this depth down to ~ 550 mbsf, reaching values of 520 mM. Chlorinity concentrations then abruptly decrease to 350 mM at ~ 700 mbsf. Below this depth, chlorinity gradually decreases to ~ 300 mM at the bottom of the borehole. Salinity also decreases rapidly with depth from 30 at ~ 450 mbsf to 18 at ~ 800 mbsf and remains at this value to the final depth.

Alkalinity, and Dissolved Sulfate and Ammonium

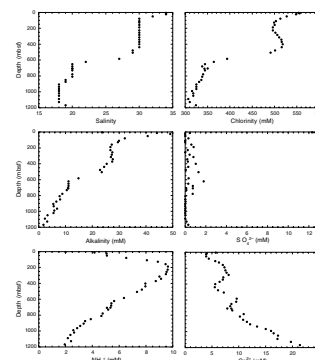
Alkalinity values drastically increase downhole in the upper 20 m from 24 to 49 mM (Fig. F52). Values decrease rapidly downhole to 27 mM at ~ 200 mbsf and remain at about this value for ~ 180 m. Alkalinity values then decrease to 2 mM in the remaining portion of the borehole. This downhole decrease is particularly abrupt in the interval between 470 and 600 mbsf. Dissolved sulfate concentrations (SO_4^{2-}) drastically decrease from 12.3 to <0.5 mM in the upper 10 m (Fig. F52). These very low values persist down throughout the borehole. Some higher values reaching 2 mM are present, however, between 400 and 600 mbsf. These higher values are probably the result of seawater contamination. Ammonium concentrations increase from 1.6 to 9.6 mM in the upper 200 m and then gradually decrease to ~ 2 mM at the final depth of the borehole (Fig. F52).

Dissolved Calcium, Magnesium, and Strontium

Concentrations of dissolved calcium (Ca^{2+}) in pore waters decrease slightly downhole in the upper 30 m of the core, from values of ~ 6 mM at the top to ~ 4 mM at 30 mbsf (Fig. F52). From this depth, Ca^{2+} con-

T16. Results of interstitial water analyses, p. 198.

F52. Distribution with depth of pore-water geochemical abundances, p. 128.



concentrations gradually increase to 8.5 mM at ~300 mbsf and decline to ~5 mM at 420 mbsf. Concentrations then gradually increase with depth to reach a maximum of 21.6 mM at the bottom of the borehole.

Concentrations of dissolved magnesium (Mg^{2+}) rapidly decrease in the upper 120 m from 49 to 26 mM, then slightly increase to 31 mM at ~350 mbsf and decline to a minimum value of 10 mM at the bottom of the borehole. This decline is particularly abrupt between 500 and 660 mbsf (Fig. F52).

Concentrations of dissolved strontium (Sr^{2+}) increase rapidly in the upper 250 m from 92 to 198 μM . Sr^{2+} concentrations then decline to 147 μM at ~480 mbsf and increase to reach a maximum of ~260 μM at the bottom of the borehole (Fig. F52).

Dissolved Sodium, Potassium, and Lithium

Concentrations of dissolved sodium (Na^+) gradually decrease downhole from 460 to 430 mM in the upper 225 m of the borehole and then increase to ~450 mM at 410 mbsf. Below this depth, Na^+ concentrations decline to a minimum value of ~250 mM at the bottom of the borehole. This decline is particularly abrupt between 450 and 600 mbsf (Fig. F52).

Concentrations of dissolved potassium (K^+) gradually decrease in the upper 200 m from 11 mM to 8 mM and remain at about this value for 300 m downhole in the core (Fig. F52). K^+ concentrations then abruptly decrease to 6 mM at ~620 mbsf and remain at this value to the bottom of Hole 1150A. K^+ concentrations in Hole 1150B exhibit a decreasing trend with depth in the remaining interval of the borehole to a minimum value of ~6 mM.

Concentrations of dissolved lithium (Li^+) gradually increase from 19 to 380 μM in the upper 220 m and decrease to ~300 μM at ~400 mbsf. Below this depth, Li^+ concentrations gradually increase to ~450 μM at 800 mbsf and then decline to 241 μM at the bottom of the borehole (Fig. F52).

Discussion

The profiles of dissolved chemical species at Site 1150 exhibit similar trends allowing the subdivision of four characteristic geochemical intervals. The upper interval corresponds to approximately the upper 200 m. This interval is characterized by (1) the gradual decrease in alkalinity, salinity, chlorinity, Na^+ , K^+ , and Mg^{2+} ; (2) the gradual increase in Li^+ , Sr^{2+} , and Ca^{2+} ; and (3) abundant methane in the sediments. The presence of gas hydrates in the sediments would explain the abundant methane and the distribution of chemical species in pore waters. In support of this preliminary interpretation, logging data indicate that this interval is also characterized by high resistivities and low density values (see "Downhole Measurements," p. 49). Similar chemical and physical characteristics have been reported for a number of gas hydrate accumulations (e.g., Hesse and Harrison, 1981; Kvenvolden and Kastner, 1990; Sloan, 1990; Malone, 1994).

This upper interval at Site 1150 also exhibits relatively high OM abundances with characteristic low (<10) C/N ratios, suggesting that most of the OM is marine in origin (Tyson, 1995). It is possible, however, that these ratios are higher because sediments, and not kerogens, were analyzed. Total nitrogen in sediments includes both organic and inorganic sources. The contribution of inorganic sources to the total

nitrogen content in sediments is generally low and typically corresponds to inorganic ammonium incorporated in the interlayer position of smectites (e.g., Muller, 1977).

The relatively high content of OM in the sediments is the result of high productivity rates prevailing in the eutrophic Oyashio Current (Handa and Tanoue, 1980). In addition to high productivity rates, high OM content in the sediments can also be the result of the high sedimentation rates estimated at the site (see "[Sedimentation Rates](#)," p. 35), causing the rapid removal of OM from the oxic conditions prevailing at the seafloor, where OM is efficiently degraded by microbial activity.

The decrease in sulfate concentrations to below detection limits or very low values in the upper 10 m can be explained by the activity of sulfate-reducing bacteria. These bacteria utilize sulfate to oxidize OM, leaving reduced sulfur as a by-product. Sulfide minerals are formed as a result of the reaction of reduced sulfur with iron and probably are the main constituent in the total sulfur content determined in the sediments (see "[Lithostratigraphy](#)," p. 14). The rapid trend in decreasing sulfate concentrations in pore waters at Site 1150 can be explained by a combination of high productivity and high sedimentation rates. In areas with high productivity rates, the sulfate-reducing zone is relatively shallow due to the large amount of labile OM delivered to the sediment, promoting the rapid utilization of sulfate by microbes (Claypool and Kaplan, 1974). In addition, fast sedimentation rates result in the rapid OM burial and cause limited exchange of sulfate between pore water and seawater (Berner, 1980).

Degradation of OM in the sulfate-reducing zone can explain the increased alkalinity at Site 1150 because bicarbonate and ammonium are created during degradation of OM. An additional source of alkalinity is the silica released during alteration of either volcanic ash or biogenic opal present in the diatomaceous silty clay of the sediments (see "[Lithostratigraphy](#)," p. 14). Bicarbonate can also be generated by the oxidation of methane in the sulfate-reducing zone. This methane is originated by the partial degradation of OM by methanogens below the sulfate-reducing zone. Evidence for methanogenic activity with depth is suggested by increasing ammonium and methane gas concentrations below the minimum of sulfate at Site 1150. In addition to OM, opal and carbonates are other biogenic sources of material in the sediments. Opal alteration in the sediments yields Li^+ (Gieskes, 1983), accounting for the gradual increase of Li^+ concentration in pore water with depth in the upper interval. Similarly, dissolution of biogenic carbonates (Gieskes, 1983) explains the increased Ca^{2+} and Sr^{2+} values in the interval.

A second characteristic geochemical interval is between ~200 and 450 mbsf and corresponds to sediments with relatively constant or slightly changing pore-water chemistry with depth. Alkalinity, chlorinity, Na^+ , K^+ , and Mg^{2+} increase slightly with depth, whereas Li^+ , Ca^{2+} , and Sr^{2+} decrease slightly with depth. The subtle increasing trend in the concentrations of dissolved chemical species could be the result of gas hydrates present in the upper interval. Formation of gas hydrates and the consequent removal of water can result in a gradient that promotes the upward and downward diffusion of dissolved chemical species (Hesse and Harrison, 1981). This migration should therefore result in increasing concentration of dissolved chemical species above and below the gas hydrates. The increased concentrations above the gas hydrates are not observed at Site 1150, probably because of dilution of pore waters with seawater.

A third interval between ~450 and 600 mbsf is characterized by an abrupt change in pore-water chemistry. Alkalinity, salinity, chlorinity, K^+ , Na^+ , and Mg^{2+} rapidly decrease with depth, whereas Li^+ , Ca^{2+} , and Sr^{2+} abruptly increase. This interval probably corresponds to the boundary between two zones with different pore-water chemistry.

The deepest interval spanning depths below ~600 mbsf is characterized by a slight change in pore-water chemistry with depth. Alkalinity, salinity, chlorinity, Na^+ , K^+ , Li^+ , and Mg^{2+} exhibit low values and a decreasing trend with depth, whereas Sr^{2+} and Ca^{2+} exhibit a slight increase coupled with an excursion in C_1 and C_2 abundances (Fig. F50).

The origin of the pore waters in the last interval is unknown; however, several scenarios might explain the low salinity and chlorinity values. One of these scenarios is influx of meteoric waters. Site 1150 is located over 100 km from shore, making the possibility of groundwater influx unlikely. Another scenario is that the pore waters were meteoric in origin at the time of accumulation of the sediments. This is also unlikely since there is no evidence for shallower environments of accumulation. The sediments at Site 1150 are hemipelagic throughout the entire borehole (see “**Lithostratigraphy**,” p. 14). In addition, the diatom assemblages identified in the record provide no evidence of less saline or brackish conditions at the time of accumulation (see “**Biostratigraphy**,” p. 23). Another scenario is in situ dewatering of smectites releasing freshwater and causing the observed profiles. Two lines of evidence preclude this possibility. The amount of smectites present in the sediments is not enough (see “**Lithostratigraphy**,” p. 14) to cause the observed decrease in salinity, and the temperature prevailing at the borehole (see “**Downhole Measurements**,” p. 49) is not high enough to promote dewatering of smectites. Another scenario involves in situ dewatering of biogenic opal, but the amount present in the sediments is not enough to account for the drastic decrease in salinity and chlorinity in pore water. The only possible scenario at the moment is that less saline conditions are caused by upwelling of water with lower salinity. The source of these waters is probably related to dewatering of deeper sediments.

PHYSICAL PROPERTIES

Measurements on whole-round core sections taken in Holes 1150A and 1150B included magnetic susceptibility, GRA bulk density, P -wave velocity, NGR activity, and thermal conductivity. P -wave velocity, shear strength, and index properties measurements were made on what appeared to be the least-disturbed portions of split-core sections. Hence, sampling was biased and favored indurated sections in XCB (112–723 mbsf) and RCB (703–1180 mbsf) cores. Descriptions of the experimental methods are provided in “**Physical Properties**,” p. 18, in the “Explanatory Notes” chapter.

Multisensor Track

Magnetic susceptibility was measured with a 2-cm sampling interval on all cores recovered in Holes 1150A and 1150B. The results of magnetic susceptibility measurements are discussed in “**Paleomagnetism**,” p. 27.

GRA bulk density was measured with a 2-cm sampling interval on all cores at this site. In addition, a number of whole-round core sections

from Hole 1150B (i.e., 42R-4, 43R-5, 44R-2, 47R-2, and 50R-5) were re-run with a 1-cm sampling interval to aid the selection of suitable whole-round core samples for postcruise laboratory tests. The GRA data are most reliable in filled APC and XCB cores, whereas RCB cores generally yield lower values because the core does not completely fill the liner. For the preliminary onboard processing, the GRA data from RCB cores in Hole 1150B were corrected because the cores did not completely fill the core liner (see “**Physical Properties**,” p. 18, in the “Explanatory Notes” chapter). In general, RCB cores in Hole 1150B had rather constant diameters and few crushed intervals (see the “**Core Descriptions**” contents list). With a diameter of 57 mm, we obtained a good fit with bulk density measurements on discrete samples and similar magnitudes as the overlapping GRA measurements on XCB cores in Hole 1150A. Finally, the density data were edited by removing values less than 1.0 g/cm³ (i.e., density of pure water). The maximum GRA bulk density is reported here because it is assumed to provide the best estimate of bulk density.

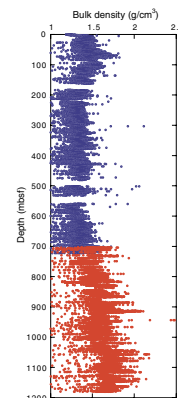
The maximum GRA bulk density values in Hole 1150A have a total range from ~1.3 to ~2.1 g/cm³, and the corrected maximum GRA bulk density values in Hole 1150B have a total range from ~1.5 to ~2.5 g/cm³ (Fig. F53). Generally, these values correspond very well with those derived from discrete samples and logging (see “**Comparison of Core and In Situ Physical Properties Measurements**,” p. 46). GRA bulk density increases from ~1.3 to ~1.8 g/cm³ in the upper 70 m of Hole 1150A. This is followed by a gradual decrease to 1.4 g/cm³ at 200 mbsf. Rather constant values, ranging from 1.3 to 1.5 g/cm³, are measured from 200 to ~620 mbsf. The GRA bulk density values increase to a maximum value of 2.1 g/cm³ at ~915 mbsf. The interval from 915 to 1047 mbsf is characterized by lower and rather constant values (1.7–1.8 g/cm³). A shift to higher and more scattered values occurs at 1047 mbsf (i.e., top of lithologic Unit IV, see “**Lithostratigraphy**,” p. 14), and GRA bulk density ranges from 1.8 to 2.2 g/cm³ to the base of Hole 1150B.

P-wave velocity in the horizontal direction was acquired with the *P*-wave logger (PWL) on full sections from the mudline to 65 mbsf and from 82 to 112 mbsf in Hole 1150A. The cores in these intervals were severely disturbed by gas expansion, which resulted in mechanical stretching and micro- to macrofracturing of the cores and explosive breakage of the core liners in two cores (186-1150A-10H and 11H). As a result, no MST measurements were made from 84 to 93 mbsf and from 96 to 103 mbsf. After the preliminary onboard processing (see “**Physical Properties**,” p. 18, in the “Explanatory Notes” chapter), the results of PWL measurements included data only from the upper 17 m of Hole 1150A. *P*-wave velocity varies between 1450 and 3237 m/s. Most values range between 1470 to 1500 m/s (Fig. F54). Higher velocities (>1650 m/s) are obtained near the edges of core sections and are assumed to be artificial.

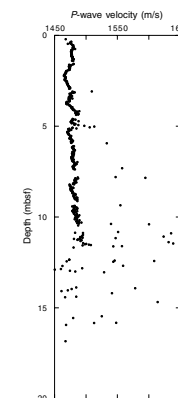
NGR activity was measured every 20 cm with 20-s-long counting periods on all cores recovered in Holes 1150A and 1150B and reported in cps with the total background radiation subtracted (12.27 cps). NGR activity has an overall range between 2 and 27 cps, and the downhole variation generally has a width of scatter of 5 to 10 cps (Fig. F55). The maximum values at each depth of NGR activity are reported here.

After a rapid increase in NGR activity from 7 cps at the seafloor to 17 cps at 7 mbsf, there is an increase to 26 cps at ~70 mbsf. Below this peak, NGR activity decreases to ~12 cps at 222 mbsf, the base of litho-

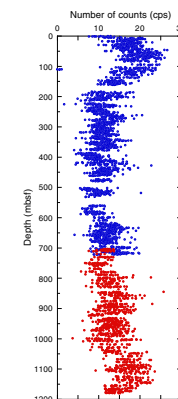
F53. Bulk density from GRA measurements, p. 130.



F54. Horizontal *P*-wave velocity from PWL measurements, Hole 1150A, p. 131.



F55. NGR activity, p. 132.



logic Unit I (see “**Lithostratigraphy**,” p. 14). The NGR activity has an oscillating and somewhat decreasing trend between 222 and 598 mbsf (i.e., lithologic Unit II), and maximum values generally range from 10 to 15 cps. Lithologic Unit III (598–1047 mbsf) is characterized by slightly higher and more scattered values (~10–20 cps). Another shift occurs at the top of lithologic Unit IV, and NGR activity decreases from ~20 cps to ~15 cps at 1180 mbsf.

Thermal Conductivity

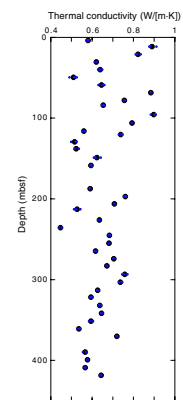
Thermal conductivity was measured at a frequency of one measurement per core down to 419 mbsf in Hole 1150A using the full-space configuration. The mean error associated with these measurements is assumed to be 0.2 W/(m·K). The average thermal conductivity, which was obtained from three measurements, ranges from 0.4 to 0.9 W/(m·K) (Fig. F56; Table T17, also available in **ASCII format**). The largest variability in values is observed in the upper 112 m of Hole 1150A (i.e., the section cored with the APC system), whereas a more uniform downhole trend is observed from 112 to 419 mbsf (i.e., the section cored with the XCB system). Apart from gas expansion, sediments cored with the APC system are little disturbed, and the variation in thermal conductivity generally has a positive correlation with bulk density and a negative correlation with porosity. On the other hand, poor correlation is obtained for thermal conductivity versus porosity and bulk density in sediments cored with the XCB system. This suggests that the drilling disturbances in XCB cores (i.e., drilling mud slurry) deteriorated the quality of the data.

P-Wave Velocity

P-wave velocity was measured in split cores with the PWS1, PWS2, and PWS3 systems. We aimed at a sampling frequency of one measurement per section. However, because of scattering and attenuation of the signal in the sediment specimen, the PWS1 and PWS2 systems could not be used below 10 mbsf, and the PWS3 system was not used from 0 to 11 mbsf and from 58 to 304 mbsf. PWS3 measurements were made through the liner (11–58 mbsf), on indurated pieces (304–710 mbsf), and on cylindrical minicores (710–1180 mbsf). For the latter, P-wave velocity was measured in two or three directions, allowing estimation of acoustic anisotropy. By combining declination data from the same depth interval as the minicores, we derived the orientation with respect to north, which provided an estimate of the azimuthal influence on the magnitude of horizontal velocity. Discrete measurements of P-wave velocity were made close to the location of samples for index properties in soft sediments and on the same piece or cylindrical minicore in more lithified sediments. The cores were much disturbed by gas expansion in Hole 1150A, which often resulted in velocity values less than 1450 m/s; therefore, they were deleted.

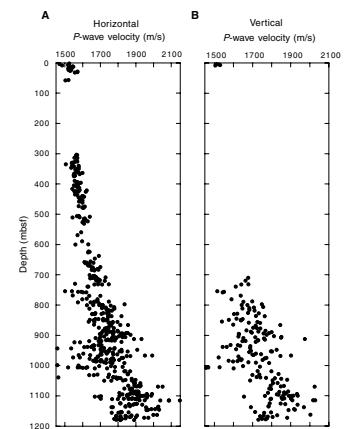
Horizontal P-wave velocity ranges from 1450 to 1570 m/s in the upper section of Hole 1150A, and the downhole trend is slightly increasing (Fig. F57; Table T18, also available in **ASCII format**). The four measurements of vertical P-wave velocity are rather constant and vary between 1510 and 1530 m/s (Fig. F57B; Table T18). Only horizontal velocity was measured from 304 to 710 mbsf; the data are well grouped and increase from ~1560 to 1750 m/s (Fig. F57A). The horizontal velocity drops to less than 1500 m/s below 750 mbsf, which is followed by a

F56. Thermal conductivity variation with depth, Hole 1150A, p. 133.



T17. Thermal conductivity, Hole 1150A, p. 199.

F57. P-wave velocity vs. depth from measurements on split cores, p. 134.



T18. P-wave velocity and anisotropy, p. 200.

generally increasing trend to 1900 m/s at the base of Hole 1150B. The lower part of Hole 1150B (920 to 1010 mbsf) comprises a zone of a wider scatter of values (1460–2000 m/s). The vertical velocity shows a similar trend as that of horizontal velocity, but with slightly lower velocities. From 710 to 1180 mbsf, vertical velocity generally increases from ~1680 to 1880 m/s (Fig. F57B). Maximum horizontal and vertical velocities in Holes 1150A and 1150B (2150 and 2090 m/s, respectively) were measured at 1115 mbsf.

Three values of anisotropy were calculated below 710 mbsf in Hole 1150B (Table T18), namely: maximum vs. minimum horizontal velocity (A_{HH}); maximum horizontal vs. vertical velocity (A_{HV}); and minimum horizontal vs. vertical velocity (A_{hV}) (see Eq. 7, p. 21, in the “Explanatory Notes” chapter). Anisotropy in the horizontal direction (A_{HH}) generally varies from 0 to 0.05, with maximum values of 0.10 at certain depths (Fig. F58A). The ranges of A_{HV} and A_{hV} are -0.04 to 0.13 and -0.08 to 0.09 , respectively (Fig. F58B). However, the vast majority of A_{HV} measurements (95%) and most A_{hV} measurements (76%) have positive values. The variation of horizontal anisotropy (A_{XY}) with azimuth was determined using paleomagnetic declination data (see “Paleomagnetism,” p. 27; see also “Physical Properties,” p. 18, in the “Explanatory Notes,” chapter). In total, 138 measurements of declination and horizontal velocity data were obtained from 731 to 1179 mbsf (Table T18). The radius of the 95% confidence circles for the paleomagnetic directions (α_{95}) varied from 1° to 51.5° . To avoid using some of the poorly constrained declinations, we selected only directions that had $\alpha_{95} \leq 4.5^\circ$. For this data set, a sinuous-shaped correlation is obtained between horizontal anisotropy and azimuth (Fig. F59). The results suggest that maximum anisotropy has an approximately west-northwest–east-southeast orientation ($\sim 120^\circ\text{N}$) and that minimum anisotropy has a north-northeast–south-southwest orientation ($\sim 30^\circ\text{N}$). The results indicate that highest, intermediate, and lowest velocities are horizontal velocities in the west-northwest–east-southeast direction, horizontal velocities in the north-northeast–south-southwest direction, and vertical velocities, respectively. However, note that the principal axes of anisotropy may deviate from purely horizontal and vertical orientations.

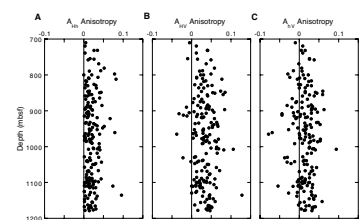
Undrained Shear Strength

For Hole 1150A cores, undrained shear strength was measured from the mudline to 27 mbsf with the vane shear device, and from 27 to 93 mbsf with the pocket penetrometer. Undrained shear strength derived from vane shear and penetrometer measurements generally increases with depth, and ranges from 17 to 69 kPa and from 29 to 118 kPa, respectively (Fig. F60; Table T19, also available in ASCII format). The cores were disturbed by gas expansion, and fractures were often developed during testing. Therefore, the obtained undrained shear strength values probably do not reflect in situ conditions.

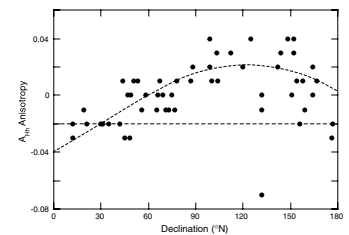
Index Properties

Index properties were determined on discrete samples recovered from Holes 1150A and 1150B using gravimetric methods. A dedicated program calculates the index properties from wet and dry mass and dry volume using a salinity of 0.035 and a pore-water density of 1.024 g/cm^3 . At this site, the salinity and density of the pore water were signifi-

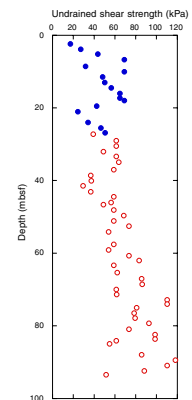
F58. Anisotropy vs. depth from measurements of vertical and horizontal P -wave velocities, Hole 1150B, p. 135.



F59. Anisotropy of horizontal P -wave velocity vs. declination, Hole 1150B, p. 136.



F60. Undrained shear strength variation with depth, Hole 1150A, p. 137.



T19. Undrained shear strength, Hole 1150A, p. 201.

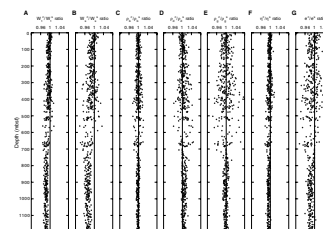
cantly different (0.034–0.018 and 1.024–1.012 g/cm³, respectively). Index properties were recalculated using in situ values of salinity and pore-water density from linear extrapolation of 39 measurements on interstitial pore-water samples (see “[Geochemistry](#),” p. 37; see also “[Physical Properties](#),” p. 18, in the “Explanatory Notes,” chapter). Figure F61 shows variation with depth of the ratio of index properties corrected for in situ salinity and pore-water density over those determined with standard salinity and pore-water density. The different salinity and pore-water density values have only minor influence on water content of total mass, porosity, and bulk density (the ratio ranges from 0.98 to 1.02). However, they have intermediate influence on dry density (the ratio ranges from 0.96 to 1.05) and significant influence on water content of mass of solids, void ratio, and grain density (the ratio ranges from 0.94 to 1.06). Index properties determined from in situ variations of salinity and density of pore water are reported here. Note that index properties included in the Janus database are calculated from standard values of salinity and pore-water density.

To cross-examine the internal quality of the data, porosity, dry density, and void ratio were calculated indirectly from the other index properties (see “[Physical Properties](#),” p. 18, in the “Explanatory Notes” chapter). The maximum differences between direct and two indirect determinations of porosity were 1.5% and –0.4%, respectively. The corresponding differences are 0.012 g/cm³ and –0.03 for dry density and void ratio, respectively. These differences lie within the estimated uncertainty of index properties measurements (± 2% of values), which implies good quality of index properties measurements.

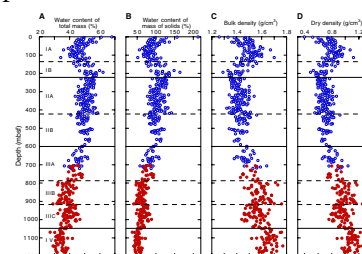
The overall plots of index properties vs. depth indicate that sediments at this site are porous and poorly consolidated. The main results of the downhole variation in porosity, bulk density, and grain density are presented below. Water content and void ratio have downhole trends similar to that of porosity, and dry density has a downhole trend similar to that of bulk density (Fig. F62; Table T20, also available in [ASCII format](#)).

There is a rapid change in porosity and bulk density in the upper section of Hole 1150A; porosity decreases from 83% at the mudline to a minimum value of 56% at 113 mbsf, and bulk density increases from 1.26 to 1.70 g/cm³ across the same interval (Fig. F62). This depth coincides with a positive peak in NGR activity and GRA bulk density values. The section from 113 to ~200 mbsf generally has inverse trends of porosity and bulk density; porosity increases to 79% and bulk density decreases to 1.29 g/cm³. Scattered grain density values (2.40–2.66 g/cm³) are measured from the mudline to ~200 mbsf. Slightly inverse trends of porosity and bulk density are measured from ~200–600 mbsf; porosity and bulk density from ~63% to ~77% and 1.56 to 1.32 g/cm³, respectively. Grain density data are more spread than porosity and bulk density data and range from 2.11 to 2.58 g/cm³. The index properties trends are marked with several minor offsets and changes in slope and one interval with slightly inverse trends of porosity and bulk density (Fig. F62). Lithologic Unit III can be divided into an upper (598–915 mbsf) and a lower (915–1047 mbsf) portion on the basis of index properties. Porosity generally decreases from 70% to a minimum value of 50% in the upper interval. The porosity has a positive offset downhole of ~10% at 915 mbsf and decreases to a minimum value of 56% in the lower interval. The bulk density variation with depth mirrors that of porosity; increasing values from 1.48 to a maximum of 1.76 g/cm³ at

F61. Corrections for in situ salinity and pore-water density, p. 138.



F62. Index properties vs. depth, p. 139.



T20. Index properties, p. 202.

915 mbsf are measured. After a negative shift of $\sim 0.2 \text{ g/cm}^3$, bulk density increases to 1.63 g/cm^3 at 1044 mbsf. Grain density data are more scattered than porosity and bulk density data; grain density ranges from 2.24 to 2.59 g/cm^3 in the upper interval, and from 2.27 to 2.48 g/cm^3 in the lower interval. The boundary between lithologic Units III and IV is marked by shifts to higher bulk density and grain density and by lower porosity values. In the basal unit of Hole 1150B, porosity is rather constant and generally ranges from 50% to 60%; bulk density increases by $\sim 0.1 \text{ g/cm}^3$ over depth and varies from 1.60 to 1.77 g/cm^3 ; and most values of grain density generally vary from 2.42 to 2.55 g/cm^3 .

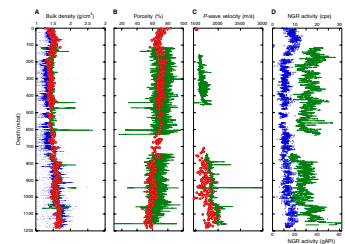
Comparison of Core and In Situ Physical Properties Measurements

Bulk density, porosity, *P*-wave velocity, and NGR activity were measured both in cores and in logs (in situ) (Fig. F63). Bulk density is measured with gravimetric (split cores) and GRA/absorption methods (whole-round cores and logs). Despite these partly different principles, there is generally an excellent correlation between core and log measurements. The main difference between core and log measurements is that the log data reveal several thin and dense horizons (i.e., dolomite and carbonate-rich horizons) that are not observed in gravimetric measurements but are sometimes seen in the GRA bulk density measurements. Porosity is measured with gravimetric (cores) and neutron absorption (log) methods. The log porosity generally indicates a wider scatter of values than the core porosity. However, the smoothed curve of log porosity correlates well with that of core porosity above 700 mbsf. Below, the core porosity is slightly lower (5%–10%) than the smoothed log porosity curve. *P*-wave velocity is determined in the vertical direction from the traveltime of sound over a known distance (both in core and log). Overlapping core and log measurements were obtained only from below 700 mbsf in Hole 1150B. Although core and log data have similar trends, the core measurements are generally lower (by $\sim 250 \text{ m/s}$) and more scattered than the log measurements. Thus, the comparison of porosity suggests that core sampling favors less porous and/or fractured sediment, whereas the opposite is suggested from comparison of velocity in core and log. NGR activity is measured using different units in core (cps) and log (gamma-ray American Petroleum Institute [gAPI]). Moreover, log data generally have a smaller statistical error than core data, mainly because the log sensors are exposed to a bigger sample than the core sensors. The NGR activity for the core demonstrates a similar but less variable and a more smoothed curve in comparison to the in situ NGR activity.

Vertical Stress

The total and effective vertical stresses were calculated from bulk density from porosity data following Equations 13, p. 23, and 8, p. 23, in the “Explanatory Notes” chapter. The bulk density data consisted of discrete measurements of bulk density in cores from 0 to 1180 mbsf and hostile environment lithodensity sonde (HLDS) bulk density from 113 to 638 and 745 to 1165 mbsf. HLDS bulk density data were converted into porosity using Equation 9, p. 23, in the “Explanatory Notes” chapter. Grain density values were estimated from linear extrapolation of discrete grain density measurements in cores, and pore-water density

F63. Comparison of physical properties from core and log measurements, p. 141.



was assumed to be 1.024 g/cm³. The total vertical and the effective vertical stresses increase linearly with depth to 10.0 and 17.6 MPa, respectively, at 1180 mbsf (Fig. F64).

Discussion

Quality of Data

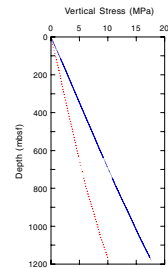
In general, the various shipboard analyses of physical properties show similar downhole trends. However, the quality of undrained shear strength and *P*-wave velocity (PWL and PWS measurements) is degraded by the presence of micro- and macrofractures in many of the APC and XCB cores. These fractures were formed by gas expansion in the cores when they were recovered to the drill floor. Gas expansion could affect GRA bulk density measurements as this method is based on core-unit measurements, whereas index properties that are based on gravimetric methods are not influenced (Blum, 1997). Maximum GRA bulk density values are apparently little affected by gas expansion in Hole 1150A because they correlate well with index properties and log bulk density. Tests of internal consistency of index properties data confirm the good quality. In general, there is good correlation between core and log index properties. Several of the XCB cores consisted of drilling biscuits surrounded by drilling mud slurry. This has resulted in low quality of thermal conductivity data in these cores (i.e., there is no correlation between thermal conductivity and porosity or bulk density).

Downhole Variation of Physical Properties

Lithology at this site is dominated by varying amounts of greenish homogeneous hemipelagic diatomaceous clay and clayey silt that become indurated with depth. The variation of physical properties data with depth is marked with five main breaks, namely at ~70–113, 200, 600, 915, and 1047 mbsf, respectively (Figs. F57, F62, F63). These breaks generally correlate with downhole chemical and lithologic changes and appear to signal variations in hydrologic and mechanic conditions.

The section from the mudline to 222 mbsf of Hole 1150A (lithologic Unit I) is largely composed of diatomaceous ooze and clays. The sediment is of Holocene to latest Pleistocene age from the mudline to 136 mbsf, and of late Pliocene age from 136 to 222 mbsf. The uppermost section is characterized by subsequent compaction of sediments (decreasing porosity and increasing bulk density and *P*-wave velocity) (Figs. F57, F62), and the sedimentation rate decreases rapidly from ~200 m/m.y. above 55 mbsf to <40 m/m.y. at 85 mbsf (see “Sedimentation Rates,” p. 35). In the interval from ~70 to 113 mbsf index properties and MST data reach peak values (Figs. F53, F55, F62), which are followed by inverse trends of index properties (increasing porosity and decreasing bulk density). The abrupt changes in trends suggest that there could be an unconformity at this depth that coincides with a change in salinity of the pore water (see “Geochemistry,” p. 37) but slightly above the unconformity indicated by biostratigraphy (see “Biostratigraphy,” p. 23). In addition, the local maximum in GRA bulk density (~1.8 g/cm³) and CaCO₃ content (~22 wt%) supports the presence of some form of change in the depositional environment. The inverse trends of index properties from 113 to ~200 mbsf suggest that the sediments are underconsolidated and that the rapid deposition (100–200

F64. Total and effective vertical stress vs. depth at Site 1150, p. 143.



m/m.y.) and impermeable nature of the sediment section (clay and calcareous rich) prohibit dewatering.

Index properties from core and log measurements are rather constant in the interval from ~200 to 600 mbsf (Fig. F63). Minor and gradual changes characterize the lithology across this interval, which is late to early Pliocene in age; diatomaceous ooze and ash layers are common down to 222 mbsf, whereas only a few ash layers and sandy silt layers are observed from 222 to 598 mbsf (Lithologic Unit II). The induration of sediment changes from soft to firm at 424 mbsf and from firm to hard at ~600 mbsf (see “[Lithostratigraphy](#),” p. 14). Porosity is high (>60%) and bulk density is low (<1.6 g/cm³) relative to the depth of burial. The constancy of index properties values across this section suggests that these deposits are also underconsolidated. Moreover, the change from constant salinity ($S = 0.029$) in the upper part of the interval to decreasing salinity from ~450 mbsf indicates that the hydrologic and mechanic conditions change in the lower portion of the interval. Geochemistry data indicate that gas hydrates may be present in sediments above 450 mbsf (see “[Geochemistry](#),” p. 37). Further analyses of seismic reflection and thermal data are required to confirm this hypothesis.

From 598 to 1047 mbsf, the lithology is dominated by lower Pliocene to upper Miocene greenish diatomaceous silty claystone and clayey siltstone with common and moderate bioturbation and a gradual increase in silt and sand particles and volcanic glass (see “[Lithostratigraphy](#),” p. 14). Porosity and bulk density values are characterized by rather uniform changes to lower and higher values, respectively. Dolomite nodules, glauconite-bearing silt and sand layers, and carbonate-rich layers are observed. Furthermore, fractures, faults, and joints are frequently observed in the cores from 598 to 787 mbsf, and their abundance increases below 787 mbsf. The wider scatter of vertical and horizontal P -wave velocities with depth probably mirrors the increasing amount of structural discontinuities (Fig. F57). The wider scatter in P -wave velocity values from ~920 to 1010 mbsf therefore indicates an increased frequency of fractures, and the interval roughly corresponds to a section with increasing fault observations in the cores (see “[Lithostratigraphy](#),” p. 14). The section between 787 and 1046 mbsf is probably normally consolidated because when the porosity and density are extrapolated to the surface, the trends match those of the top section of this site (Fig. F62). This would indicate that the mechanical state of sediment changes from underconsolidated to normally consolidated across the interval from 598 to 787 mbsf and that the presence of faults and joints has facilitated dewatering of the sediment. There is a shift to lower porosity and higher bulk density and P -wave velocity at 1047 mbsf, which coincides with the boundary of lithologic Units III and IV. The sediments become harder and have higher resistivity below 1047 mbsf, but there is no major change in the frequency of structural discontinuities, rate of sedimentation, or age of sediments (see “[Lithostratigraphy](#),” p. 14; “[Sedimentation Rates](#),” p. 35; “[Biostratigraphy](#),” p. 23; “[Downhole Measurements](#),” p. 49). The shift in physical properties probably reflects a downhole increase of induration of the sediment.

The overall downhole trend of NGR activity generally mimics that of porosity, which points to the intimate relationship between physical properties and the mineralogical composition of sediments (Figs. F55, F62). Local peak or trough values in NGR activity generally correlate well with peak or trough values in clay content (smectite, illite, and/or

kaolinite and chlorite) of the sediment. It also seems clear that the diatomaceous nature of the sediment results in higher porosity and lower bulk density than in diatom-free lithologies. The peak intensity of the opal-A hump is a measure of the diatom content, and there is a general tendency of porosity to increase with the opal-A hump peak intensity (Fig. F65A). Cementation, which may uncouple the relationship between porosity and consolidation, often occurs in carbonate-rich sediment (e.g., Karig, 1996). At this site, the carbonate content is generally low (see “Geochemistry,” p. 37). Nevertheless, porosity tends to increase with carbonate content (especially at higher porosities) (Fig. F65B). Local peak values in log and GRA bulk density often correlate with denser dolomite- and carbonate-rich layers that are observed as layers of low resistivity in FMS and resistivity logs (see “Downhole Measurements,” p. 49). These may act as local seals and are often associated with minor shifts in physical properties data.

DOWNHOLE MEASUREMENTS

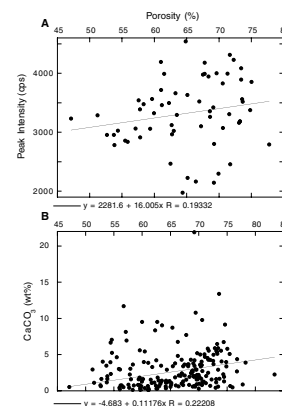
Introduction

Downhole measurements were used to determine in situ physical properties, geologic structures, and thermal structure, especially in sections where core recovery was poor. They also enabled us to evaluate borehole conditions such as hole geometry, stress orientation, and stability in the lower part of the borehole, where downhole instruments were expected to be installed. Logs also provide high-resolution records that will be used to study the paleoceanographic history in the western Pacific region and the nature of compaction, lithification, and deformation processes in the drilled forearc region. Logs are also used to generate synthetic seismograms for comparison with field seismic records to correlate reflections with drilled geological boundaries.

Operation

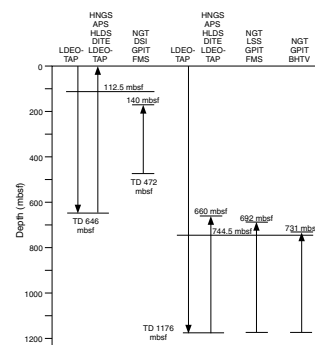
Logging operations at Site 1150 are summarized in Table T21 and Figure F66. Five logging runs were made from 1 through 3 July 1999. An obstruction was encountered at 646 mbsf during the first run, so the triple combo was logged from 646 mbsf to the seafloor. The wireline heave compensator was used on all runs and performed well because maximum ship heave was ~3 m for most of the operations. Because another obstruction was encountered at 473 mbsf during the second run, the FMS/dipole shear sonic imager (DSI) string was logged from 472 to 140 mbsf. No shear velocity or crossed-dipole data could be acquired by the DSI tool, apparently because of malfunctioning modes of the tool. Therefore, the DSI was run in a mode that allowed the tool to automatically pick the traveltime and calculate the compressional velocity. Unfortunately, the complete wave forms cannot be saved in this mode. After the pipe was lowered to 745 mbsf, the third run went within 7 m of bottom without any problems. The triple combo was logged from 1174 to 660 mbsf. The FMS/long-spaced sonic imager (LSS) string, which replaced the DSI, was deployed in the fourth run in the interval of 1176 to 692 mbsf. Finally, the BHTV string was deployed in fifth run in the interval of 1174 to 731 mbsf.

F65. Porosity vs. mineral composition, p. 144.



T21. Summary of logging operations, p. 203.

F66. Summary of logging operations, p. 145.



Data Quality

The wireline logs recorded in Holes 1150B are generally of high quality except for the neutron porosity log due to excessive borehole enlargement (Fig. F18). Density, resistivity, sonic, and FMS data recorded in the drill pipe cannot be interpreted. The NGR logs are highly attenuated and should be interpreted only qualitatively.

Hole 1150B was drilled with an RCB bit with a diameter of 9 $\frac{7}{8}$ in (~25 cm). The hole diameter was generally >48 cm (i.e., maximum extension of the one-arm caliper) in the interval from 200 to 350 mbsf, possibly because of washouts within low-porosity zones. As a result, the FMS images in these sections are degraded. Nevertheless, the density log in this interval is of high quality because of good contact with the borehole wall regardless of washouts. The FMS calipers in the fourth descent (713–1174 mbsf) revealed that the hole generally has an oval shape with a short axis close to the bit size (~25 cm) and a long axis of ~30–38 cm. The image quality along the short axis is very good, whereas that along the long axis is poorer because of the rugosity of the borehole wall and poor pad contact with the borehole wall. The compressional velocity data from the LSS log is of higher quality than the DSI compressional velocity data. A minor amount of cycle skipping is present in the raw data, but shipboard processing of the traveltime eliminated these excursions. Thin intervals of especially abrupt velocity changes corresponded to hard, thin layers or washouts. The overall quality of BHTV data is poorer than what was originally expected and difficult to interpret at this site. This is because of eccentric motion of the BHTV tool during logging, and because the formation/borehole impedance ratio (~2 at this site) is much lower in the diatomaceous claystone than the normal range (~10) for the tool.

Results

Bulk Density

In situ bulk density measurements were collected from 113–638 and 740–1170 mbsf by the HLDS as a part of the triple combo string (Fig. F18). Downhole density measurements correlate closely with core measurements (Fig. F63). The downhole densities are generally of similar magnitude to the discrete core-based values, whereas they are higher than the semicontinuous GRA bulk density core-based values down to ~700 mbsf. The in situ bulk density is anticipated to be higher than the core-based measurements because of core decompaction and disturbances. It is assumed that the discrete samples tended to be more indurated than surrounding core sections and, therefore, that they were less affected by decompaction and disturbance.

Bulk density values in the lithologic Unit I decrease with depth from 1.7 to 1.4 g/cm³. A large excursion, which reaches values as high as 1.95 g/cm³, occurs at the interval of 137 to 138 mbsf. This peak coincides with the boundary between lithologic Subunits IA and IB and may be caused by pebble clasts observed in Section 186-1150A-16X-1 (see “Lithostratigraphy,” p. 14).

Bulk density values fluctuate mainly between 1.4 and 1.5 g/cm³ in lithologic Unit II. Large excursions up to 2.2 g/cm³ occur at the intervals of 440–441, 472–473, and 474–475 mbsf. The excursion in the interval of 440–441 mbsf can be correlated with a 12-cm-thick dolomite layer in Core 186-1150A-47X (see “Lithostratigraphy,” p. 14). An increase in

bulk density to 1.6 g/cm^3 occurs at 598 mbsf, corresponding to the boundary between lithologic Units II and III.

Bulk density values in the logged section of lithologic Subunit IIIA fluctuate mainly between 1.4 and 1.6 g/cm^3 . A large excursion up to 2.2 g/cm^3 occurs at the interval of 602–604 mbsf. An abrupt increase in bulk density from 1.5 to 1.7 g/cm^3 occurs at 794 mbsf, corresponding to the boundary between lithologic Subunits IIIA and IIIB. Bulk density values in lithologic Subunits IIIB and IIIC fluctuate in a range of $\pm 0.1 \text{ g/cm}^3$ and decrease with depth from 1.65 to 1.55 g/cm^3 . A large decrease in bulk density occurs at 918 mbsf and can be correlated with the boundary between lithologic Subunits IIIB and IIIC. Large excursions up to 2.2 g/cm^3 occur at 810 and 946 mbsf. The excursions can be correlated with a 5-cm-thick dolomite layer recovered in Core 186-1150B-12R and a 17-cm-thick dolomite layer recovered in Core 26R, respectively (see “[Lithostratigraphy](#),” p. 14).

An increase in bulk density from 1.5 to 1.7 g/cm^3 occurs at ~1050 mbsf, corresponding to the boundary between lithologic Units III and IV. The average value of bulk density is $\sim 1.7 \text{ g/cm}^3$ throughout the unit. A number of large excursions as high as 2.0 g/cm^3 occur at the interval of 1055–1063 mbsf. One of the excursions can be correlated with an ~20-cm-thick carbonate-rich layer observed in Core 186-1150A-38R. A large excursion of low-density values of $< 1.2 \text{ g/cm}^3$ is identified in the interval of 1066–1067 mbsf, which corresponds to a large washout identified by the caliper logs.

Sonic Velocity

In situ sonic velocity measurements were acquired by the DSI and LSS tools. The upper interval (152–458 mbsf) was logged by the DSI tool, and the lower part (746–1161 mbsf) was logged by the LSS tool. Borehole-compensated *P*-wave velocity in the upper part shows a gradual increase from 1600 to 1800 m/s with depth. In the upper part of the hole where the DSI sonic tool was used, the velocity values for dolomite layers are lower than expected, possibly because the tool was used in the “digital first motion detection” mode instead of the normal operation mode because of the malfunction of an electronic part.

In situ *P*-wave velocity values in the lower part show better quality than those in the upper part. Velocity values in lithologic Subunit IIIA are in the range of 1700 to 1800 m/s. A large excursion up to 2100 m/s occurs at the top of lithologic Subunit IIIB. Velocity values in lithologic Subunits IIIB and IIIC fluctuate between 1750 and 1850 m/s in the interval of 791–865 mbsf and between 1800 and 1900 m/s in the interval of 865–1050 mbsf. Velocity excursions as high as 2300 m/s occur at 808 and 3300 m/s at 943–944 mbsf. The excursions can be correlated with a 5-cm-thick dolomite layer recovered in Core 186-1150B-12R and a 17-cm-thick dolomite layer recovered in Core 26R, respectively (see “[Lithostratigraphy](#),” p. 14). Thin low-velocity excursions occur at 1045 and 1064 mbsf, which corresponds to a major washout identified by the caliper logs. *P*-wave velocity increases gradually from 1900 to 2000 m/s in the interval between two washouts. A thin high-velocity excursion can be identified at 1056 mbsf, which can be correlated with an ~20-cm-thick carbonate-rich layer observed in Core 186-1150A-38R (see “[Lithostratigraphy](#),” p. 14). The velocity values fluctuate around 2000 m/s below the two washouts. The *P*-wave velocity values acquired with the LSS tool are slightly higher and more tightly grouped than are the *P*-wave measurements from discrete core specimens (Fig. [F63](#)).

Electric Resistivity

In situ electric resistivity measurements were collected from the seafloor to 646 mbsf and 747–1170 mbsf by the dual induction tool as part of the triple combo string. The deep-, medium-, and shallow-resistivity logs in Figure F18 show similar trends throughout the logged intervals, indicating good hole conditions. However, the shallow resistivity log in lithologic Unit I and Subunit IIA shows a smaller amplitude as a result of borehole enlargement indicated by the caliper log.

Deep resistivity values in lithologic Unit I decrease with depth from 1.2 to 0.7 Ωm . Significant drops in resistivity from 1.2 to 0.9, 1.1 to 0.8, and 0.9 to 0.7 Ωm occur at 118, 139, and 175 mbsf, respectively. The resistivity increases in short intervals between these three depths. The same trend can be observed in the bulk density log. Deep resistivity shows cyclic changes between 0.65 and 0.85 Ωm and a gradual decrease with depth in lithologic Subunit IIA. The resistivity abruptly increases from 0.65 to 0.8 Ωm at the top of lithologic Subunit IIB. The resistivity values fluctuate between 0.7 and 0.8 Ωm and show several major cycles in lithologic Subunit IIB. Excursions up to 1.4 and 2.1 Ωm occur in the intervals of 440–441 and 472–475 mbsf, respectively. The excursion in the interval of 440–441 mbsf can be correlated with a 12-cm-thick dolomite layer in Core 186-1150A-47X (see “[Lithostratigraphy](#),” p. 14). The resistivity value abruptly increases from 0.8 to 1.1 Ωm at the top of lithologic Unit III. The resistivity fluctuates between 0.9 and 1.0 Ωm in lithologic Subunit IIIA. An abrupt change in resistivity from 1.0 to 1.3 Ωm occurs at 792 mbsf, corresponding to the boundary between lithologic Subunits IIIA and IIIB. Resistivity values in lithologic Subunits IIIB and IIIC fluctuate in a range of ± 0.2 Ωm and decrease with depth from 1.2 to 1.0 Ωm . Large excursions up to 1.9 Ωm and 1.7 Ωm occur at 810 and 945 mbsf, respectively. The excursions can be correlated with a 5-cm-thick dolomite layer recovered in Core 186-1150B-12R and a 17-cm-thick dolomite layer recovered in Core 26R, respectively (see “[Lithostratigraphy](#),” p. 14).

Low frequency cycles (50- to 100-m scale) and high frequency cycles (5- to 10-m scale) can be identified in lithologic Subunits IIIB and IIIC. An increase in resistivity from 1.1 to 1.4 Ωm occurs at ~1050 mbsf, corresponding to the boundary between lithologic Units III and IV.

Resistivity values in lithologic Unit IV fluctuate in a range of ± 0.1 Ωm and decrease with depth from 1.4 to 1.1 Ωm . A large excursion up to 1.9 Ωm occurs at 1057 mbsf, which can be correlated with an ~20-cm-thick carbonate-rich layer observed in Core 186-1150A-38R (see “[Lithostratigraphy](#),” p. 14). Negative excursions in shallow resistivity down to 1.0 Ωm are identified at 1046 and 1066 mbsf, which corresponds to large washouts.

Natural Gamma Radiation

In situ NGR measurements were collected from the seafloor to 623 mbsf and 745–1165 mbsf by the hostile environment natural gamma-ray sonde (Fig. F18). The log responds to mineral composition and therefore indicates change in lithology. Potassium and thorium values show a similar trend throughout the logged section, although potassium values are more sensitive and variable with depth. The potassium values show a decreasing trend from 115 to 140 mbsf and an increasing trend from 140 to 175 mbsf. A large decrease from 0.012 to 0.007 wt% occurs from 175 mbsf, and values decrease down to 0.005 wt% with

depth in lithologic Unit I. Lithologic Subunits IIA and IIB are characterized by regular oscillations of the range of ± 0.005 wt% in 10- to 20-m intervals. Relatively high K (0.006–0.010 wt%) zones were identified in the intervals of 290–372 and 425–528 mbsf and low K (0.004–0.008 wt%) zones were identified in the intervals of 215–290, 372–425, and 528–598 mbsf. Uranium values show regular oscillations between 1 and 2 ppm with ~ 70 -m cycles throughout lithologic Unit I and Subunit IIA. Several excursions in Th and K correspond to those of resistivity and density curves, suggesting volcanic ash layers in lithologic Subunit IIB. The averaged potassium value yields 0.007 with relatively small fluctuations in lithologic Subunit IIIA. A large increase in K (from 0.008 to 0.013 wt%) and Th (from 2.5 to 4 ppm) occurs at the boundary between lithologic Subunits IIIA and IIIB. In lithologic Subunit IIIB, potassium values show regular oscillations between 0.007 and 0.012 wt% in ~ 5 -m intervals. In lithologic Subunit IIIB, the average potassium value yields 0.008 wt%. In the interval of 964–1030 mbsf, potassium values show regular oscillation between 0.005 and 0.012 wt% in 10-m intervals. An increase in K (from 0.008 to 0.012 wt%) and Th (from 3 to 5 ppm) occurs at the boundary between lithologic Units III and IV. Two excursions as high as 0.015 wt% in potassium values occur in the intervals of 1047–1150 and 1150–1145 mbsf.

Borehole Geometries and Images

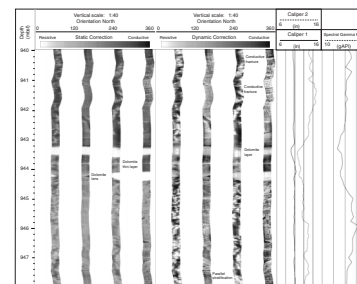
Electrical microresistivity images were recorded in the intervals of 140–472 and 692–1176 mbsf. FMS caliper data document borehole geometries (Fig. F18). In the upper part, Caliper 1 (C1) and Caliper 2 (C2) logs show similar values. The hole geometry above 400 mbsf was enlarged to more than 40 cm. C1 and C2 logs indicate different borehole diameters in the lower part. The azimuth of C1 and C2 is roughly north-northwest–south-southeast and east-northeast–west-southwest, respectively, throughout the lower part. The C1 log shows constant values of 25 ± 1 cm, which is close to the bit size. On the other hand, the C2 log changes from 30 to 38 cm, suggesting the borehole shape is elongated, roughly in the east-northeast–west-southwest direction.

FMS images clearly show five sharp resistive layers (at 440.01–440.70, 793.43–793.55, 810.69–811.03, 945.81–946.05, and 1058.04–1058.52 mbsf). A typical image of a sharp resistive layer from 943.3 to 944.4 mbsf is shown in Figure F67. The sharp resistive layer in the interval of 442.0–422.7 mbsf can be correlated with a 12-cm-thick dolomite layer in Core 186-1150A-47X (see “Lithostratigraphy,” p. 14). A sharp resistive layer in the intervals of 808.1–808.5 and 943.3–944.4 mbsf can be correlated with a 5-cm-thick dolomite layer recovered in Core 186-1150B-12R and a 17-cm-thick dolomite layer recovered in Core 26R, respectively (see “Lithostratigraphy,” p. 14). The sharp resistive layer at the interval of 1055.7–1056.0 mbsf can be correlated with an ~ 20 -cm-thick carbonate-rich layer observed in Core 186-1150A-38R (see “Lithostratigraphy,” p. 14).

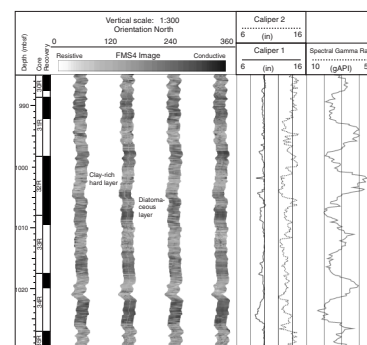
The microresistivity images also demonstrate patterns that coincide with the variation in NGR log (Fig. F68). In the intervals of 820–870, 895–920, and 960–1030 mbsf, striped patterns can be identified clearly with ~ 5 -, ~ 5 -, and 10-m frequency, respectively. These cyclic changes in microresistivity correspond to changes in resistivity, density, and NGR logs. Resistive zones correspond to high density and high NGR zones.

Conductive and resistive fractures were imaged by FMS. Preliminary shipboard analyses of fracture orientations from lithologic Units III and

F67. FMS images across a carbonate zone at 943.3–944.4 mbsf, p. 146.



F68. FMS images from 985 to 1030 mbsf in Hole 1150B, p. 147.



IV are shown in Figure F69. Fractures are developed in the east-northeast and west-southwest direction. These azimuthal data agree well with the magnetic-oriented core analysis (see “Structural Geology,” p. 60). The fracture dips mainly range from 20°–50° for conductive fractures to 40°–60° for resistive fractures. Fracture distribution in azimuth imaged by FMS coincides with the direction of borehole elongation indicated by FMS calipers.

Temperature Measurements

Equilibrium temperatures obtained from the APC temperature tool and the DVTP are shown in Table T22 and Figure F70 and are also shown as a function of depth in Figure F71. The errors were determined subjectively, based on the stability of the equilibration record and tool performance. The geothermal gradient at Hole 1150A is 29°C/km ($R = 0.997$) in the interval from 0 to 164.4 mbsf. Extrapolation of this gradient suggests an in situ temperature of ~35°C at the instrument depth (~1200 mbsf). Heat flow is estimated from the in situ equilibrium temperature measurements and the thermal conductivity values measured on board (Fig. F56). The inverse of the slope of the temperature vs. the cumulative thermal resistance (Fig. F71) yields a direct measure of heat flow. The heat flow is 20 mW/m² ($R = 0.996$) in the interval from 0 to 154.8 mbsf.

The raw temperature data recorded with the Lamont-Doherty Earth Observatory temperature/acceleration/pressure tool are shown in Figure F72. The geothermal gradient gradually decreases with depth in the upper interval (115–646 mbsf), whereas it gradually increases with depth in the lower interval (660–1174 mbsf).

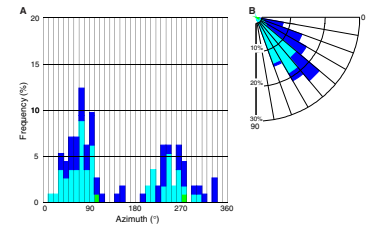
Summary of Core-Log Integration

Cyclic Changes in Sediment Composition

The cores recovered from Site 1150 show quite monotonic sedimentary facies except for occasional ash and dolomite layers. Although several peaks in thorium indicate volcanic ash layers, NGR logs were not generally useful for detecting ash layers. Carbonate/dolomite layers typically have weak negative peaks in gamma ray. However, NGR logs are useful in determining the lithologic change such as the diatom/clay ratio, which is a primary factor of the change in sedimentary composition throughout the whole section at Site 1150.

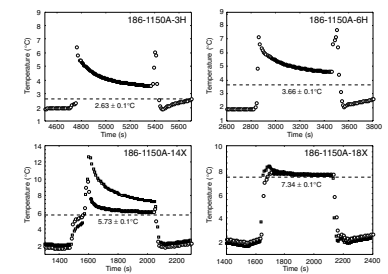
The composite profile made from NGR logs and MST NGR counts indicate the composition changes in three different modes: (1) first-order cycles, which include high gamma-ray activity in the interval from 0 to ~200 mbsf, low gamma-ray activity in the interval from ~200 to ~800 mbsf, and high gamma-ray activity in the interval from ~800 mbsf to the bottom; (2) second-order cycles, which include medium scale fluctuations in 50- to 100-m intervals, which basically correspond to lithologic units and subunits; and (3) third-order cycles, which include regular oscillations in 5- to 20-m intervals. The first- and second-order cycles coincide well with the vertical variations in the clay and opal concentrations shown by XRD analyses throughout the whole section (see “Lithostratigraphy,” p. 14). NGR logs contain third-order cycles, which record high-resolution compositional changes in sediments, mainly in the lithologic Unit II and Subunits IIIB and IIIC. The third-order cycles can be observed in MST measurements (GRA bulk density

F69. Fracture analysis using FMS images from lithologic Units III and IV, p. 148.

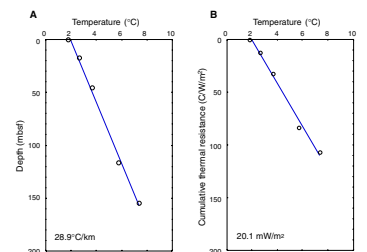


T22. Summary of in situ temperature measurements, Hole 1150A, p. 204.

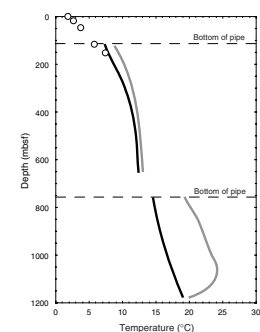
F70. Temperature data vs. time from the APC Adara temperature tool and the DVTP, p. 149.



F71. Temperature vs. depth, temperature vs. cumulative thermal resistance, and calculated mean heat flow, p. 150.



F72. Temperature logs recorded in Hole 1150B, p. 151.



and NGR) in lithologic Unit II. Low core recovery prevented identification of the third-order oscillation in cores from lithologic Subunits IIIB and IIIC. However, several complete cycles were identified in Cores 186-1150B-22R, 28R to 30R, and 32R and correlated well with the gamma-ray logs.

Dewatering, Consolidation, and Lithification Processes

Resistivity logs recorded dewatering, consolidation, and lithification processes. The resistivity values increase discontinuously with depth at ~400, ~600, ~800, and ~1050 mbsf and correspond to the degree of lithification defined by the VCD (see “[Lithostratigraphy](#),” p. 14). Dolomite layers can be identified at most of the discontinuities of resistivity values. Dolomite can be easily identified as large excursions in resistivity values and can be correlated well with core descriptions and XRD analyses. Although the resistivity values increase abruptly at ~400 and ~600 mbsf, bulk density values do not change very much. These two depths of changes in resistivity can be correlated with two major changes in salinity in interstitial water (see “[Geochemistry](#),” p. 37). At ~800 and ~1050 mbsf, the bulk density values increase with depth corresponding to the increases in resistivity values. However, no change in pore-water chemistry can be identified at the two discontinuities. The different responses in resistivity, bulk density, and pore-water chemistry suggest that the hydrologic property may produce large effects on the electromagnetic property in 200–600 mbsf, and pore-space reduction affects the electromagnetic property of the formation from 600 mbsf to the bottom of the hole.

Figure F73 shows a crossplot of shallow resistivity vs. total spectral gamma ray by lithologic units. All data are divided into three sets: (1) conductive and low gamma ray, (2) intermediate, and (3) resistive and high gamma ray. The conductive set consists of lithologic Subunits IB, IIA, and IIB and is characterized by less variation of resistivity values with larger variation of gamma-ray values than in other units. This trend suggests that the electromagnetic property in sediments does not change because of a change in the diatom/clay ratio. The resistive set is characterized by a steep slope in the linear relationship between resistivity and gamma ray in lithologic Subunits IIIB and IIIC and large variations in resistivity in lithologic Unit IV. This trend suggests that the electromagnetic property is sensitive to change in the opal/clay ratio in lithologic Subunits IIIB and IIIC. Changes in the opal/clay ratio, however, correlate poorly with resistivity changes in lithologic Unit IV. This poorer correlation between resistivity and gamma ray in the deeper part may correspond to the occurrence of opal-CT in the sediments (see “[Lithostratigraphy](#),” p. 14). The intermediate set shows a transitional trend between conductive and resistive sets.

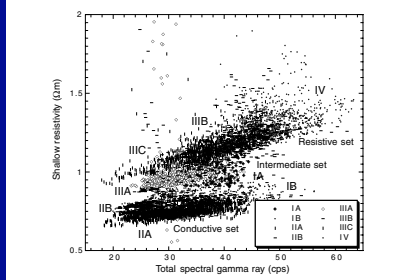
Dewatering, consolidation, and lithification processes estimated from core and logs are (1) normal dewatering and consolidation from 0 to ~100 mbsf, (2) pore water preventing the consolidation from ~100 to ~600 mbsf because of high pore pressure and/or the diatomaceous nature of the sediment, (3) dewatering and consolidation proceeding from ~600 to 1050 mbsf, and (4) lithification from ~1050 mbsf downward.

Log-Seismic Correlation

A synthetic seismogram was constructed at Site 1150 (Fig. F74) for a correlation between the in situ properties of sediments and rocks at this



F73. Crossplot of shallow resistivity vs. spectral gamma ray, p. 152.



F74. Core-log seismic integration at Site 1150, p. 153.

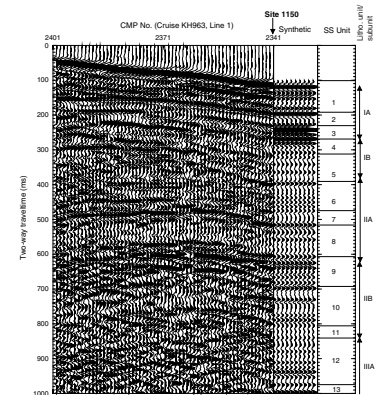
site and the seismic reflections observed on field seismic data collected near the site. The field seismic trace is from shot gather no. 1171 from the seismic cruise KH96-3, Line 1, which has a CMP 2341. Hole 1150B was drilled near CMP 2337, which is ~100 m east of CMP 2341. Because the stacked seismic data was not available in digital format on board, CMP 2341 was selected for log-seismic correlation because it has a higher signal/noise ratio than the adjacent traces. A portion of Line 1 that is crossing Site 1150, together with the synthetic seismogram, is shown in Figure F75. From this comparison, the lithologic units from core descriptions (see “**Lithostratigraphy**,” p. 14) and the major seismic stratigraphy (SS) units are identified.

The density-depth profile shown in Figure F74 is a combination of in situ bulk density logs (HLDS) and laboratory GRA bulk density data measured on whole-round core (see “**Physical Properties**,” p. 41). The bulk density and *P*-wave velocity logs in the logged intervals are generally of good quality. However the DSI responses for hard formations like dolomite underestimate the expected in situ values, because the DSI tool had an electronic problem as described in “**Operations**,” p. 2. For the intervals without logging, from the seafloor to 113 mbsf and from 638 to 745 mbsf, GRA bulk density values from MST measurements were used. Anomalous values caused by measurement errors were removed, and corrections were made for elastic rebound using the density logs from the intervals where MST and logging densities overlap. For the middle depth interval without logging, the average shift applied to the GRA bulk density data is ~0.1–0.2 g/cm³. For the two intervals without logging, velocity profiles were derived from the corrected GRA bulk density (e.g., Sun, in press).

Using these log-core combined density and velocity (GRA-HLDS density and DSI or LSS) profiles, a reflection coefficient series was calculated and then convolved with an estimated Ricker wavelet with a center frequency of 55 Hz to obtain the synthetic seismogram. The center frequency for the source wavelet was determined from spectral analysis of the field seismic record CMP 2341. Finally, both synthetic and field seismograms were converted to depth from two-way traveltimes using integrated velocity profiles from log and core data. Some mismatches are caused by poor core recovery in the intervals without logging and by off-plane seismic reflections and other noises in the field record for the logged intervals. The effect of spherical divergence was not considered in generating the synthetic seismogram; however, the energy decay caused by first-order multiple backscattering was taken into account. Comparison of the synthetic and field record shows that the overall amplitude-depth dependence can be explained by considering this simple mechanism of seismic energy decay.

The overall quality of correlation between the synthetic and field records is quite good. All the major seismic stratigraphy units on the two-dimensional seismic section (cruise KH96-3, Line 1) can be identified on downhole log responses using the synthetic seismogram (Fig. F75). We determined 16 SS units on the field seismic section for the drilled-depth interval. All the lithologic boundaries coincide with SS boundaries within the resolution of the seismic record (10–20 m) (see “**Lithostratigraphy**,” p. 14). Although the dolomite layers are typically ~<0.5 m thick (see “**Lithostratigraphy**,” p. 14), some of them can be identified on both synthetic and field seismic traces because their large impedance contrasts with the adjacent hemipelagic layers generate strong amplitude reflections. On the other hand, because of the presence of thin layers of dolomite and their strong reflection amplitudes,

F75. A portion of the seismic section from Line 1 of cruise KH96-3 crossing Site 1150 together with synthetic seismogram, p. 155.



the seismic reflections from the lithologic boundaries between hemipelagic formations appear to be relatively weak.

BOREHOLE INSTRUMENT STATUS

Introduction

Site 1150 is in a seismically active zone (Fig. F76). Recent significant interplate thrust earthquakes in this zone (39°–40°N) occurred in 1968, 1989, and 1992. The 1968 event (magnitude $[M] = 7.2$) is considered an aftershock of the 1968 Tokachi-oki earthquake (moment magnitude $[M_w] = 8.2$). The 1992 events are suggested to have been accompanied by a slow earthquake releasing seismic moment of $M_w 7.3$ – 7.7 (Kawasaki et al., 1995). Both the 1989 (five $M = >6$ events during 27 October–7 November) and the 1992 (six $M = >6$ events during 16–29 July) activities were of swarm type. The ocean-bottom seismometer aftershock observations delineated the seismically active zones as a number of distinct clusters (Nishizawa et al., 1990; Hino et al., 1996). These swarm activities were confined between 143° and 143.8°E.

We installed the geophysical observatory at Site 1150 to physically relate these earthquakes, plate motion, and seismic structures to earthquake cycles and dynamics. This site is ideal for testing how stable and unstable plate slips (regular to slow earthquakes to creep) exist in space and time and how this affects the surrounding stress/strain conditions.

Operation

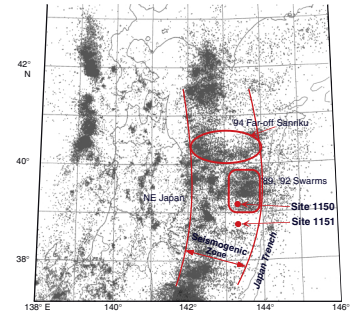
The installation of the geophysical observatory at Hole 1150D proceeded as shown in Table T23. Based on core descriptions and logging results from Hole 1150B, the strainmeter was emplaced at 1120 mbsf (Fig. F77) in a relatively uniform and higher density ($\sim 1.7 \text{ g/cm}^3$) and higher P -wave velocity ($\sim 1960 \text{ m/s}$) section.

Attaching four cables to the casing pipe proceeded much faster than planned (see Step 7 in Table T23). Centralizers (9 $\frac{5}{8}$ -in outside and 3-in height) were attached $\sim 3 \text{ m}$ from each side of every joint (Fig. F78). The cables were attached to the casing pipe by tie wraps covered with duct tape. Joining the 4 $\frac{1}{2}$ -in casing pipes (API-J55-STC, 10.5 lb/ft, $\sim 11.7\text{-m}$ length each) took longer than normal because the “iron neck” could not be used.

As a result, $\sim 48 \text{ hr}$ elapsed between the final drilling of Hole 1150D and the initial entry of the instrument assembly into the hole. Hole penetration resistance increased to the extent that it was possible to achieve entry only to a depth of 23 m less than required. Since it was necessary to redrill the open-hole section, the seafloor package (hanger/riser with MEG) with attached 1.1-km in-hole assembly was brought back to the moonpool. At this point, we checked the system and found all sensors to be operational. In effect, four unarmored cables withstood the pressure and the rubbing against the hole walls and the VIT guide sleeve. Instead of pulling out completely, the string below the hanger/riser was hung from the moonpool ceiling, keeping the cabled casing pipe link intact (see “Operations,” p. 2) so that reinstallation could be much quicker than the initial attempt.

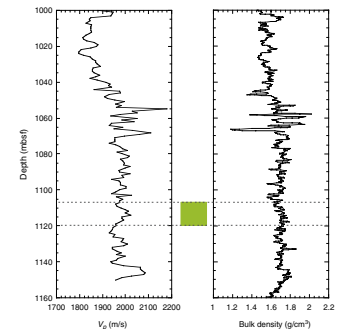
The 95.2-m-long, 9 $\frac{3}{4}$ -in open-hole section was redrilled on 25 July in 5.5 hr (17.3 m/hr). The hole was then washed with water to clear cuttings but was not stabilized with heavy mud. Installation of the instru-

F76. Seismic activity of the Japan Trench area off northeast Japan, p. 157.

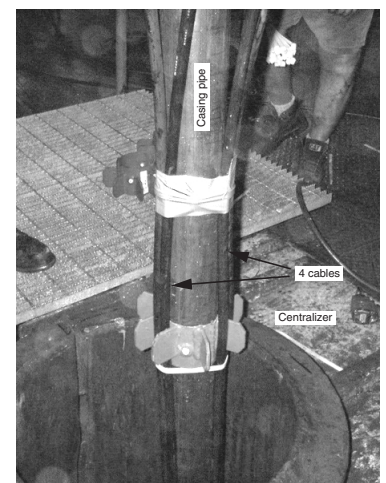


T23. Instrument package deployment, p. 205.

F77. Logging data of bulk density and P -wave velocity, p. 158.



F78. Cable link between the borehole and seafloor, p. 159.



ment string then proceeded successfully. The bottom of the hole was filled with cement with 1.9 g/cm³ density and 10.8 m³ volume (Step 21 in Table T23). This volume can fill 213 m height of 10-in-diameter hole or 150 m of 0.7-m² hole, assuming an elliptical shape based on caliper measurements of a corresponding depth range at Hole 1150B. This cementing method is required for the strainmeter operation, and the scouring action of the cement flowing past the 1-in clearance around the strainmeter probably ensured a clean hole. For other sensors, the cementing likely provides the best coupling to the surrounding rocks compared to other methods that utilize mechanical arms, pads, or sand. Unlike other methods, cementing prevents water motion and temperature fluctuation from becoming noise sources.

After successfully cementing the instruments, the power access terminal (PAT) battery frame was made up in the moonpool. The PAT was hung at three points by three cables from the dual acoustic releases (Fig. F79). The drill pipe passed through the PAT center and the guide sleeve of the VIT. The actual lowering started after waiting for daylight since the operation was complicated, involving many weight transfers while the ship's heave was a few meters. The frame was lowered successfully onto the reentry cone (see Step 24 in Table T23) by using the logging cable, which allowed precise depth measurements and good heave compensation. After the PAT landed on the reentry cone, the acoustic release system was commanded by a transducer hung from the port side of the ship. Upon release, three small glass sphere buoys attached to the three cables pulled the cables up.

The installation was completed after successful disconnection of the J-tool to decouple the drill string from the observatory, although that operation took longer than anticipated. The electrical connection between the MEG and the PAT was made in September by the remotely operated vehicle (ROV).

Borehole Instruments

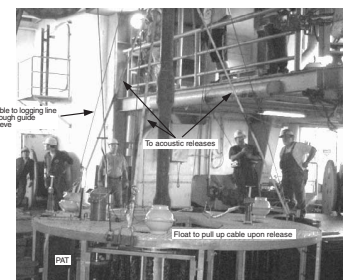
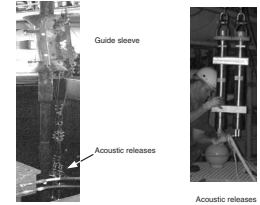
The array of emplaced instruments (Fig. F80) from bottom to top in Hole 1150D consists of the three-component strainmeter, three-component broadband PMD seismometer, two-component tiltmeter, and three-component CMG broadband seismometer (see “**Borehole Instruments**,” p. 5, in the “Borehole Instrument Package” chapter). We chose to emplace the three-component strainmeter at this site rather than at Site 1151 because of the tectonic setting as described in “**Tectonic and Seismic Setting**,” p. 4, in the “Leg Summary” chapter. A 3-m-long stinger pipe with centralizers was attached to the strainmeter bottom. This length was chosen for optimal safety upon reentry. The sensors other than the strainmeter were attached to the coupling tube that was bolted to the strainmeter (Fig. F81).

Each sensor was checked three times through the MEG: before installation, after retrieval, and just before reinstallation. All sensors performed consistently with no problem.

Seafloor-Borehole Link

As described in “**Installation Techniques**,” p. 3, in the “Borehole Instrument Package” chapter, the cable link between the hole bottom and the seafloor is supported by the 4½-in casing pipe. This way the cables can be protected, the installation depth is precisely predetermined, and the casing string does not heave inside the hole because the hanger/

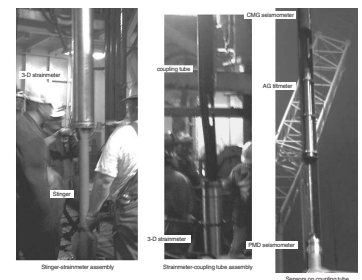
F79. Battery frame bridal assembly, p. 160.



F80. Array of emplaced instruments from bottom to top in Hole 1150D, p. 161.



F81. Stinger strainmeter coupling tube assembly, p. 162.



riser is coupled to the reentry cone. The centralizers further protect the cables. Figure F78 shows how the four cables were attached to the casing pipe string. Four cable reels were placed on the foreside of the moonpool and fed through sheaves (600-mm diameter × 84-mm groove width) hung from the ceiling.

A total of 95 joints of casing pipe hangs the instruments. The cables were cut at the moonpool 60 cm longer than the length required to attach the underwater mateable connectors (UMCs) to the MEG bottom stab plate, in case the need for reheading occurred. The cable termination took ~13 hr with six people working on two cables in parallel.

Seafloor Instruments

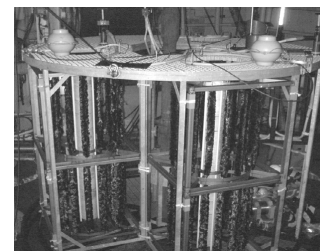
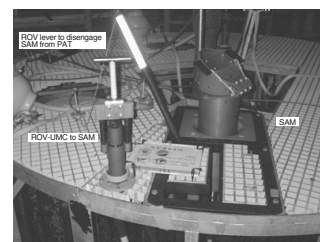
All the components were successfully emplaced. These are the power supply (seawater battery [SWB]), data recorder (storage acquisition module [SAM]), and a unit to merge and digitize data and control the observatory (MEG) (see “[Seafloor Instruments](#),” p. 11, in the “Borehole Instrument Package” chapter). The MEG was slid into its holder attached to the hanger/riser pipe connected to the four cables on its bottom side. To avoid plug contamination, an ROV dummy receptacle is on the top. Zinc anodes were attached wherever necessary to prevent corrosion of important components, such as at the stainless-steel stab plates attached to the bottoms of the stainless-steel MEG and the titanium SAM.

The PAT consists of three units of SWBs (see “[Seafloor Instruments](#),” p. 11, in the “Borehole Instrument Package” chapter). The SAM data recorder package is placed near the center of PAT on which the oil-filled 8-conductor cable is placed (Fig. F82). An ROV must disconnect one end of the cable from the parking position and connect it to the top of the MEG after removing the dummy receptacle. From the VIT camera check, the relative position of the MEG and the UMC parking position was found to be farthest apart, 180° around the center (Fig. F6). Table T24 depicts the tasks to be accomplished by an ROV.

Summary

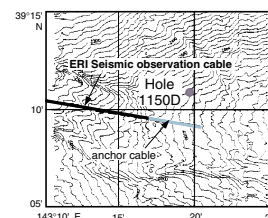
The establishment of the first seafloor borehole geophysical observatory (‘Neath Seafloor Equipment for Recording Earth’s Internal Deformation [NEREID-1]) was successful. All the tasks planned for Leg 186 at this site were completed. Although the borehole sensors are physically inaccessible, the seafloor components are designed to be replaceable by an ROV. The MEG can be replaced. The SAM must be replaced as the data disks are filled after ~1 yr of recording (72 GB). Batteries can be revived by replacing the magnesium anodes. The system status can be checked by the back from ocean bottom (BOB) module by an infrared communication link to the SAM. The site is only a few kilometers from the termination point of the fiber-optic cable observatory system installed in 1996 by the University of Tokyo. Our plan is to connect our observatory to this cable once we prove that the borehole observatory is producing reliable data (Fig. F83). Then the power can be supplied directly from land and the data disseminated in real time.

F82. The PAT and the SAM, p. 163.



T24. ROV tasks to start the NEREID system, p. 206.

F83. Plan of future cable connection to land, p. 164.



STRUCTURAL GEOLOGY

In this section we describe the brittle structures focusing on those with lengths that are greater than core diameter. Numerous smaller-scale structures are also visible, particularly when the core surface has dried, but detailed description of these is beyond the scope of the shipboard analyses. The brittle structures were observed in cores from lithologic Subunit IIB and below in Holes 1150A and 1150B. The highest number of structures were observed in RCB cores, although some structures were also observed in XCB cores. Probably, drilling disturbances in XCB cores overprinted many structures.

For the large-scale structures, we have assessed the abundance and type of structures that occur. For abundances, we have divided fractures into two types: open and healed. Most of the brittle structures were healed and filled with fine-grained dark gray clayey gouge. The width of the infill varies from 2 mm to a few tenths of a millimeter. No secondary mineralization or recrystallization (fibrous crystal growth) were observed. Open structures, though not as common as healed structures, were also abundant. These were probably drilling induced, although they were often formed along pre-existing weakness planes. These fractures were not considered in the structural interpretation unless they were partially filled.

Within the healed fracture category, we have further assessed the abundance of faults and joints. The distinction between faults and joints is based on the visible apparent displacement. The displacement was estimated primarily from the offset of burrows, carbonate nodule-like accumulations, and dissolution and precipitation rims around manganese or iron because sedimentary layering was rarely observed. As a result, the number of faults per meter is probably underestimated and the number of joints is overestimated.

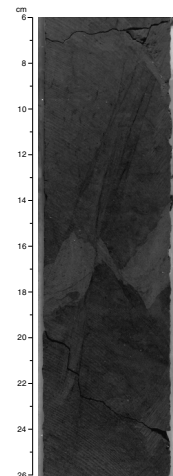
In addition, we measured the apparent dip of the large-scale structures with a conventional contact goniometer. The apparent dip is less than or equal to the real dip of any plane; therefore, dip angles that are reported here are minimum values. For curved fault traces (e.g., listric faults), the predominant apparent dip was measured. True dip measurements of faults are presented in “[Downhole Measurements](#),” p. 49. Finally, we reconstructed the orientation of healed and open fractures and bedding planes relative to geographical north using paleomagnetic directions.

Observation of Structures

Faults

The observed faults generally had the following appearance: (1) relatively straight with sharp fault traces, (2) relatively straight and sharp parallel fault sets with variable spacings (0.5–10 cm), (3) relatively straight and sharp conjugate fault sets, that often had the same (usually high) dip angle, but opposite dip directions, (4) anastomosing fault traces that generally occurred as close- and wide-spaced thin branches that diverged and rejoined over distances of a few millimeters to several centimeters (Fig. F84), (5) wavy or slightly curved faults (e.g., listric faults), (6) sets of two faults at a spacing of ~3–7 mm that were slightly curved toward each other at their termination, and (7) minor or secondary straight-branching splay faults that departed at acute angles from a major fault. The apparent dip angle varies from 10° to 75°, with

F84. Photograph of a set of steep-dipping, parallel-anastomosing normal faults, p. 165.



the majority (>45%) being steep-dipping fault traces. Locally, single isolated faults that are mostly very sharp and thin cross the core at moderate angles.

The displacement along faults generally varies from 0 to 4.5 cm, although the offset most often is a few millimeters in length. On the other hand, an offset greater than the scale of the core was observed for some rare faults (see “Downhole Measurements,” p. 49).

Normal faults are most commonly observed (~67% of all faults) (Figs. F84, F85). In addition, oblique faults and a few generally low-angle reverse faults were found. The strike-slip component of the oblique faults appeared to be on average 25% of the related dip-slip component.

Uncertainties in the interpretation of the sense of displacement originate from observations of (1) core surfaces that show the trace of an oblique normal fault and (2) extremely steep reverse faults that are parallel or anastomosing. For oblique normal faults, which have a low dip angle, the strike-slip component of the oblique offset may appear as reverse-fault displacement at the fault’s trace. For steep reverse faults, the movement may have partially consisted of small rotation of one fault block due to complicated interference of the fault and joint pattern and related space problems.

Joints

The observed joints generally had the following appearance: (1) small and thin joints, (2) small and thin parallel joint sets, (3) small and thin conjugate planes near major faults, (4) anastomosing joints, with some closely spaced and showing partly similar features and shapes as dewatering structures described by Knipe (1986) (Fig. F86), and (5) shear joints, which occur at acute to perpendicular angles to major faults (Fig. F85). A considerable number of these joints are steeply dipping (80°–90°). Often, the dip angle changes along the length of the joint.

Most joints appear to be extensional; however, the distinction between shear and extension joints is not always clear because of abundant hybrids between both end-members. As a result, both types are referred to simply as joints.

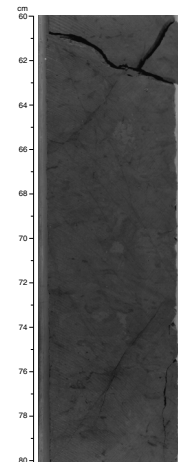
Frequency of Fractures

The different kinds of structures were counted in each core from Cores 186-1150B-1R through 50R, and then the total number was divided by recovered length in meters (Fig. F87; Table T25, also available in ASCII format). The number of healed fractures (joints and faults) increases with depth and has distinct peaks, whereas the number of open fractures (moderate to steep-dipping open fractures that were formerly healed fractures) changes little downhole (Fig. F87). A clear relationship can be seen between the joint and fault numbers per meter. The number of faults, though underestimated, is generally higher than the number of joints; otherwise, the two have similar downhole variation.

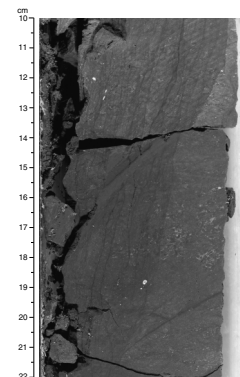
Interpretation of the State of Stress

The calculated effective vertical stress increases linearly with depth, from ~5 MPa at 700 mbsf to 10 MPa at 1180 mbsf (Fig. F64). The fracture pattern is useful for constraining the timing and mechanisms of the deformation and the properties of the affected rocks.

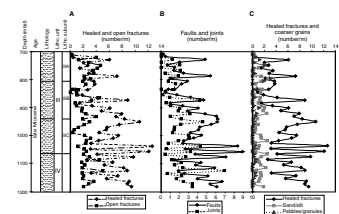
F85. Photograph of thin normal faults crosscutting and displacing an anastomosing parallel joint set, p. 166.



F86. Photograph of a strongly anastomosing, closely spaced parallel joint set, p. 167.



F87. Number of fractures with depth, Hole 1150B, p. 168.



T25. Number of deformational structures, Hole 1150B, p. 207.

For clayey sediments, the curve of porosity against burial depth usually shows a very characteristic flat shape at the beginning, representative of a large decrease in porosity, which means that the primarily high water-bearing sediments are very sensitive to pressure increase (Fig. F62). The mechanical behavior changes in conjunction with this compaction and with loss of water and porosity. When the brittle regime is reached, the observed changes with depth should include (1) a steepening of fracture planes, (2) a decrease in anastomosing and complexity of fracture branching, and (3) a decrease in number of faults with an increase in the amount of displacement on the rarer major faults.

As can be seen in Figure F87A, the number of healed fractures per meter increases on average with depth (basic minimum values increase), contrary to the above predictions. However, the change in porosity with depth is rather minor and probably cannot account for great changes in rock properties (see "Physical Properties," p. 41). Also, because of the observation of dewatering features, it is unlikely that the sediments are brittle over the entire length of the study interval. A more likely interpretation is that the increase of the number of healed fractures per meter results from overprinting by the two fault zones at 900–950 and 1030–1070 mbsf. Alternatively, the observed increase in clay content with depth may have permitted more healed fractures to form and thus account for compaction-related volume change (e.g., Guiraud and Seguret, 1987).

The porosity also has an important influence on the dip and the shape of the fracture traces. Fractures tend to become steeper and sharper with decreasing porosity. In clay-rich sediments, the process of fracturing starts with local rotation of clay particles to shear parallel orientation before a fracture plane evolves. In finer grained sediments, these zones are thinner than in coarser grained sediments. Also, continuing movement leads to an intensification of this fabric and consequently to a thinning of the fault gauge (Maltman, 1987). Furthermore, at smaller porosity, fractures tend to be sharper and fewer anastomosing faults occur. However, the observed fractures do not change shape or type with increasing depth. Again, multiple fracturing events, where more recent fractures overprint older ones, and downhole variations in lithology could be factors. The overprinting explanation is supported by FMS and resistivity data from Hole 1150B, which indicate that steeper faults tend to be active and flatter faults tend to be inactive (see "Downhole Measurements," p. 49).

There are several assumptions that can be made concerning the regional stress field. The steep joints visible through the whole examined depth interval indicate a three-dimensional stress field with a dominant vertical effective principal stress and low confining horizontal effective principal stresses (at least one low value of stress in one horizontal direction). When confining pressure increases, hybrid shear-extension fractures form, becoming progressively flatter and evolving a shear component on the plane of failure. The abundant very small branching and anastomosing fissile microcracks and cracks, which could not be taken into account for statistics and are only mentioned in the VCDs, are thought to have formed in the first stages of brittle failure (Hobbs et al., 1976; Maltman, 1987; Knipe, 1986). With continued stress, they could unite to form through-going fault planes, if this is mechanically easier than creating new fractures. This evidence also accounts for the scoured and wavy shapes of a large part of the fractures.

Taking into account the obvious displacement and steepness of the joints and faults, it follows that a combined stress field is present. Some

randomly distributed faults show unusually high amounts of displacement (several centimeters) not typical for simple compaction. Additionally, the majority of normal faults are moderate to steep dipping, which requires on the one side a low water content and on the other side a low confining pressure (especially for the subvertical joint fractures). Borehole logging results that show an elliptical diameter of the Holes 1150A and 1150B and the stereoplots of the FMS-detected faults indicate a combined stress field. The observed fracture pattern mirrors a superposition of a common sedimentary basin stress field and the Japan Trench-related forearc stress field. That means a predominant vertical maximum stress caused by an overload of the sedimentary column and an extension component with the lowest horizontal stress directed east-west.

Reconstruction of Orientation of Structures

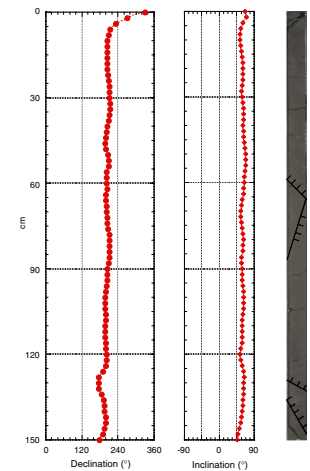
We reconstructed orientations of healed and open fractures and bedding planes using characteristic magnetic directions obtained from cores in Hole 1150B. Dip azimuths for these surfaces were reoriented into geographic coordinates (i.e., relative to true north) using stable magnetic declinations. The method of restoring the azimuthal orientation of cores by paleomagnetic directions has been applied to identify an original structural attitude in many past DSDP and ODP studies. Fractures, which are commonly developed in the slope region of subduction zones, have been reoriented and utilized to indicate the stress field (e.g., Niitsuma, 1986). In Hole 1150B we recovered a fractured sequence in cores (see “[Lithostratigraphy](#),” p. 14) that have fairly constant magnetic directions, making these suitable for reorientation (Fig. F88).

We focused our study on continuous pieces of core that were 20 cm long or longer. Pieces of these lengths are required to determine magnetic directions accurately and to ensure the direction is constant over the interval (Fig. F88). Planes of fractures were measured in three dimensions using all surfaces of the working half in the core-face coordinates system (Shipboard Scientific Party, 1995). In this coordinates system the plane of the split-core surface is called the apparent horizontal plane. A 360° orientation net is used with pseudo-north (0°) in the upcore direction. Dip azimuths (perpendicular to the strike) and dip angles were then rotated into the ODP core reference scheme by a 90° counterclockwise rotation about a horizontal east-west axis. We sketched positions of fractures to record which piece was measured. When the piece had a stable magnetization, it was reoriented into geographic coordinates using the paleomagnetic declination. The example in Figure F89 demonstrates the effectiveness of paleomagnetic reconstruction, which is evident from the improvement in clustering of healed fracture planes once they are placed in geographic coordinates. In Hole 1150B we did not correct the azimuths for the deviation of the hole from vertical because the hole deviations were negligible (<3.5°).

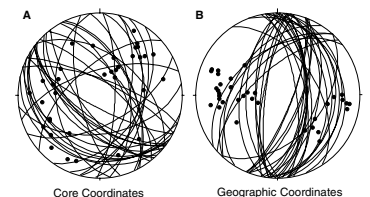
Healed Fractures

We made measurements of 369 healed fractures, 290 of which could be reoriented (Table T26, also available in [ASCII format](#)). Because the pattern of the horizontal frequency of measurements is similar to that of the occurrence of healed fractures (Fig. F90A) (see “[Lithostratigraphy](#)”

F88. Declination, inclination (after 30 mT demagnetization), and core image of Section 186-1150B-30R-2, p. 169.

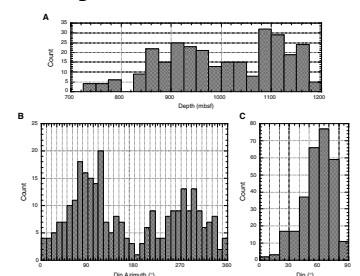


F89. Stereoplot of planes of healed fractures reoriented using paleomagnetic declination, Cores 186-1150B-23R through 25R, p. 170.



T26. Orientations of healed fractures, Hole 1150B, p. 208.

F90. Frequency of healed fractures and distribution of dip azimuth and dip angle of healed fracture planes after reorientation, Hole 1150B, p. 171.



phy," p. 14), the results should be representative of healed fractures in this hole.

Histograms of all dip azimuths and dip angles are shown in Figures F90B and F90C. The two clusters of reoriented dip azimuths are nearly antiparallel and clearly bimodal with clusters near 90° and 270°. On the other hand, the distribution of dip angles shows a unimodal pattern with most angles ranging between 45° and 80°. The mode of the directions shows a similar pattern with the fracture analysis from the FMS logging data (see "Downhole Measurements," p. 49).

The downhole variation of the dip azimuth can be subdivided into domains (Fig. F91):

1. The upper domain, spanning the interval between 703 and 940 mbsf, shows bimodal clustering of the dip azimuths.
2. The middle domain, spanning the interval between 940 and 1050 mbsf, shows scattered azimuths.
3. The lower domain, spanning the interval between 1050 and 1180 mbsf, shows loosely clustered azimuths.

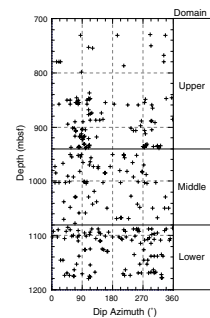
Plotting and contouring the poles to the fracture planes on stereoplots (Fig. F92) illustrates the differences between domains. In the upper domain poles cluster into separate west and east groups with a greater number in the west. The middle domain shows similar bimodal clusters, although the clusters are less concentrated than in the upper domain. Additionally, minor clusters are recognized in the diagonal direction. In the lower domain the poles are more scattered than in the upper domain, and the clusters have a northwest-southeast trend.

The plots indicate that eastward- and westward-dipping fracture planes exist throughout the sedimentary column, with a bias for eastward-dipping planes in the upper and middle domains. In the lower domain, southeast and northwest-dipping planes dominate. The middle domain appears to be a mixture of both the upper and lower domains. These domain boundaries generally coincide with frequency of fractures (see "Lithostratigraphy," p. 14). An increasing frequency of fractures generally occurs in the middle domain. This indicates that the fracture pattern in the middle is a mixture of two pattern systems of east-west and southeast-northwest fracturing planes. Horizontal and vertical *P*-wave velocities have larger dispersion in the interval between 920 and 1010 mbsf, which could be related to the higher number of healed fractures and possibly the more variable fracture plane orientations that occur in this interval.

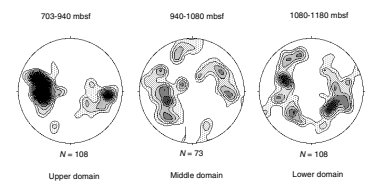
Two dominant fracture orientations, east-west and northwest-southeast, have apparently formed in different stress fields. The orientation of healed fractures in the upper domain strongly suggests an east-west extensional stress field. This agrees with borehole breakout information that indicates north-south compression and east-west extension. The bias toward eastward-dipping healed fractures might suggest an asymmetric sense of the extension.

However, the fracture direction in the lower domain indicates a northwest-southeast extensional field although the interval is accompanied by other minor directions. An analysis of conjugate healed faults with paleomagnetic orientation revealed an extensional direction of 117° at Site 584 (Niitsuma, 1986). The direction is consistent with the motion of the Eurasian plate relative to the Pacific plate (~120°). Niitsuma considered that structures were formed during uplift of the middle slope related to accretionary processes in the trench. The direction

F91. Downhole variation in dip azimuths of healed fracture planes in Hole 1150B, subdivided into domains, p. 172.



F92. Contour diagram of poles of healed fracture planes in Hole 1150B, subdivided into domains, p. 173.



derived from the lower domain is consistent with the direction at Site 584, possibly caused by the same mechanism as Site 584.

Open Fractures

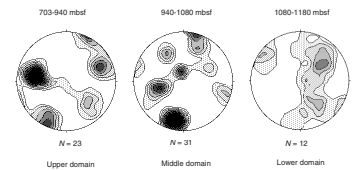
Sixty-six open fractures through the hole were reoriented in the same manner as the healed fractures (Table T27, also available in ASCII format). Poles to the fracture planes (Fig. F93) are divided into the same three domains as the healed fractures. The open fractures have a high density of poles in the south for the middle domain and in the south-east and northeast for the lower domain. The open fractures may have resulted from release of the north-south compressional stress in the hole. The concentration of poles to the west in the upper domain may indicate that many of the open fractures originated from healed fractures that were cracked during drilling or handling of cores.

Bedding

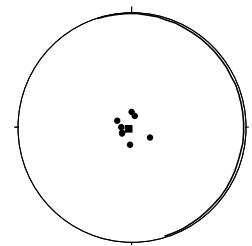
We also obtained several orientation data of bedding planes through the hole (Fig. F94). After reorientation, bedding planes have a gentle dip with a mean bedding plane dipping slightly, but insignificantly, to the east.

T27. Orientations of open fractures, Hole 1150B, p. 209.

F93. Contour diagram of poles of open fracture planes in Hole 1150B, subdivided into domains, p. 174.



F94. Bedding orientation from Hole 1150B, p. 175.



REFERENCES

- Akiba, F., 1986. Middle Miocene to Quaternary diatom biostratigraphy in the Nankai trough and Japan trench, and modified lower Miocene through Quaternary diatom zones for middle-to-high latitudes of the North Pacific. In Kagami, H., Karig, D.E., Coulbourn, W.T., et al., *Init. Repts. DSDP*, 87: Washington (U.S. Govt. Printing Office), 393–481.
- Barron, J.A., and Gladenkov, A.Y., 1995. Early Miocene to Pleistocene diatom stratigraphy of Leg 145. In Rea, D.K., Basov, I.A., Scholl, D.W., and Allan, J.F. (Eds.), *Proc. ODP, Sci. Results*, 145: College Station, TX (Ocean Drilling Program), 3–19.
- Berner, R.A., 1980. *Early Diagenesis: A Theoretical Approach*: Princeton, NJ (Princeton Univ. Press).
- Blum, P., 1997. Physical Properties Handbook: a Guide to the Shipboard Measurements of Physical Properties of Deep-sea Cores. *ODP Tech. Note*, 26.
- Claypool, G.E., and Kaplan, I.R., 1974. The origin and distribution of methane in marine sediments. In Kaplan, I.R. (Ed.), *Natural Gases in Marine Sediments*: New York (Plenum), 99–139.
- Gieskes, J.M., 1983. The chemistry of interstitial waters of deep-sea sediments: interpretation of deep-sea drilling data. In Riley, J.P., and Chester, R. (Eds.), *Chemical Oceanography* (Vol. 8): London (Academic), 221–269.
- Guiraud, M., and Seguret, M., 1987. Soft sediment microfaulting related to compaction within the deltaic infill of the Soria strike slip basin (northern Spain). In Jones, M.E., and Preston, R.M.F. (Eds.), *Deformation of Sediments and Sedimentary Rocks*. Geol. Soc. Spec. Publ. London, 29:123–136.
- Handa, N., and Tanoue, E., 1980. Organic matter in the Bering Sea and adjacent areas. In Hood, D.W., and Calder, J.A. (Eds.), *The Eastern Bering Sea Shelf: Oceanography and Resources* (Vol. 1): Seattle (NOAA), 359–381.
- Heath, G.R., Burckle, L.H., et al., 1985. *Init. Repts. DSDP*, 86: Washington (U.S. Govt. Printing Office).
- Hesse, R., and Harrison, W.E., 1981. Gas hydrates (clathrates) causing pore-water freshening and oxygen isotope fractionation in deep-water sedimentary sections of terrigenous continental margins. *Earth Planet. Sci. Lett.*, 55:453–462.
- Hino, R., Kanazawa, T., and Hasegawa, A., 1996. Interplate seismic activity near the northern Japan Trench deduced from ocean bottom and land-based seismic observations. *Phys. Earth Planet. Inter.*, 93:37–52.
- Hobbs, B.E., Means, W.D., and Williams, P.F., 1976. *An Outline of Structural Geology*: New York (Wiley and Sons).
- Ishiwada, Y., and Ogawa, K., 1976. Petroleum geology of offshore areas around the Japanese Islands. *United Nations ESCAP, CCOP Tech. Bull.*, 10:23–34.
- Kagami, H., Karig, D.E., Coulbourn, W.T., et al., 1986. *Init. Repts. DSDP*, 87: Washington (U.S. Govt. Printing Office).
- Karig, D.E., 1996. Uniaxial reconsolidation tests on porous sediments: mudstones from Site 897. In Whitmarsh, R.B., Sawyer, D.S., Klaus, A., and Masson, D.G. (Eds.), *Proc. ODP, Sci. Results*, 149: College Station, TX (Ocean Drilling Program), 363–373.
- Kawasaki, I., Arai, Y., Tamura, Y., Sagiya, T., Mikami, N., Okada, Y., Sakata, M., and Kasahara, M., 1995. The 1992 Sanriku-Oki, Japan, ultra-slow earthquake. *J. Phys. Earth*, 43:105–116.
- Keigwin, L.D., Rio, D., Acton, G.D., et al., 1998. *Proc. ODP, Init. Repts.*, 172: College Station, TX (Ocean Drilling Program).
- Knipe, R.J., 1986. Microstructural evolution of vein arrays preserved in Deep Sea Drilling Project cores from the Japan Trench, Leg 57. In Moore, J.C. (Ed.), *Structural Fabric in Deep Sea Drilling Project Cores from Forearcs*. Mem.—Geol. Soc. Am., 166:75–87.

- Koizumi, I., 1992. Diatom biostratigraphy of the Japan Sea: Leg 127. *In* Pisciotta, K.A., Ingle, J.C., Jr., von Breyman, M.T., Barron, J., et al., *Proc. ODP, Sci. Results*, 127/128 (Pt. 1): College Station, TX (Ocean Drilling Program), 249–289.
- Koizumi, I., and Tanimura, Y., 1985. Neogene diatom biostratigraphy of the middle latitude western North Pacific, Deep Sea Drilling Project Leg 86. *In* Heath, G.R., Burckle, L.H., et al., *Init. Repts. DSDP*, 86: Washington (U.S. Govt. Printing Office), 269–300.
- Kvenvolden, K.A., and Kastner, M., 1990. Gas hydrates of the Peruvian outer continental margin. *In* Suess, E., von Huene, R., et al., *Proc. ODP, Sci. Results*, 112: College Station, TX (Ocean Drilling Program), 517–526.
- Lowrie, W., 1990. Identification of ferromagnetic minerals in a rock by coercivity and unblocking temperature properties. *Geophys. Res. Lett.*, 17:159–162.
- Malone, R.D., 1994. Hydrate characterization research overview. *In* Sloan, E.D., Happel, J., and Hnatow, M.A. (Eds.), *Natural Gas Hydrates*. Ann. NY Acad. Sci.), 358–363.
- Maltman, A., 1987. Shear zones in argillaceous sediments: an experimental study. *In* Jones, M.E., and Preston, R.M.F. (Eds.), *Deformation of Sediments and Sedimentary Rocks*. Geol. Soc. Spec. Publ. London, 29:77–87.
- Müller, P.J., 1977. C/N ratios in Pacific deep sea sediments: effect of inorganic ammonium and organic nitrogen compounds sorbed by clays. *Geochim. Cosmochim. Acta*, 41:765–776.
- Niitsuma, N., 1986. Paleomagnetic results, Nankai Trough and Japan Trench, Deep Sea Drilling Project Leg 87. *In* Kagami, H., Karig, D.E., Coulbourn, W.T., et al., *Init. Repts. DSDP*, 87: Washington (U.S. Govt. Printing Office), 757–786.
- Niitsuma, N., and Akiba, F., 1986. Magnetostratigraphy and diatom biostratigraphy of Site 584, Deep Sea Drilling Project Leg 87, and implications for the tectonic evolution of Japanese Island Arcs. *In* Kagami, H., Karig, D.E., Coulbourn, W.T., et al., *Init. Repts. DSDP*, 87: Washington (U.S. Govt. Printing Office), 555–571.
- Nishizawa, A., Kono, T., Hasegawa, A., Hirasawa, T., Kanazawa, T., and Iwasaki, T., 1990. Spatial distribution of earthquakes off Sanriku, Northeastern Japan, in 1989 determined by ocean-bottom and land-based observation. *J. Phys. Earth*, 38:347–360.
- Opdyke, N.D., and Channell, J.E.T., 1996. *Magnetic Stratigraphy*: New York (Academic Press).
- Scientific Party, 1980. *Init. Repts. DSDP*, 56, 57: Washington (U. S. Govt. Printing Office).
- Shackleton, N.J., Crowhurst, S., Hagelberg, T., Pisias, N.G., and Schneider, D.A., 1995. A new late Neogene time scale: application to Leg 138 sites. *In* Pisias, N.G., Mayer, L.A., Janecek, T.R., Palmer-Julson, A., and van Andel, T.H. (Eds.), *Proc. ODP, Sci. Results*, 138: College Station, TX (Ocean Drilling Program), 73–101.
- Shipboard Scientific Party, 1995. Explanatory notes. *In* Shipley, T.H., Ogawa, Y., Blum, P., et al., *Proc. ODP, Init. Repts.*, 156: College Station, TX (Ocean Drilling Program), 39–68.
- Sloan, E.D., 1990. *Clathrate Hydrates of Natural Gases*: New York (Marcel Dekker).
- Storms, M.A., Natland, J.H., et al., 1991. *Proc. ODP, Init. Repts.*, 132: College Station, TX (Ocean Drilling Program).
- Sun, Y.F., in press. Core-log-seismic integration for marine sediments at the Juan de Fuca Ridge. *In* Fisher, A.T., Davis, E.E., Escutia, C. (Eds.), *ODP Sci Results*, 168: College Station, TX (Ocean Drilling Program).
- Tamaki, K., Pisciotta, K., Allan, J., et al., 1990. *Proc. ODP, Init. Repts.*, 127: College Station, TX (Ocean Drilling Program).
- Thompson, R., and Oldfield, F., 1986. *Environmental Magnetism*: London (Allen and Unwin).
- Tsuru, T., Park, J.-O., Takahashi, N., Kodaira, S., Kido, Y., Kaneda, Y., and Kono, Y., in press. Tectonic features of the Japan Trench convergent margin off Sanriku, north-eastern Japan revealed by multi-channel seismic reflection data. *J. Geophys. Res.*

- Tyson, R.V., 1995. *Sedimentary Organic Matter: Organic Facies and Palynofacies*: London (Chapman & Hall).
- von Huene, R., Klaeschen, D., Cropp, B., and Miller, J., 1994. Tectonic structure across the accretionary and erosional parts of the Japan Trench margin. *J. Geophys. Res.*, 99:22349–22361.
- Yanagisawa, Y., and Akiba, F., 1998. Refined Neogene diatom biostratigraphy for the northwest Pacific around Japan, with an introduction of code numbers for selected diatom biohorizons. *J. Geol. Soc. Jpn.*, 104:395–414.

Figure F1. Map of the Japan Trench area off northeast Japan.

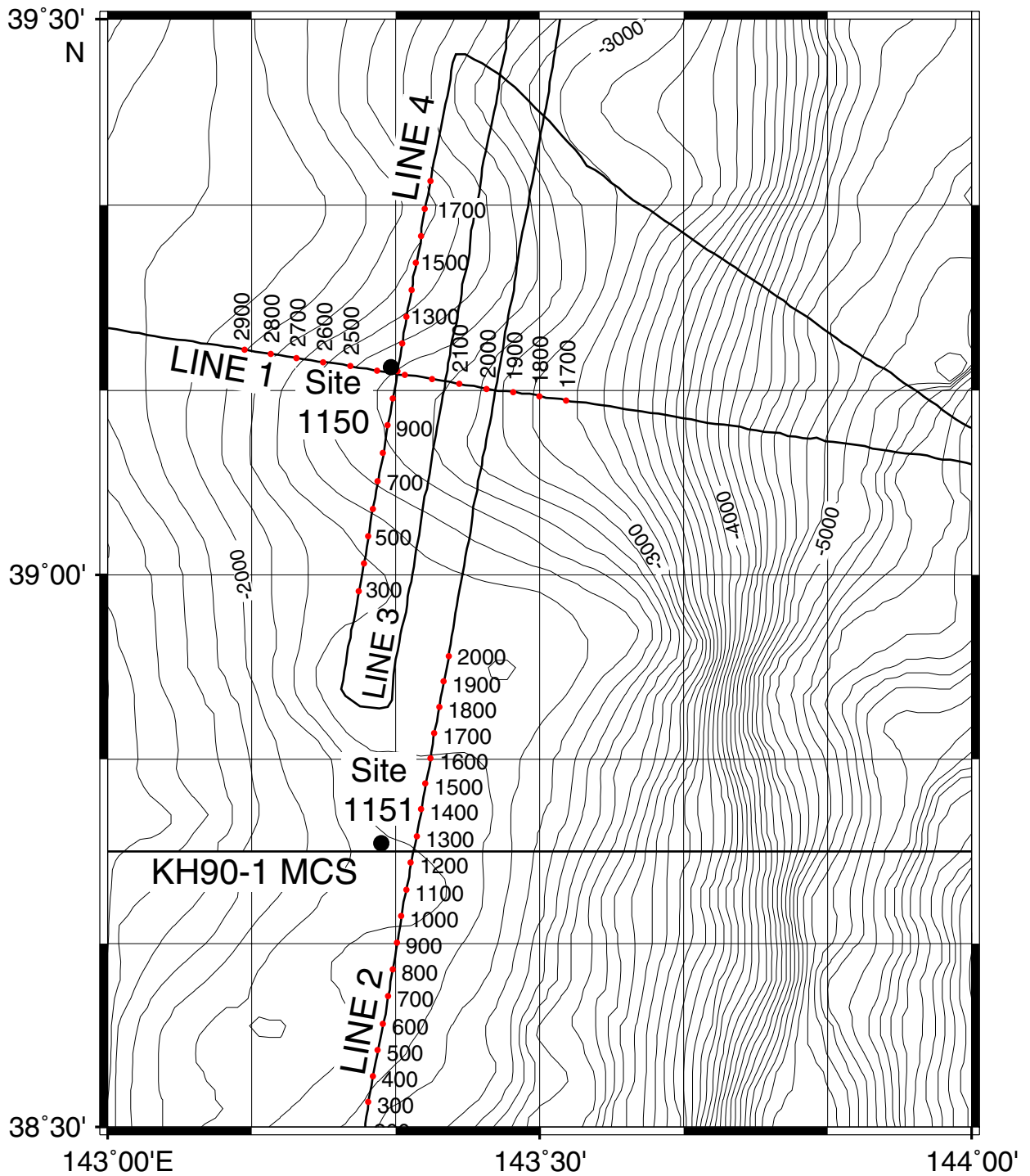


Figure F2. Seismic reflection profile crossing Site 1150.

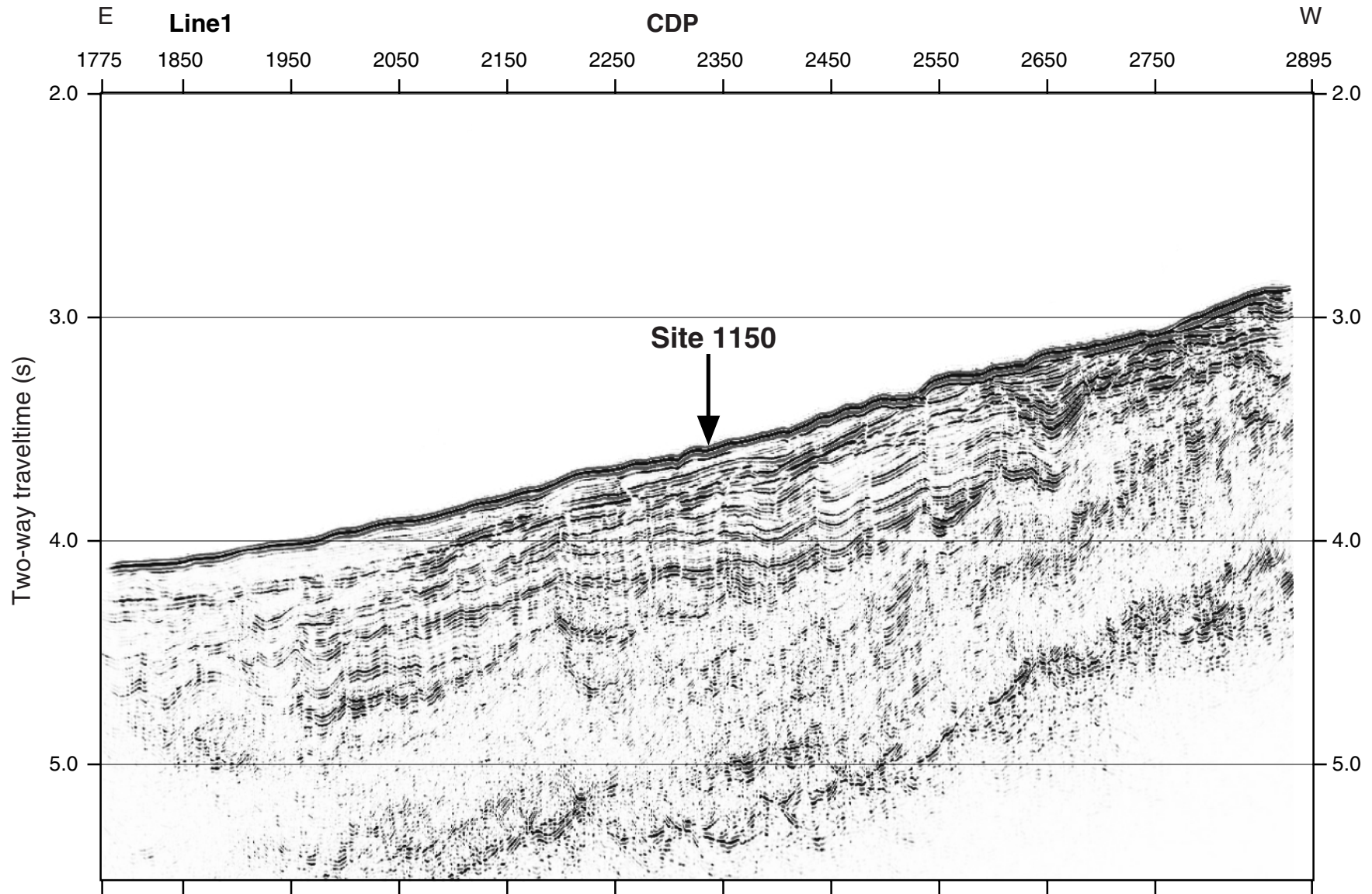


Figure F3. Schematic of equipment used in the borehole installation at Site 1150. The depths listed are those of the final installation in Hole 1150D.

Hole 1150D Reentry Cone Installation Schematic

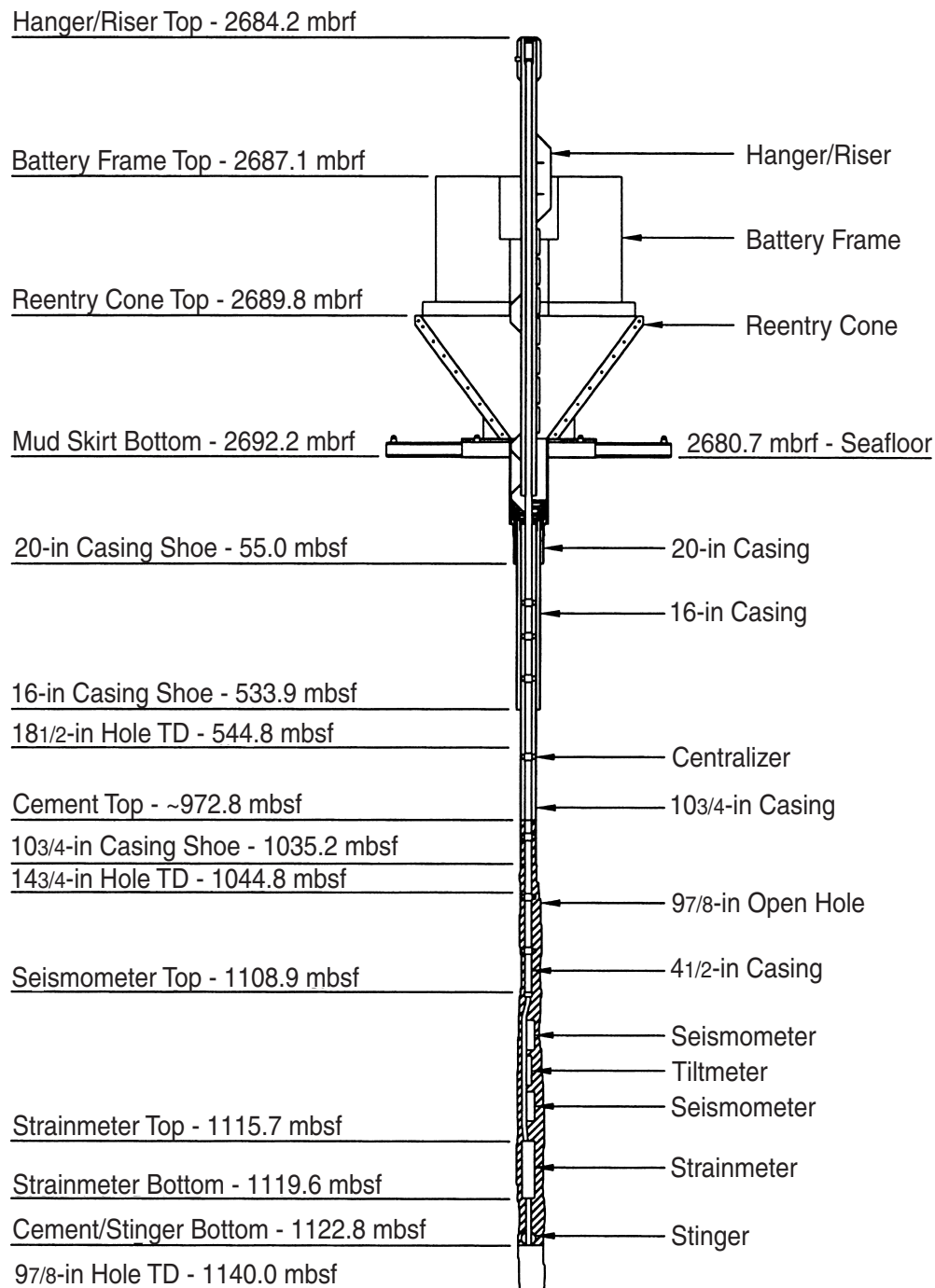


Figure F4. An image of part of the 10¾-in casing string as it falls into the reentry cone at Hole 1150C.

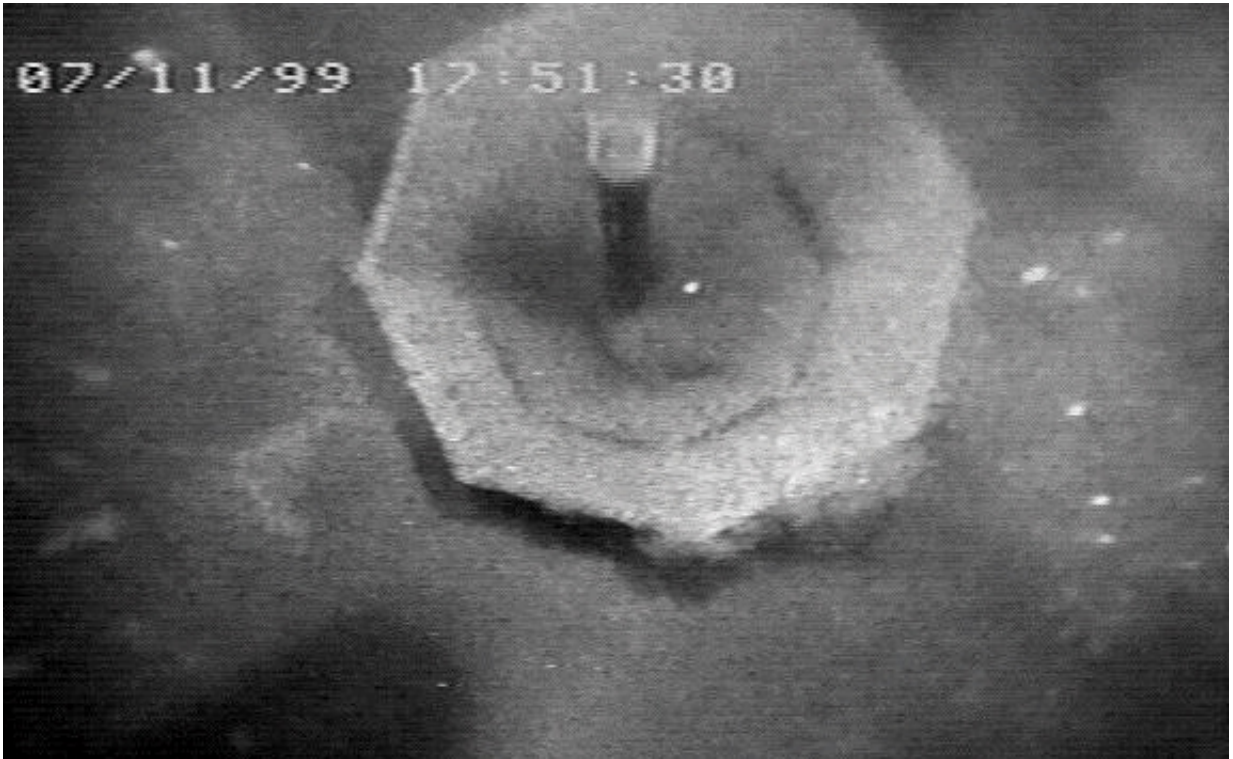


Figure F5. Configuration of riser, cables, and casing elevators used to hang off the instrument string in the moonpool area.



Figure F6. Three images of the successfully installed battery frame at Hole 1150D.

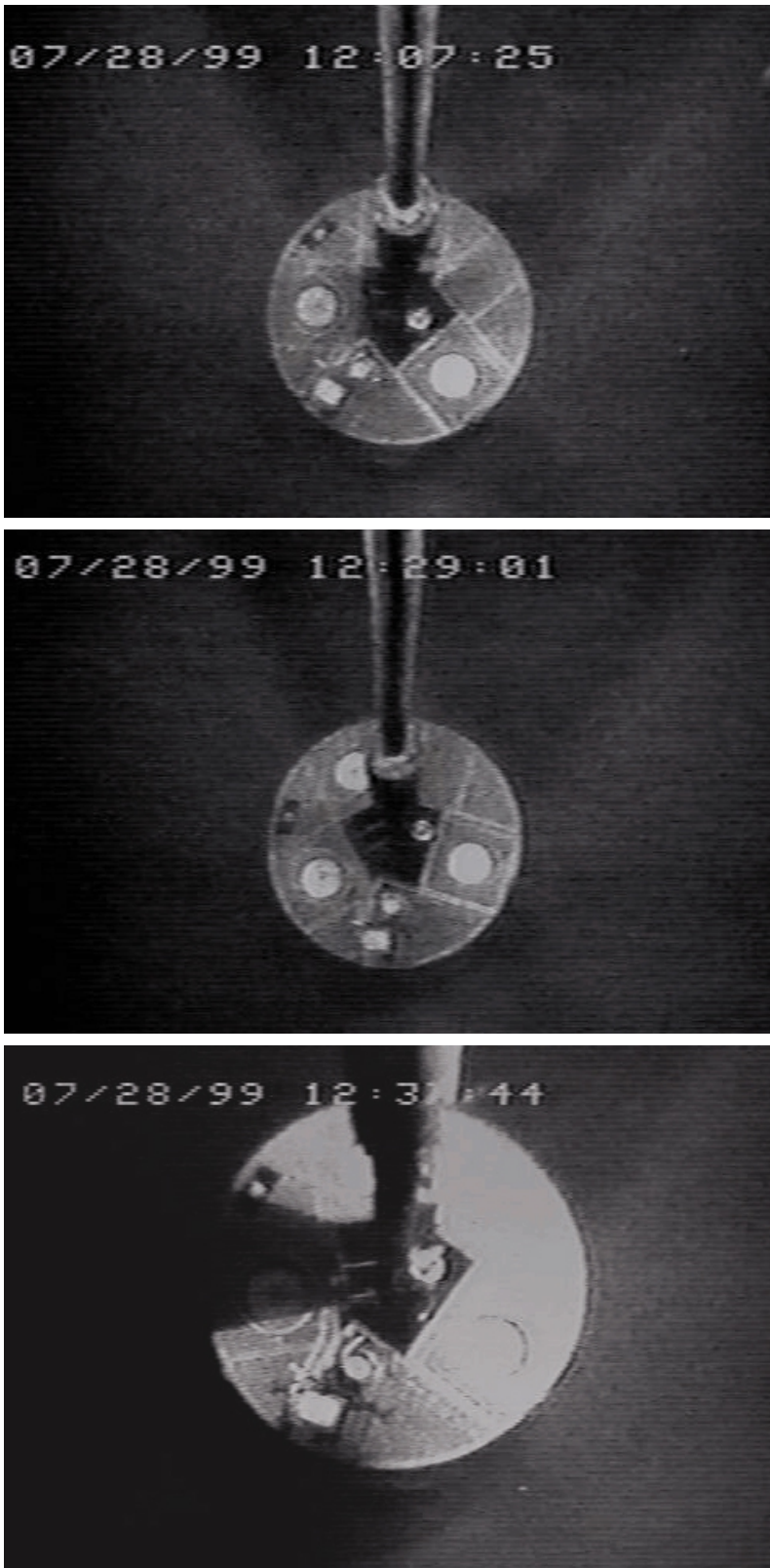
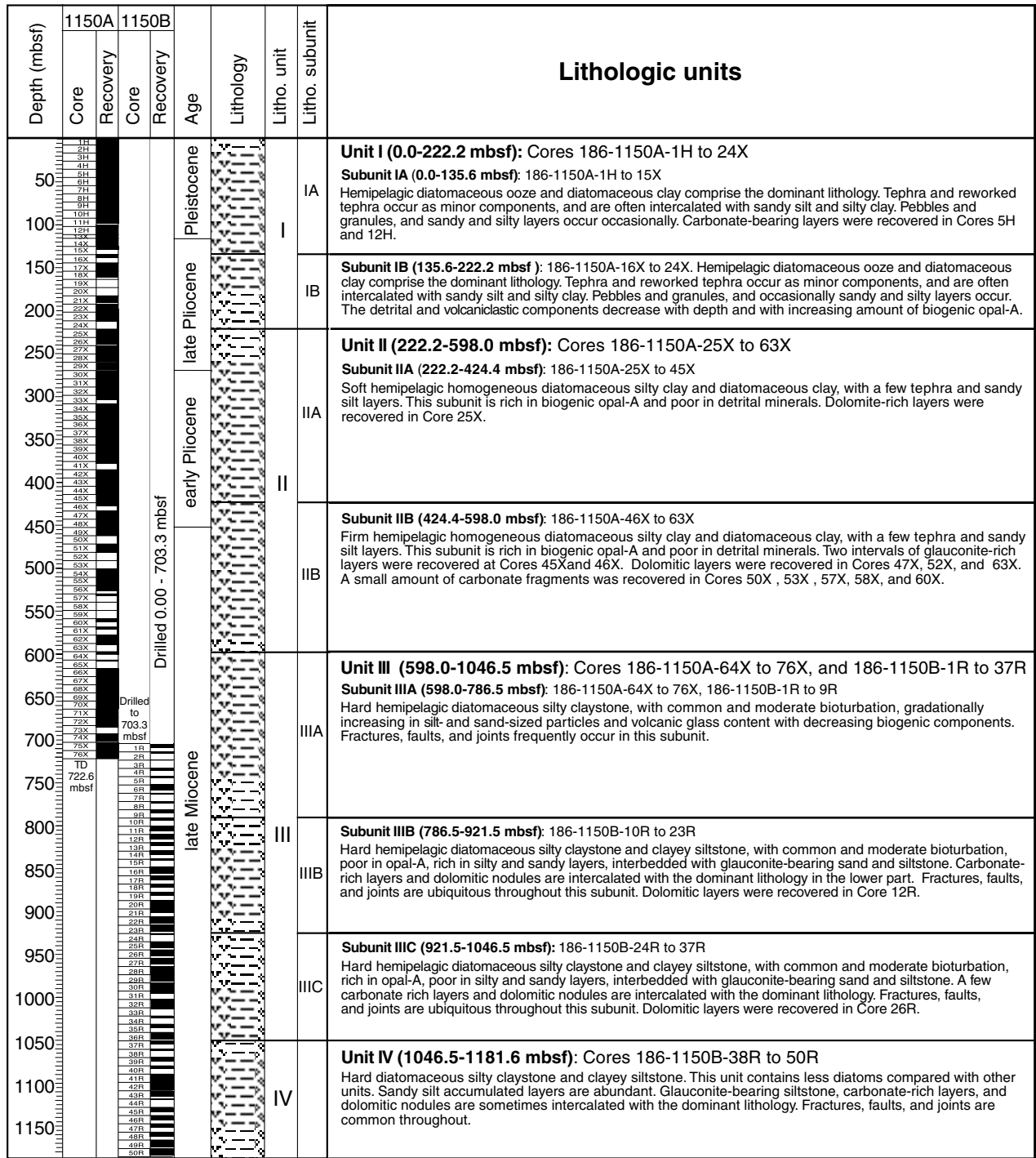


Figure F7. Site 1150 lithologic units and color reflectance. (Continued on next page.)



TD 1181.6 mbsf

Figure F7 (continued).

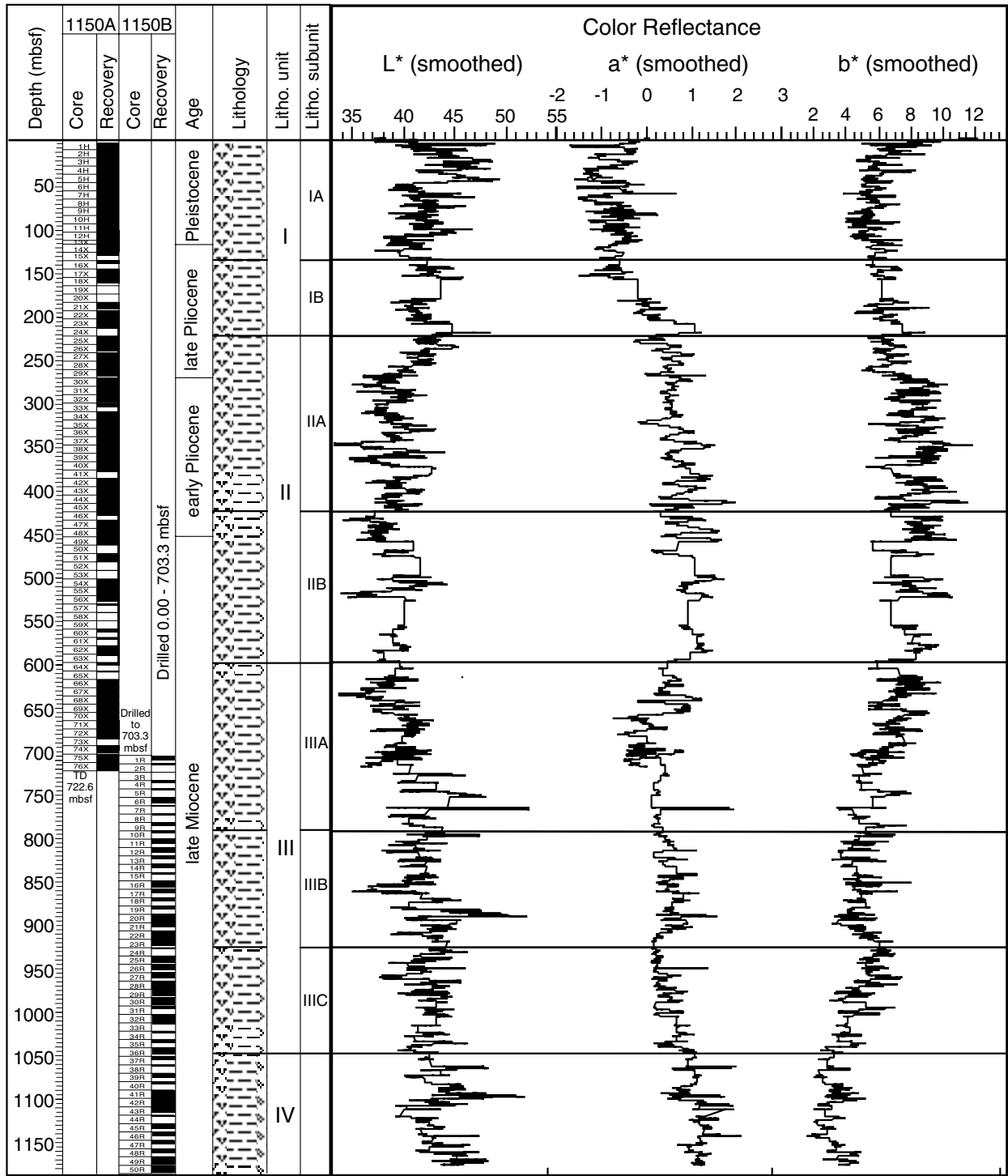


Figure F8. Histogram of the three major sediment types (biogenic, siliciclastic, and volcanoclastic) and other components. The components are estimated in percent from smear-slide observations.

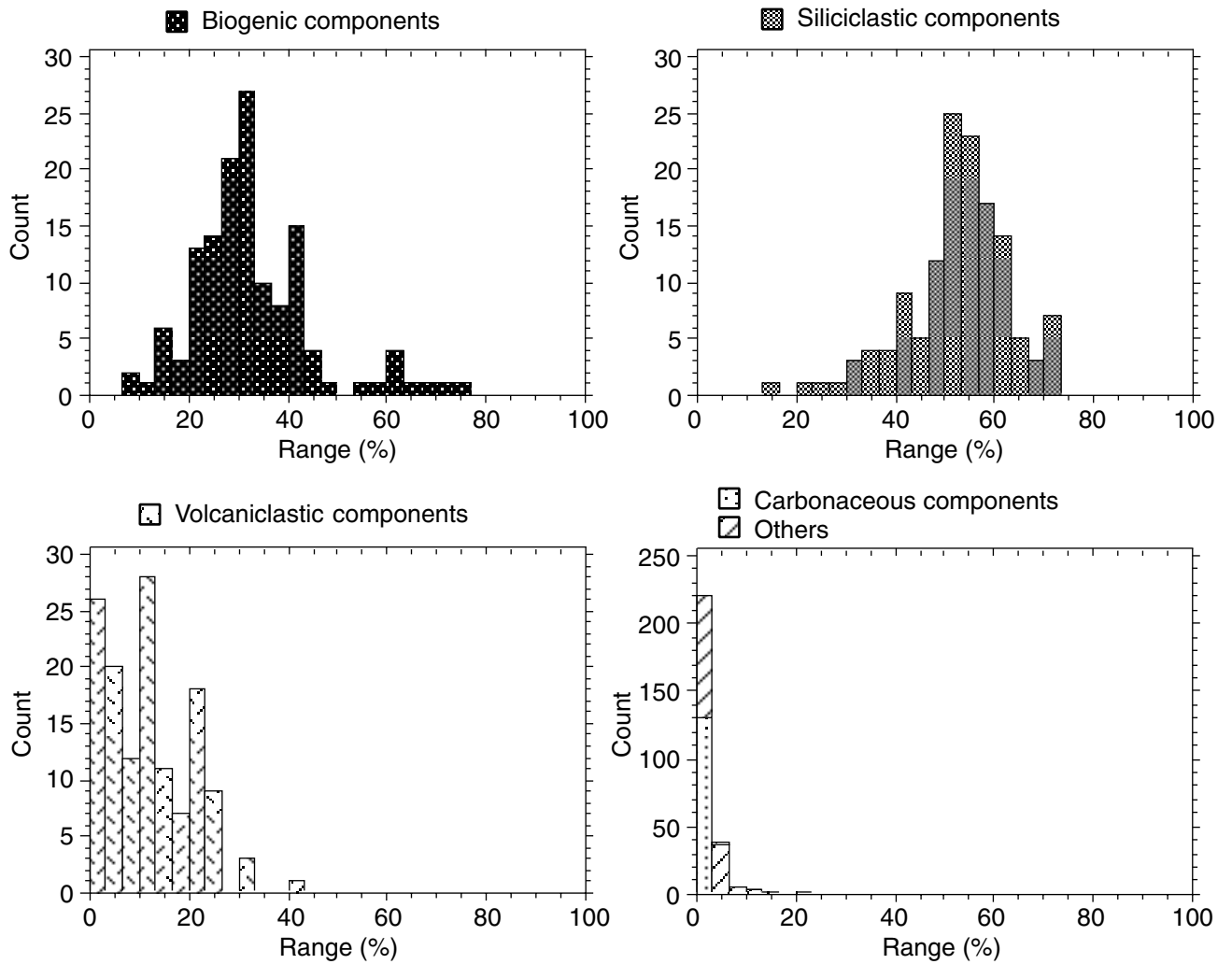


Figure F9. Downhole variations of biogenic, siliciclastic, and volcanoclastic sediments, and other components from smear-slide observations; variations of minor lithologies. Magnetic susceptibility data are plotted as raw corrected values and after smoothing and removing the peak values.

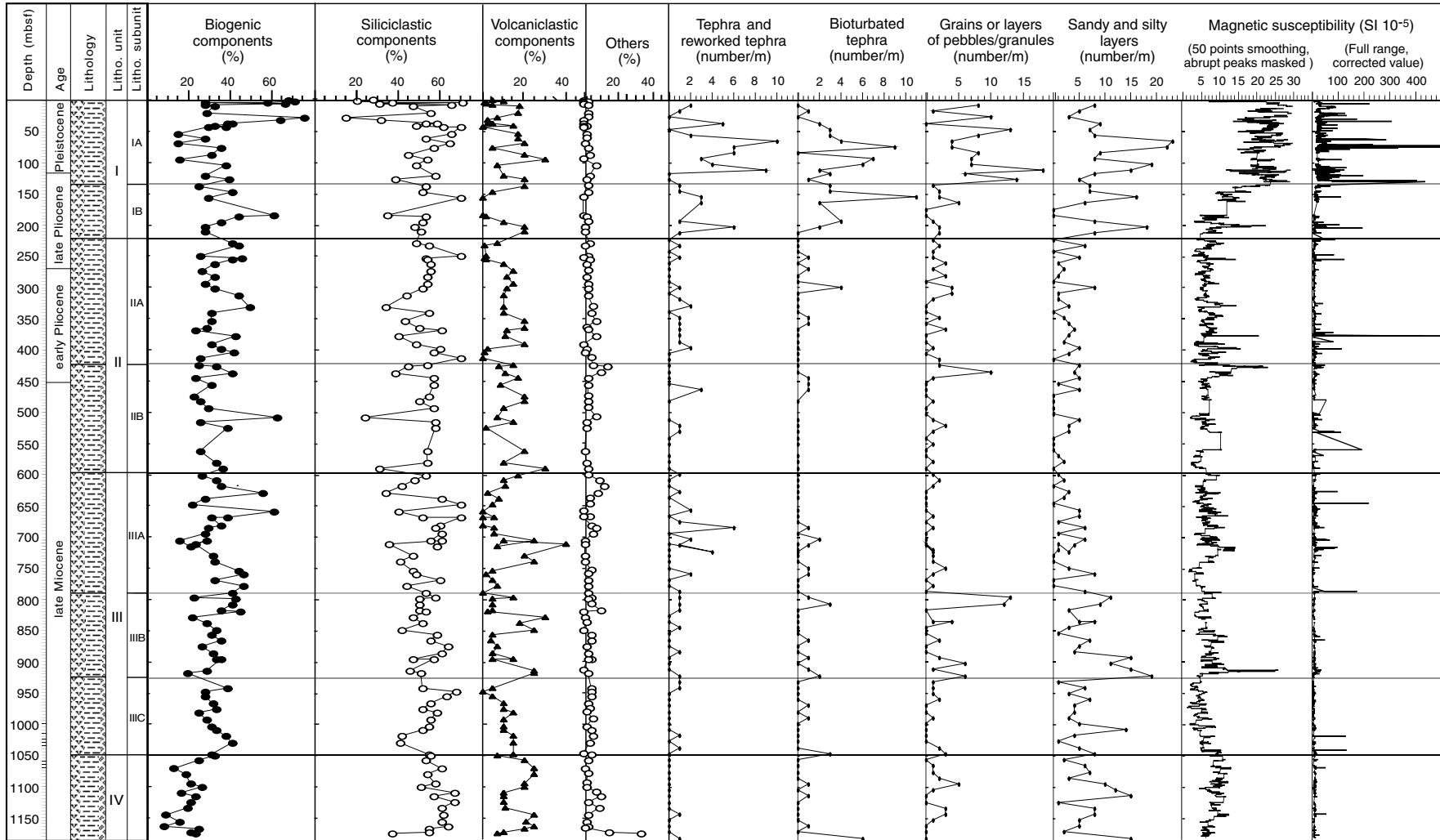


Figure F10. Photograph of typical “coring biscuits” by XCB coring (interval 186-1150A-47X-3, 50–100 cm).

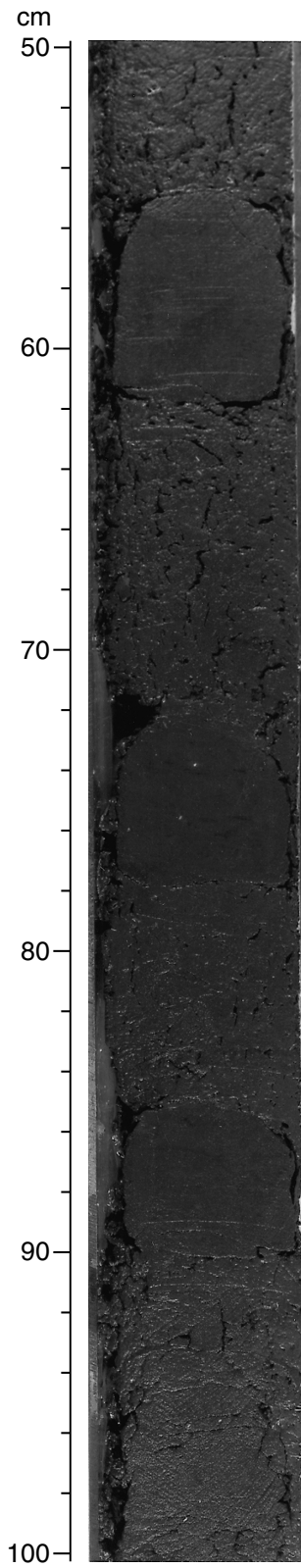


Figure F11. Photograph of ichnofossils. A. A healed fracture cuts *Planolites* (interval 186-1150B-20R-6, 21–32 cm). B. *Chondrites* (interval 186-1150B-27R-4, 20–35 cm). (Continued on next page.)

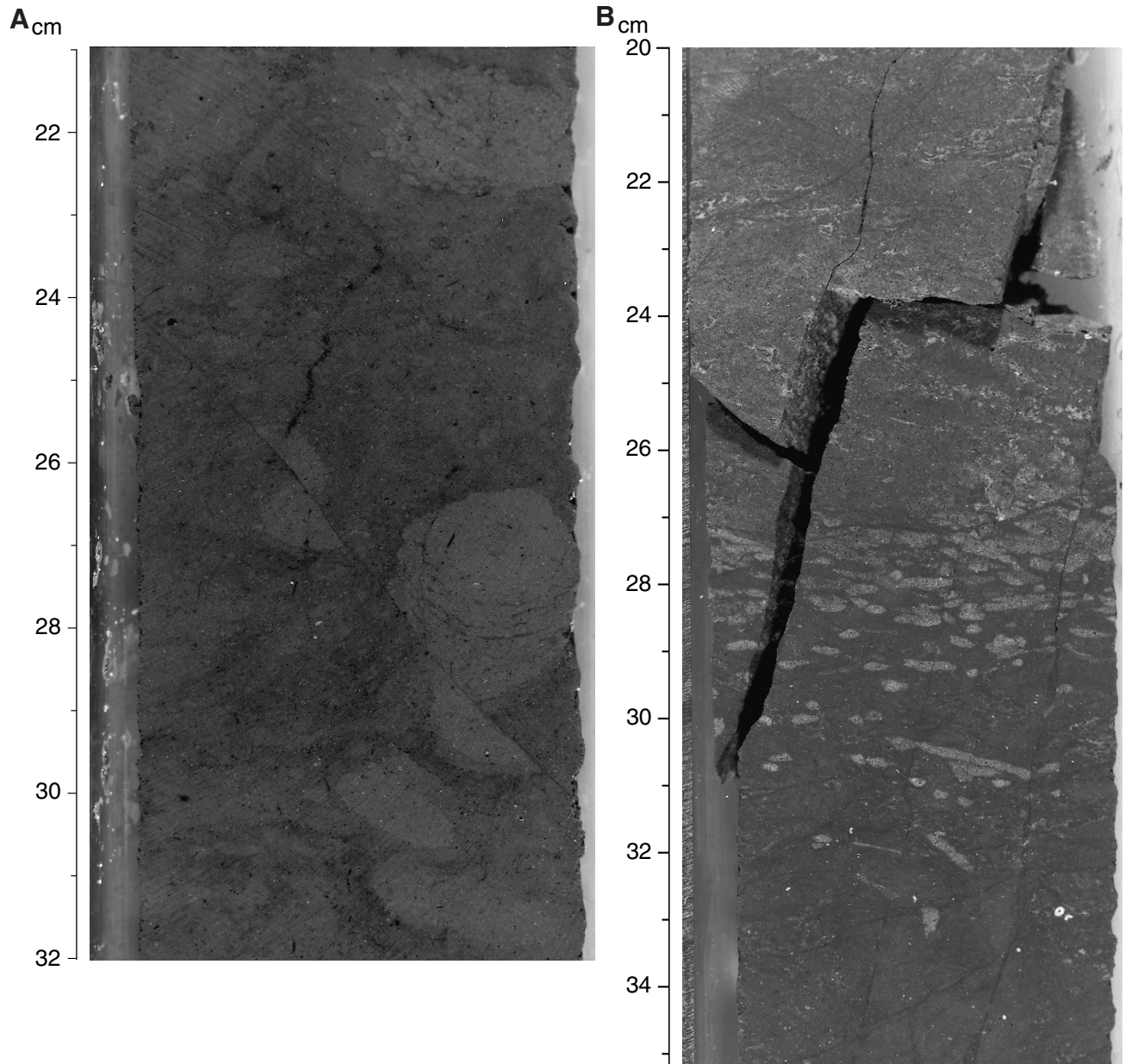


Figure F11 (continued). *C. Zoophycos* (interval 186-1150B-43R-3, 26–40 cm).

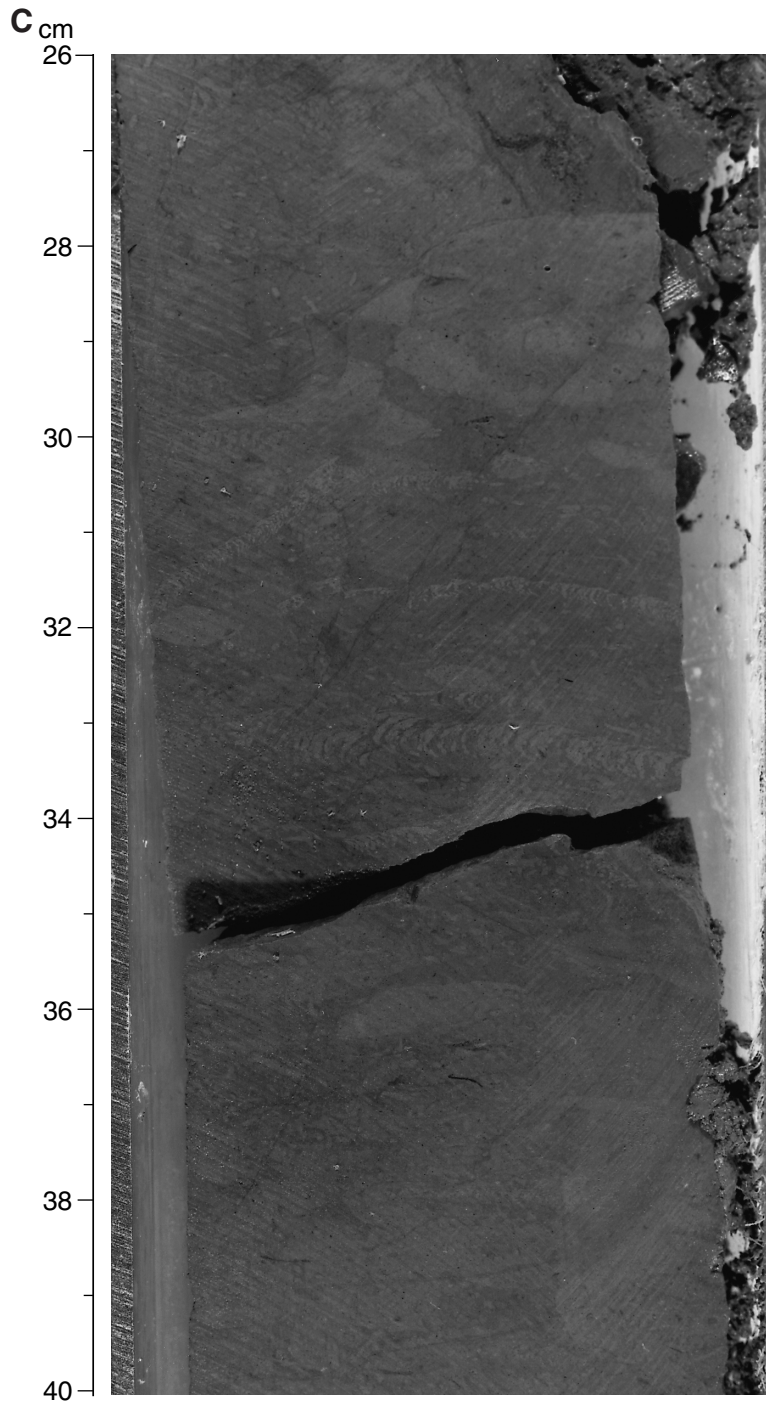


Figure F12. Downhole variations of each lithologic component from smear-slide observations. (Continued on next two pages.)

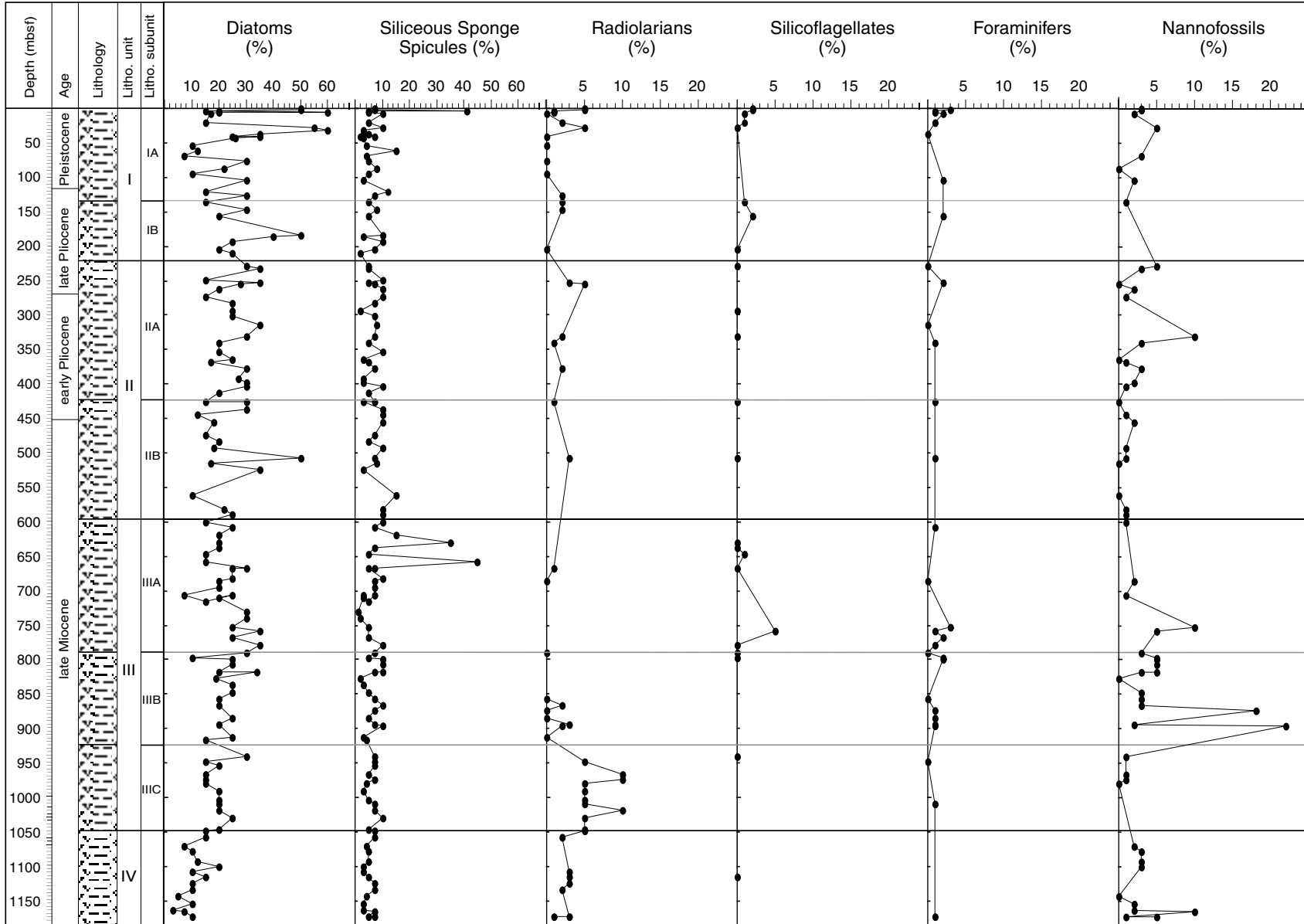


Figure F12 (continued).

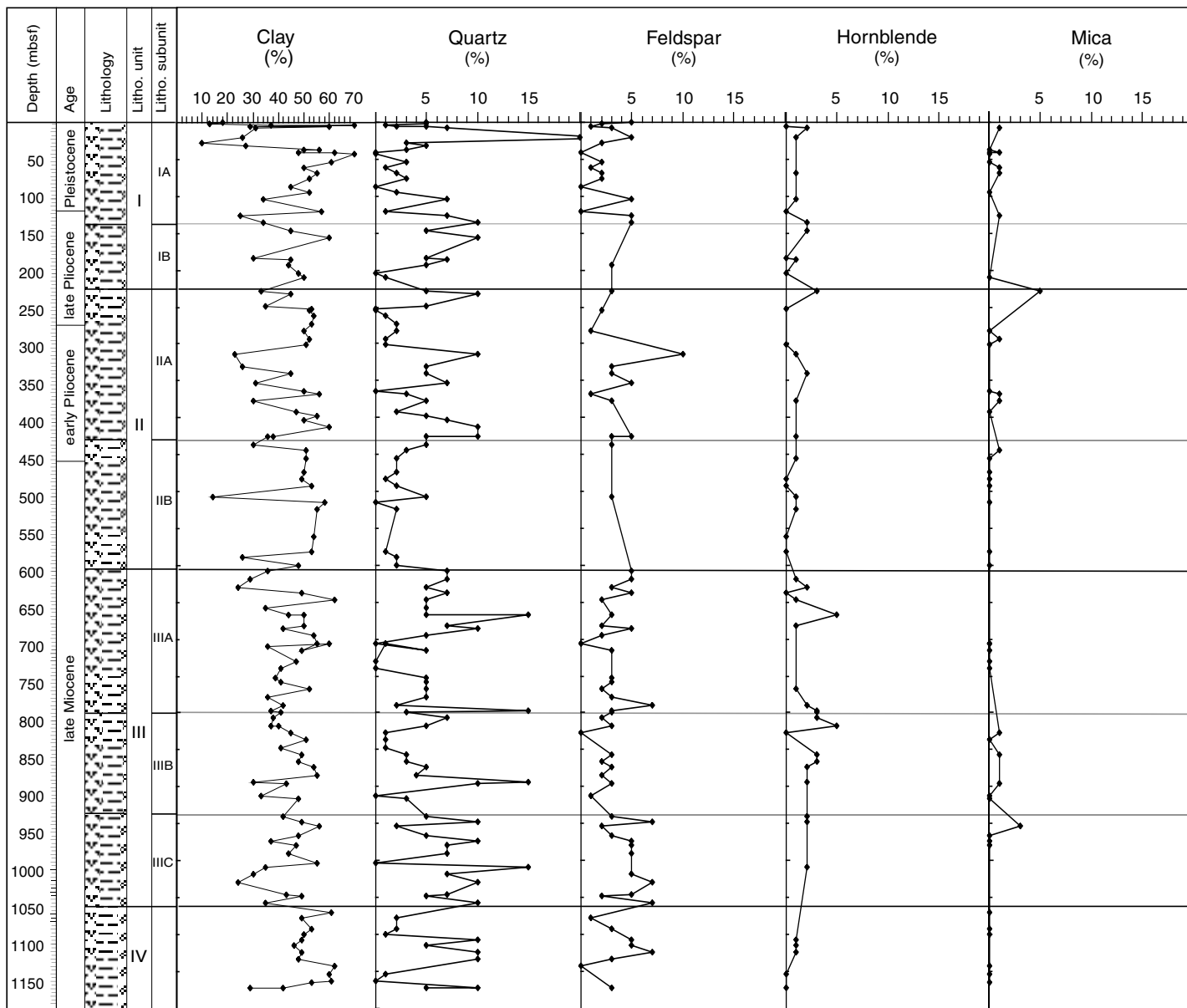


Figure F12 (continued).

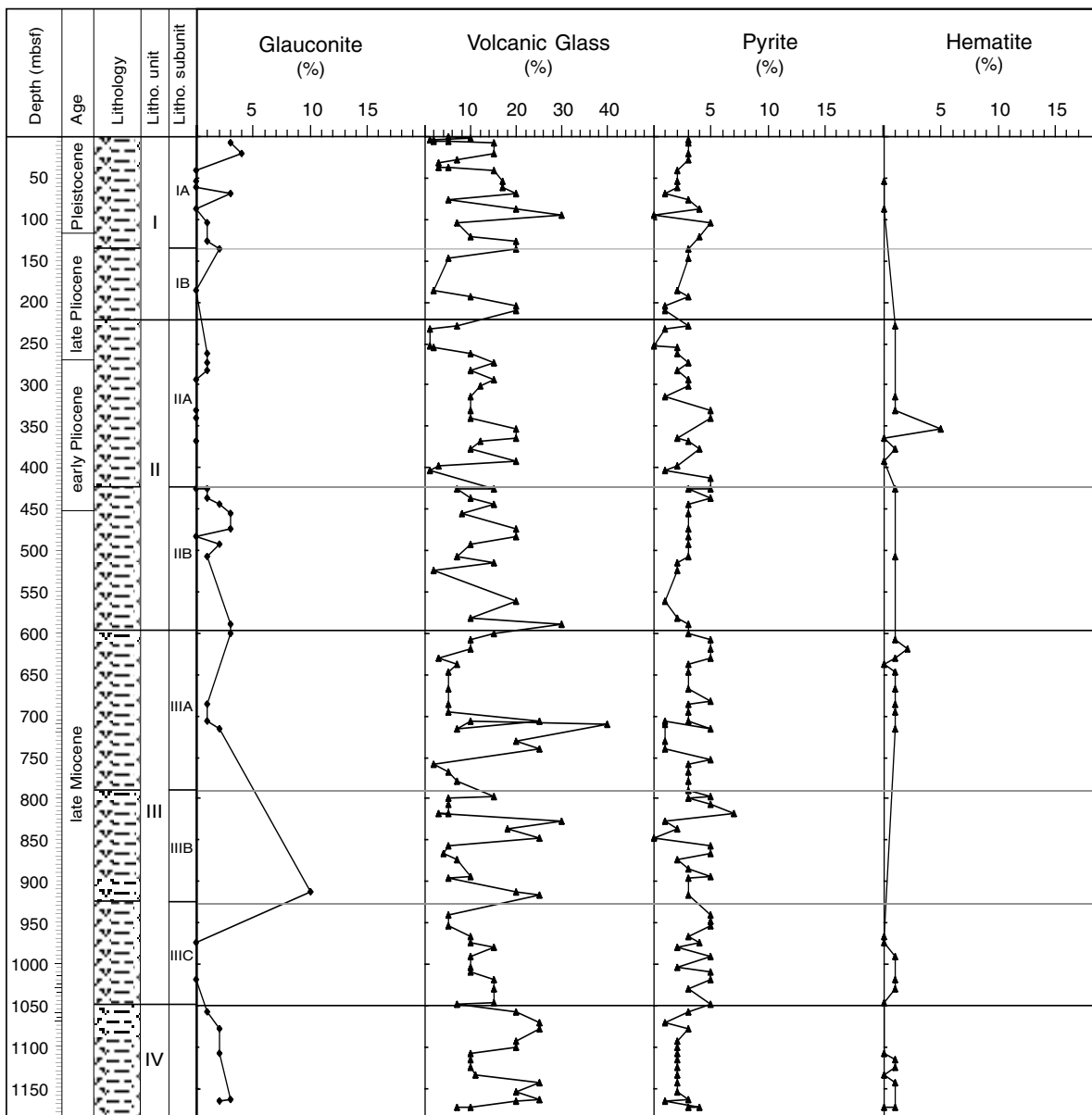


Figure F13. A. X-ray diffractograms of the major lithology at Site 1150. Samples are selected from each lithologic unit. (Continued on next two pages.)

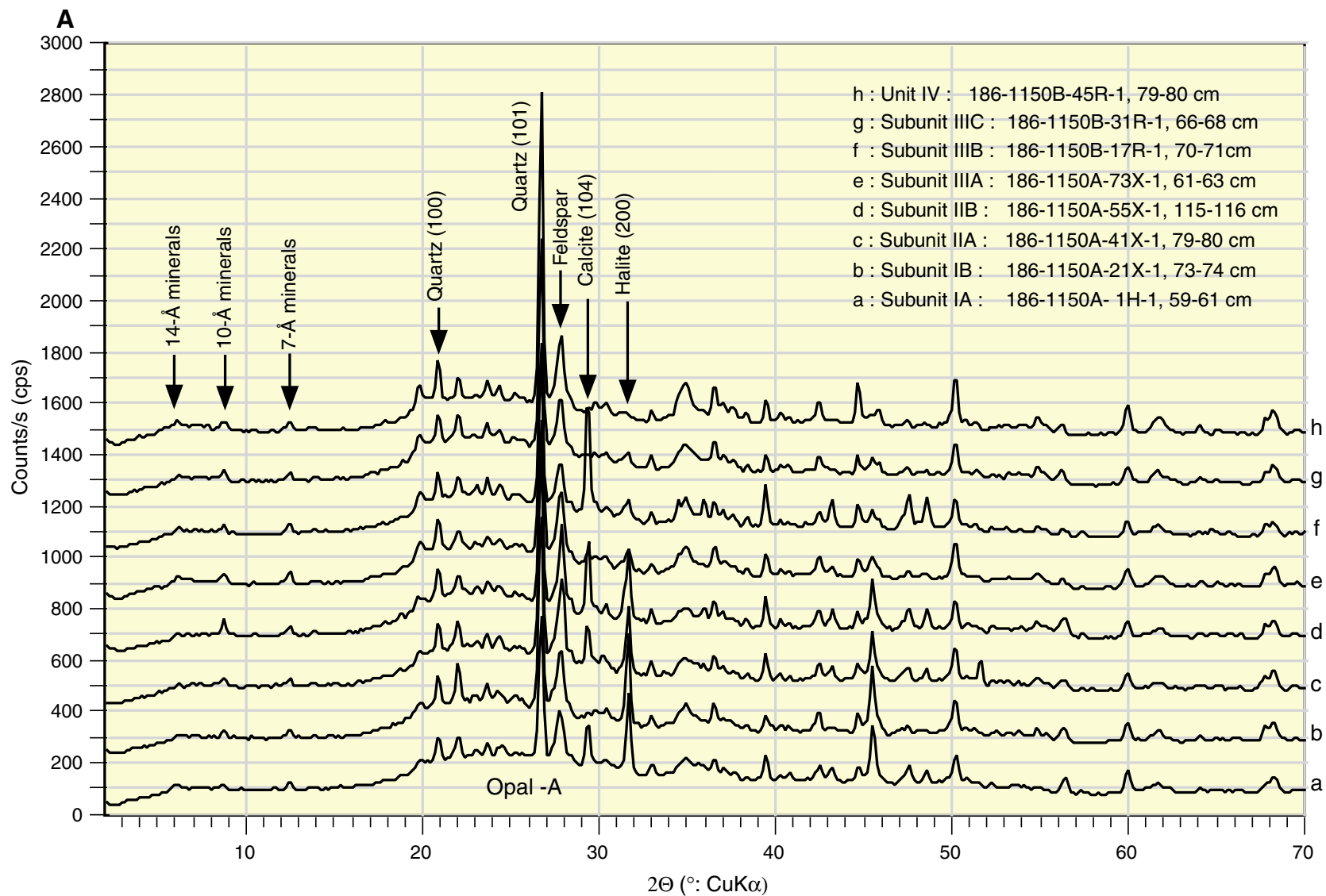


Figure F13 (continued). B. Typical X-ray diffractograms of a minor silt layer (interval 186-1150A-9H-1, 95–96 cm).

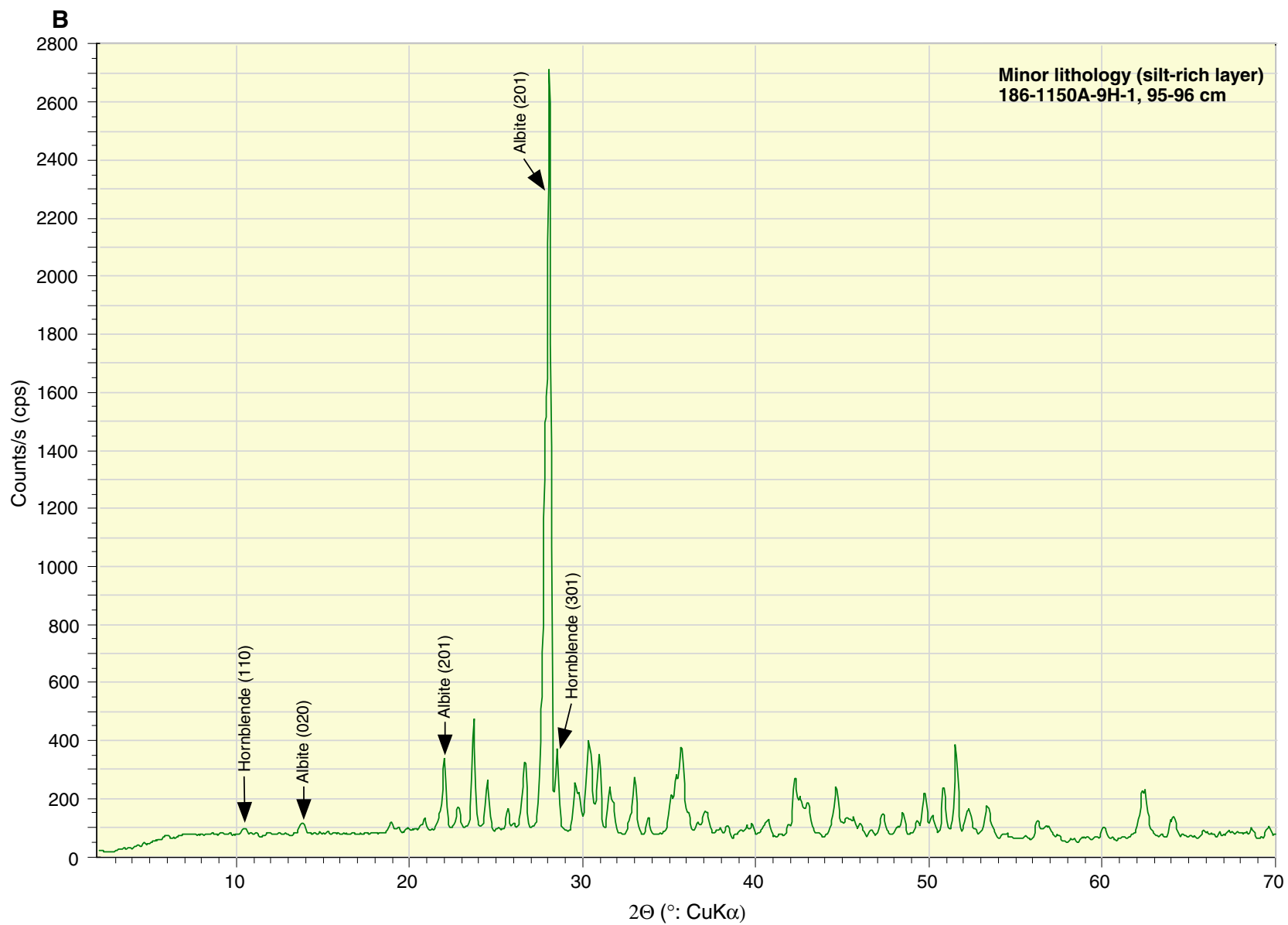


Figure F13 (continued). C. Typical X-ray diffractograms of a dolomitic layer (interval 186-1150A-63X-CC, 23–24 cm).

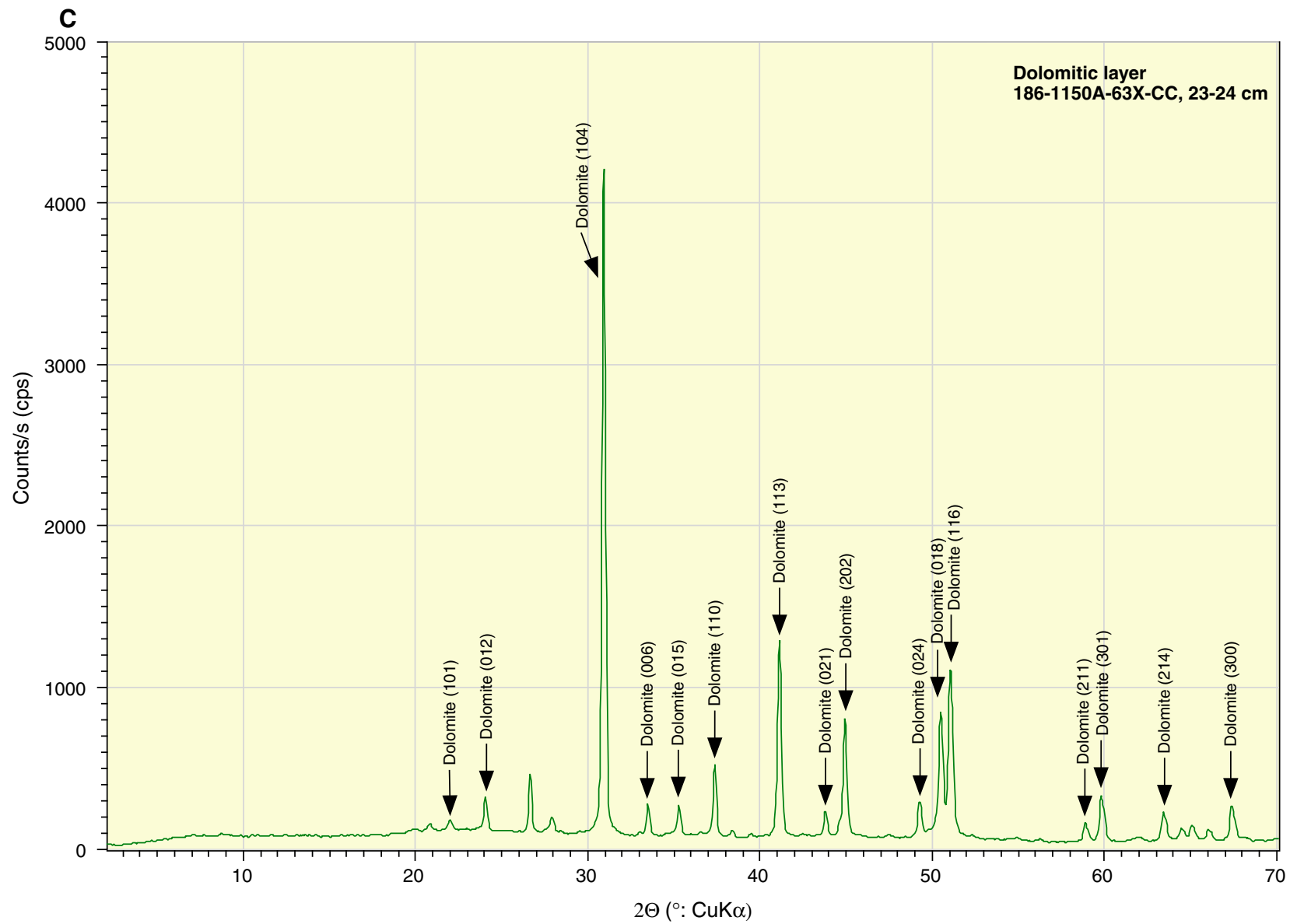


Figure F14. The variations of major minerals by XRD. Depth-series data are compiled as XRD intensities (in counts per second) for each mineral. (Continued on next two pages.)

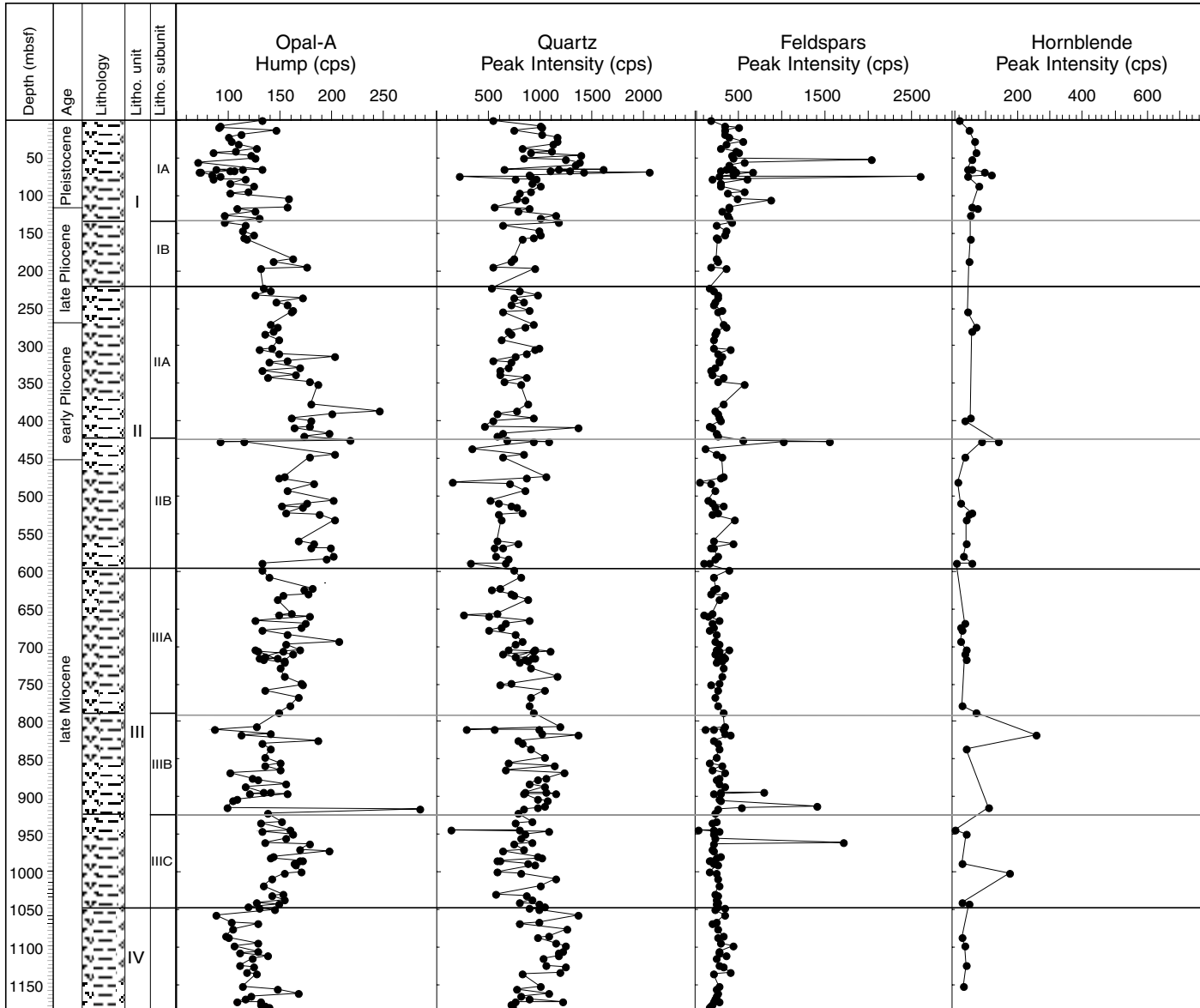


Figure F14 (continued).

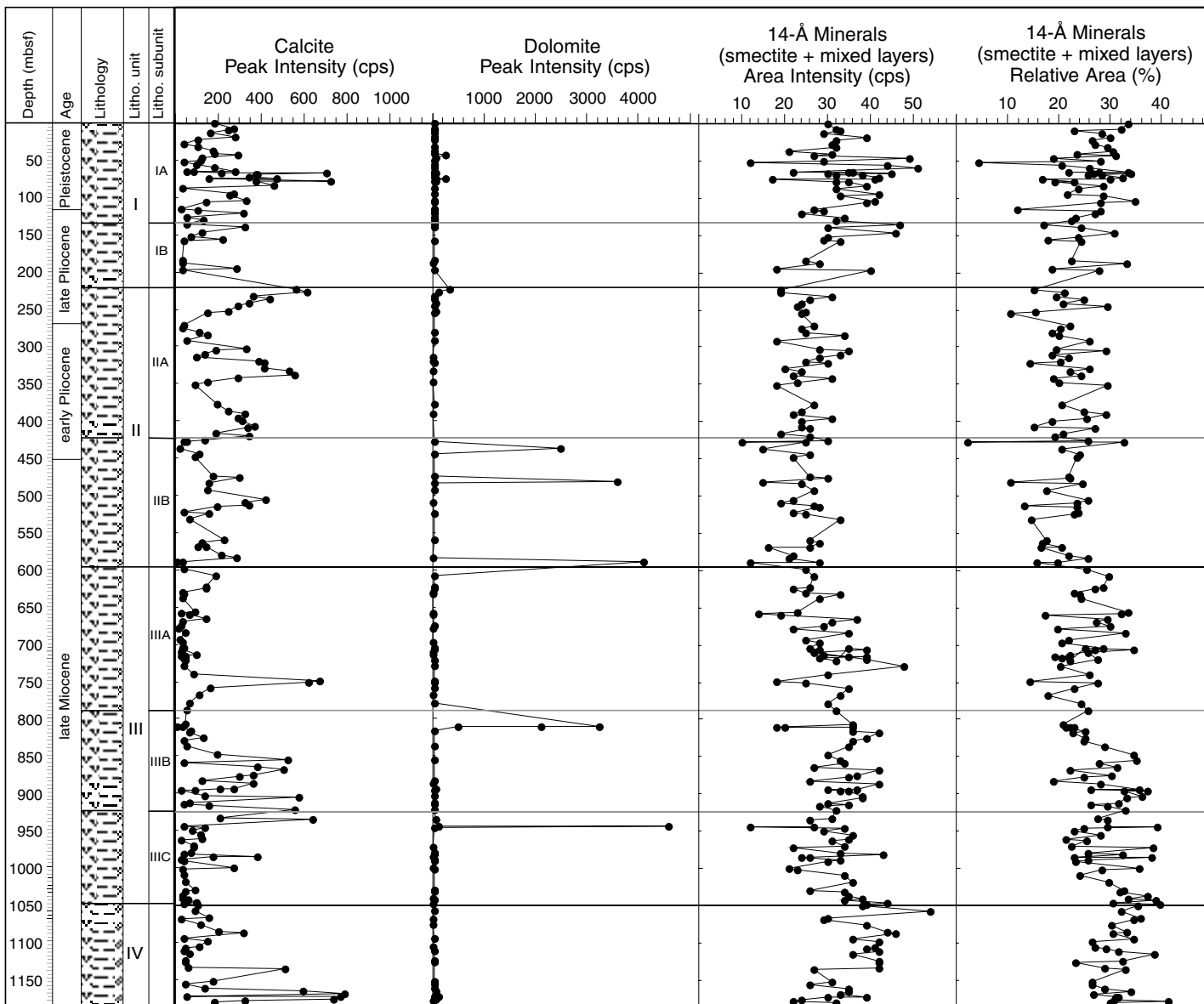


Figure F14 (continued).

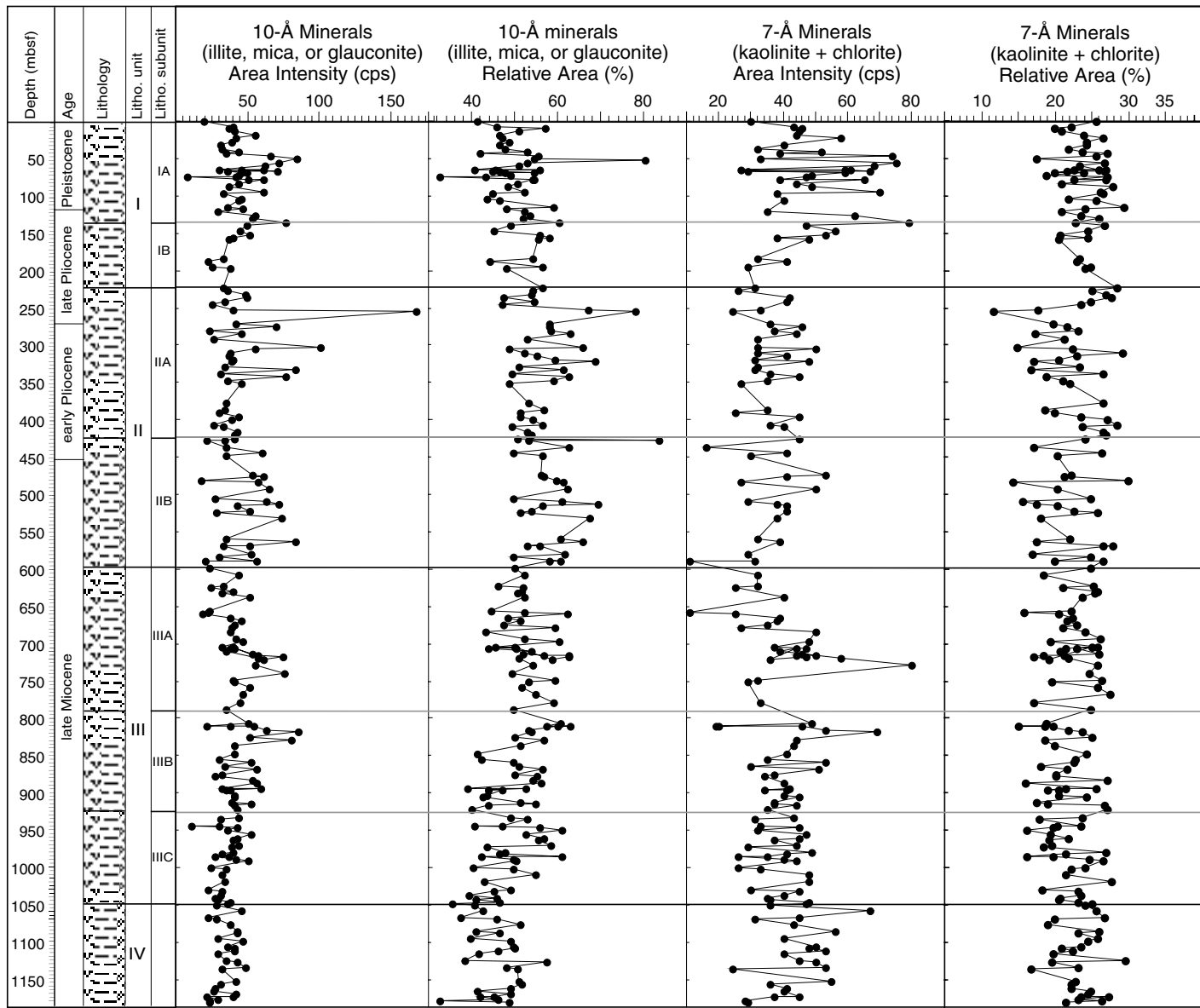


Figure F15. Variations of color (a^*), opal-A, quartz, and 14-Å minerals. Natural gamma-ray intensities and magnetic susceptibility are from multi-sensor track measurements, and resistivity data are from downhole measurements. Dolomite layers are based on recovered cores and downhole measurements. MST = multisensor track.

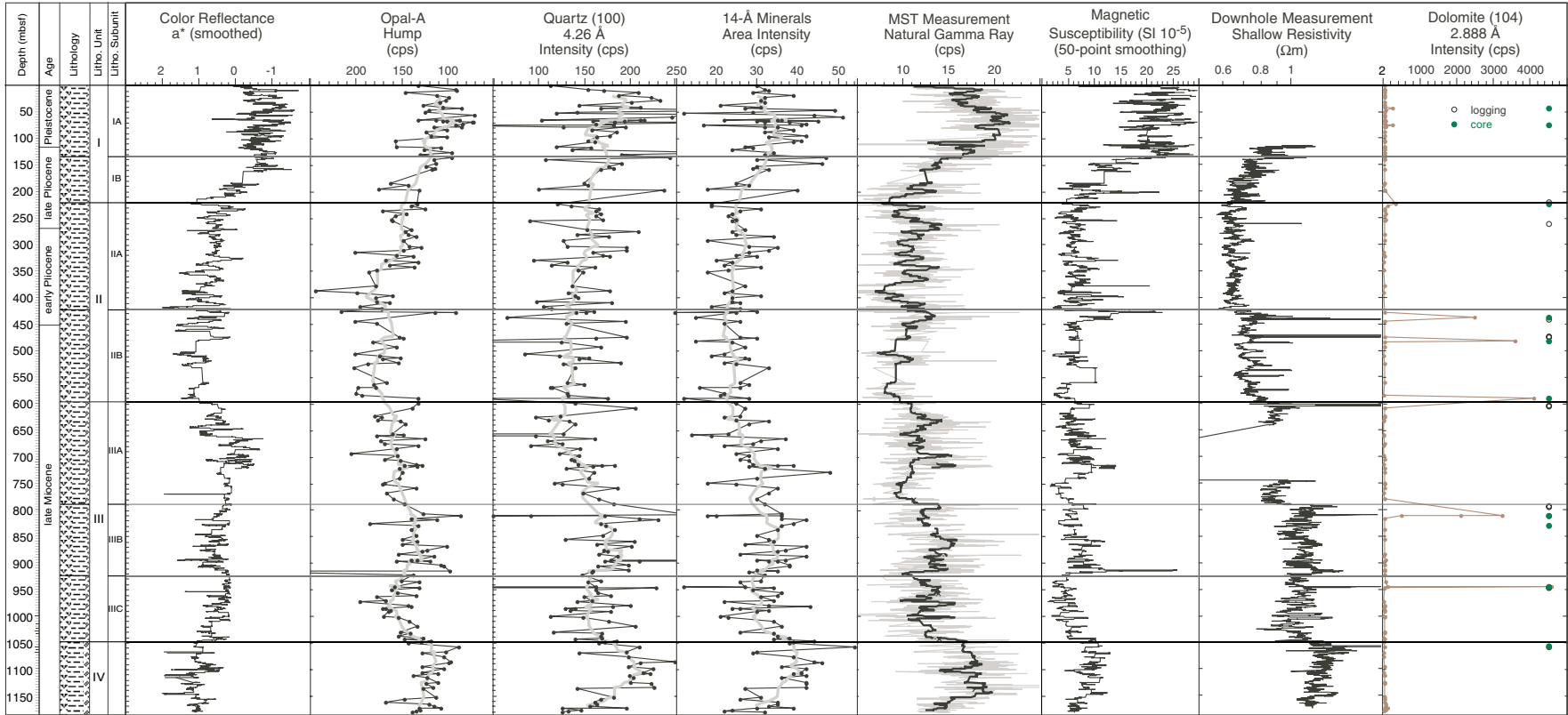


Figure F16. Core-scale cyclic variations of color (L^* , a^* , and b^*), gamma-ray attenuation (GRA) bulk density, magnetic susceptibility, and natural gamma radiation by MST measurement. The diatom-rich intervals correspond to slightly higher a^* values (reddish), low resistivity, low NGR counts, and low density. In contrast, clay-rich intervals show a slightly lower a^* value (light reddish or light greenish), high resistivity, high NGR counts, and high density.

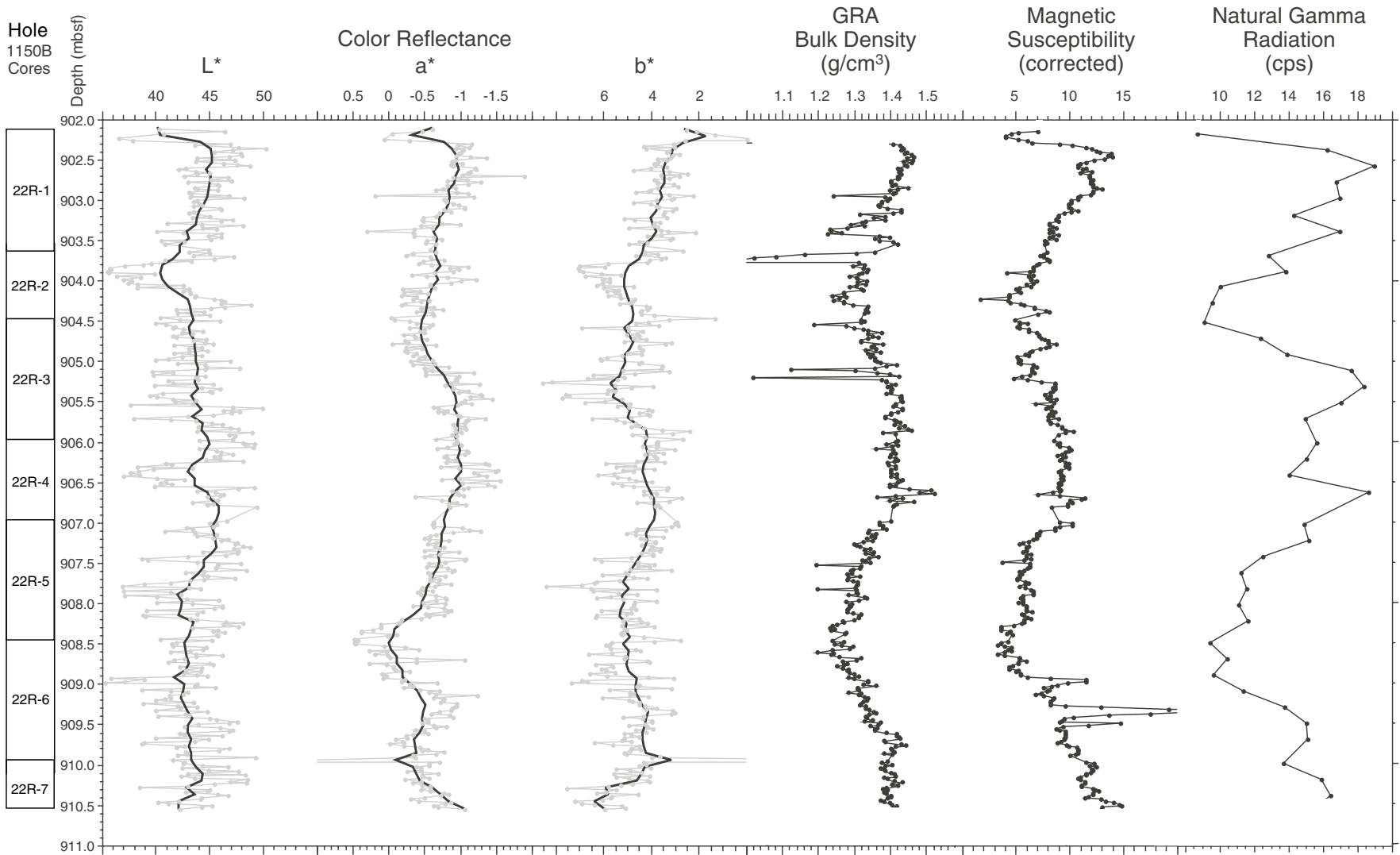


Figure F17. Lithification and diagenesis at Site 1150.

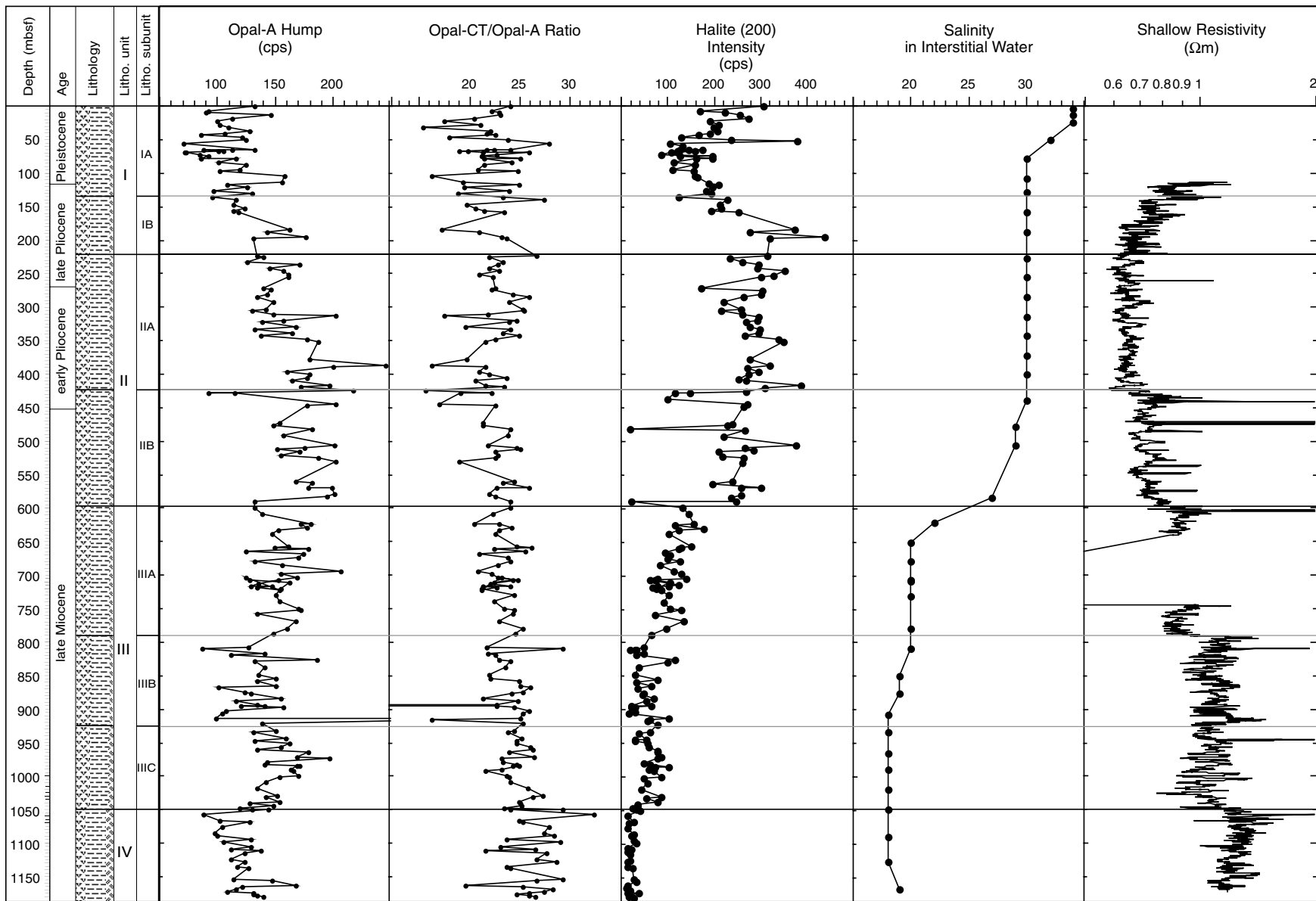


Figure F18. Summary of logs at Hole 1150B compared with the lithologic units (see "Lithostratigraphy," p. 14).

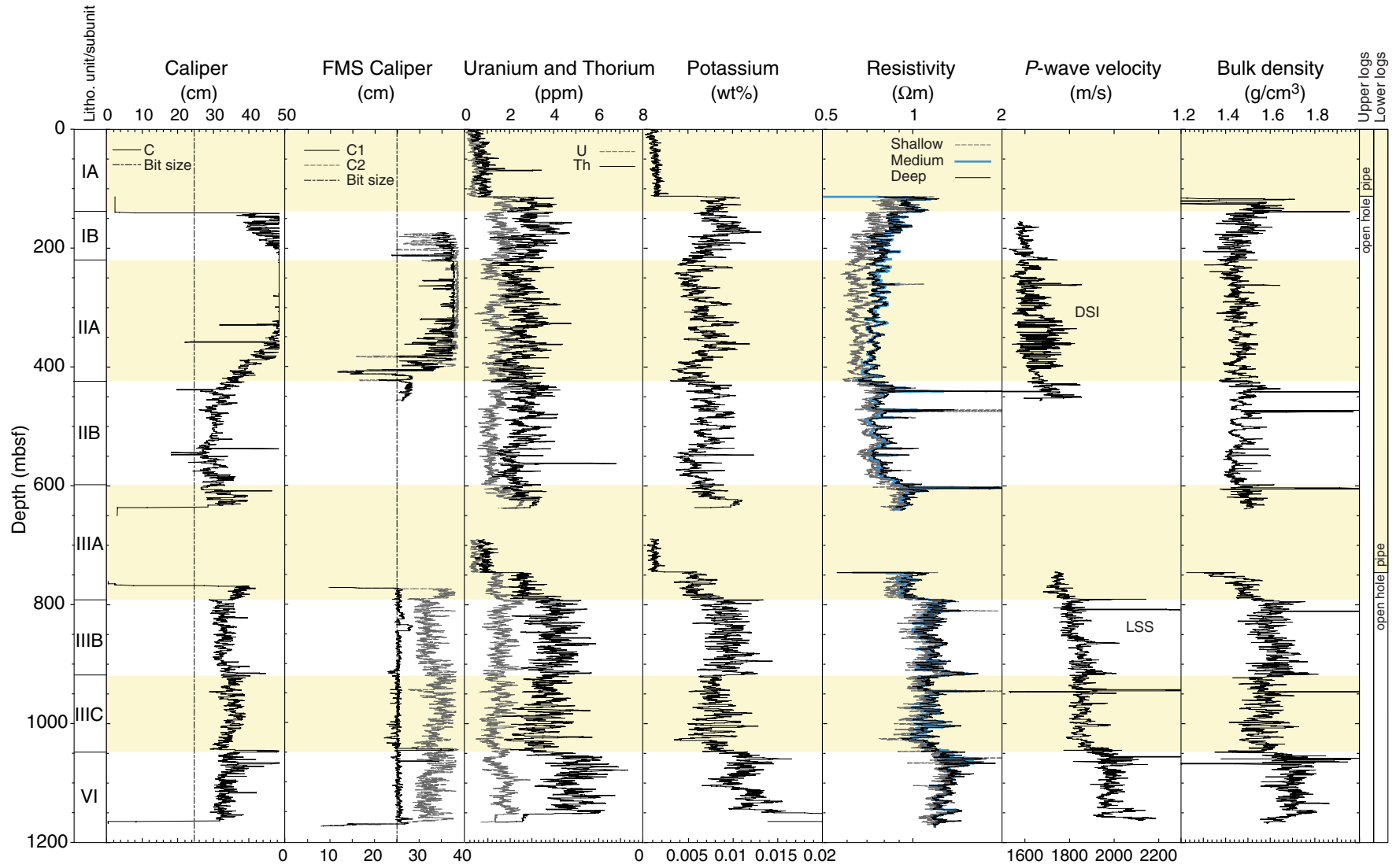


Figure F19. Photograph of a typical pumice layer recovered at Site 1150 (interval 186-1150A-8H-6, 40–60 cm).

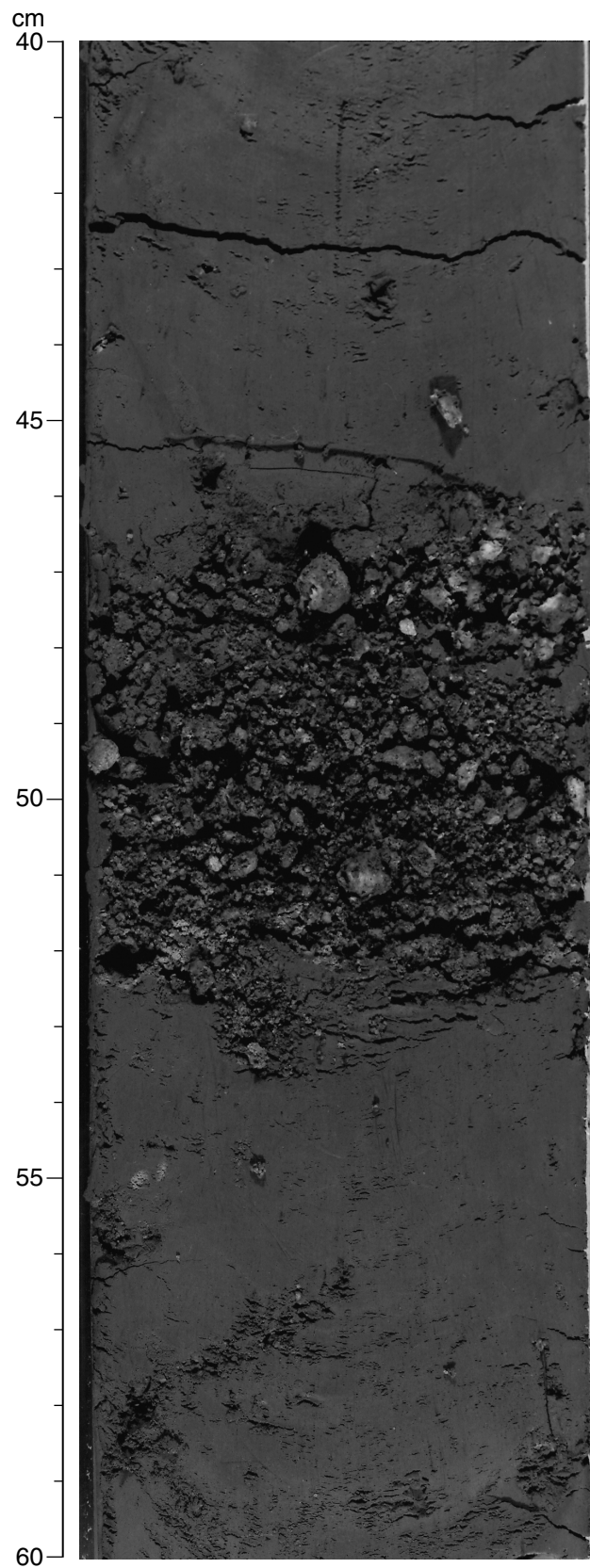


Figure F20. Photograph of typical primary ash layers. A. Interval 186-1150A-3H-CC, 15–30 cm. B. Interval 186-1150A-7H-7, 48–57 cm.

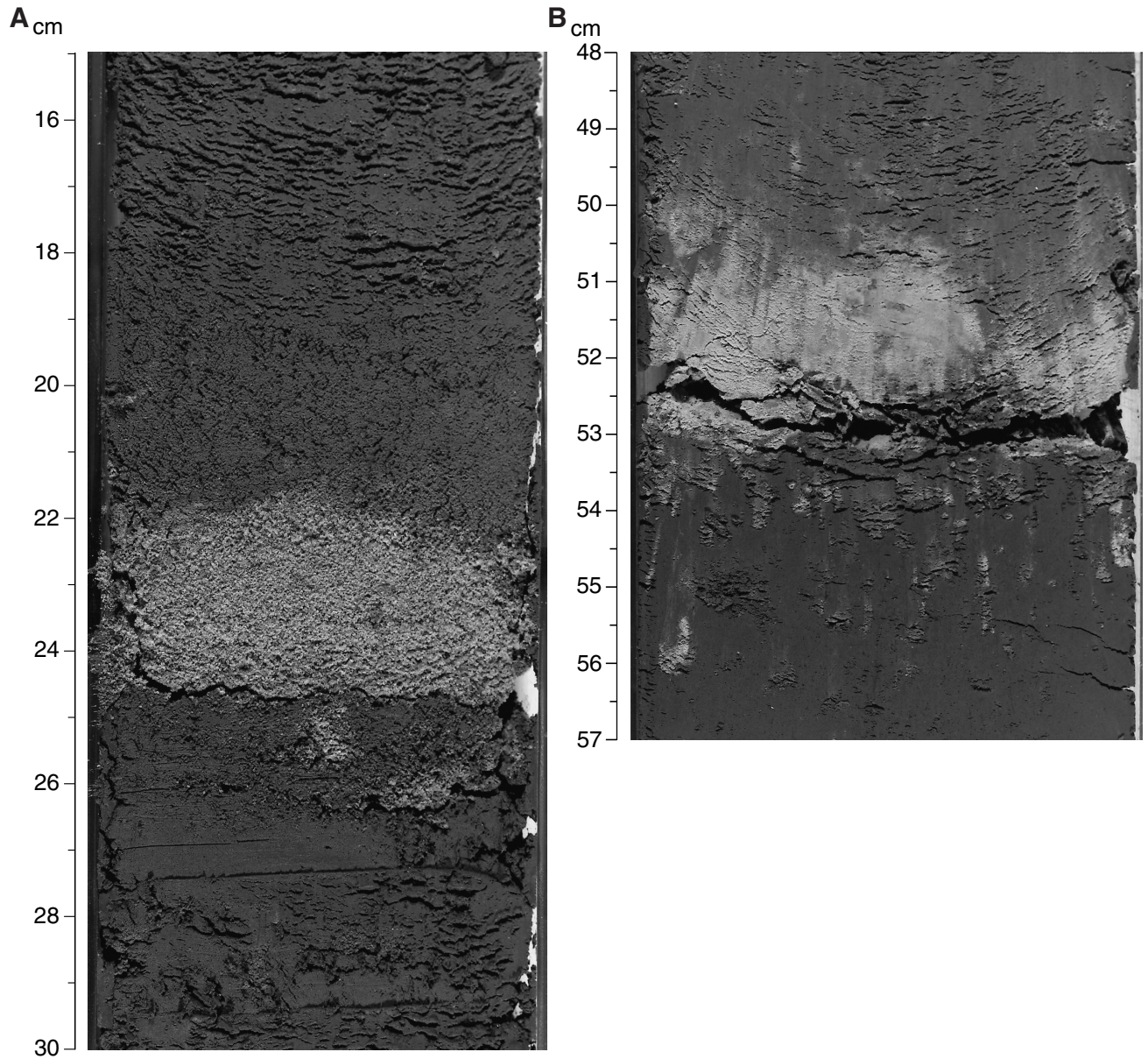


Figure F21. Photograph of typical reworked ash layers (interval 186-1150A-7H-6, 128–138 cm).

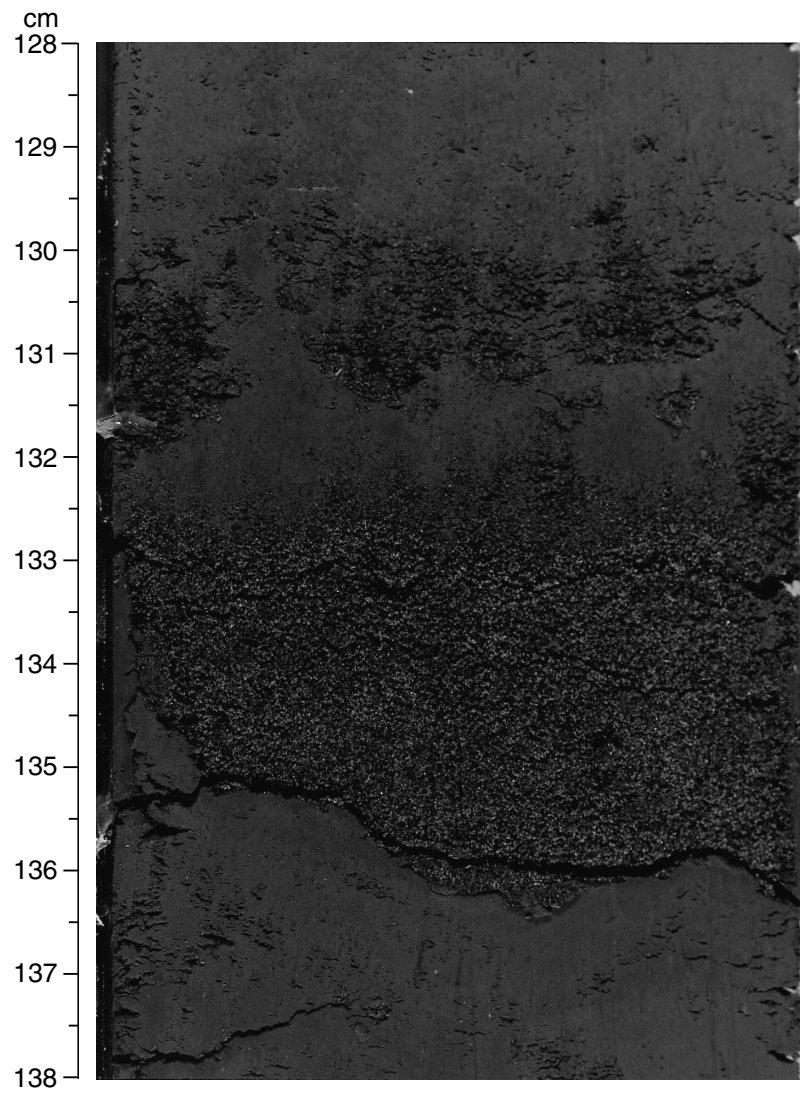


Figure F22. Photograph of typical bioturbated ash "patches" (interval 186-1150A-4H-5, 75–105 cm).

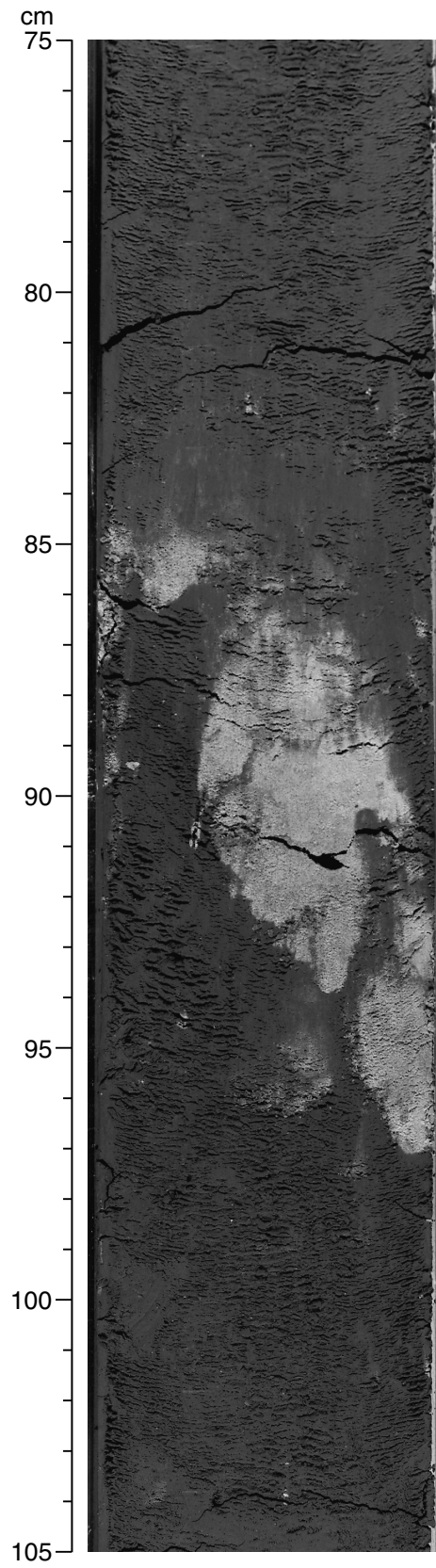


Figure F23. Photograph of typical reworked ash layers, interval 186-1150A-8H-6, 15–30 cm.

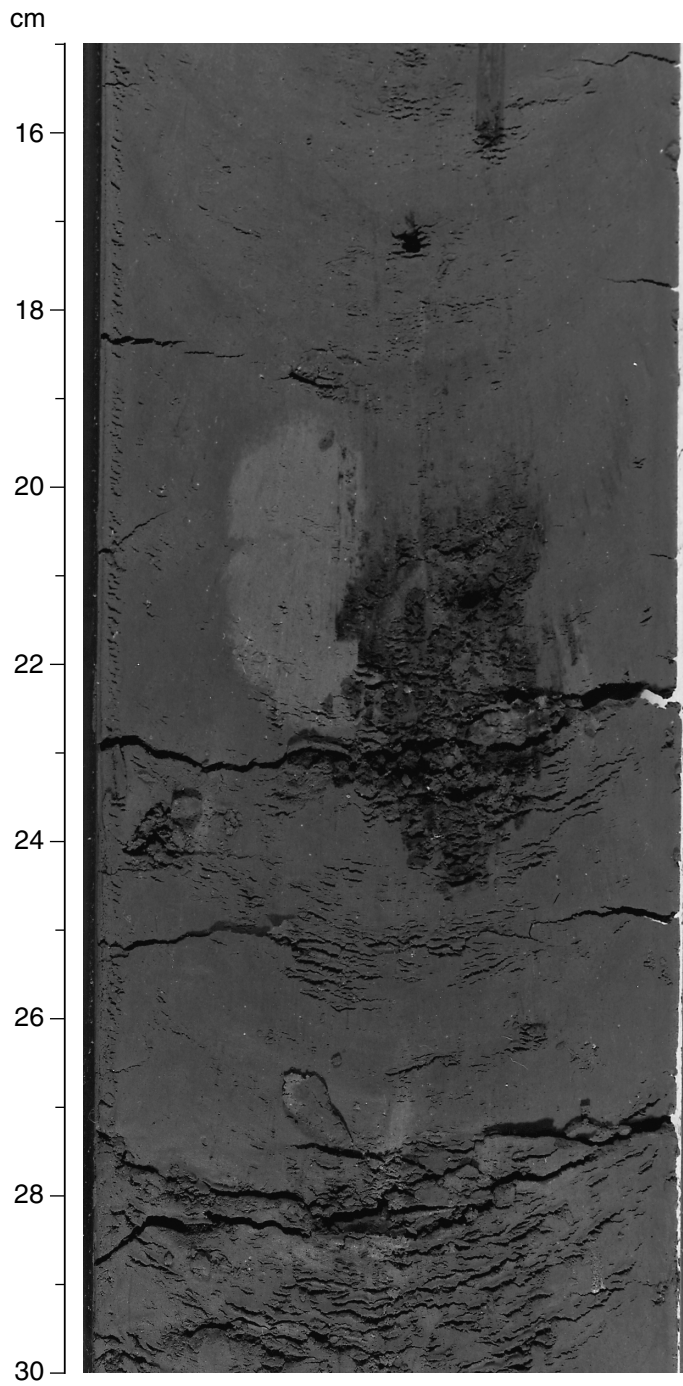


Figure F24. A. Photograph of a dolomite layer (interval 186-1150A-47X-2, 35–65 cm). B. Photograph of a fragmented dolomite layer (interval 186-1150B-26R-3, 40–75 cm).

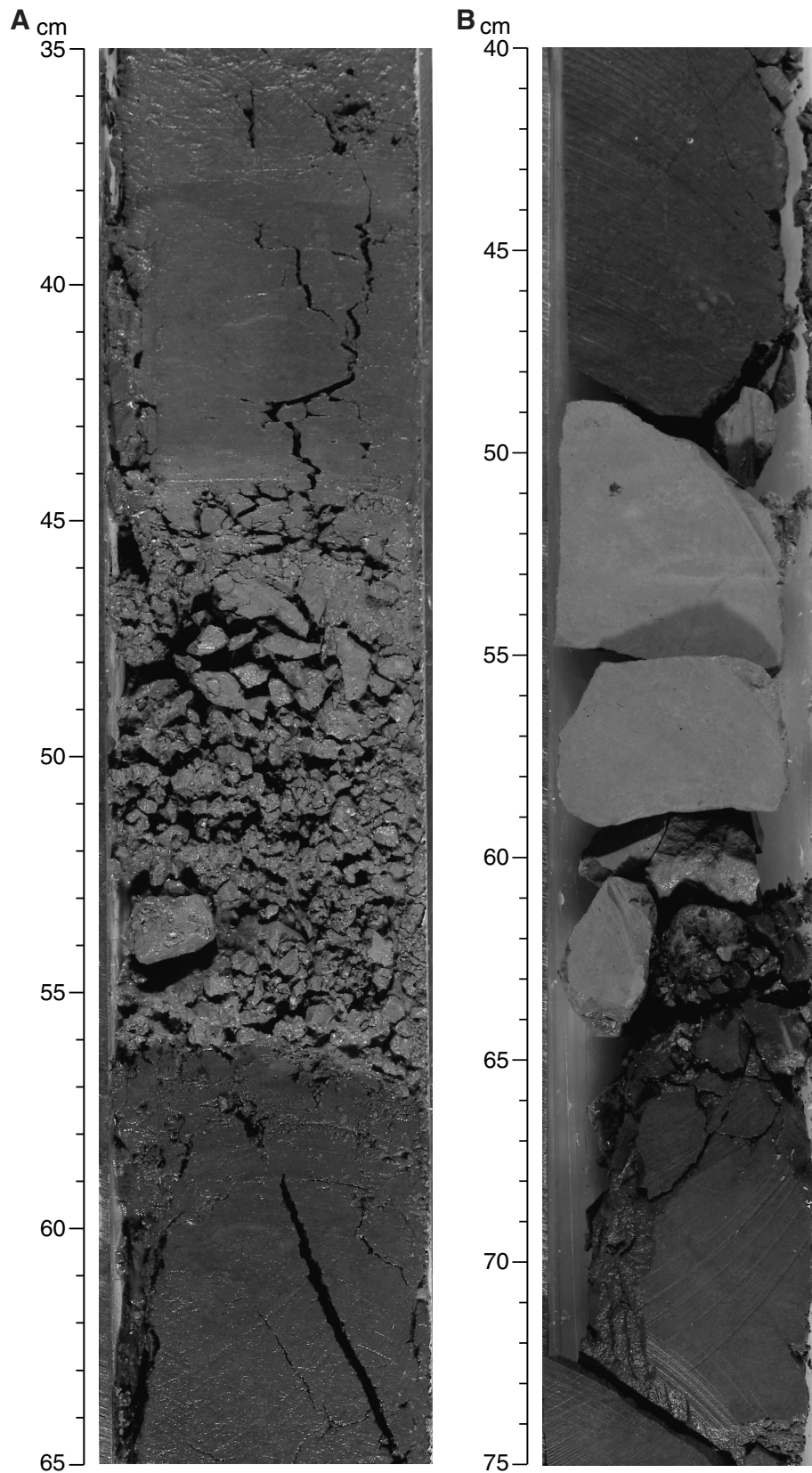


Figure F25. Split-core declination, inclination, and intensity of magnetization prior to AF demagnetization and whole-core susceptibility (given in raw meter units, which can be converted to SI units by multiplying by $\sim 0.7 \times 10^{-5}$) for Site 1150.

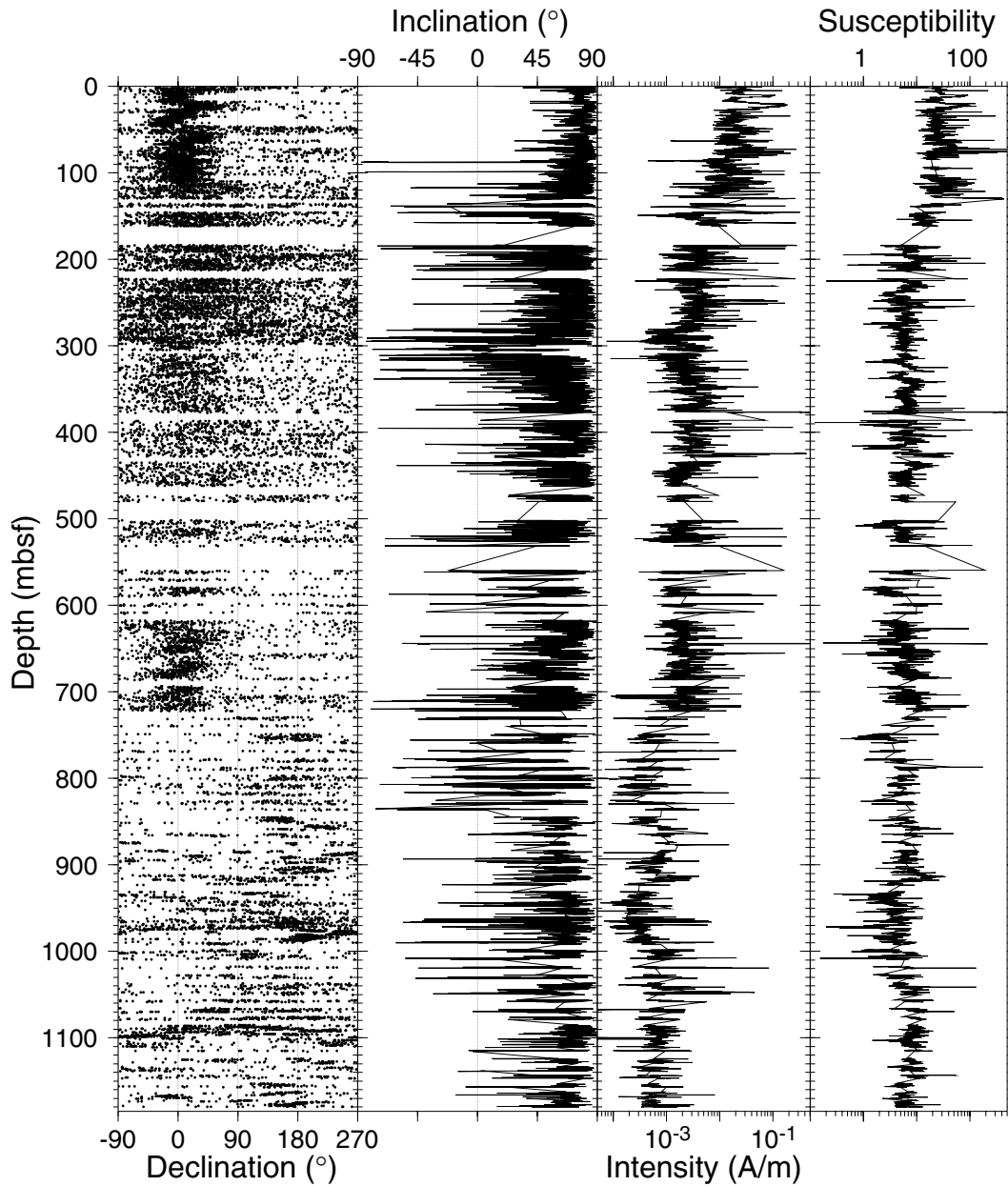


Figure F26. Ratios of magnetization removed from split cores after 10 mT alternating-field (AF) demagnetization along the x-, y-, and z-axes of the core. The core orientation system is shown in the lower right corner along with the a schematic of the vertical and radial overprint. As discussed in the text, much more magnetization is removed along the z-axis than along the x- or y-axes, which is a result of removal of a large vertical drill-string overprint. The ratio of z:y removed is much larger than z:x removed, particularly for APC cores, which indicates the presence of a radial overprint. APC = advanced hydraulic piston corer; XCB = extended core barrel; and RCB = rotary core barrel.

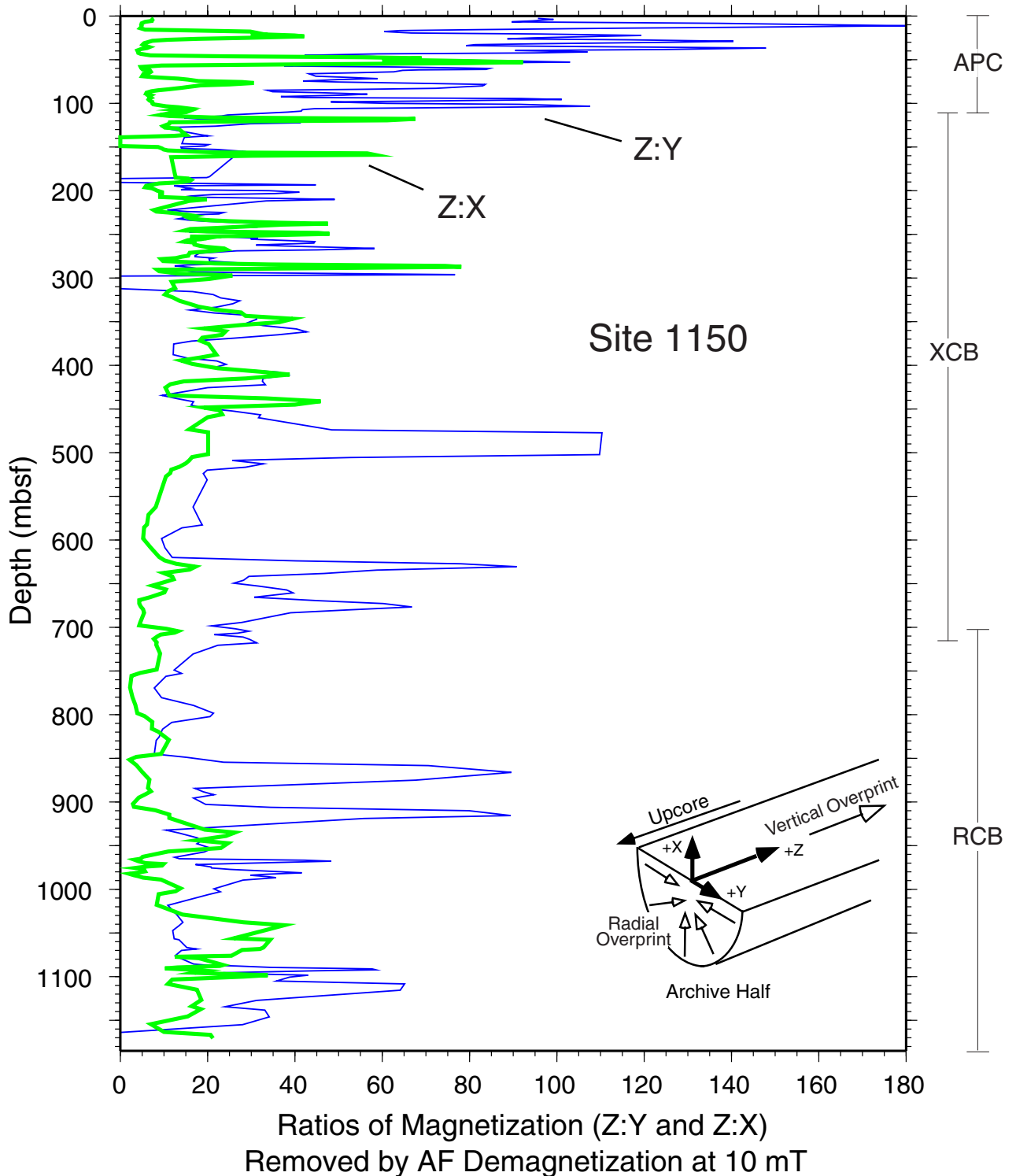


Figure F27. Magnetization remaining after alternating-field (AF) demagnetization of the split cores at 10, 20, and 30 mT. APC = advanced hydraulic piston corer; XCB = extended core barrel; and RCB = rotary core barrel.

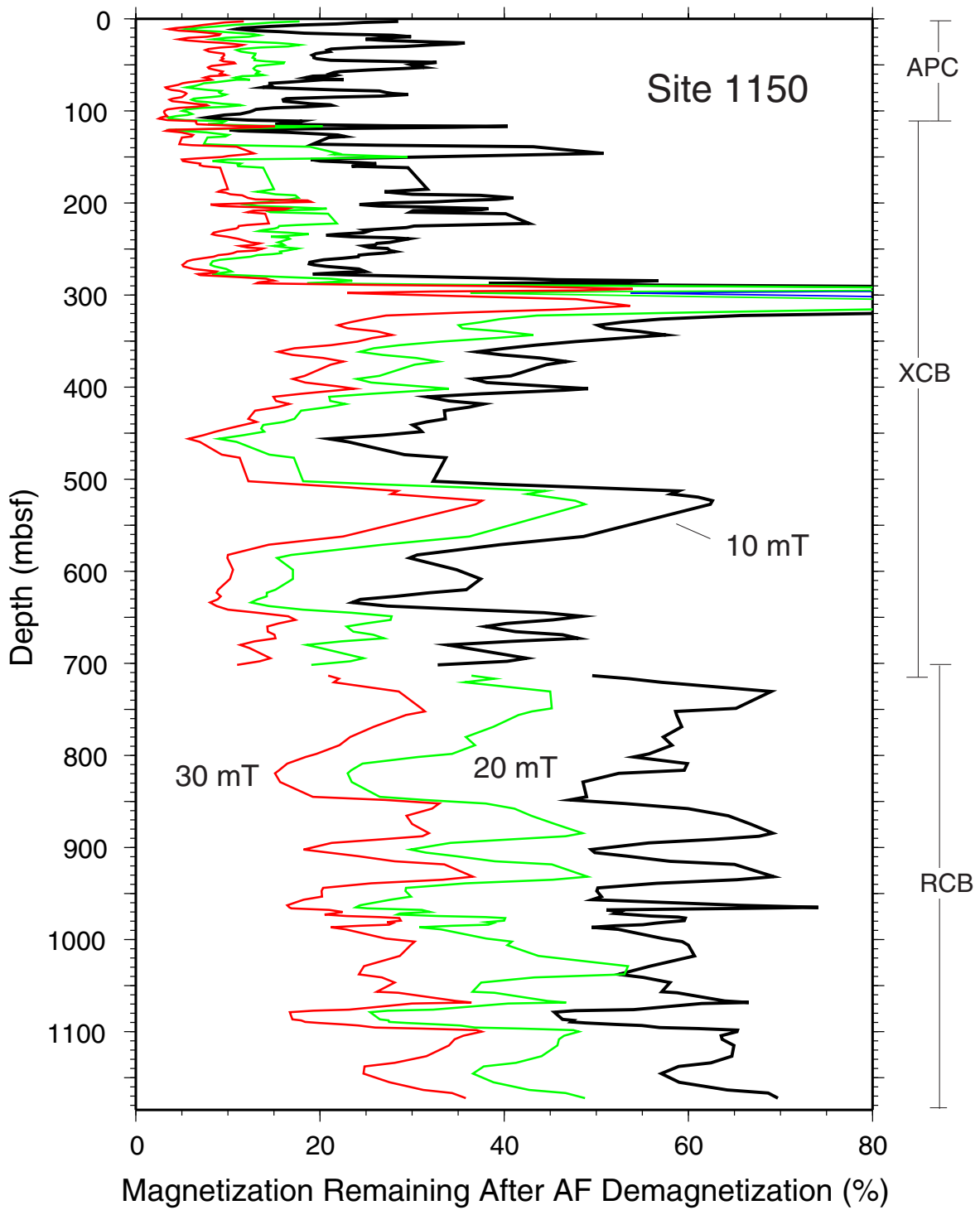


Figure F28. Split-core declination, inclination, and intensity of magnetization for Site 1150 after AF demagnetization at 30 mT.

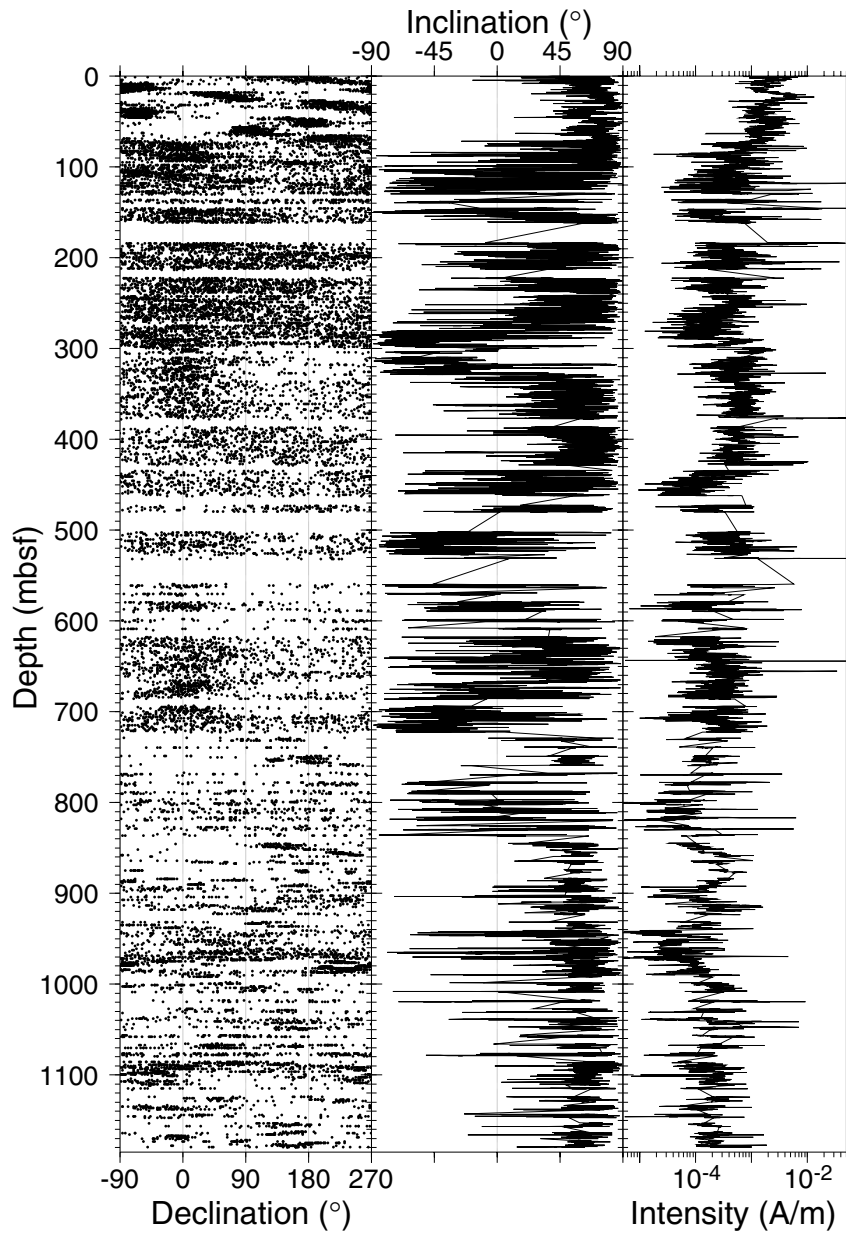


Figure F29. Histogram of declinations for Cores 186-1150A-3H to 8H (A) before and (B) after the Tensor-tool orientation correction was applied.

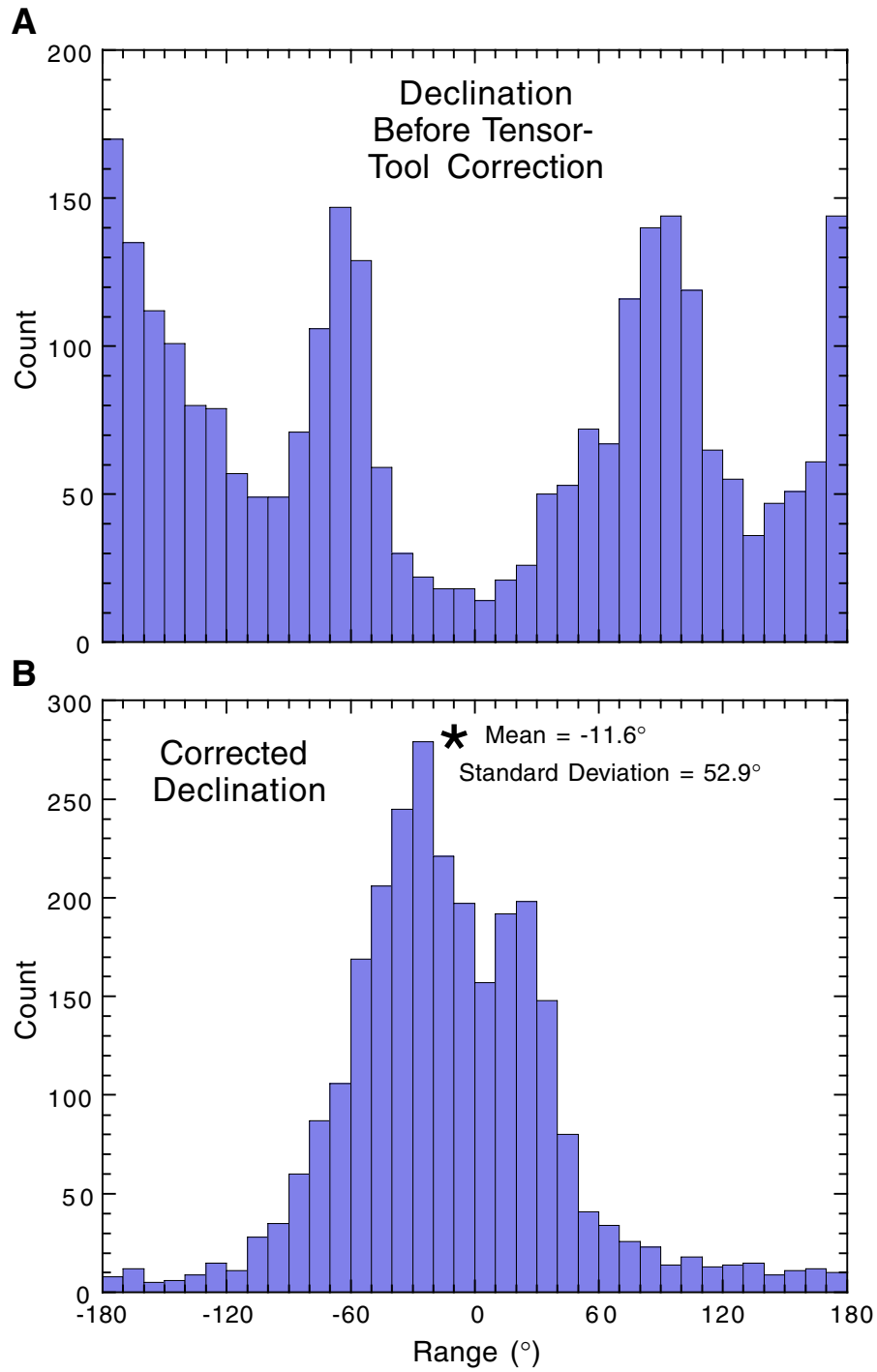


Figure F30. Split-core and discrete declination, inclination, and intensity of magnetization for the upper 120 mbsf in Hole 1150A after AF demagnetization at 20 mT. Discrete data are large gray dots (NP2 magnetometer) and gray diamonds (cryogenic magnetometer), and split-core data are small dots for declinations and lines for inclination and intensity.

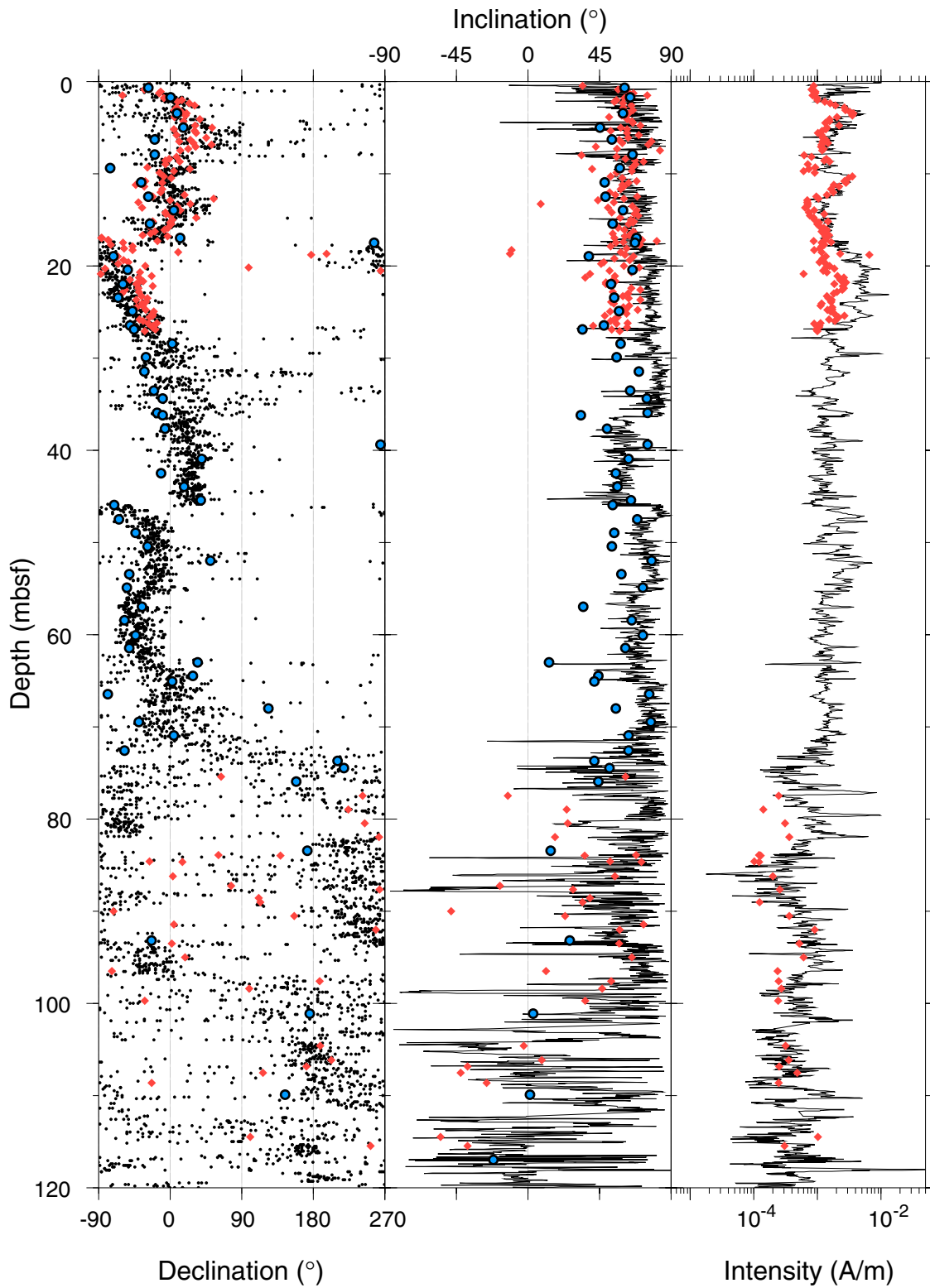


Figure F31. Histograms of difference in the discrete and split-core inclinations for (A) all cores and (B) APC cores only. AF = alternating field; APC = advanced hydraulic piston corer.

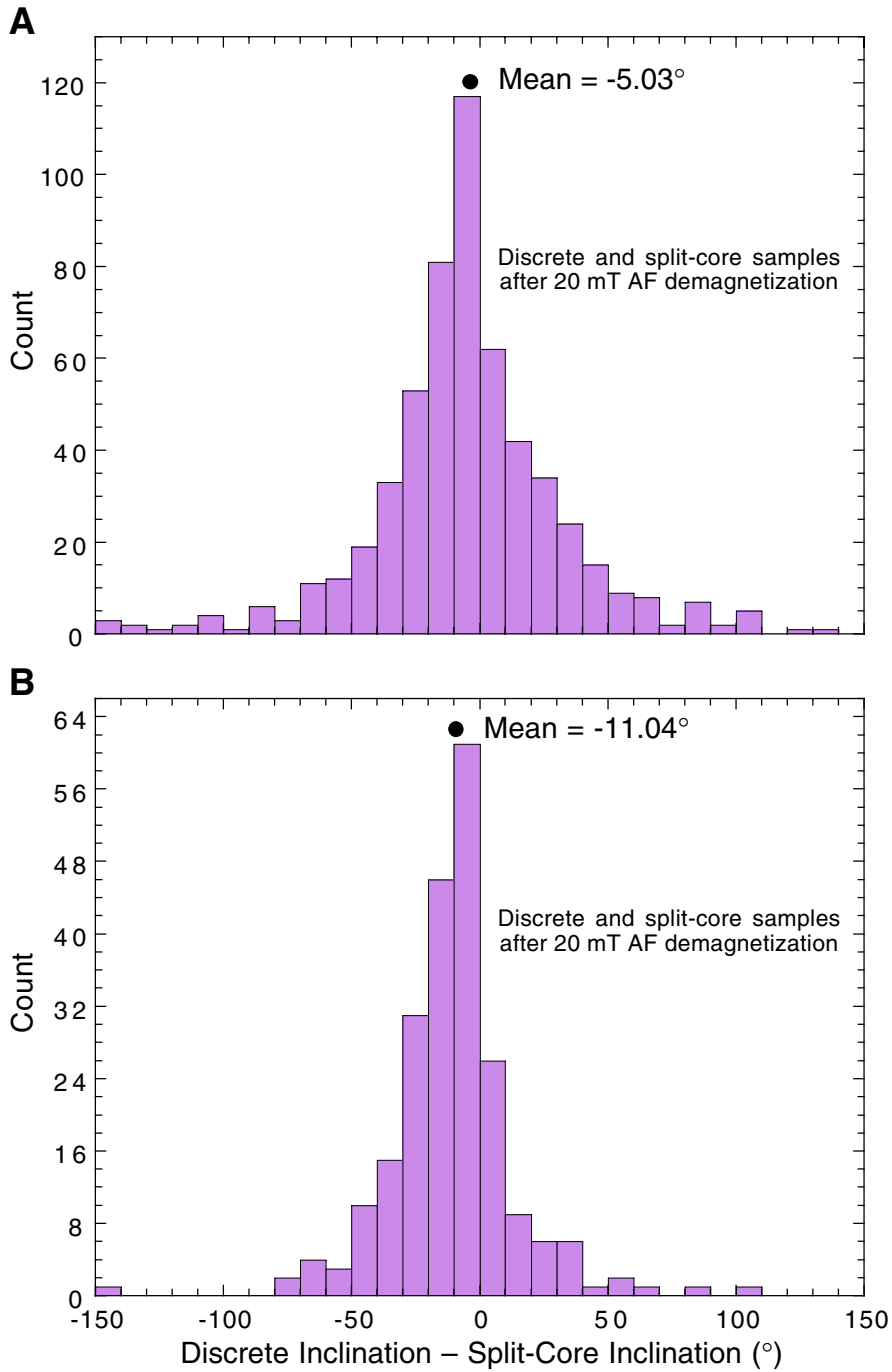


Figure F32. Demagnetization behavior of Samples 186-1150A-1H-2, 6 cm, and 186-1150A-1H-2, 24 cm. The top section shows normalized change in the intensity during demagnetization. The middle section shows orthogonal projections of the end points of the remanence vectors. Open and solid symbols represent the vertical and horizontal projection, respectively. The bottom section shows an equal-area projection of the remanence vector for each demagnetization step.

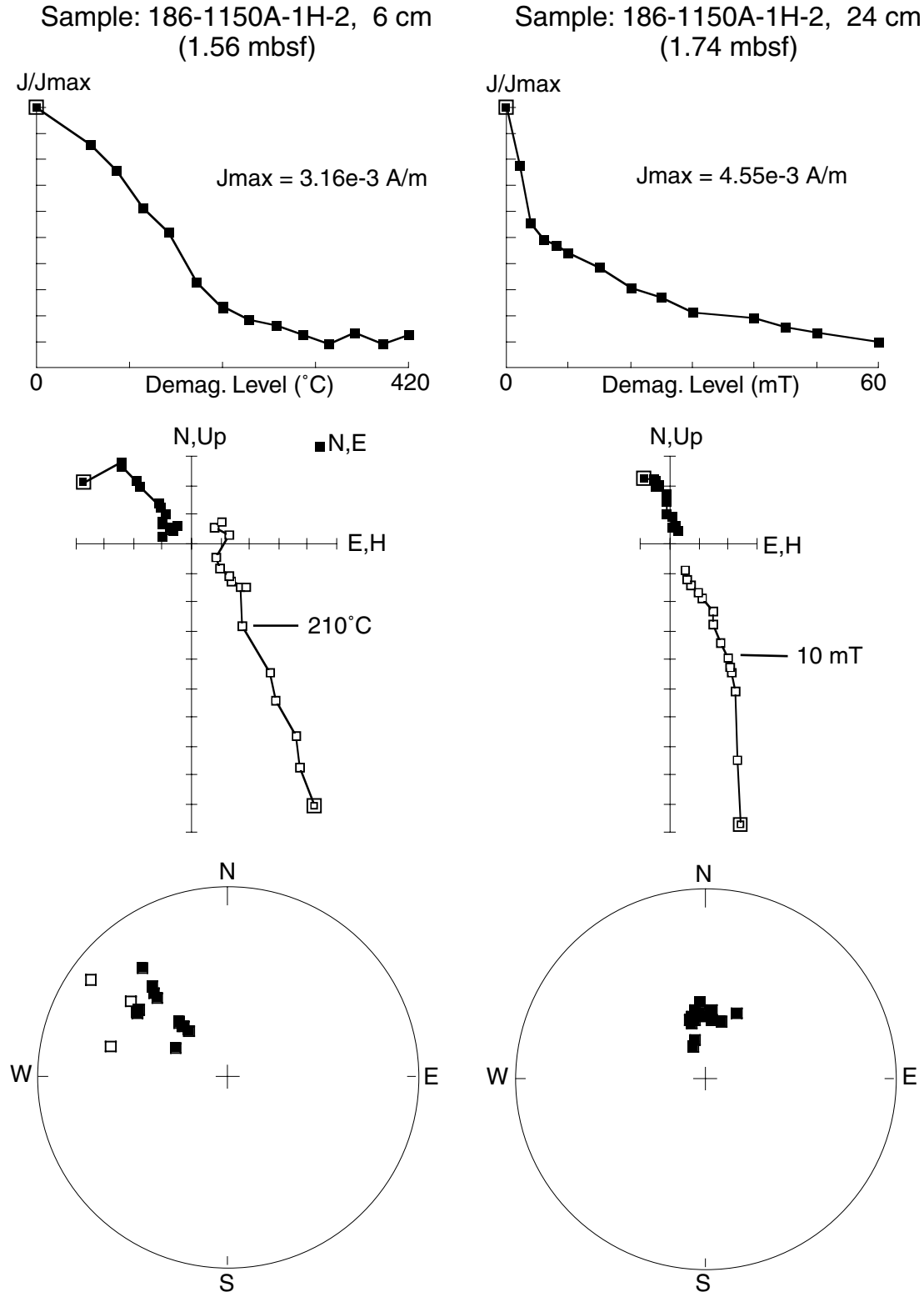


Figure F33. Demagnetization behavior of Samples 186-1150A-1H-4, 144 cm, and 186-1150A-1H-5, 6 cm. The top section shows normalized change in the intensity during demagnetization. The middle section shows orthogonal projections of the end points of the remanence vectors. Open and solid symbols represent the vertical and horizontal projection, respectively. The bottom section shows an equal-area projection of the remanence vector for each demagnetization step.

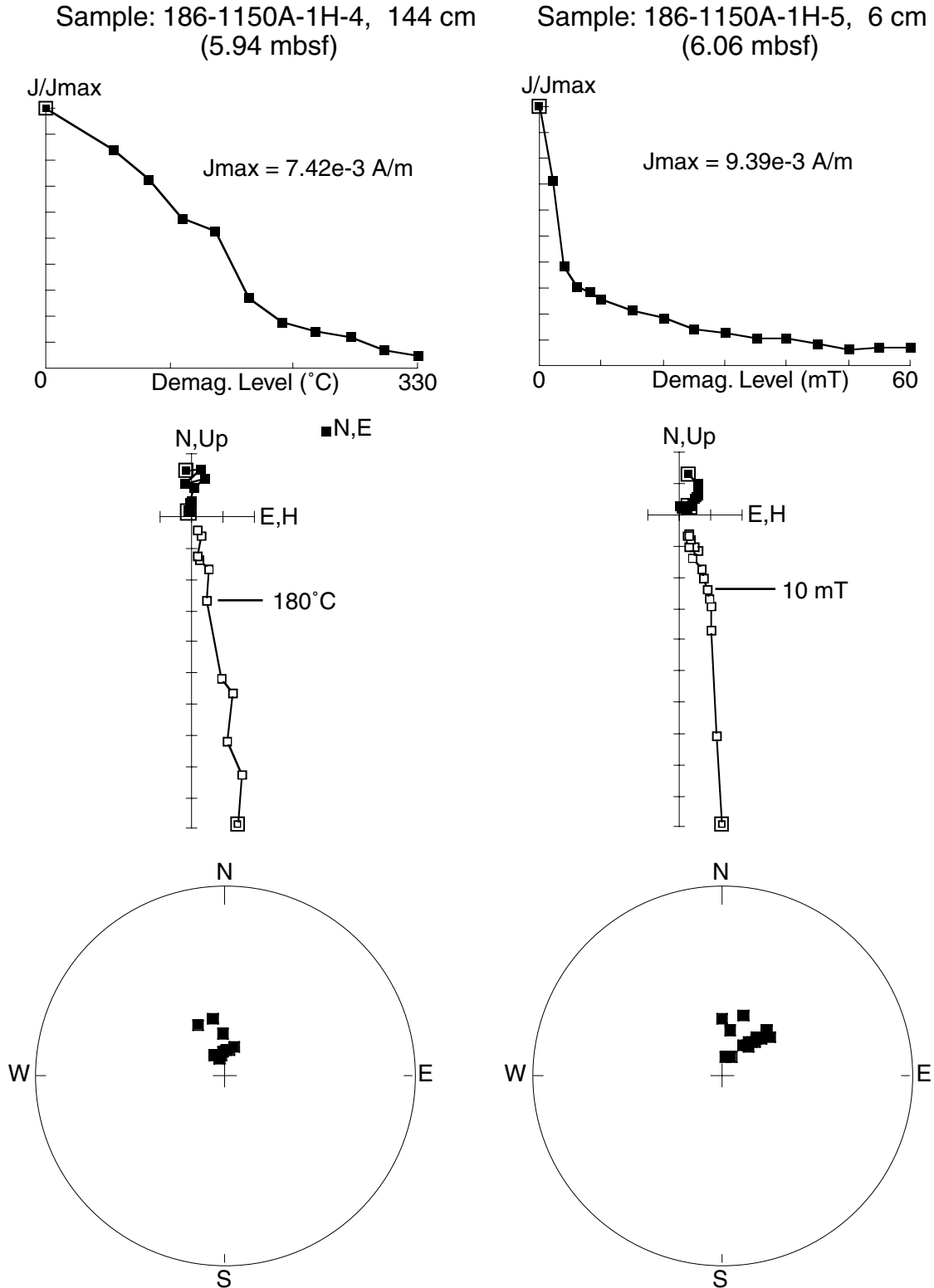


Figure F34. Demagnetization behavior of Samples 186-1150A-3H-4, 106 cm, and 186-1150A-3H-6, 106 cm. The top section shows normalized change in the intensity during demagnetization. The middle section shows orthogonal projections of the end points of the remanence vectors. Open and solid symbols represent the vertical and horizontal projection, respectively. The bottom section shows an equal-area projection of the remanence vector for each demagnetization step.

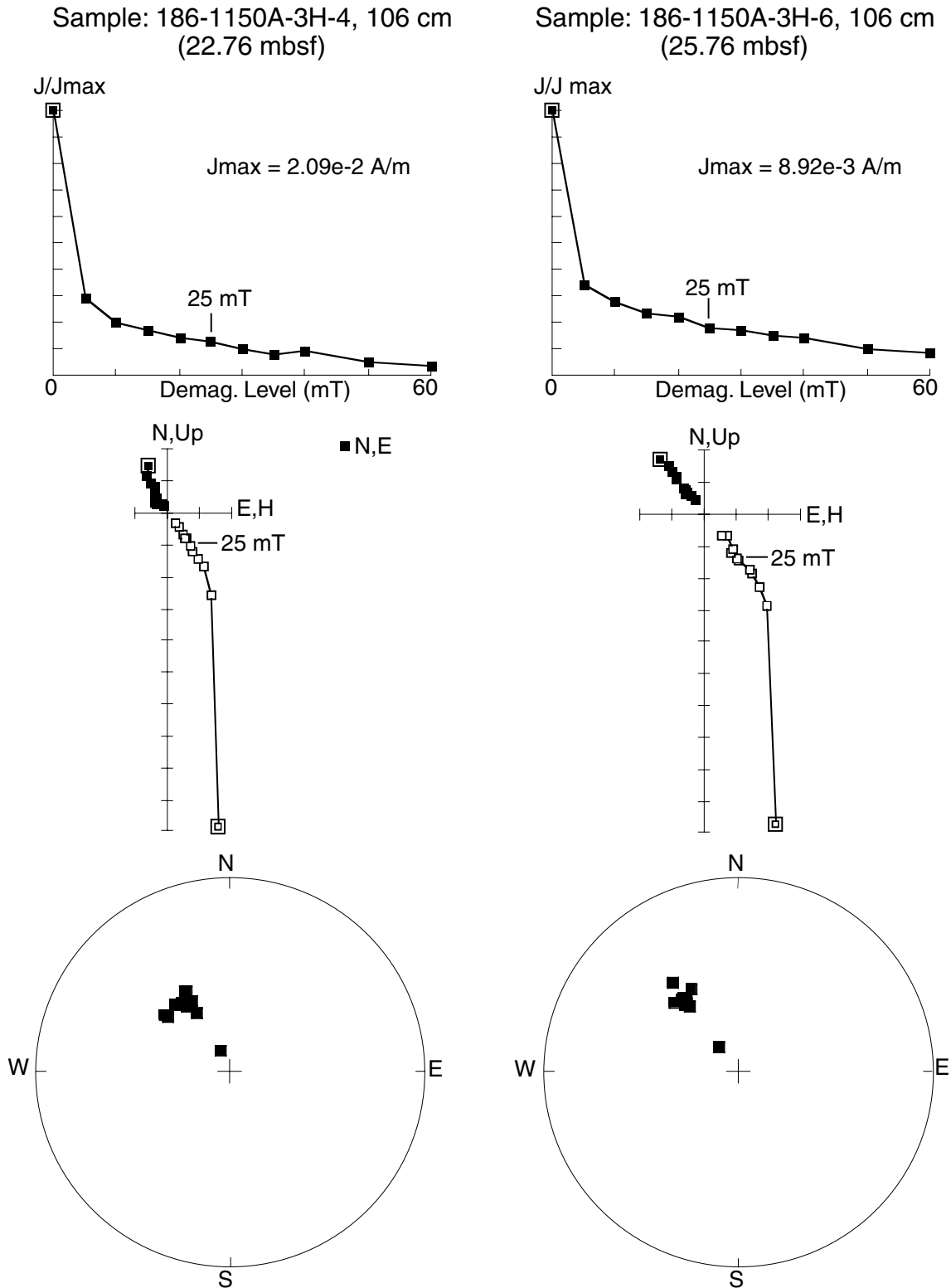


Figure F35. Demagnetization behavior of Samples 186-1150A-10H-1, 20 cm, and 186-1150A-12H-2, 39 cm. The top section shows normalized change in the intensity during demagnetization. The middle section shows orthogonal projections of the end points of the remanence vectors. Open and solid symbols represent the vertical and horizontal projection, respectively. The bottom section shows an equal-area projection of the remanence vector for each demagnetization step.

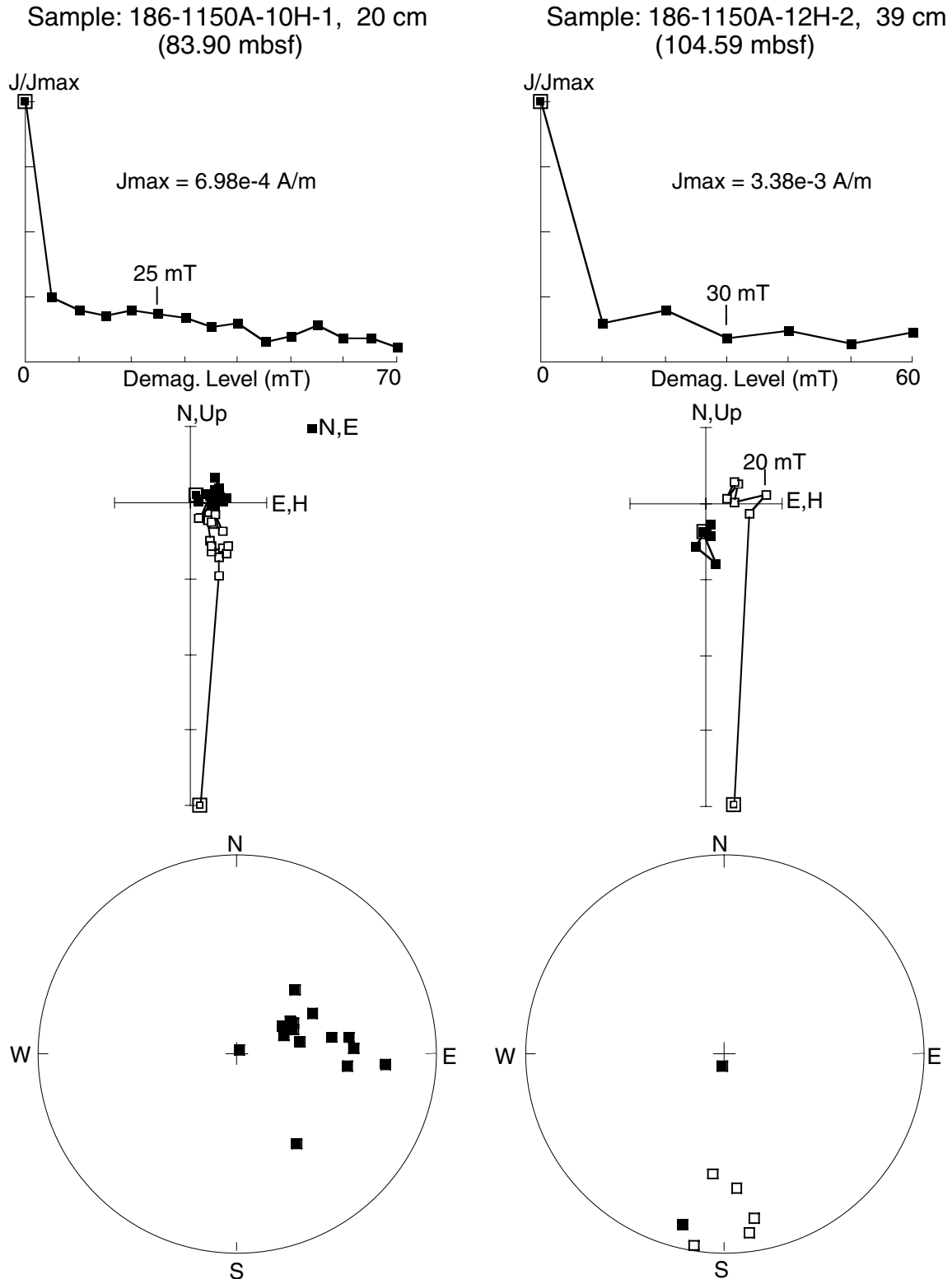


Figure F36. Demagnetization behavior of Samples 186-1150A-34X-4, 48 cm, and 186-1150A-69X-1, 8 cm. The top section shows normalized change in the intensity during demagnetization. The middle section shows orthogonal projections of the end points of the remanence vectors. Open and solid symbols represent the vertical and horizontal projection, respectively. The bottom section shows an equal-area projection of the remanence vector for each demagnetization step.

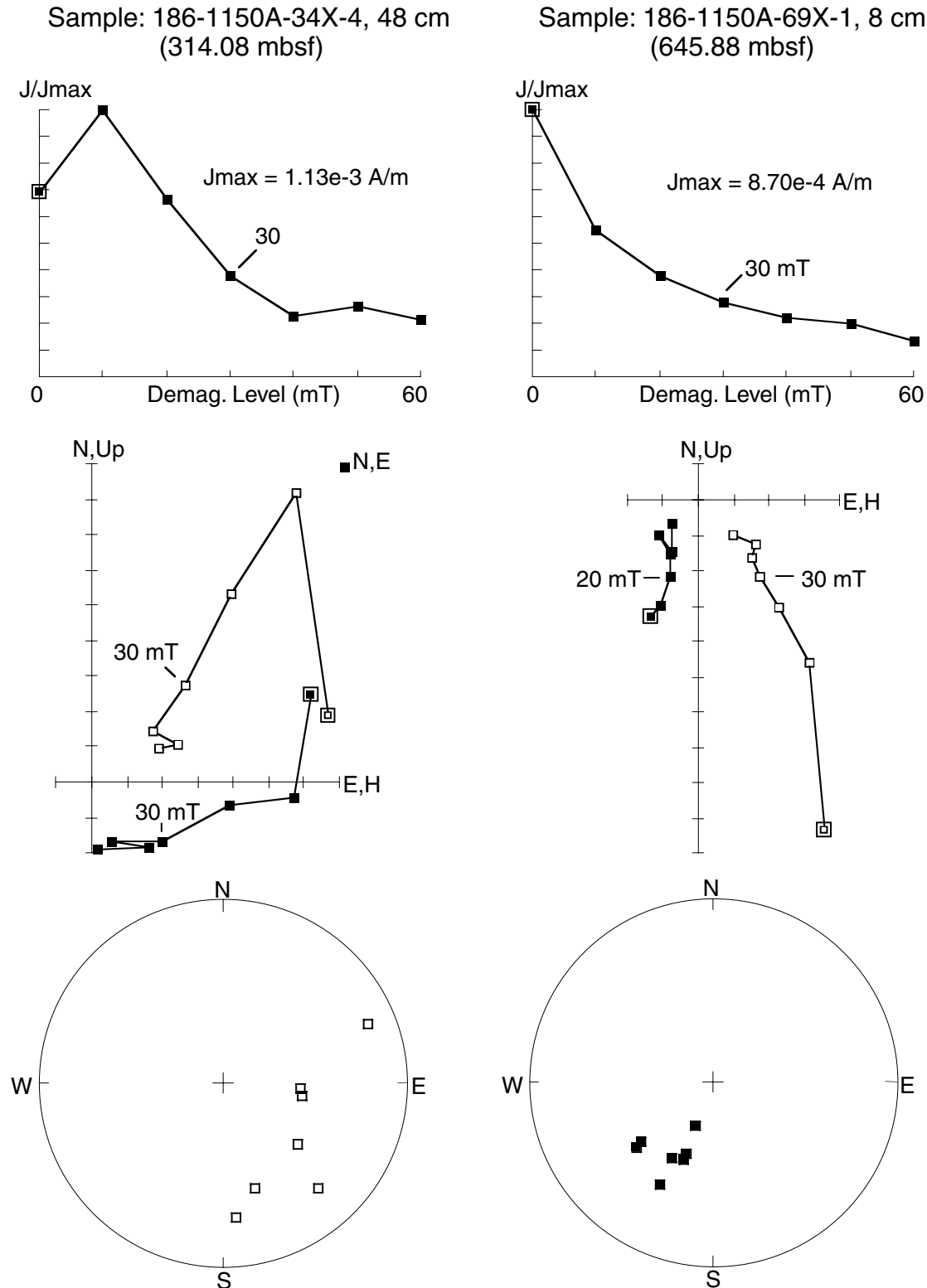


Figure F37. Demagnetization behavior of Samples 186-1150B-17R-3, 57 cm, and 186-1150B-28R-2, 16 cm. The top section shows normalized change in the intensity during demagnetization. The middle section shows orthogonal projections of the end points of the remanence vectors. Open and solid symbols represent the vertical and horizontal projection, respectively. The bottom section shows an equal-area projection of the remanence vector for each demagnetization step.

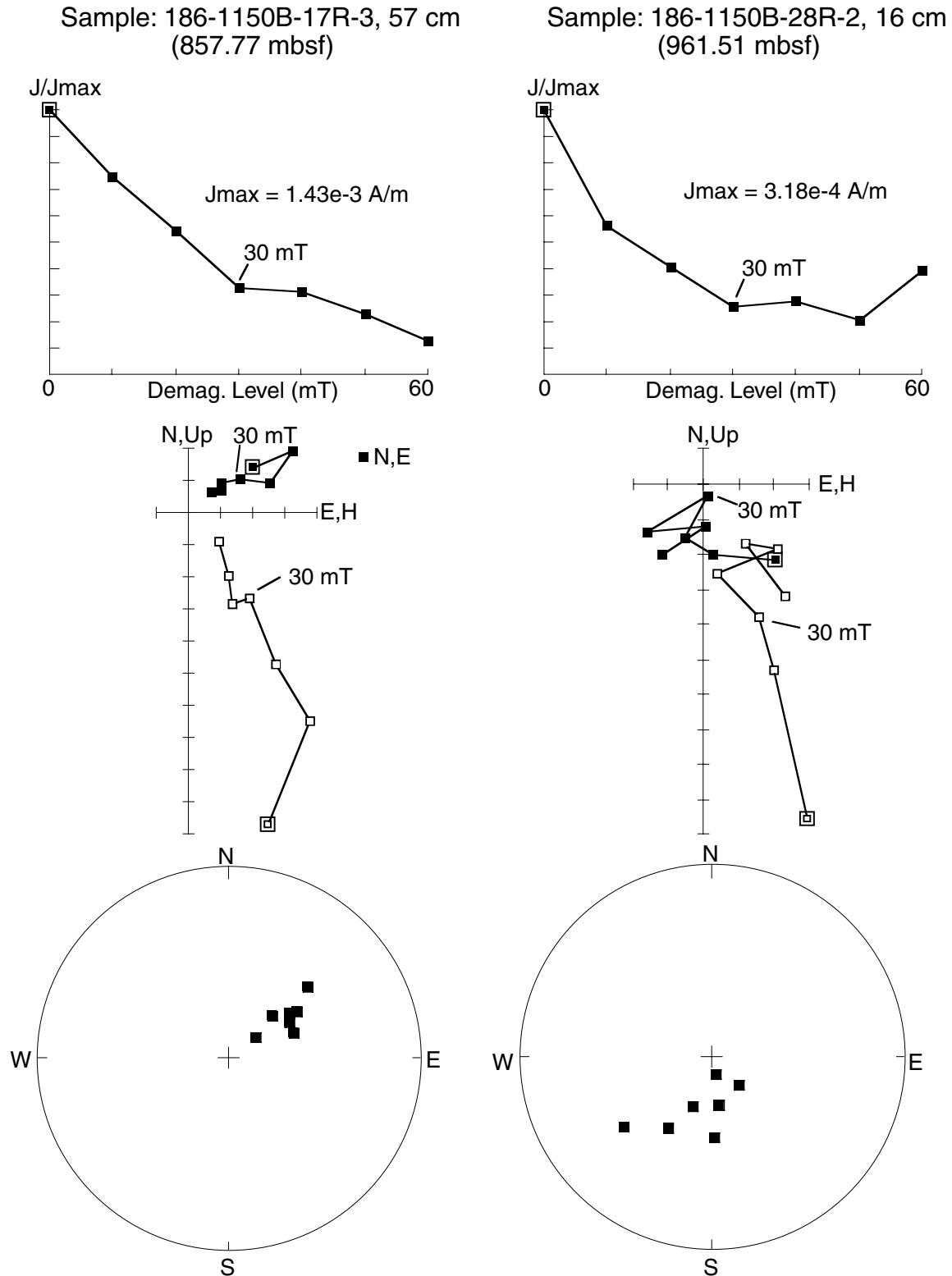


Figure F38. Demagnetization behavior of Samples 186-1150B-35R-1, 73 cm, and 186-1150B-48R-1, 108 cm. The top section shows normalized change in the intensity during demagnetization. The middle section shows orthogonal projections of the end points of the remanence vectors. Open and solid symbols represent the vertical and horizontal projection, respectively. The bottom section shows an equal-area projection of the remanence vector for each demagnetization step.

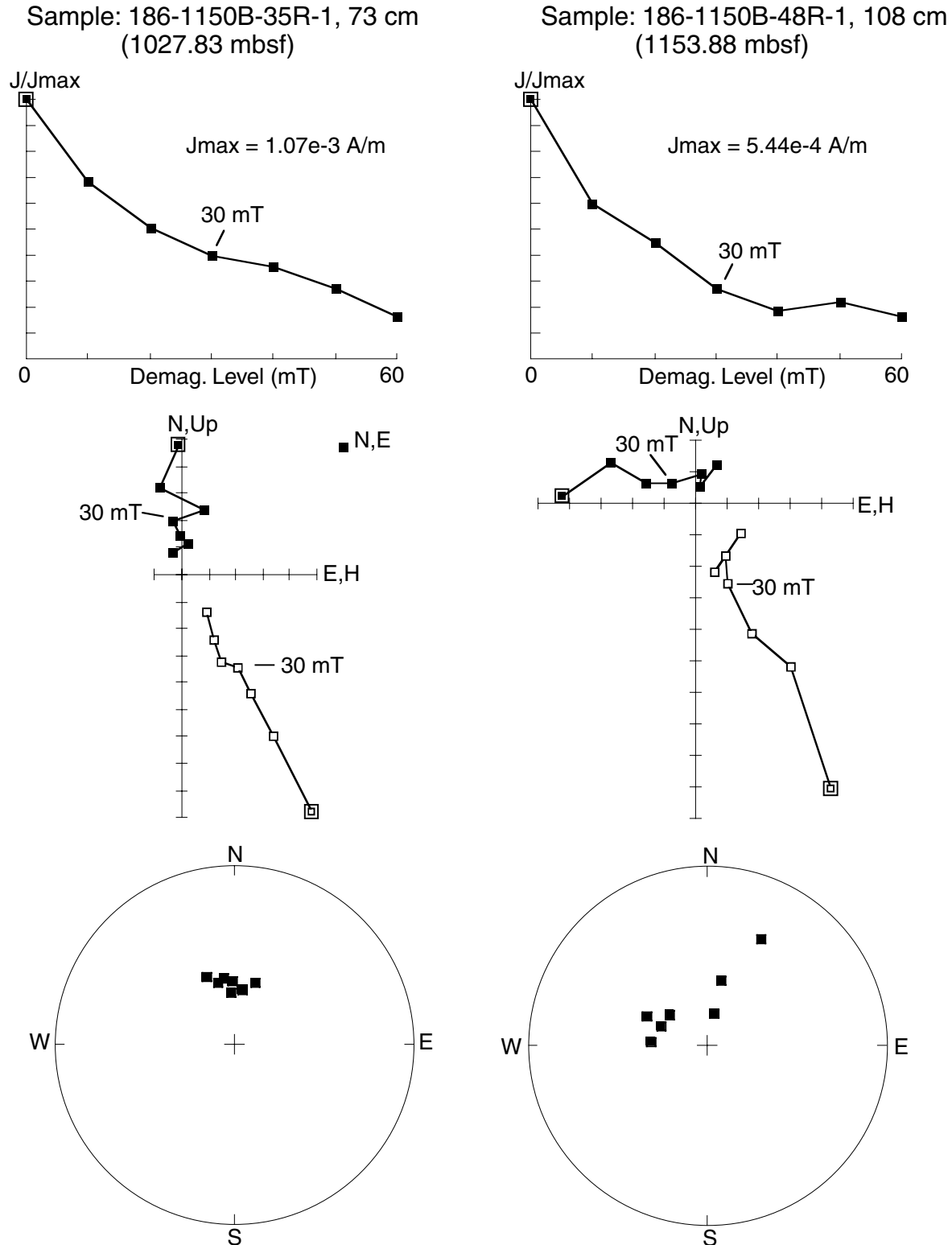


Figure F39. Example of progressive thermal demagnetization of a discrete sample (186-1150B-32R-2, 36–38 cm) (A) after 5 mT AF demagnetization after each thermal demagnetization step and (B) before 5 mT AF demagnetization was applied. The open circles are the projections of vector end points on the vertical plane; solid circles are the projections on the horizontal plane.

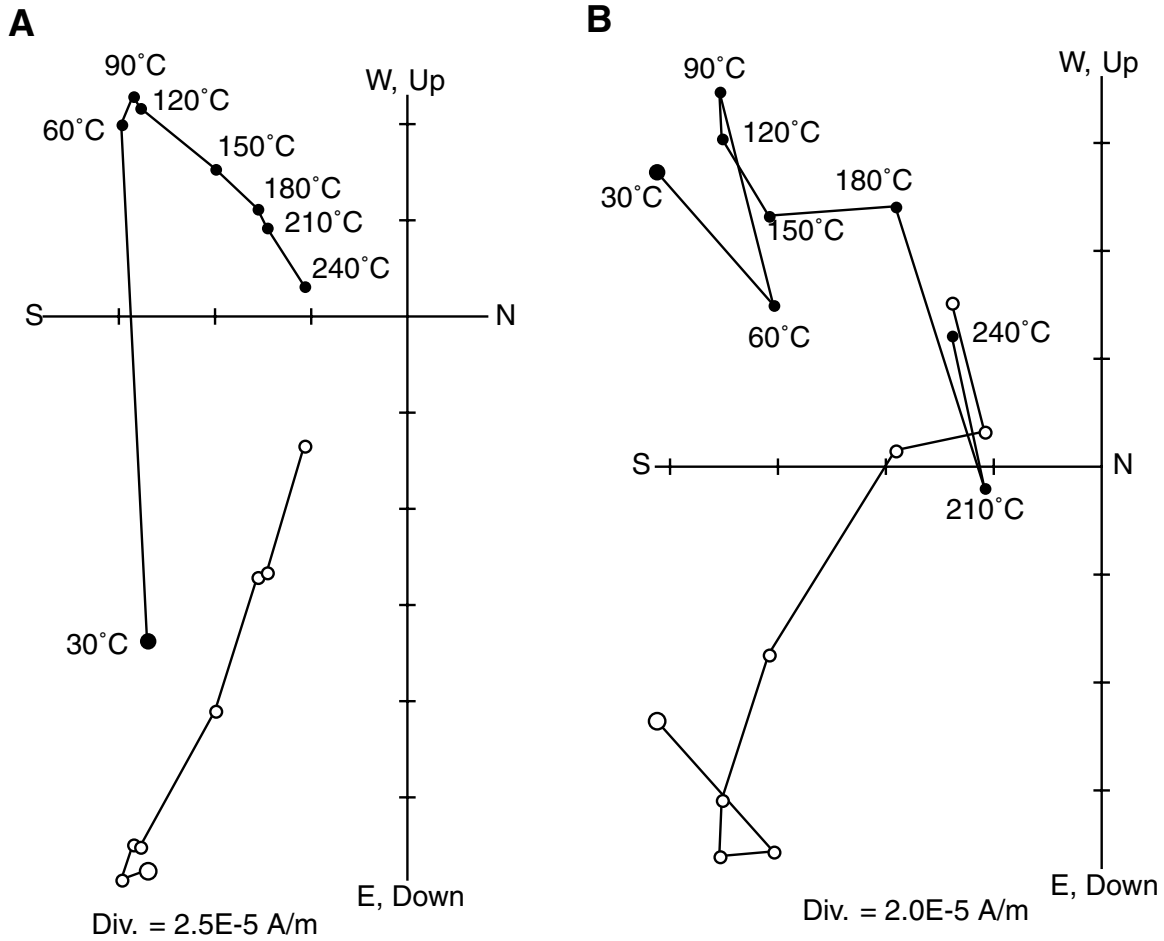


Figure F40. Discrete sample results from the NP-2 spinner magnetometer. **A.** Susceptibility (raw meter values). **B.** Natural remanent magnetization (NRM) intensity. **C.** Anhyseretic remanent magnetization (ARM) intensity. **D.** Median destructive field (MDF) of the NRM. **E.** MDF of the ARM. **F.** The NRM intensity divided by the ARM intensity. In the plots with multiple lines, the bold line is prior to demagnetization, the medium-thick line is after 10 mT demagnetization, the thin line is after 20 mT demagnetization, the thick dashed line is after 30 mT demagnetization, and the thin dashed line is after 40 mT demagnetization. Whole-core susceptibility is in raw meter units, which can be converted to SI units by multiplying by $\sim 0.7 \times 10^{-5}$.

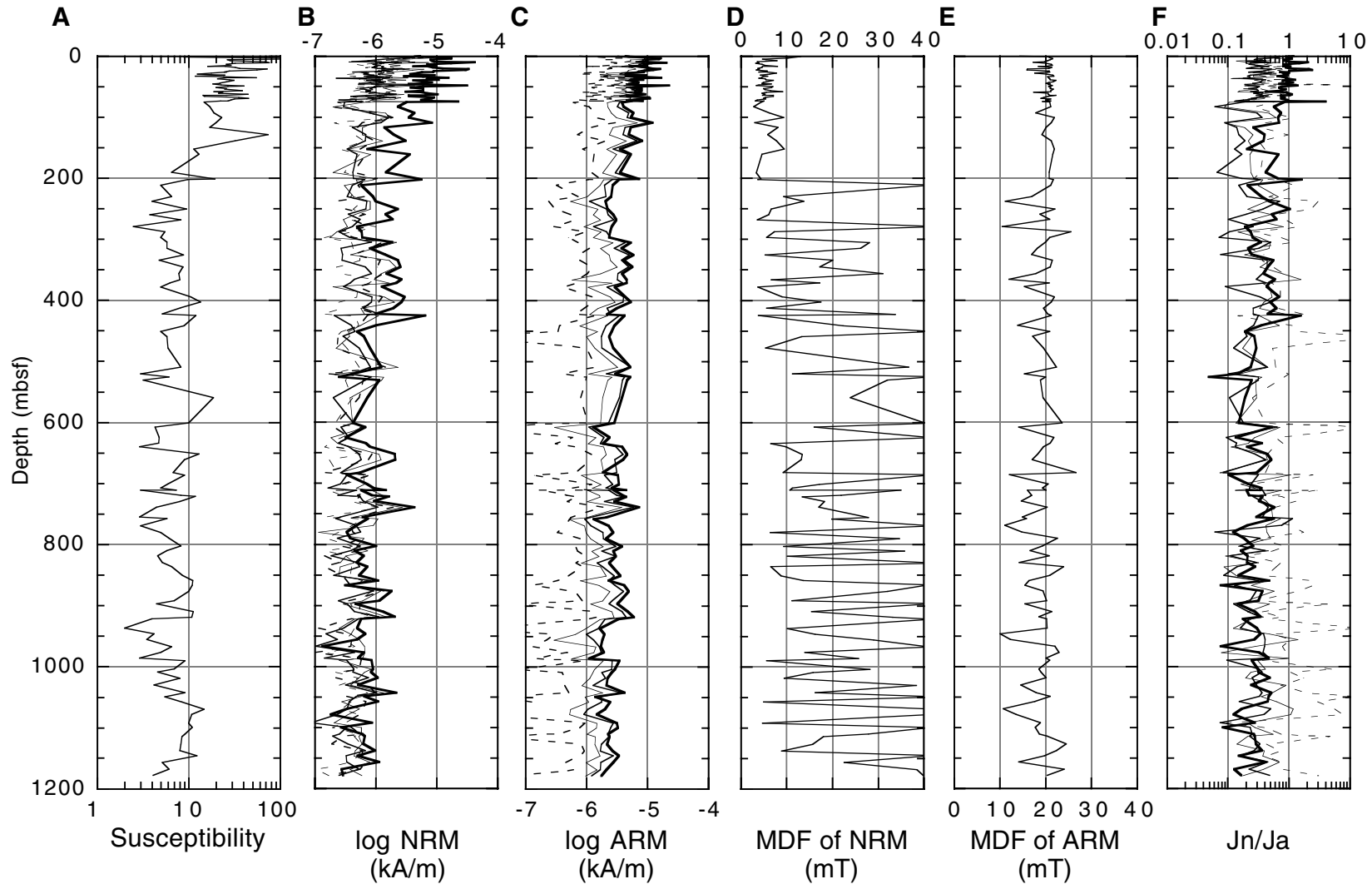


Figure F41. Results from the NP-2 spinner magnetometer for discrete samples from the top 120 mbsf of Hole 1150A. **A.** Susceptibility (in raw meter units, which can be converted to SI units by multiplying by $\sim 0.7 \times 10^{-5}$). **B.** Natural remanent magnetization (NRM) intensity. **C.** Anhysteretic remanent magnetization (ARM) intensity. **D.** Median destructive field (MDF) of the NRM. **E.** MDF of the ARM. **F.** The NRM intensity divided by the ARM intensity. In the plots with multiple lines, the bold line is prior to demagnetization, the medium-thick line is after 10 mT demagnetization, the thin line is after 20 mT demagnetization, the thick dashed line is after 30 mT demagnetization, and thin dashed line is after 40 mT demagnetization.

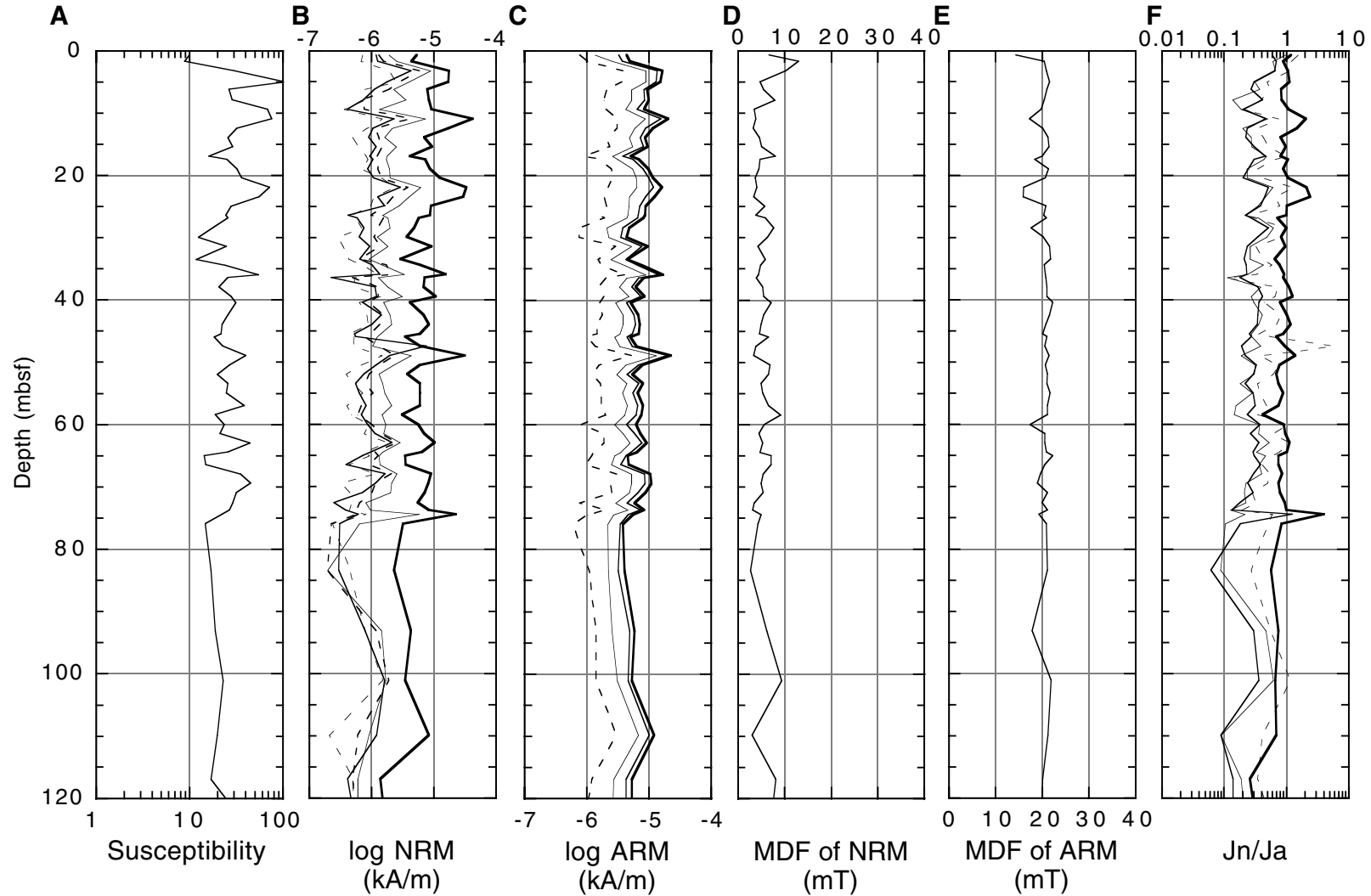


Figure F42. Normalized change in the intensity during thermal demagnetization for four samples from Hole 1150B.

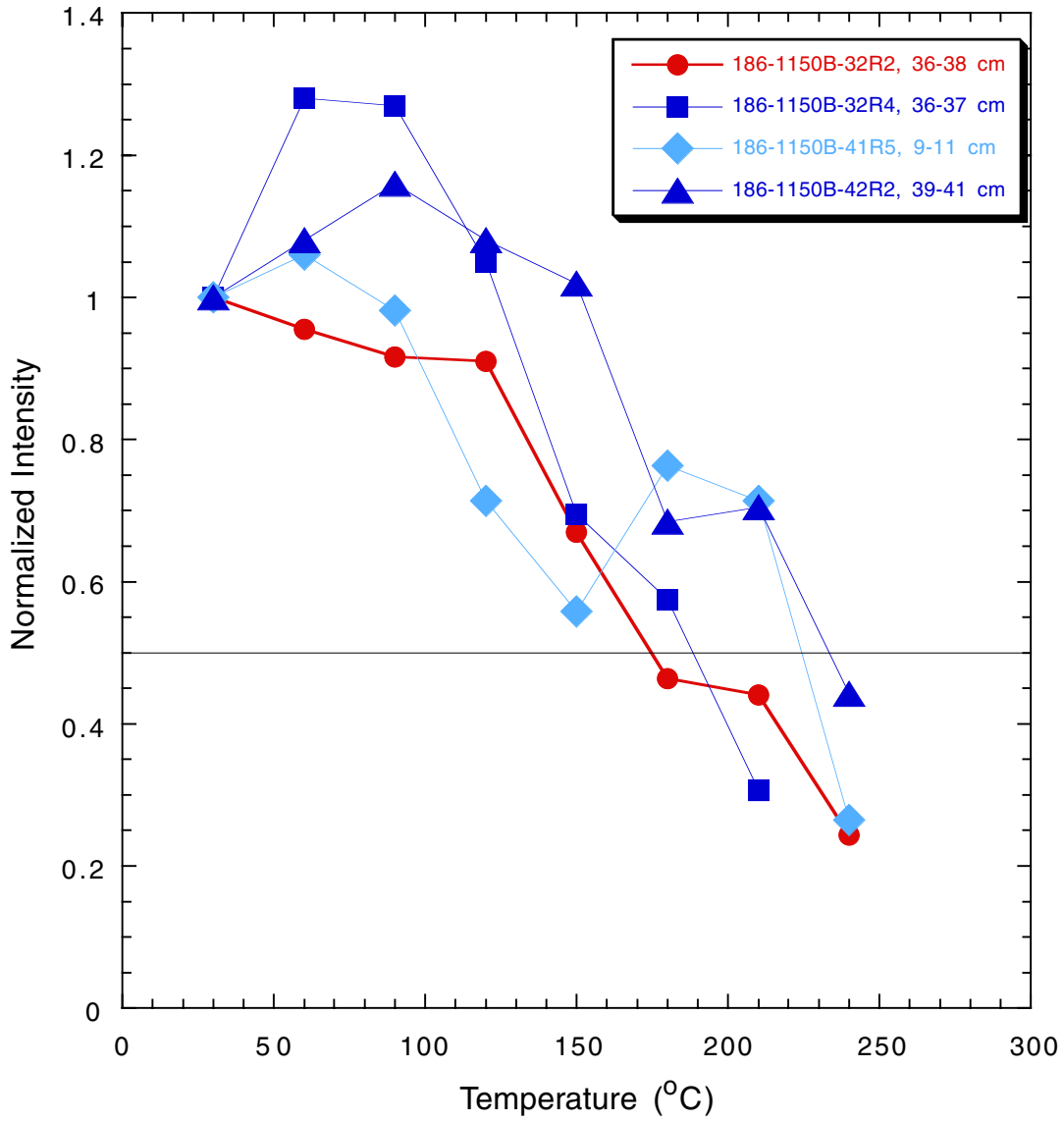


Figure F43. Thermal demagnetization of isothermal remanent magnetizations, imparted along the x- (0.1 T; circle), y- (0.3 T; square), and z- (1 T; triangle) axes.

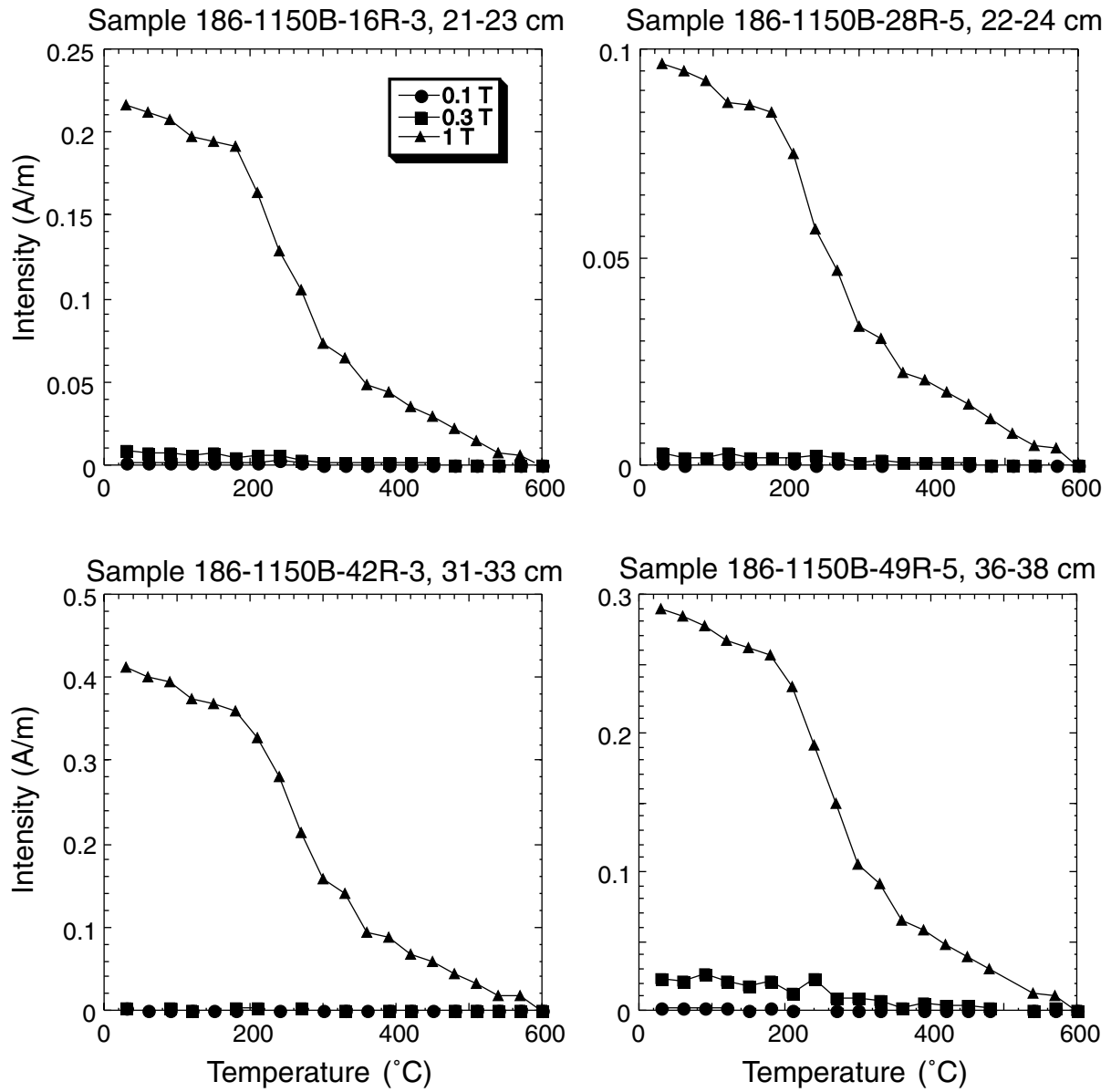


Figure F44. Isothermal remanent magnetization (IRM) acquisition results from four samples from Hole 1150A APC cores.

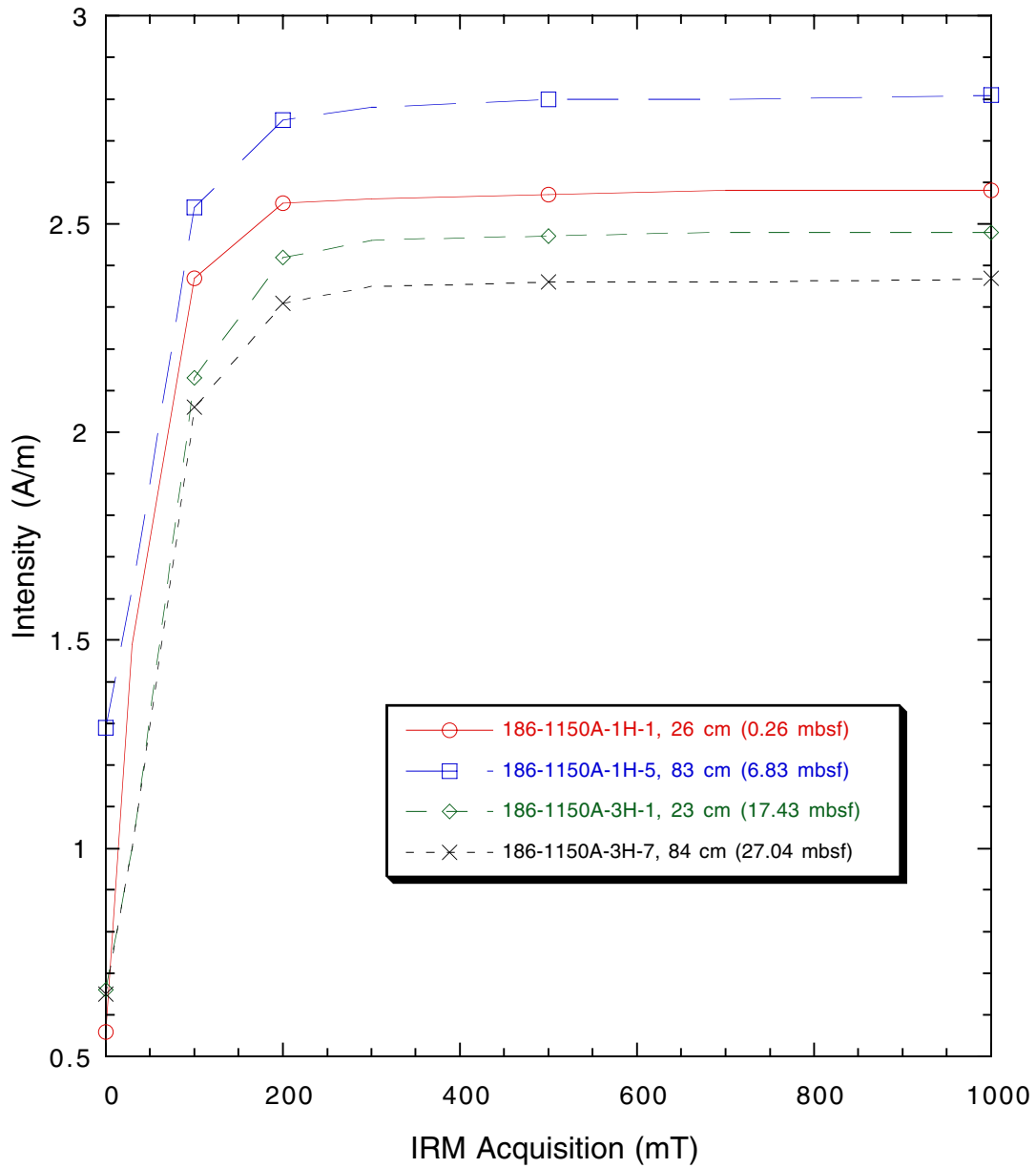


Figure F45. Relative paleointensity for a short interval from the APC cores. NRM = natural remanent magnetization; ARM = anhysteretic remanent magnetization; and IRM = isothermal remanent magnetization. Note that from ~10 to 12 mbsf, the relative paleointensity values for NRM/ARM and NRM/IRM disagree with the NRM/susceptibility record. This indicates the presence of a component that has a significant susceptibility, but that either does not retain the ARM and IRM imparted or has a coercivity higher than 1 T.

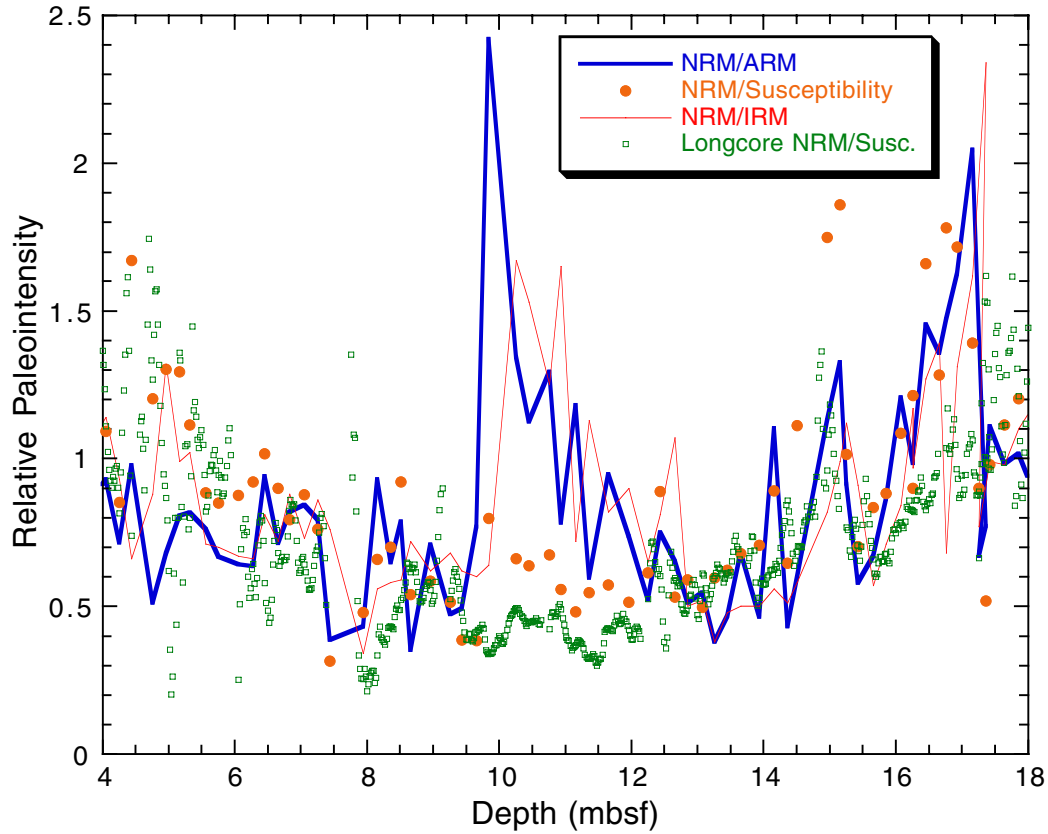


Figure F46. Magnetic property changes caused by chemical treatments. The samples are from core catchers from Cores 186-1150A-21X, 41X, and 61X, and Cores 186-1150B-28R, 36R, 40R, and 48R.

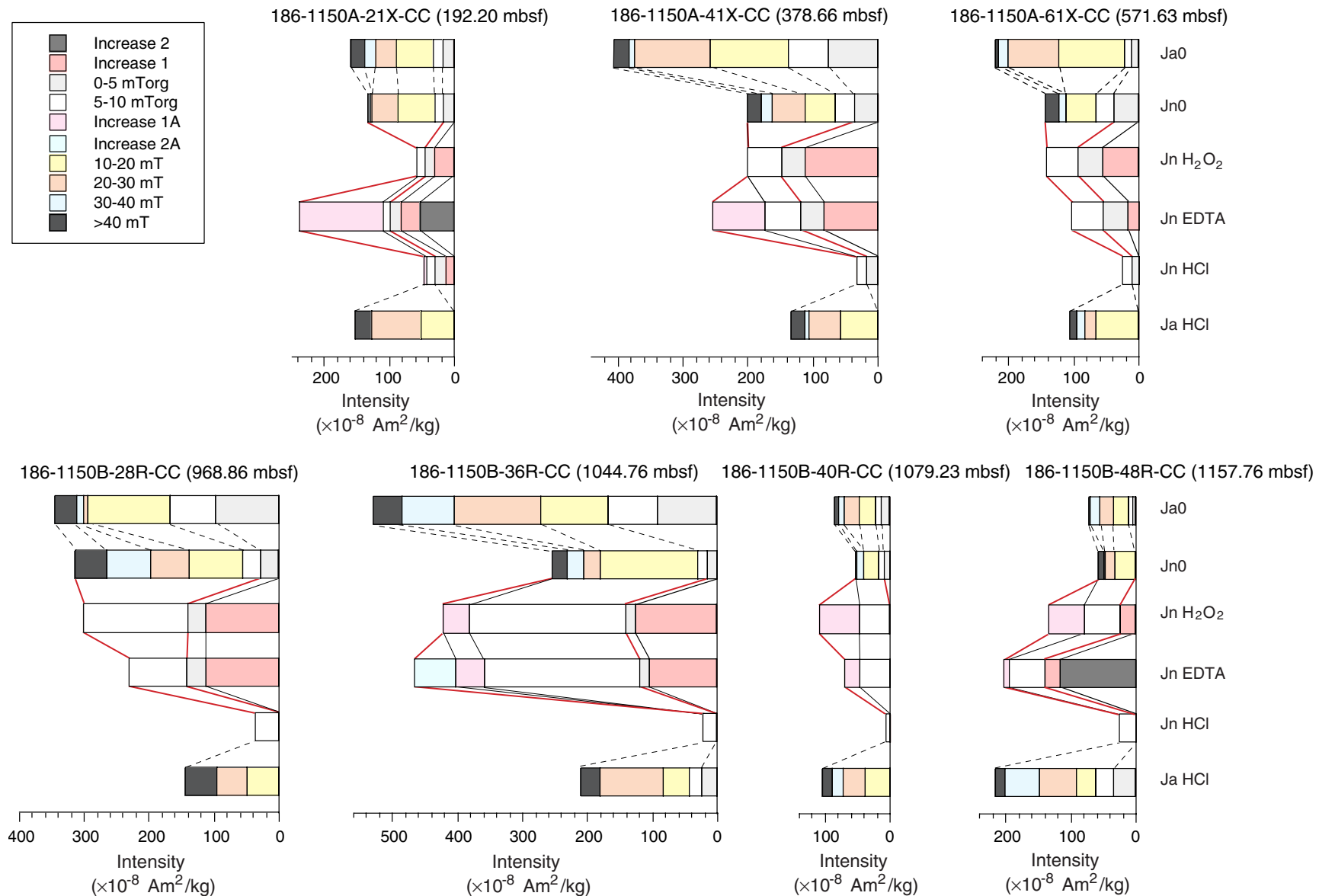


Figure F47. Magnetostratigraphic models based on calcareous nannofossil datums, diatom datums, and diatom datums adjusted to agree with the prominent geomagnetic reversals.

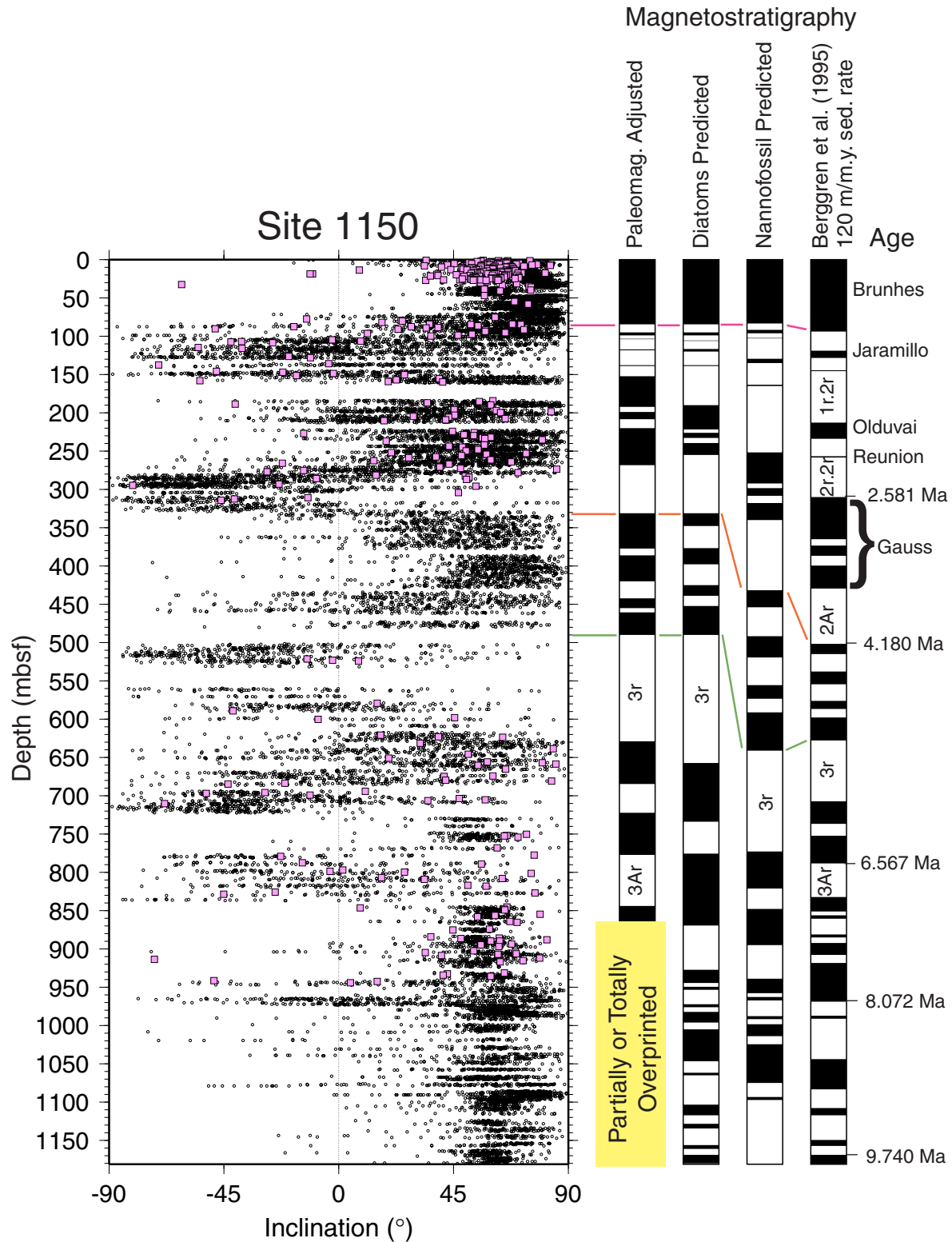


Figure F48. Age-depth relationship for Site 1150, based on diatom (open circle) and nannofossil (open triangle) datums, and geomagnetic-reversal boundaries (open square). Numbers at the age control points correspond to datum events of Table T13, p. 195. Curves of DSDP Sites 438 and 584 are modified after Niitsuma and Akiba (1986). Dashed lines show hiatuses or unconformities.

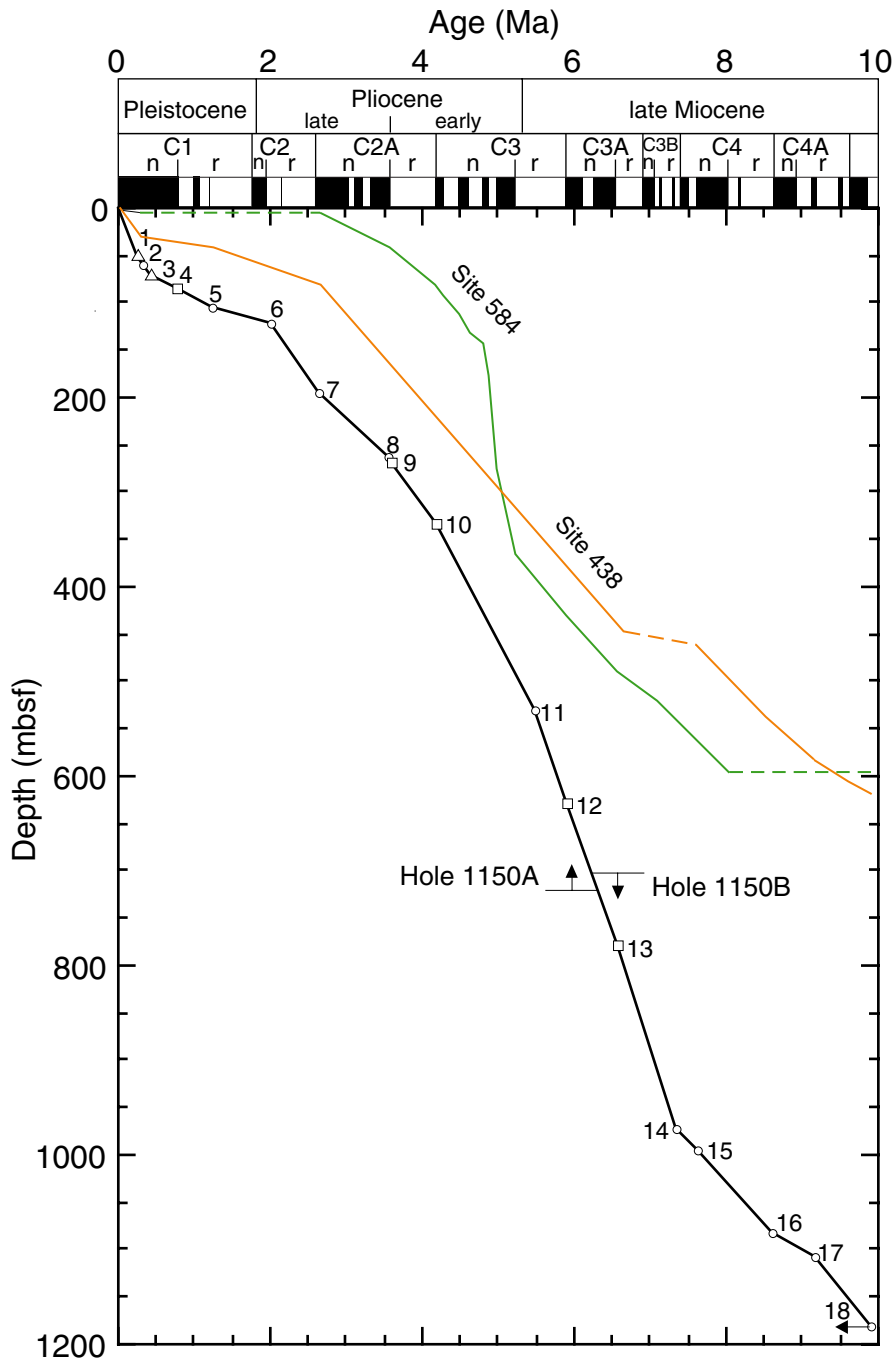


Figure F49. Sedimentation rate vs. age at Site 1150 based on the age control points from Table T13, p. 195.

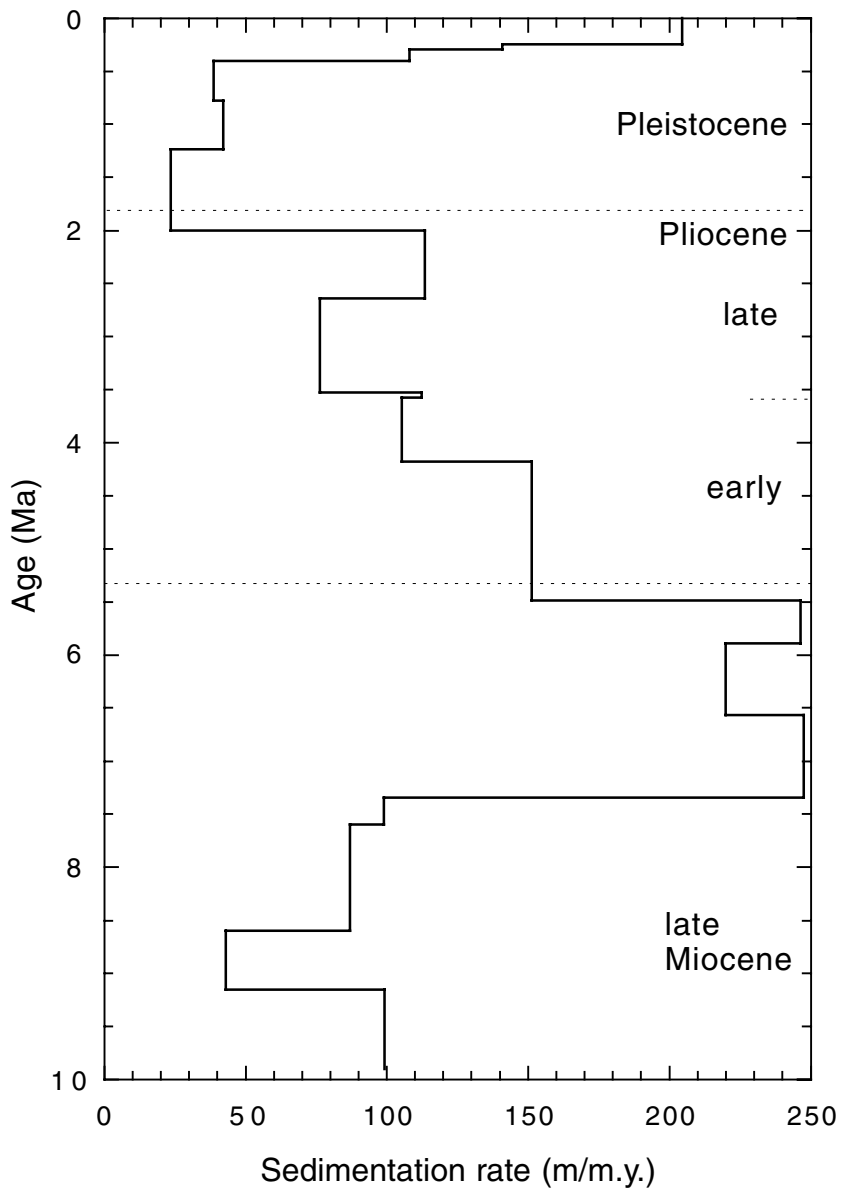


Figure F50. Distribution with depth of headspace concentrations of methane (C_1) and ethane (C_2), and C_1/C_2 ratios at Site 1150.

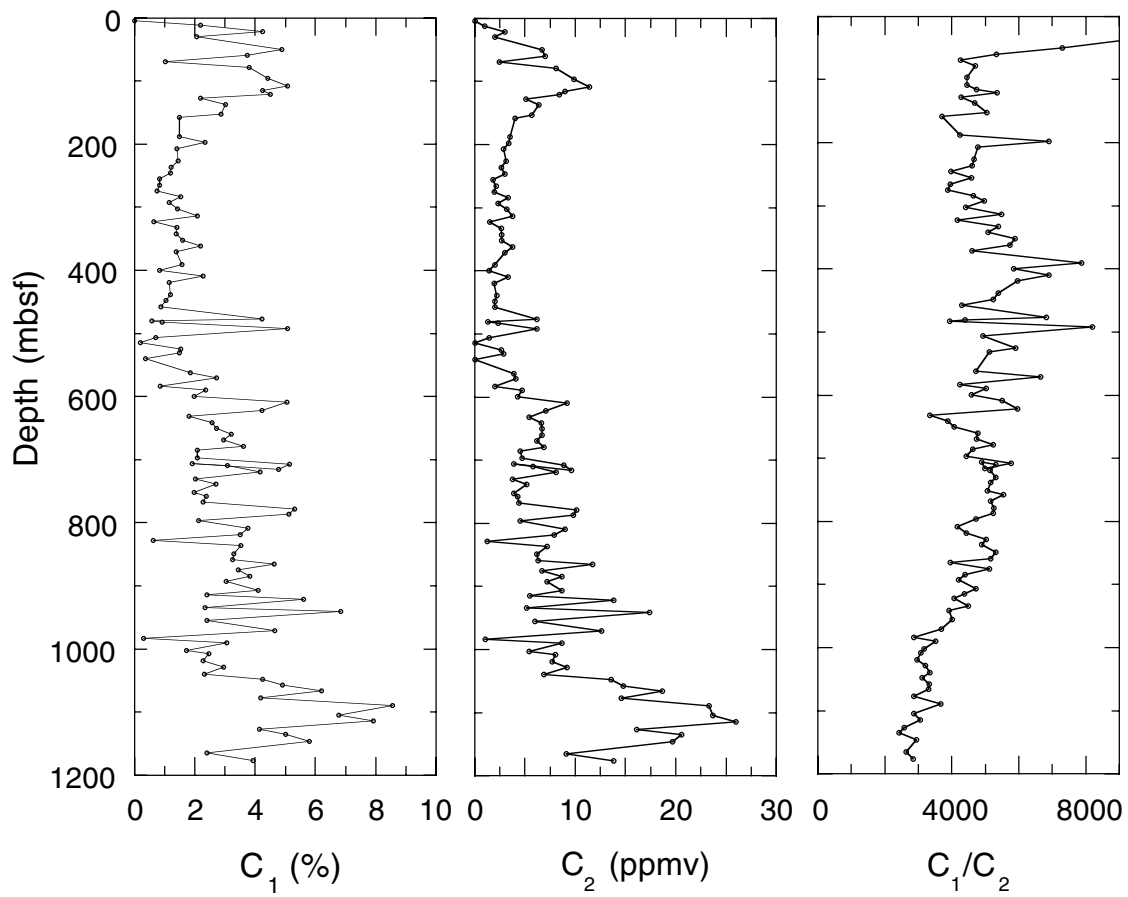


Figure F51. Distribution of carbonate, organic carbon (C_{org}), organic carbon/nitrogen (C_{org}/N) ratios, and sulfur (S) abundances with depth in sediments at Site 1150. Organic matter appears to be mostly marine in origin because C_{org}/N ratios are typically lower than 10.

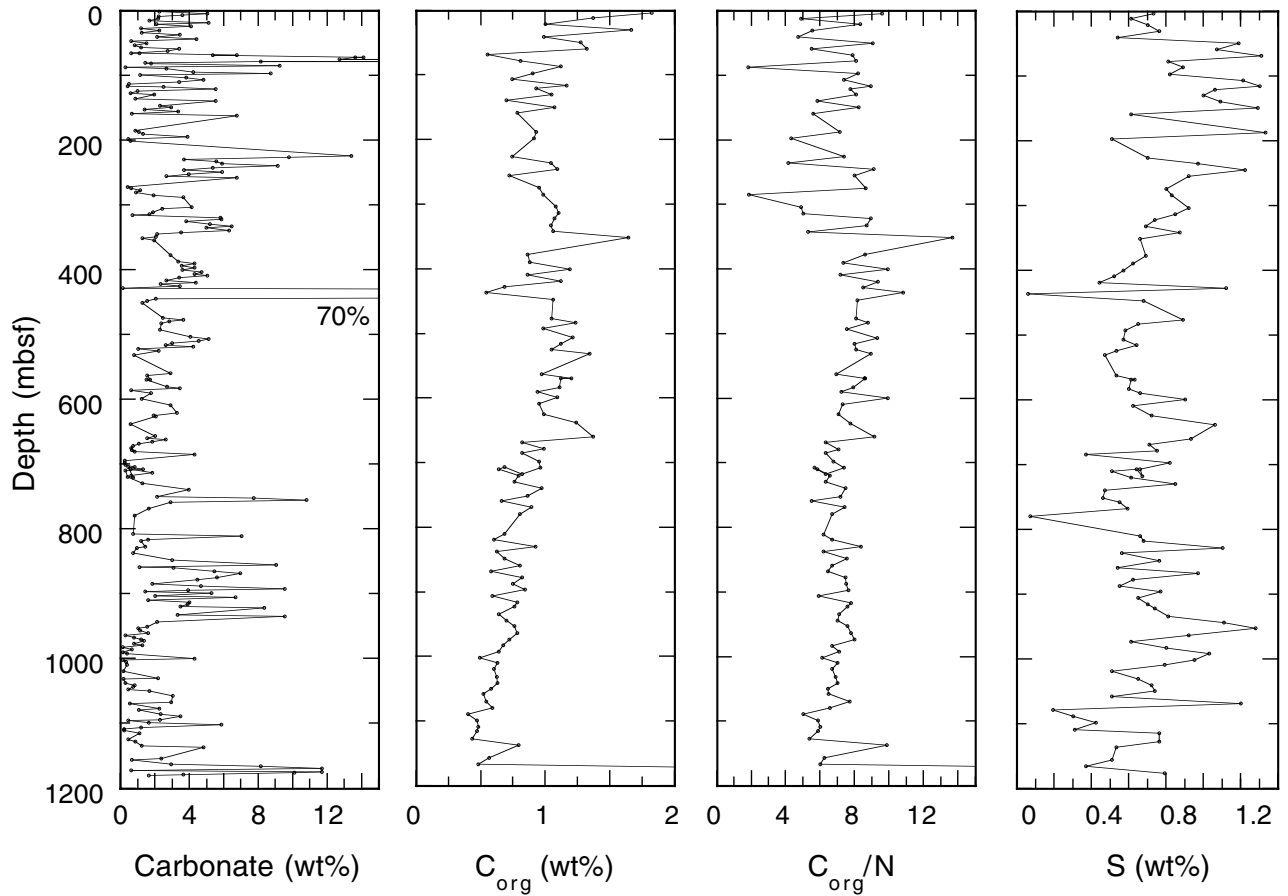


Figure F52. Pore-water salinity, chlorinity, and alkalinity, and pore-water concentrations of dissolved sulfate (SO_4^{2-}), ammonium (NH_4^+), calcium (Ca^{2+}), magnesium (Mg^{2+}), strontium (Sr^{2+}), sodium (Na^+), potassium (K^+), and lithium (Li^+) at Site 1150. (Continued on next page.)

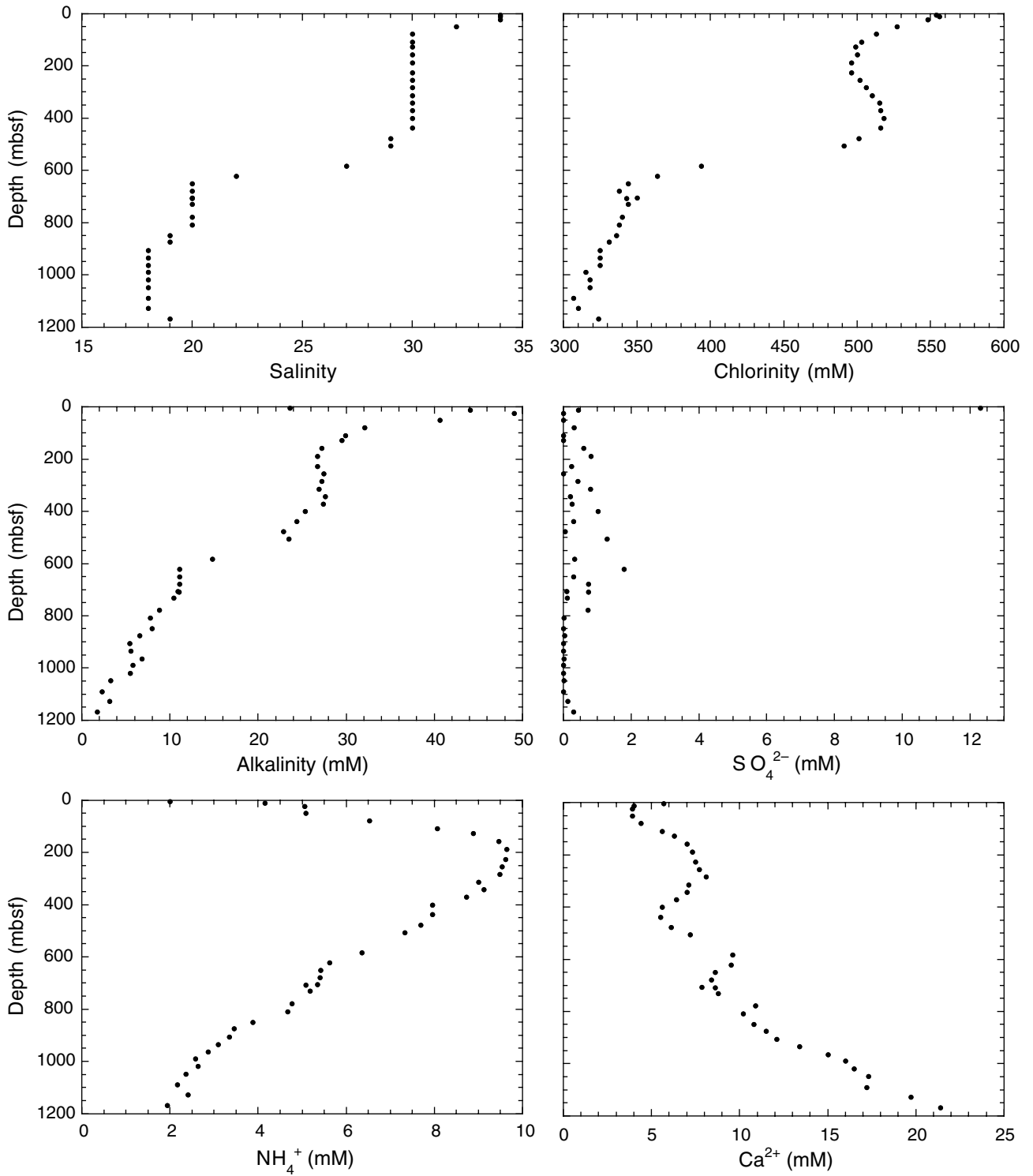


Figure F52 (continued).

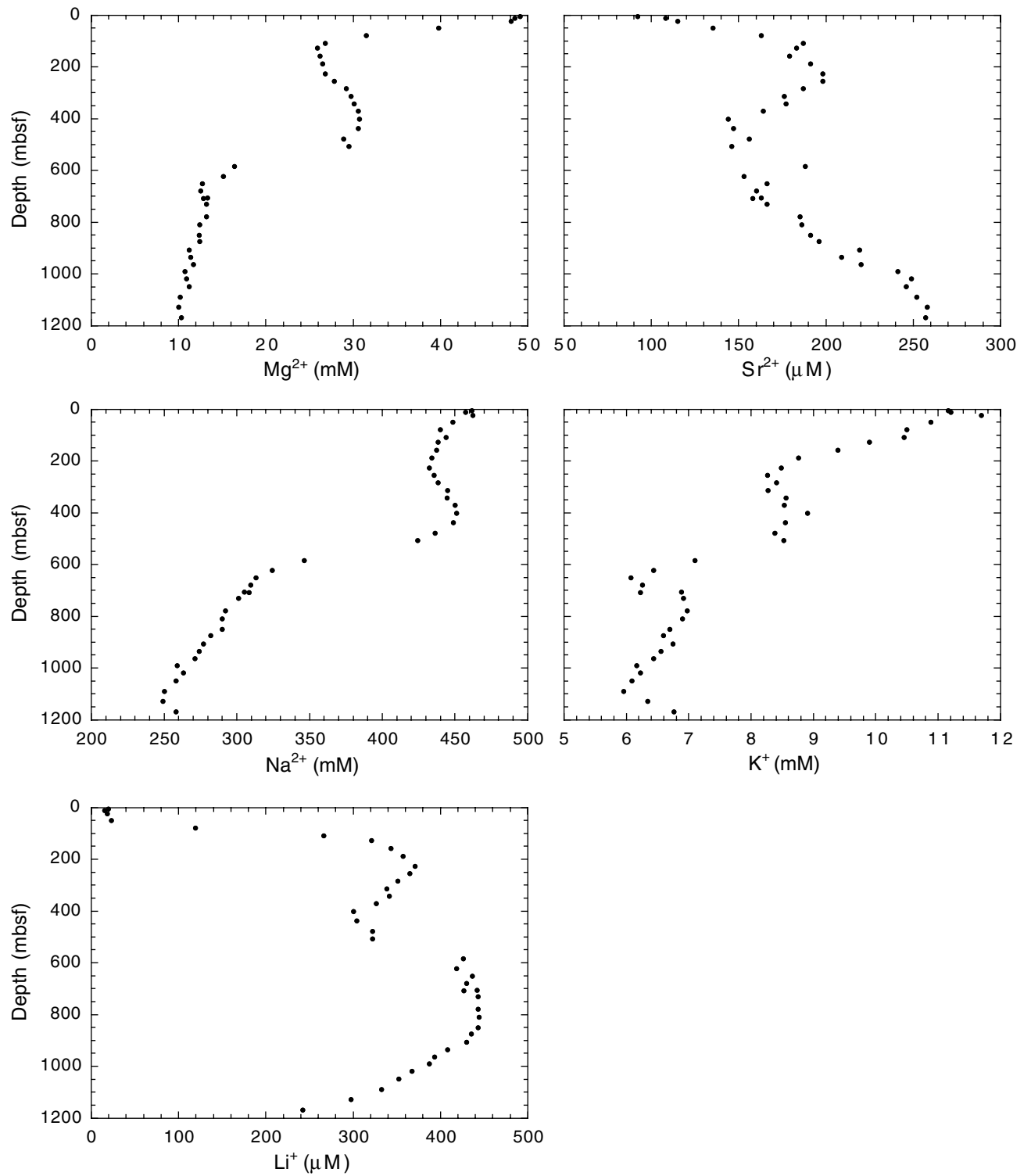


Figure F53. Bulk density from GRA measurements on cores at Site 1150. Open blue circles = uncorrected GRA bulk density data from Hole 1150A; solid red circles = corrected GRA bulk density data from Hole 1150B.

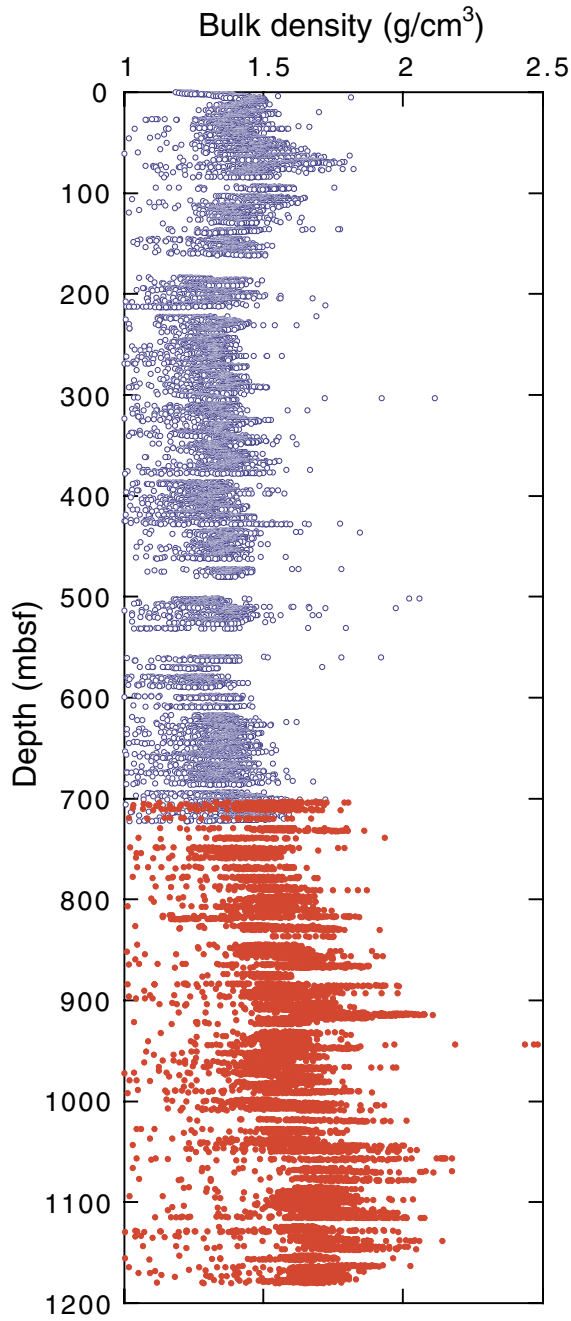


Figure F54. Horizontal *P*-wave velocity from PWL measurements on cores in Hole 1150A.

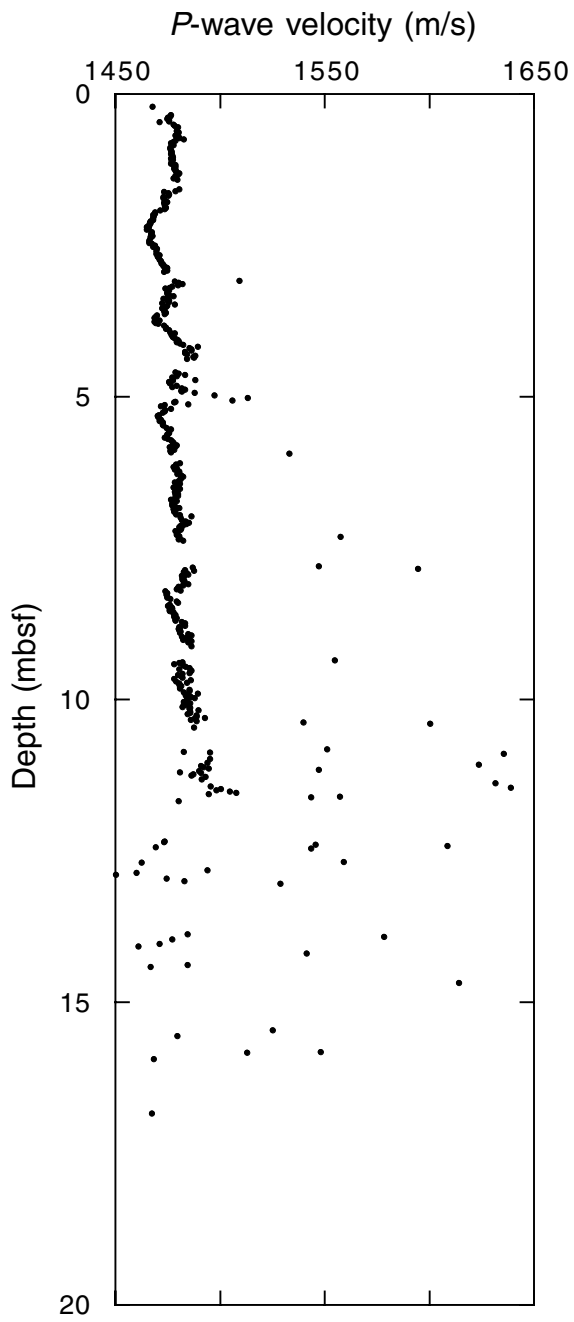


Figure F55. NGR activity of cores at Site 1150. Open blue circles = data from Hole 1150A; solid red circles = data from Hole 1150B.

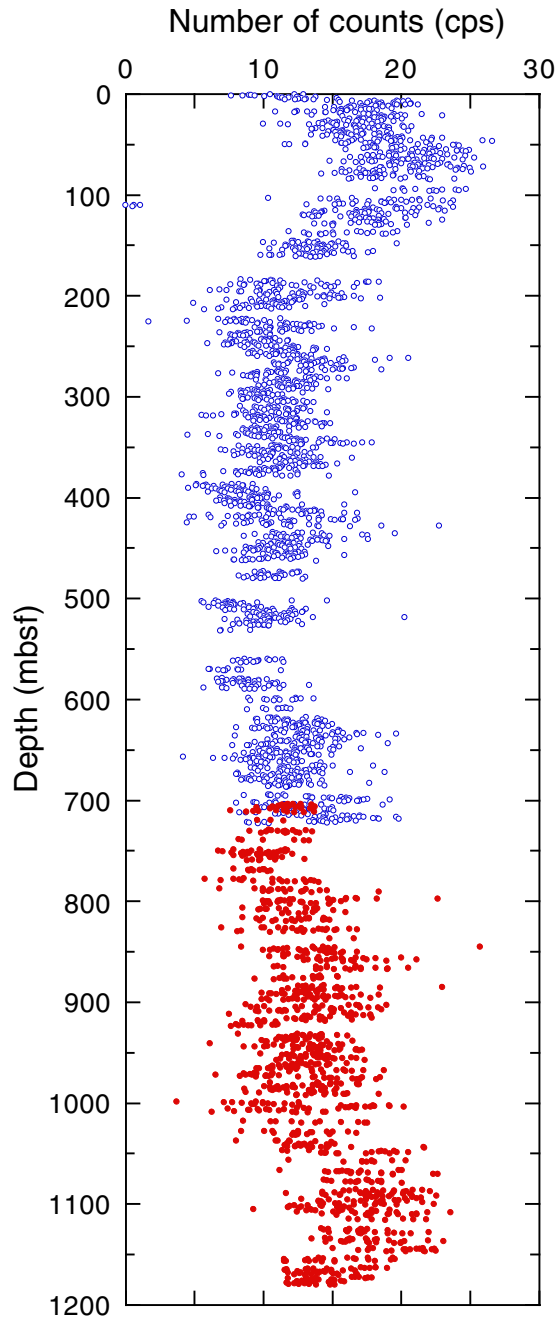


Figure F56. Thermal conductivity variation with depth in Hole 1150A. Solid circles show the average thermal conductivity; open circles show individual thermal conductivity measurements.

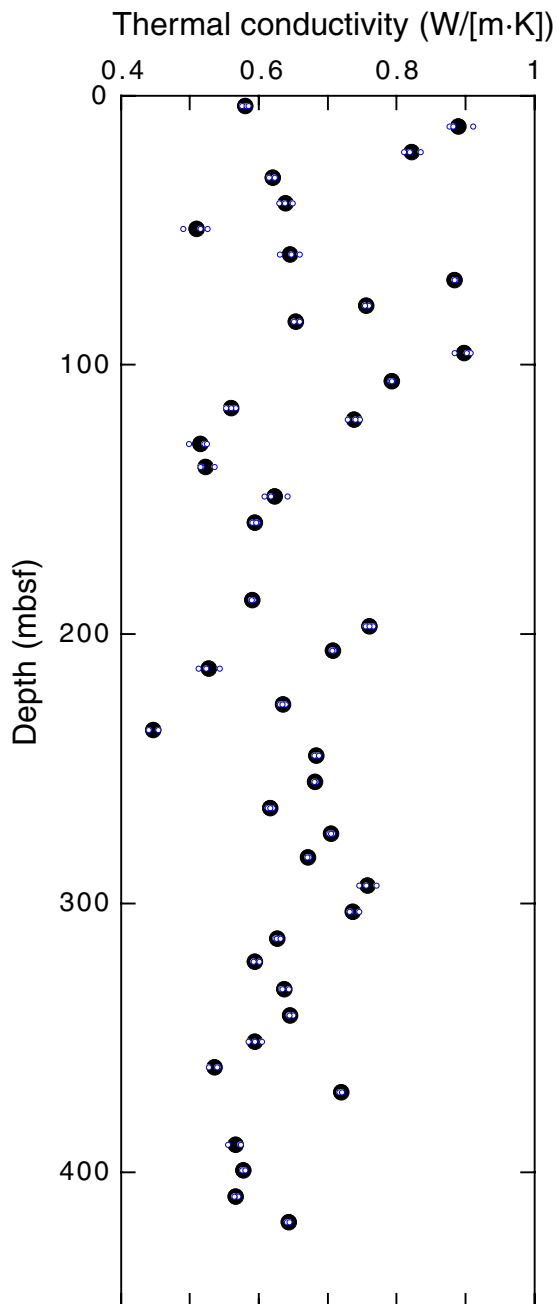


Figure F57. *P*-wave velocity vs. depth from measurements on split cores at Site 1150. A. *P*-wave velocity in horizontal directions (V_x and V_y). B. *P*-wave velocity in vertical direction (V_z).

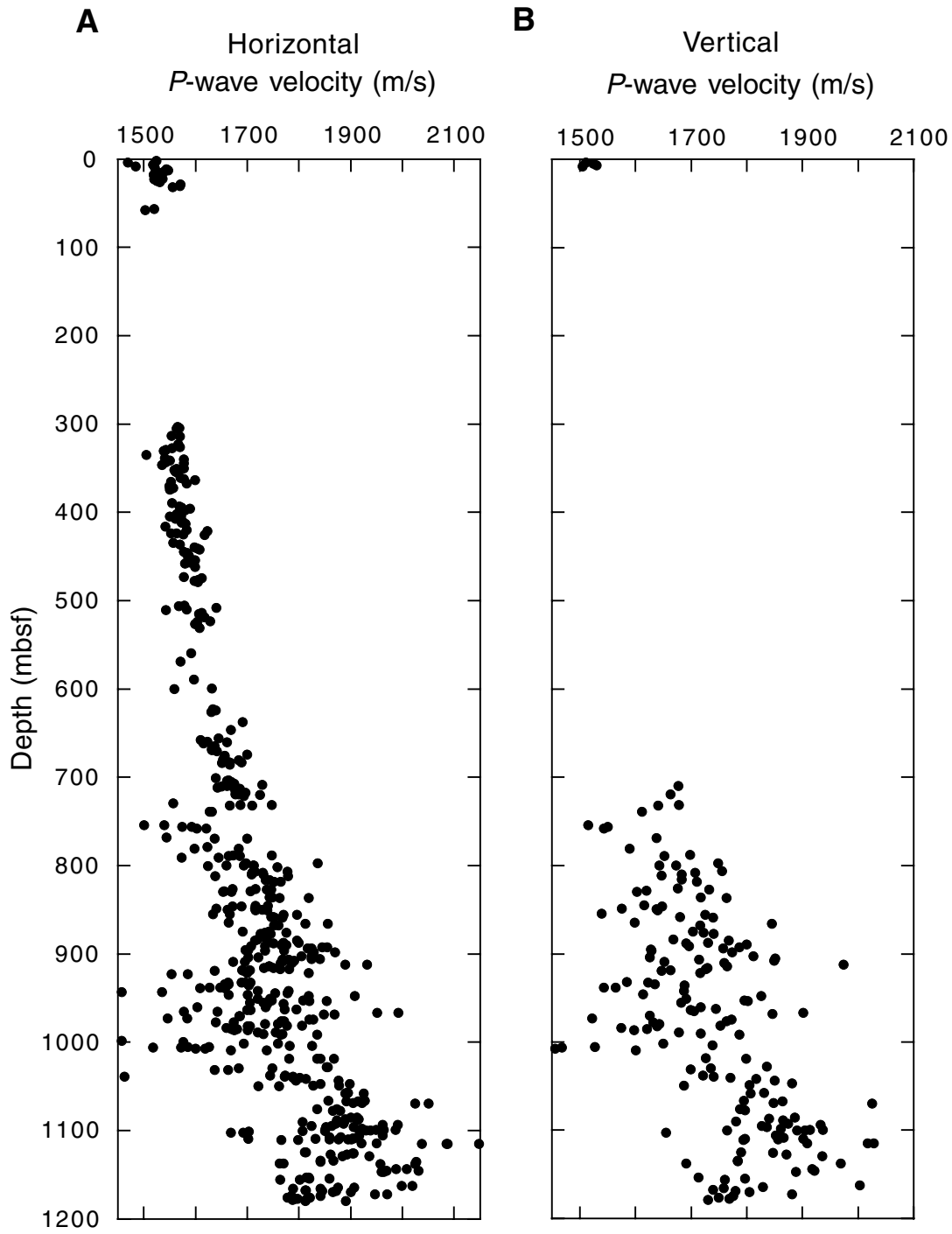


Figure F58. Anisotropy vs. depth from measurements of vertical and horizontal P -wave velocities in Hole 1150B. A. Anisotropy of maximum vs. minimum horizontal P -wave velocity (A_{Hh}). B. Anisotropy of maximum horizontal vs. vertical P -wave velocity (A_{HV}). C. Anisotropy of minimum horizontal vs. vertical P -wave velocity (A_{hV}).

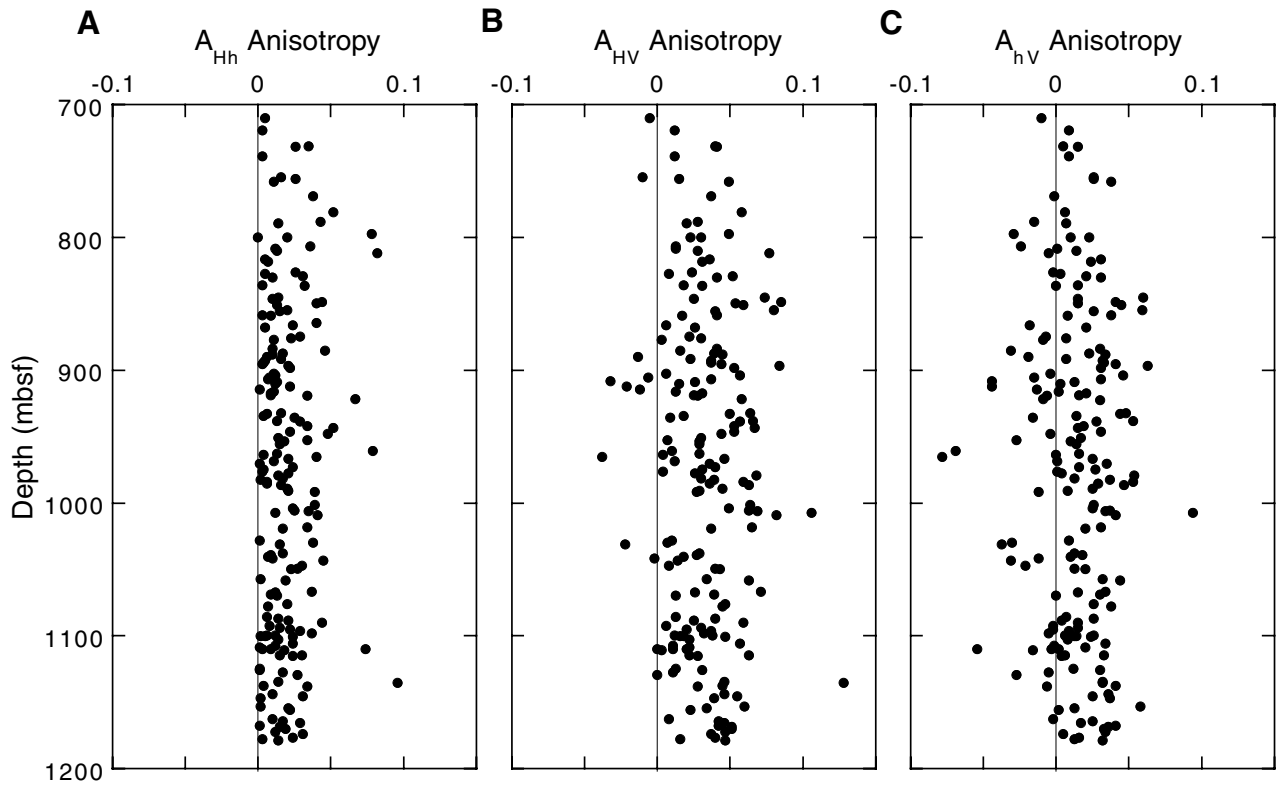


Figure F59. Anisotropy of horizontal P -wave velocity (A_{Hh}) vs. declination in Hole 1150B. The mean declination data have a 95% confidence limit $\leq 4.5^\circ$. The dotted curve shows a sinusoid that is centered at $A_{\text{Hh}} = -0.02$ (dotted line) with an amplitude of 0.04, fitted so that the maximum is at 120°N .

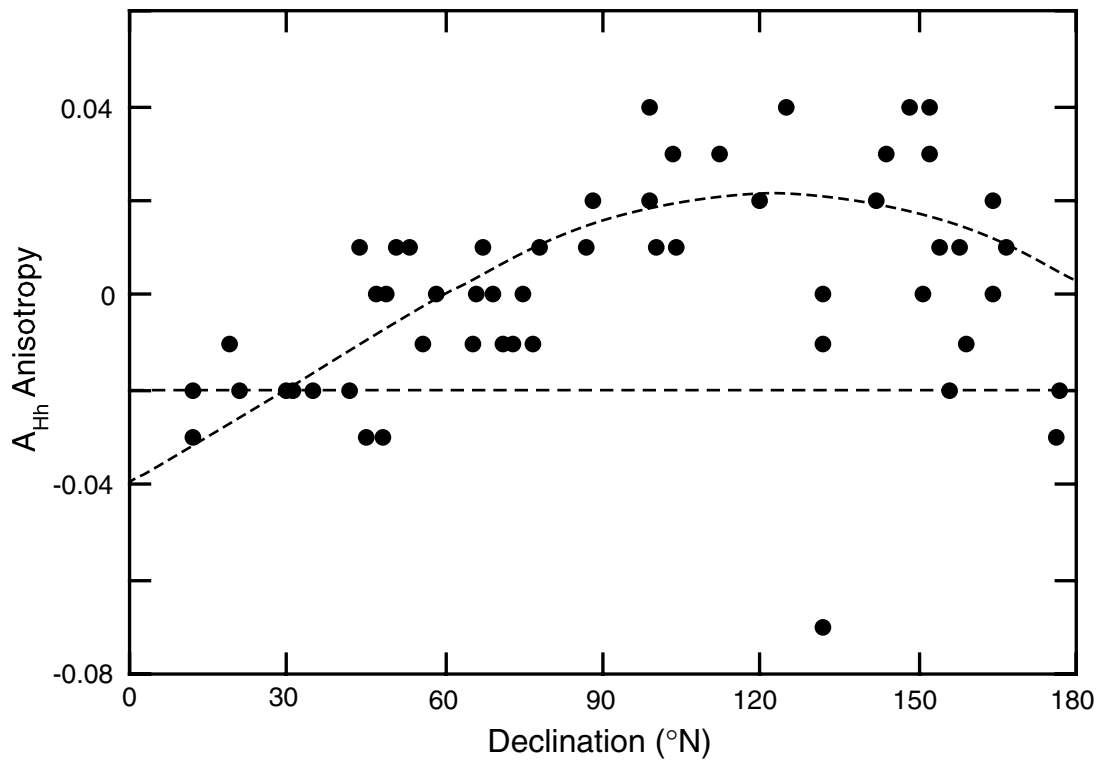


Figure F60. Undrained shear strength variation with depth in Hole 1150A. Solid blue circles = vane shear measurements; open red circles = penetrometer measurements.

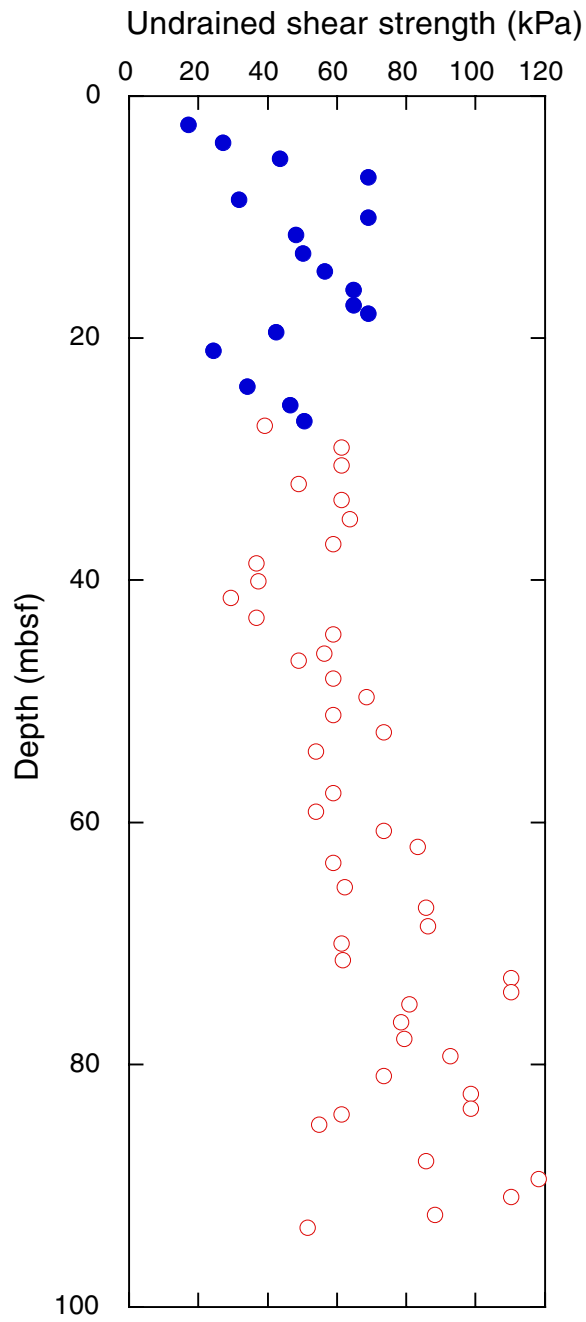


Figure F61. Corrections for in situ salinity and pore-water density at Site 1150. Plotted in the diagrams are the variation vs. depth of the ratio of index properties calculated (c) from in situ values over index properties calculated from ODP standard values (s) (Blum, 1997). **A.** Water content of total mass (W_t^c/W_t^s ratio). **B.** Water content of mass of solids (W_s^c/W_s^s ratio). **C.** Bulk density (ρ_b^c/ρ_b^s ratio). **D.** Dry density (ρ_d^c/ρ_d^s ratio). **E.** Grain density (ρ_g^c/ρ_g^s ratio). **F.** Porosity (η^c/η^s ratio). **G.** Void ratio (e^c/e^s ratio).

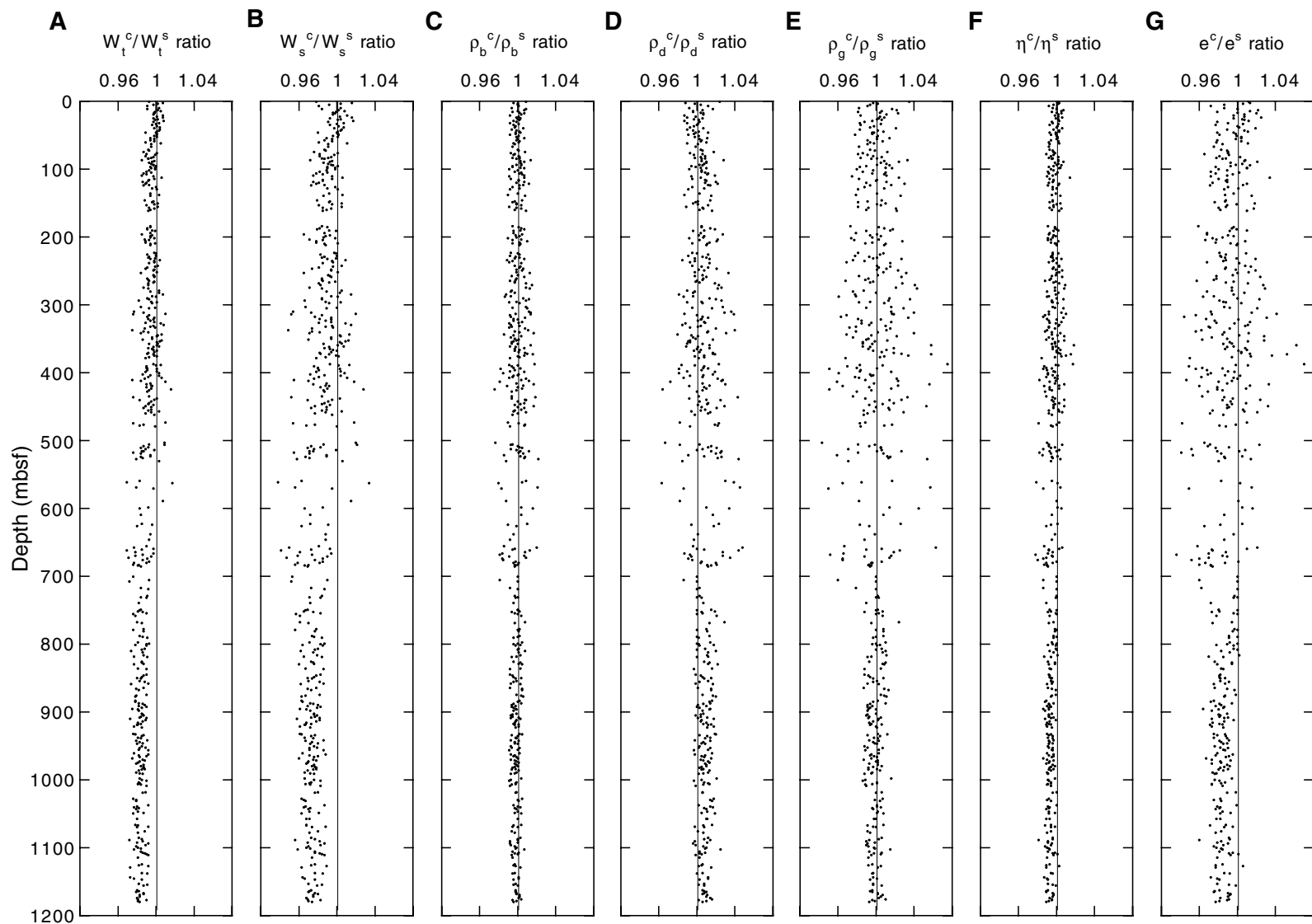


Figure F62. Index properties vs. depth at Site 1150. The calculation of index properties is based on in situ values of salinity and density of pore water. Solid lines = lithologic units; dotted lines = lithologic subunits; open blue circles = data from Hole 1150A; and solid red circles = data from Hole 1150B. **A.** Water content of total mass (W_t^c/W_t^s) ratio. **B.** Water content of mass of solids (W_s^c/W_s^s) ratio. **C.** Bulk density (ρ_b^c/ρ_b^s) ratio. **D.** Dry density (ρ_d^c/ρ_d^s) ratio. (Continued on next page.)

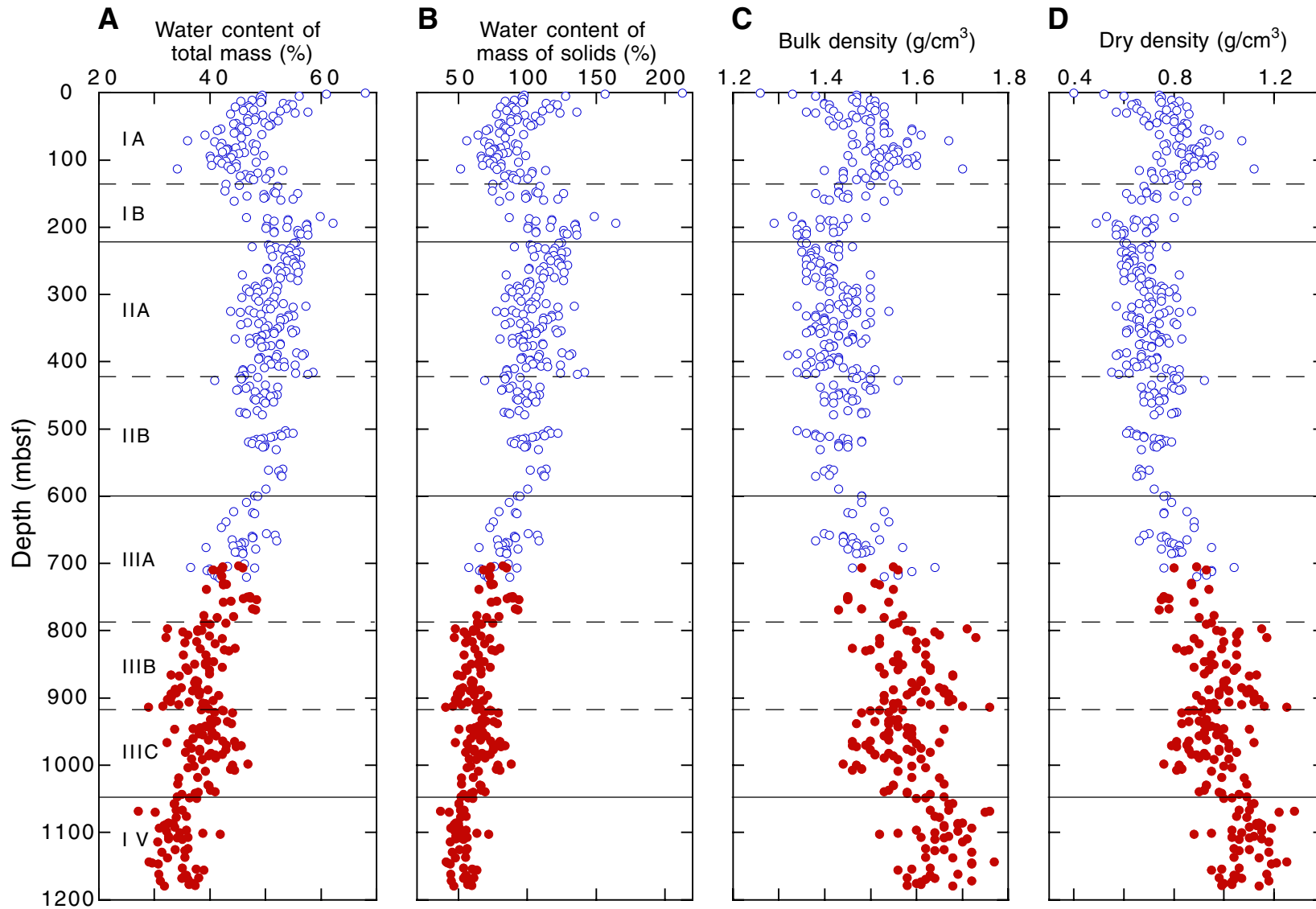


Figure F62 (continued). E. Grain density (ρ_g^c/ρ_g^s) ratio. F. Porosity (η^c/η^s) ratio. G. Void ratio (e^c/e^s) ratio.

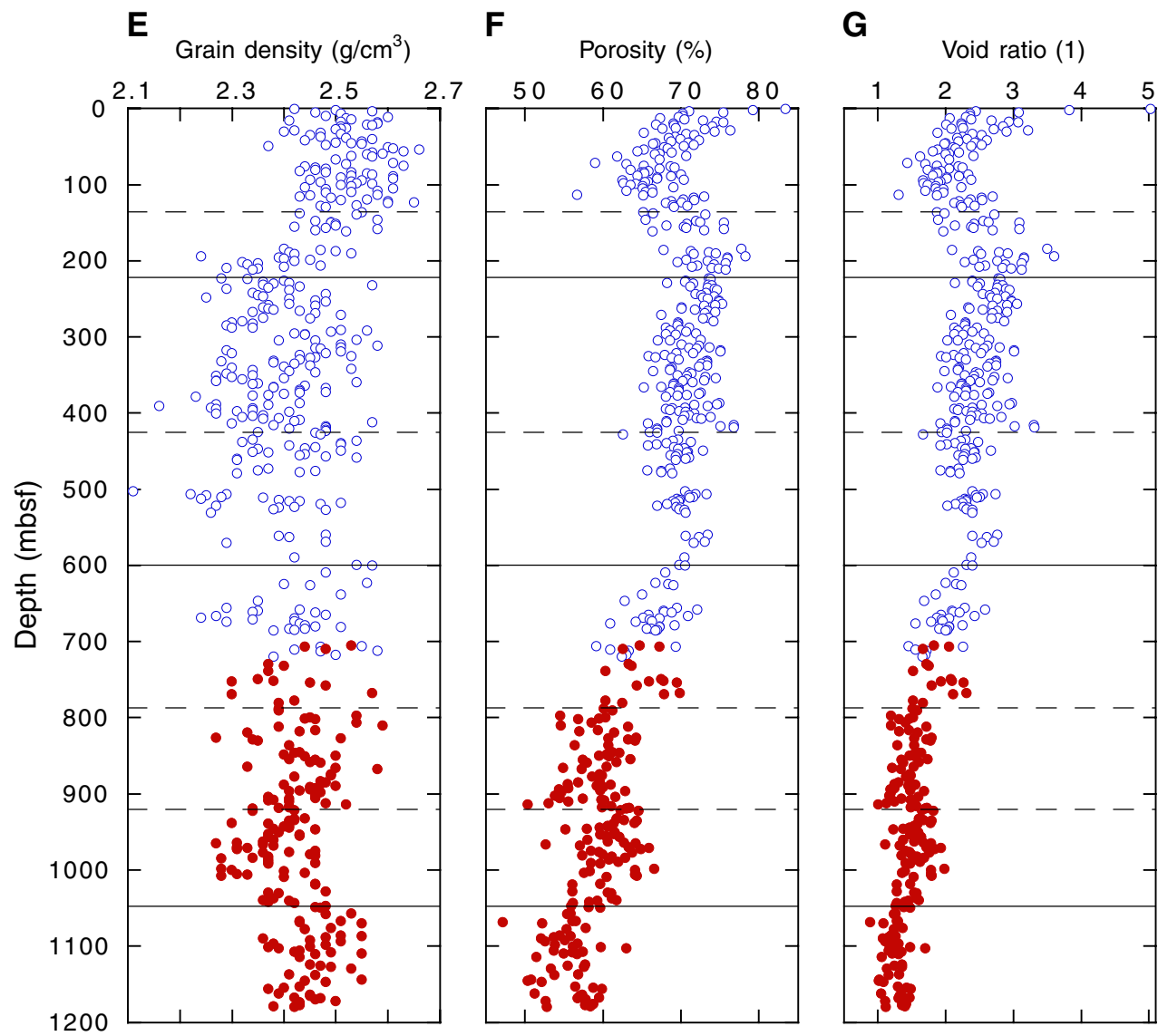


Figure F63. Comparison of physical properties from core and log measurements. Small blue solid circles = data from whole-round core measurements; open red circles = data from split core measurements; and solid green lines = data from log measurements. **A.** Bulk density. **B.** Porosity. **C.** *P*-wave velocity in vertical direction. **D.** Natural gamma radiation (NGR) activity. cps = counts per second, gAPI = gamma-ray American Petroleum Institute. (**Figure shown on next page.**)

Figure F63. (Caption on previous page.)

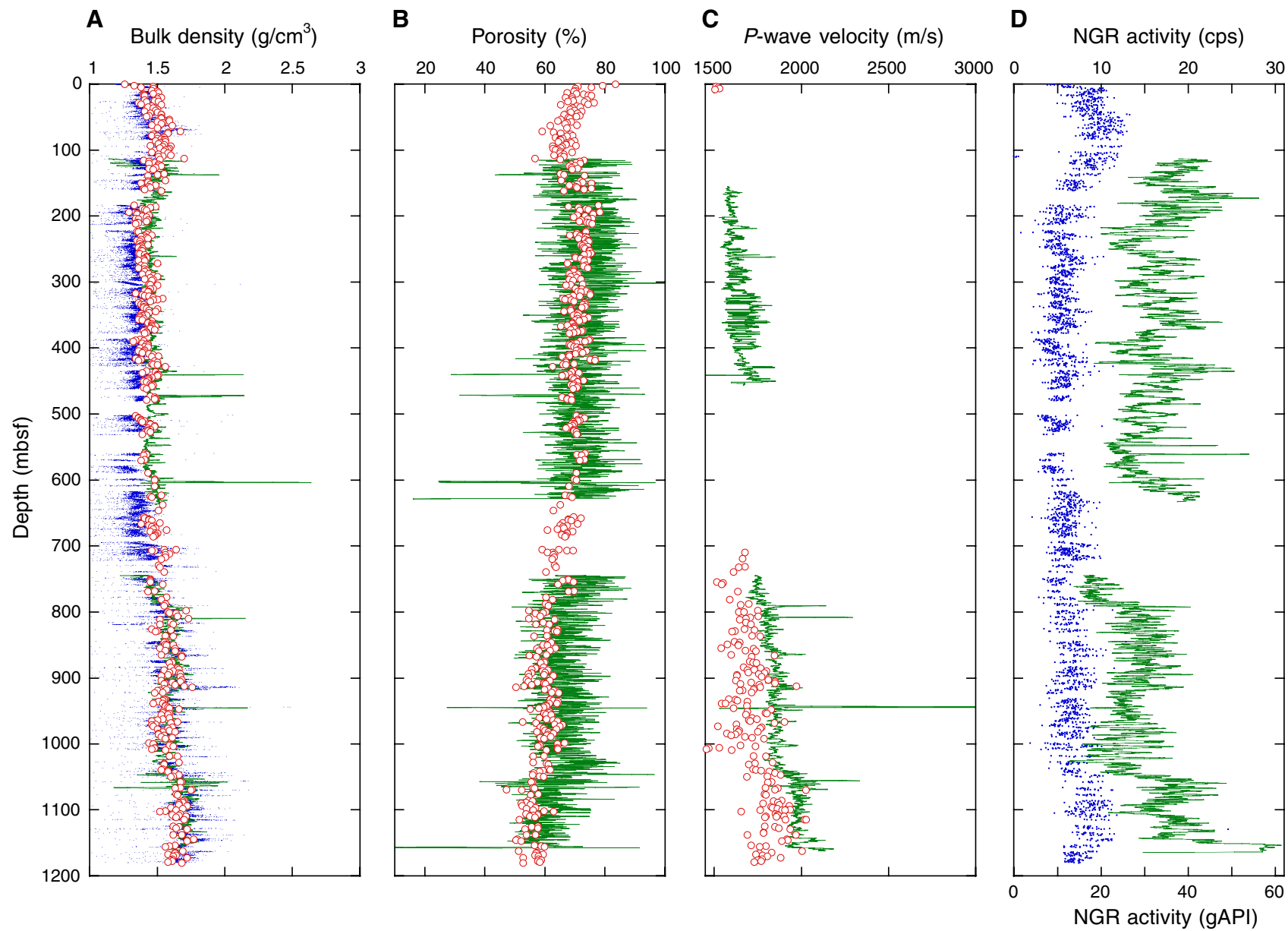


Figure F64. Total and effective vertical stress vs. depth at Site 1150. Linear fit of the data show that the total and effective vertical stresses have the following depth relationships: $\sigma_v = -0.13619 + 0.0148370 \times z$ ($R > 0.999$) and $\sigma_v' = -0.27000 + 0.0084323 \times z$ ($R = 0.998$). The weight of seawater (27.0 MPa) was excluded when calculating total vertical stress. Blue line = σ_v = total vertical stress; dotted red line = σ_v' = effective vertical stress; and z = depth.

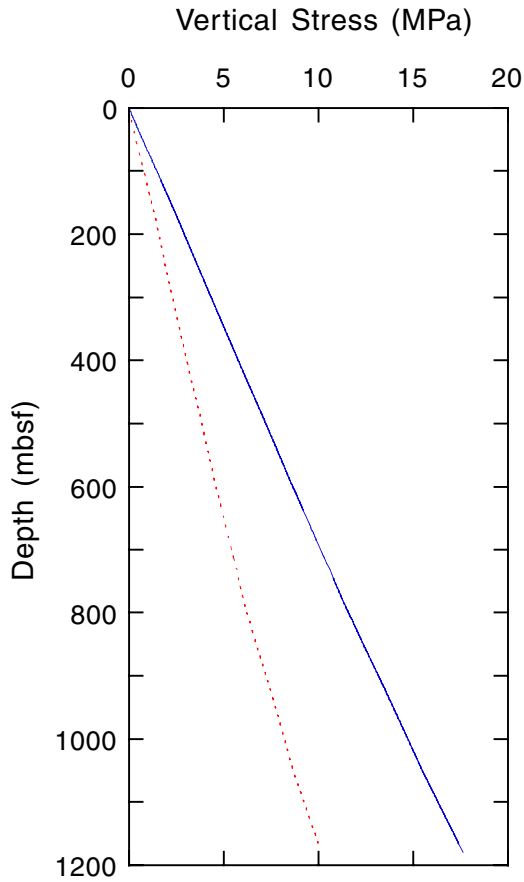


Figure F65. Porosity vs. mineral composition at Site 1150. A. Porosity vs. peak intensity of opal-A hump. B. Porosity vs. carbonate (CaCO₃) content.

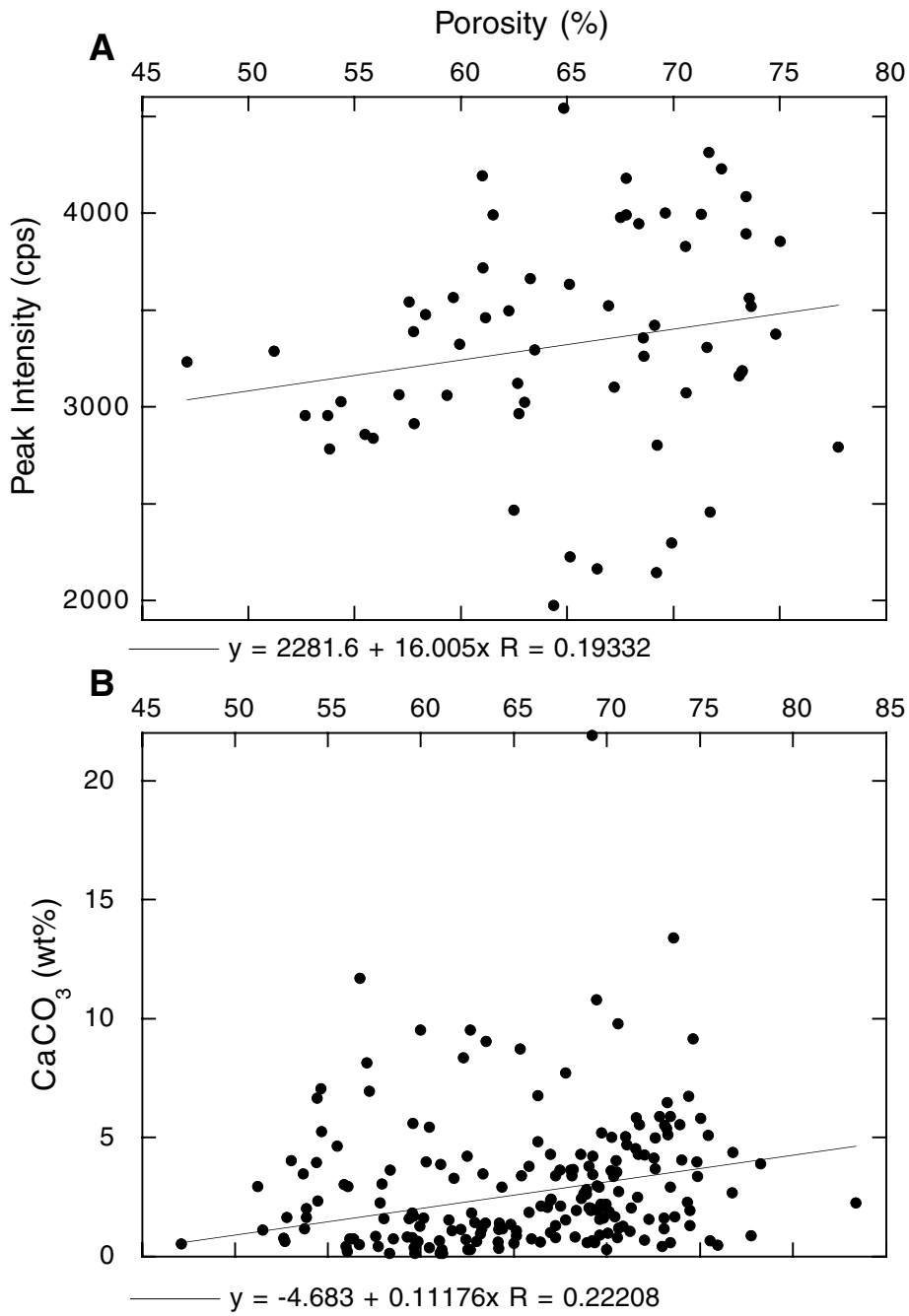


Figure F66. Summary of Site 1150 logging operations. LDEO-TAP = Lamont-Doherty Earth Observatory temperature/acceleration/pressure tool; HNGS = hostile-environment natural gamma-ray sonde; APS = accelerator porosity sonde; HLDS = hostile environment lithodensity sonde; DITE = dual induction tool; NGT = natural gamma-ray tool; DSI = dipole shear sonic imager; GPIT = general purpose inclinometer tool; FMS = Formation MicroScanner; LSS = long-spaced sonic imager; BHTV = borehole televiewer; and TD = total depth reached by each tool string.

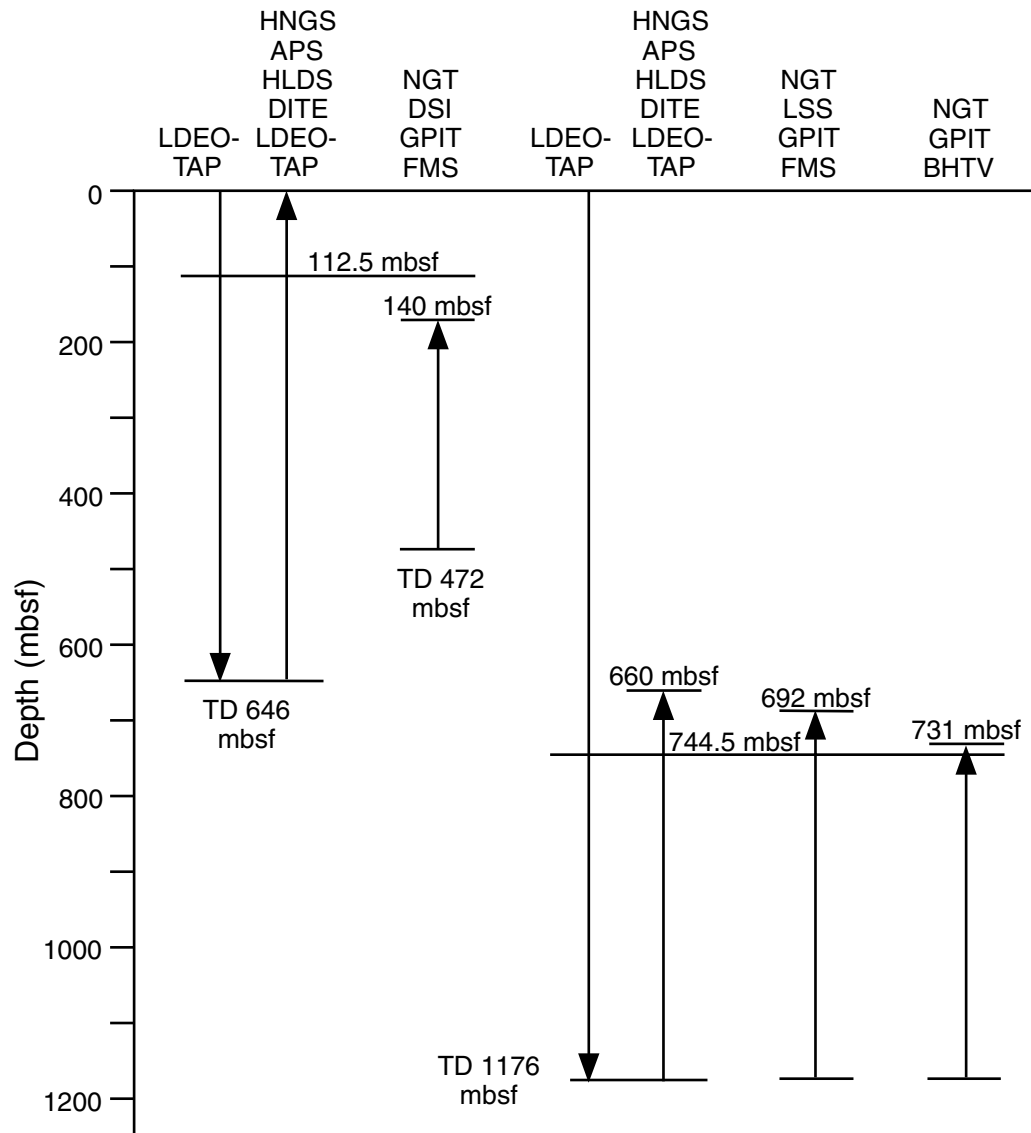


Figure F67. FMS images across a carbonate zone at 943.3–944.4 mbsf. This zone was correlated with a section in Core 186-1150B-26R and to major seismic reflector at CMP 2341 of cruise KH 96-3, Line 1. The FMS images show the carbonate zone consists of two parts: (1) relatively resistive beds with conductive features (bioturbation?) below, and (2) relatively conductive beds with fractures above. The images to the left are displayed with a range of resistivity values that are fixed for the entire logged interval (“static correction”); the images at the right allow for a greater range of grayscale to be displayed using normalized gains for a smaller user-specified depth interval (dynamic equalization). Both images are from 940 to 948 mbsf. gAPI = gamma-ray American Petroleum Institute.

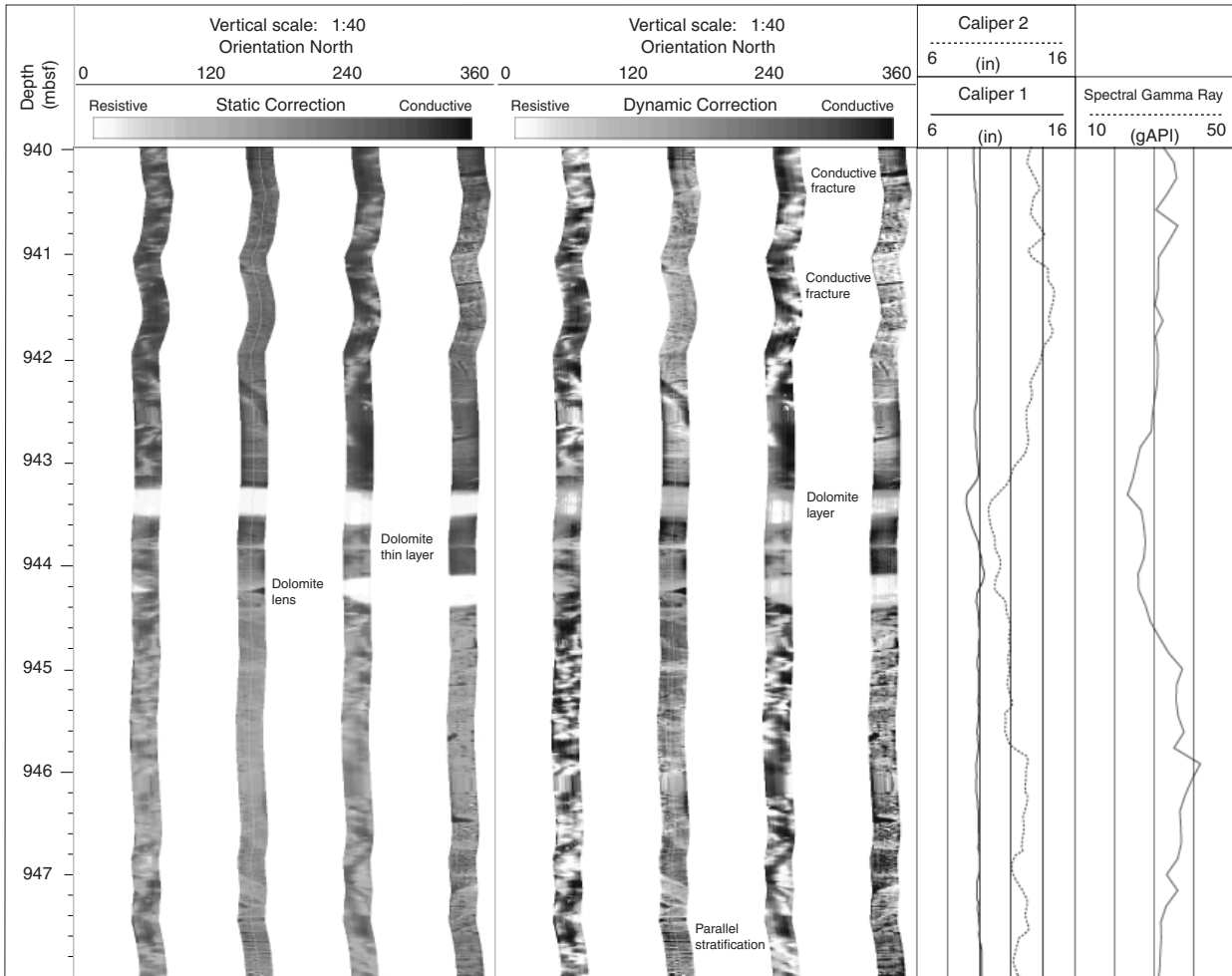


Figure F68. Formation MicroScanner (FMS) images from 985 to 1030 mbsf in Hole 1150B showing alternating beds of silty claystone and diatomaceous siltstone in an ~10-m cycle with fine stratifications. The sedimentary cycles can be correlated well with natural gamma radiation. See Figure F67, p. 146, for an explanation of the FMS display. Note that Caliper 1 (north-south) shows a constant diameter of 25 cm throughout the section and is close to the bit size, whereas Caliper 2 (east-west) varies from 30 to 35 cm. gAPI = gamma-ray American Petroleum Institute.

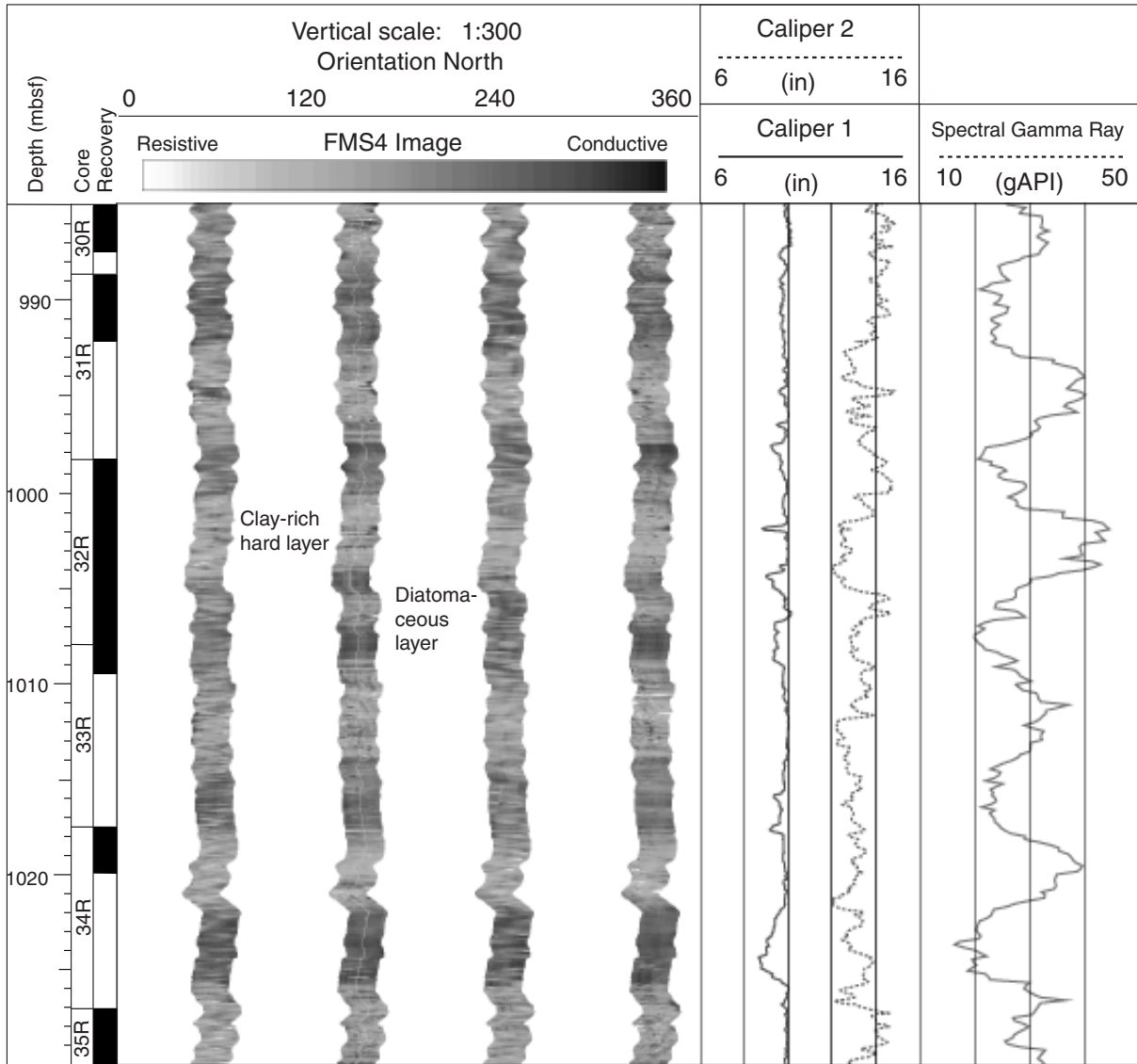


Figure F69. Fracture analysis using FMS images from lithologic Units III and IV. A. Frequency of fracture azimuth. B. Frequency of fracture dip. Light gray indicates resistive fractures, and dark gray indicates conductive fractures.

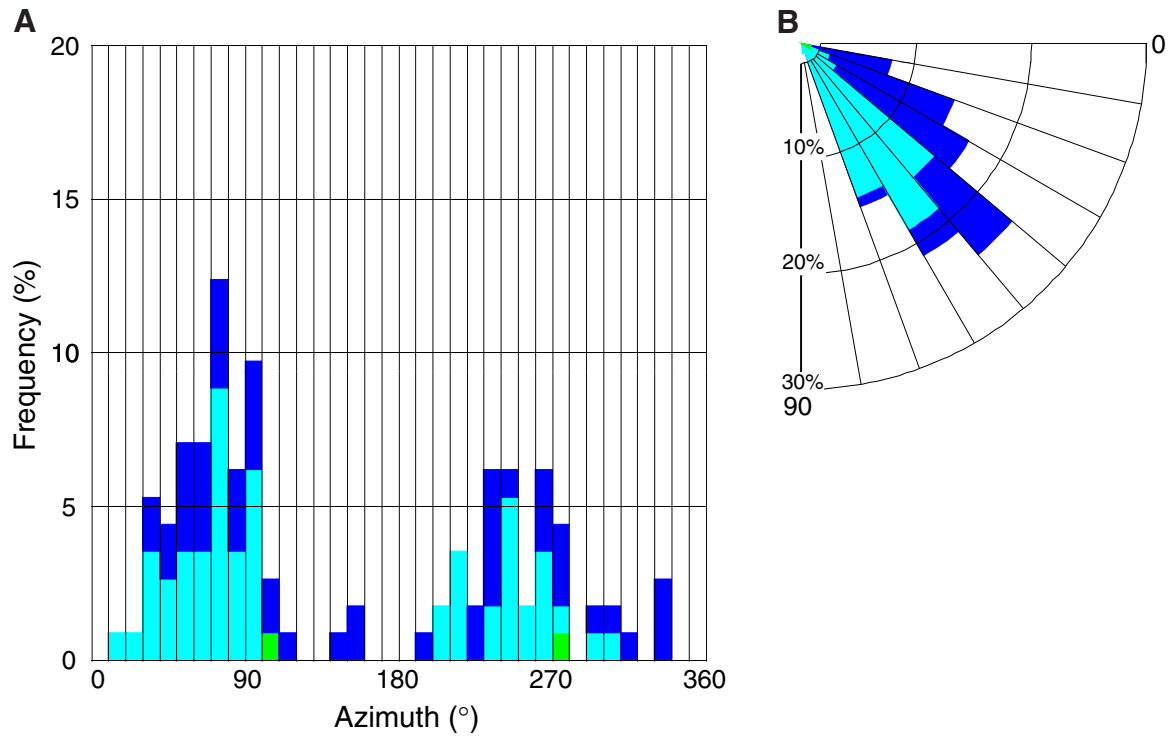


Figure F70. Temperature data vs. time from the APC Adara temperature tool and the DVTP at Hole 1150A. The dashed line in each panel indicates the estimated equilibrium temperature determined by curve fitting to the equilibration record. Circles and square for the DVTP indicate temperature data from the upper and lower thermistors, respectively. The portion of the equilibration curve used for the curve fitting is indicated with solid circles.

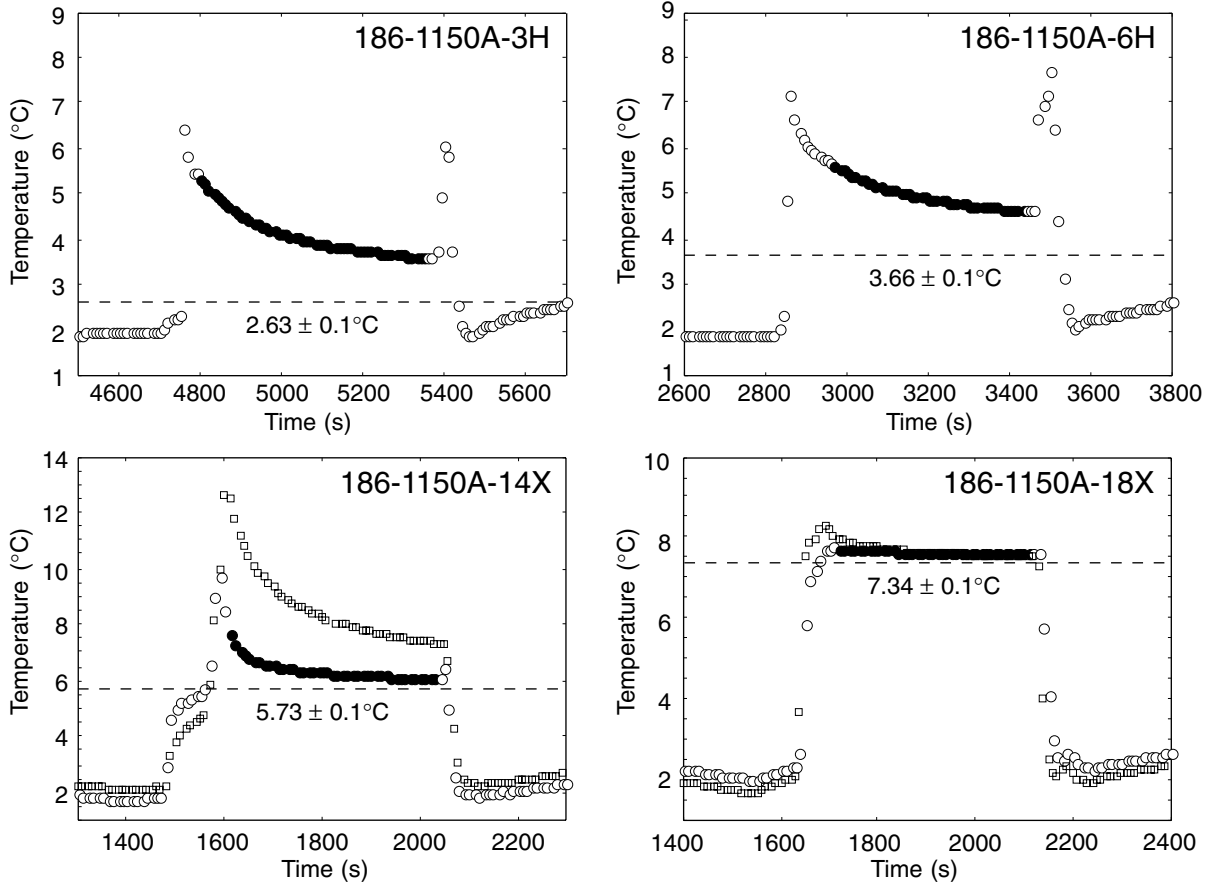


Figure F71. A. Temperature vs. depth at Site 1150. Thermal gradients are also shown. B. Temperature vs. cumulative thermal resistance and calculated mean heat flow.

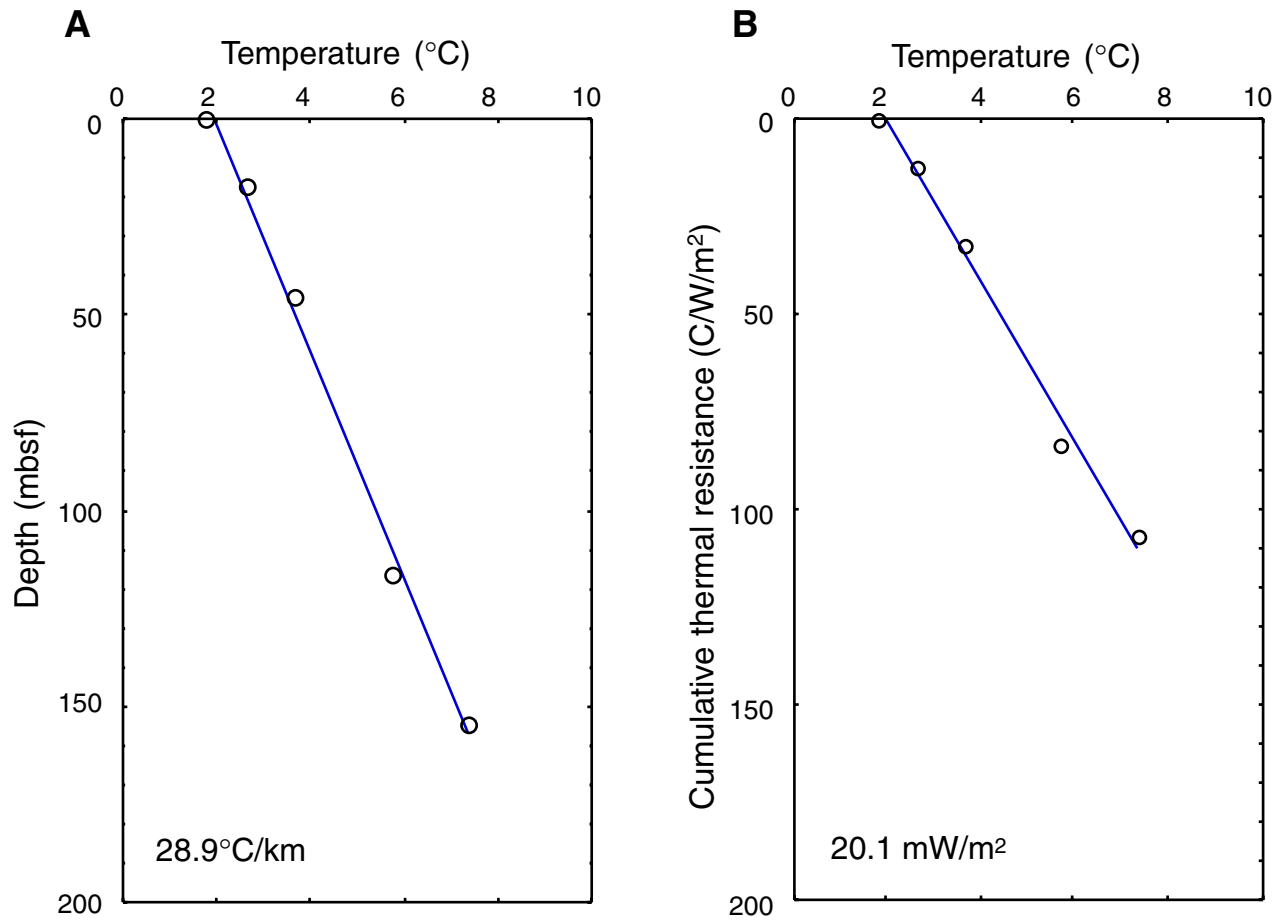


Figure F72. Temperature logs recorded in Hole 1150B. The circles represent the station measurements recorded with the Adara temperature tool and the DVTP, the black line corresponds to the downgoing LDEO-TAP log, and the gray line corresponds to the upgoing LDEO-TAP log.

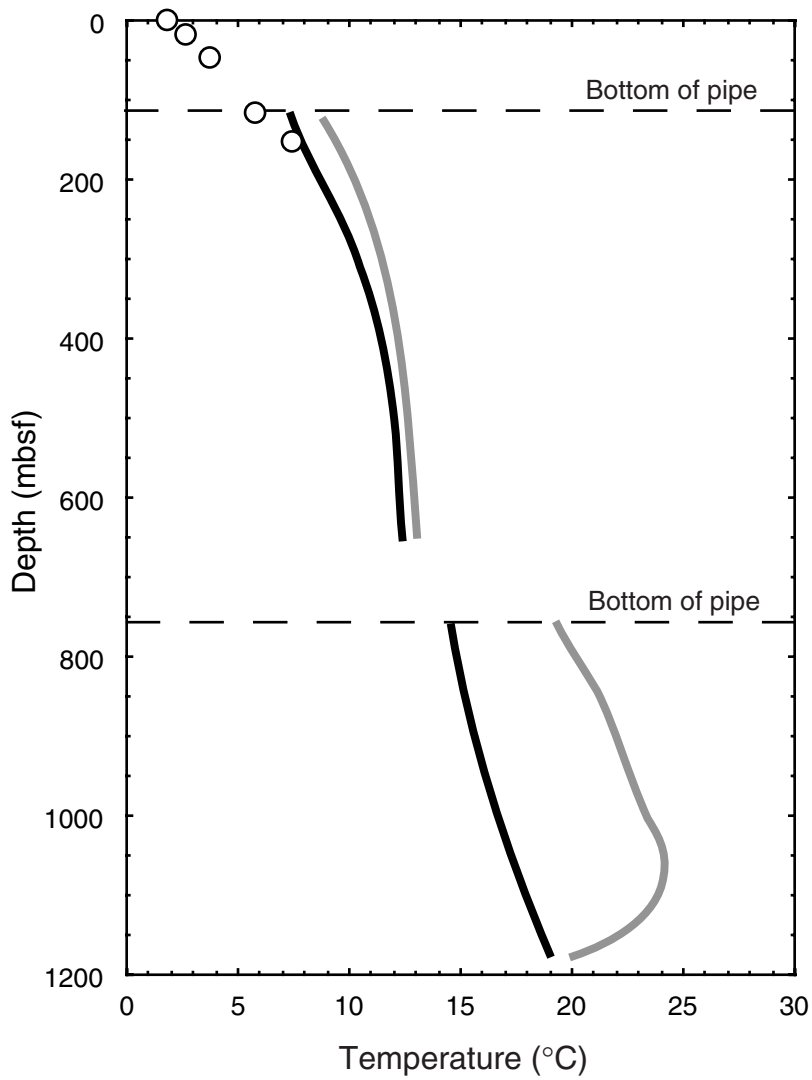


Figure F73. Crossplot of shallow resistivity vs. spectral gamma ray. Lithologic units (I-IV) are plotted by different symbols.

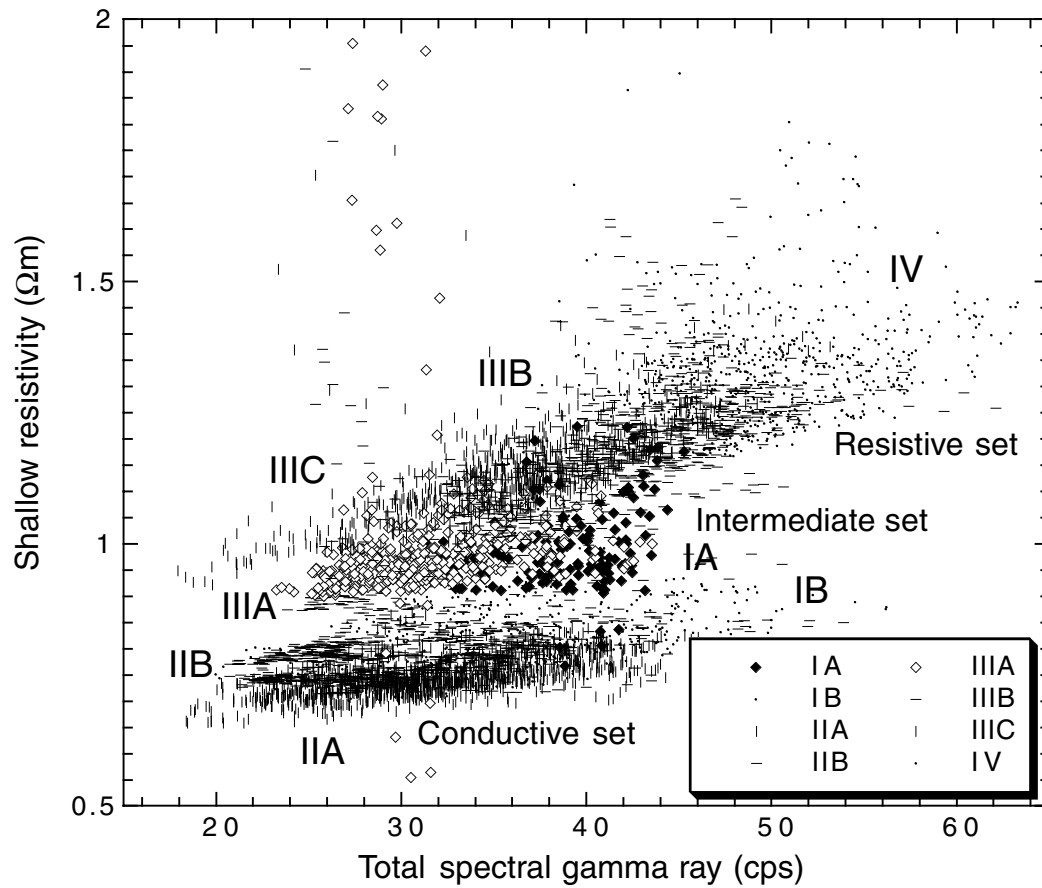


Figure F74. Core-log seismic integration at Site 1150. Density: combined density profile from HLDS logs and corrected MST GRA bulk density. Velocity: dotted curve = DSI velocity log (upper part) and LSS velocity log (lower part); solid curve = GRA-HLDS density-derived velocity. Synthetic: synthetic seismogram (in true amplitudes) plotted in 10 traces in depth. CMP 2341: field seismic trace (in true amplitudes) near to Site 1150 plotted in 10 traces in a converted depth from two-way traveltime. Seismic stratigraphy (SS) Units 1–16 derived from comparison of the synthetic trace with the field record and the two-dimensional seismic section; the corresponding lithologic units (IA–IV) from core descriptions are also shown. CMP = common midpoint. (Continued on next page.)

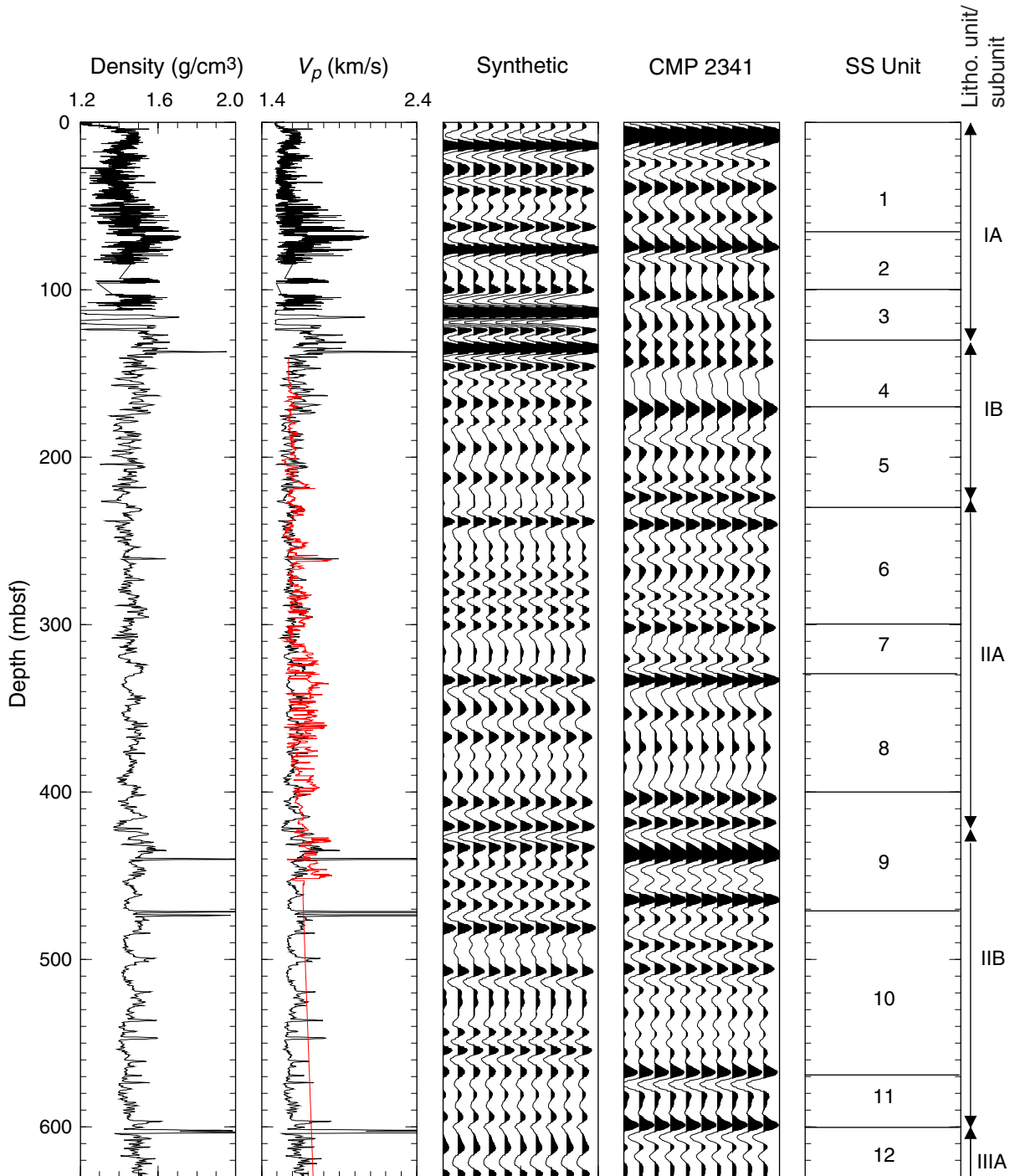


Figure F74 (continued).

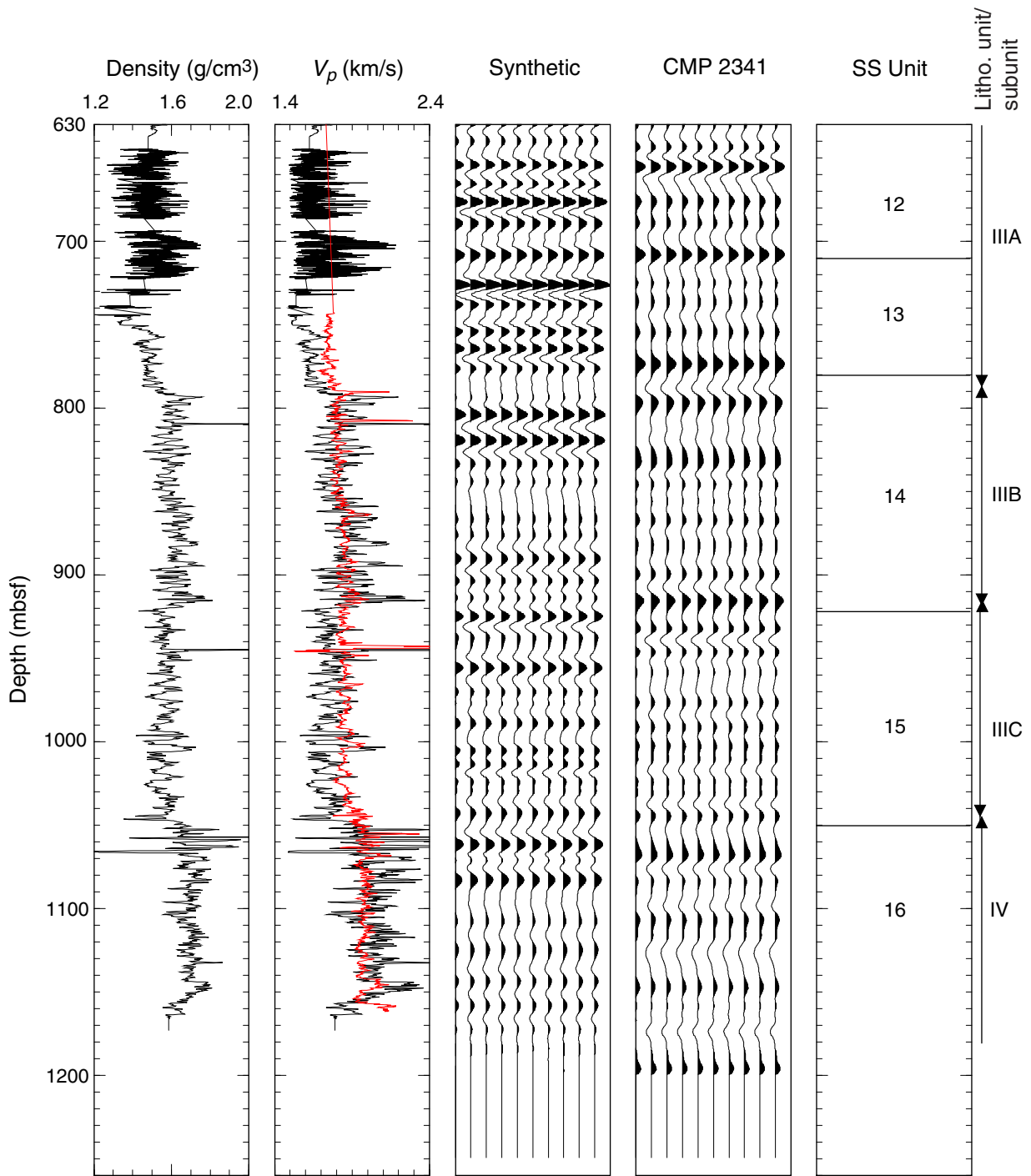


Figure F75. A portion of the seismic section from Line 1 of cruise KH96-3 crossing Site 1150 together with the synthetic seismogram. Identification of the lithologic units from core descriptions (see “**Lithostratigraphy**,” p. 14) with the major seismic stratigraphy (SS) units was obtained from the depth correlation of the synthetic seismogram with the field seismic record in this figure. CMP = common midpoint. (Continued on next page.)

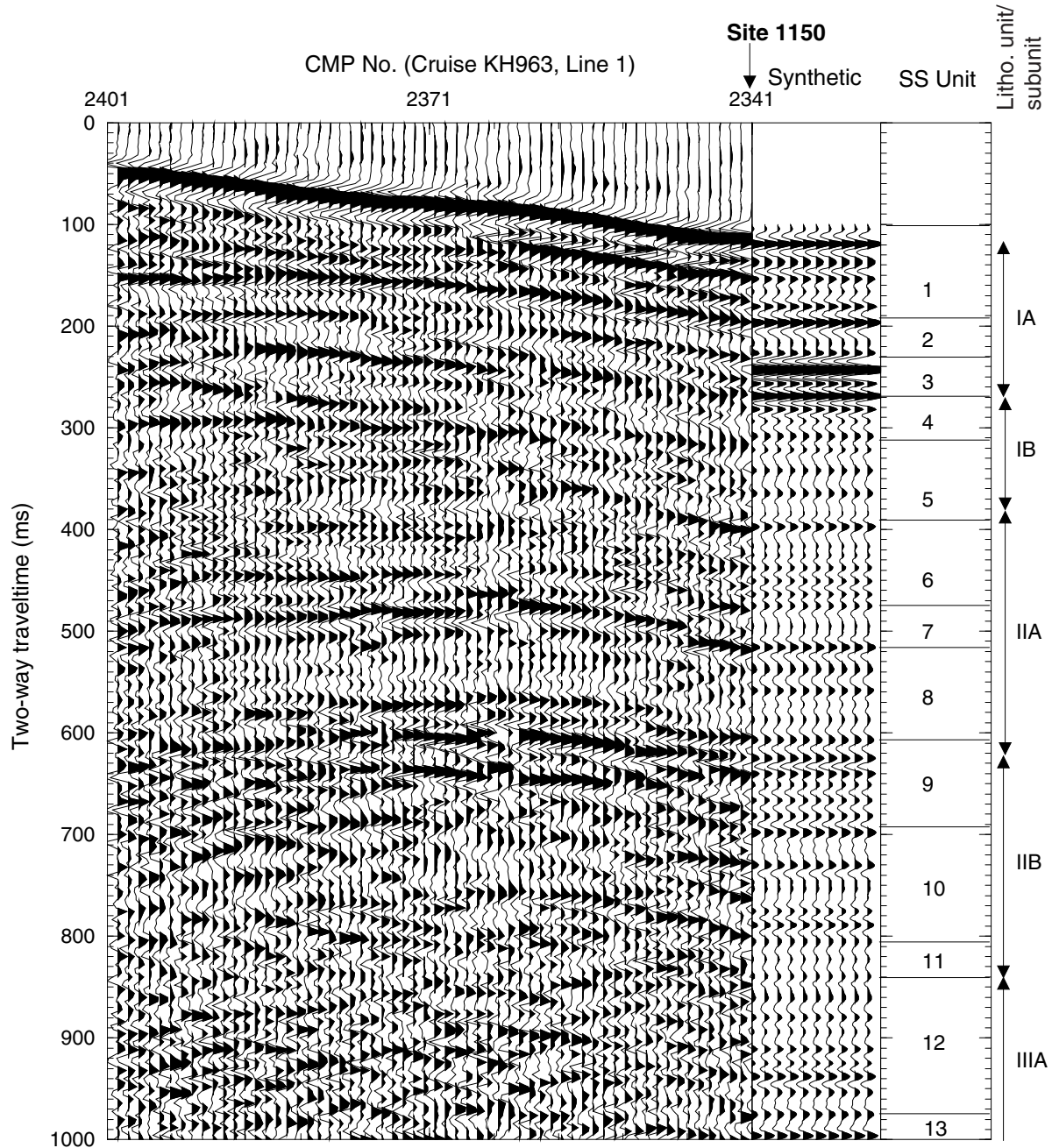


Figure F75 (continued).

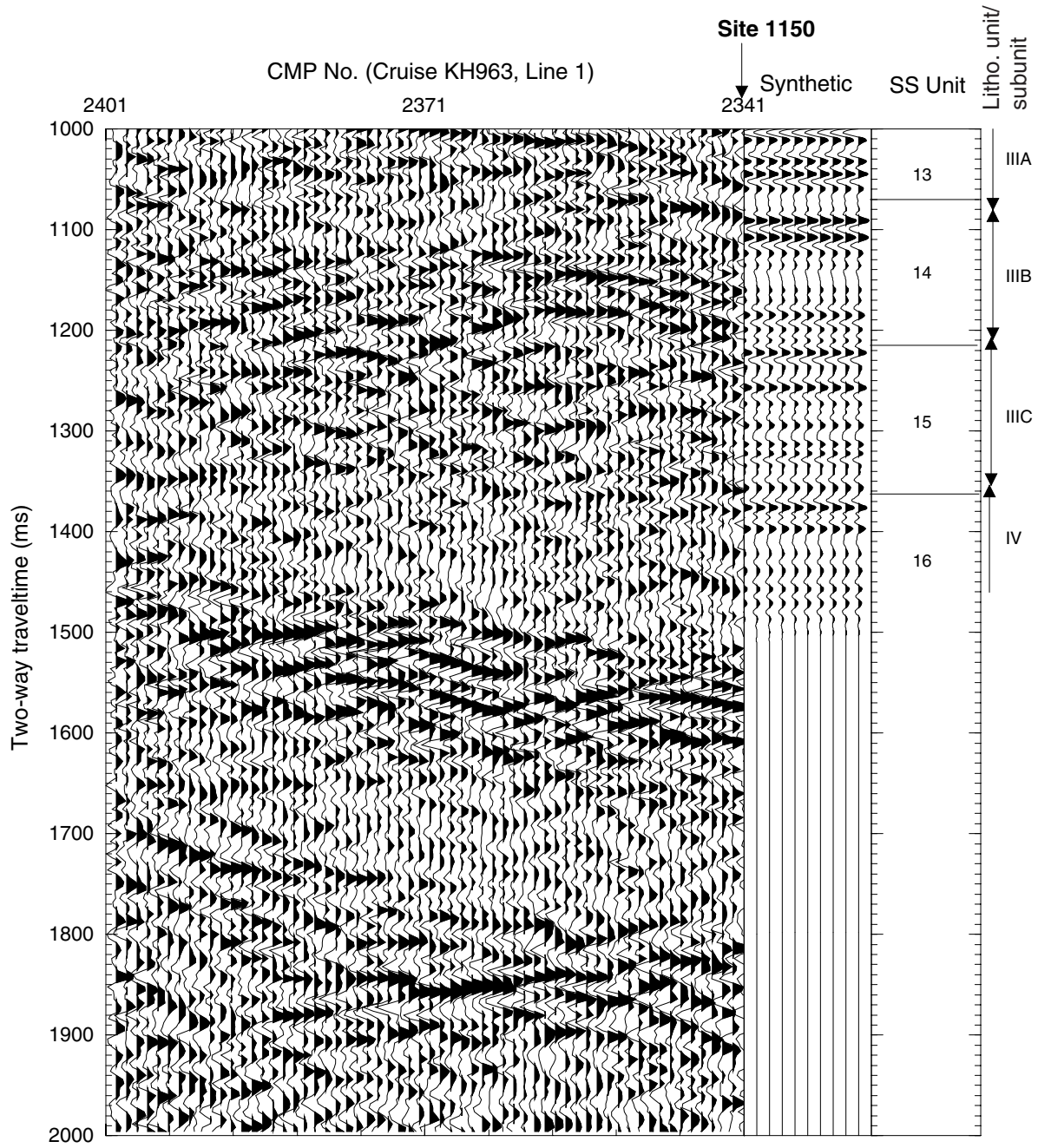


Figure F76. Seismic activity of the Japan Trench area off northeast Japan.

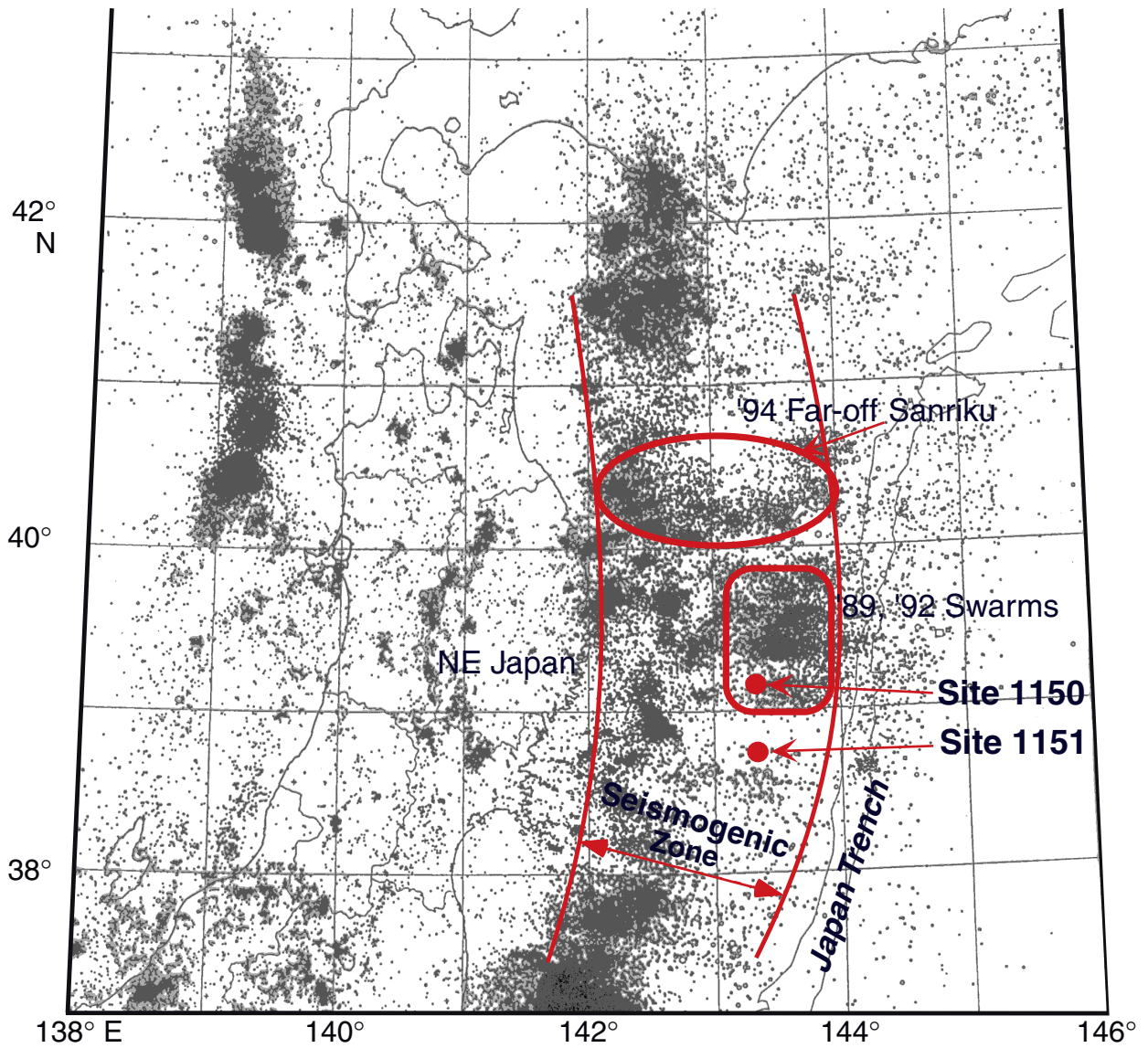


Figure F77. Logging data of bulk density and P -wave velocity. Shaded square shows the entire length of the sensor section.

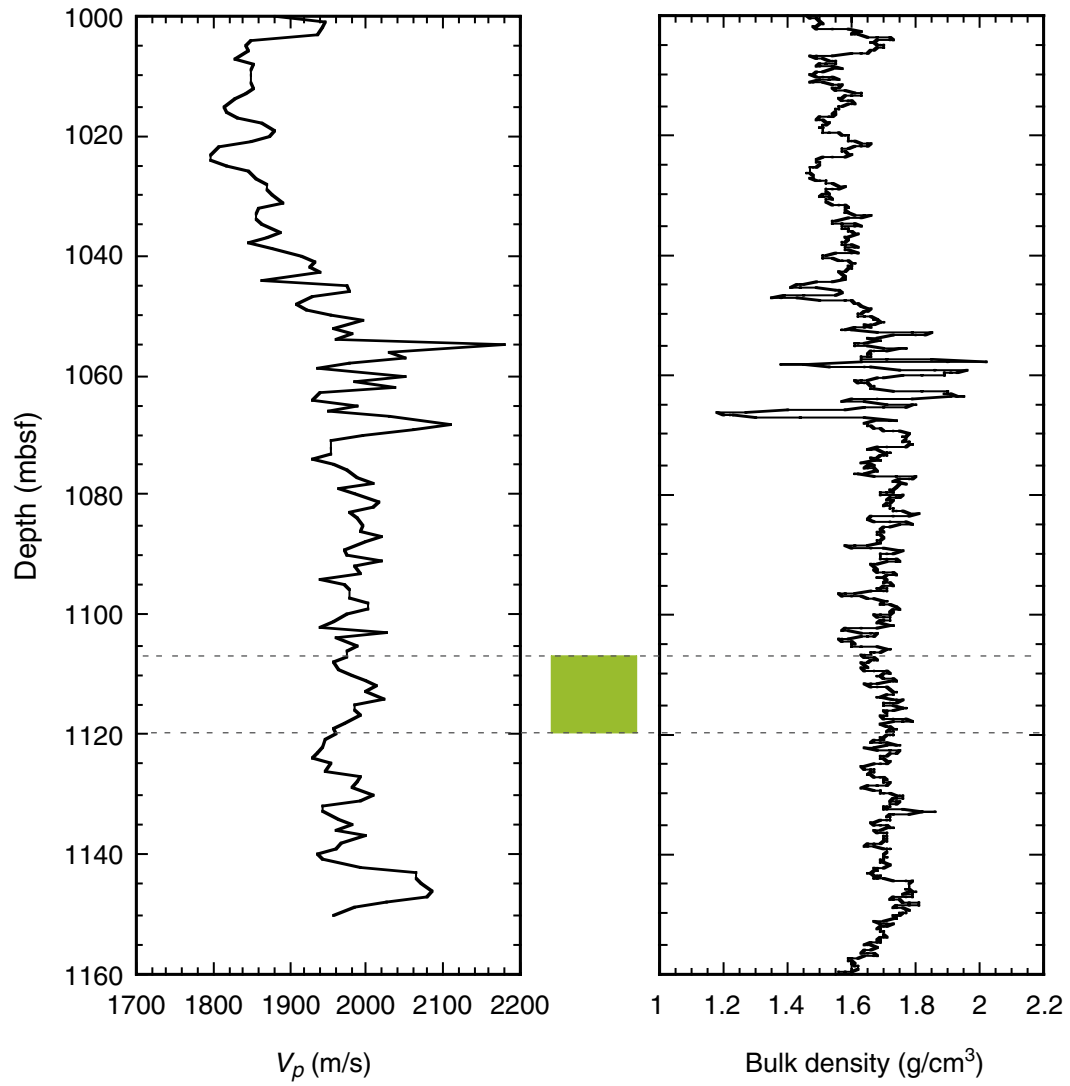


Figure F78. Cable link between the borehole and seafloor. Casing pipes with centralizers were used.

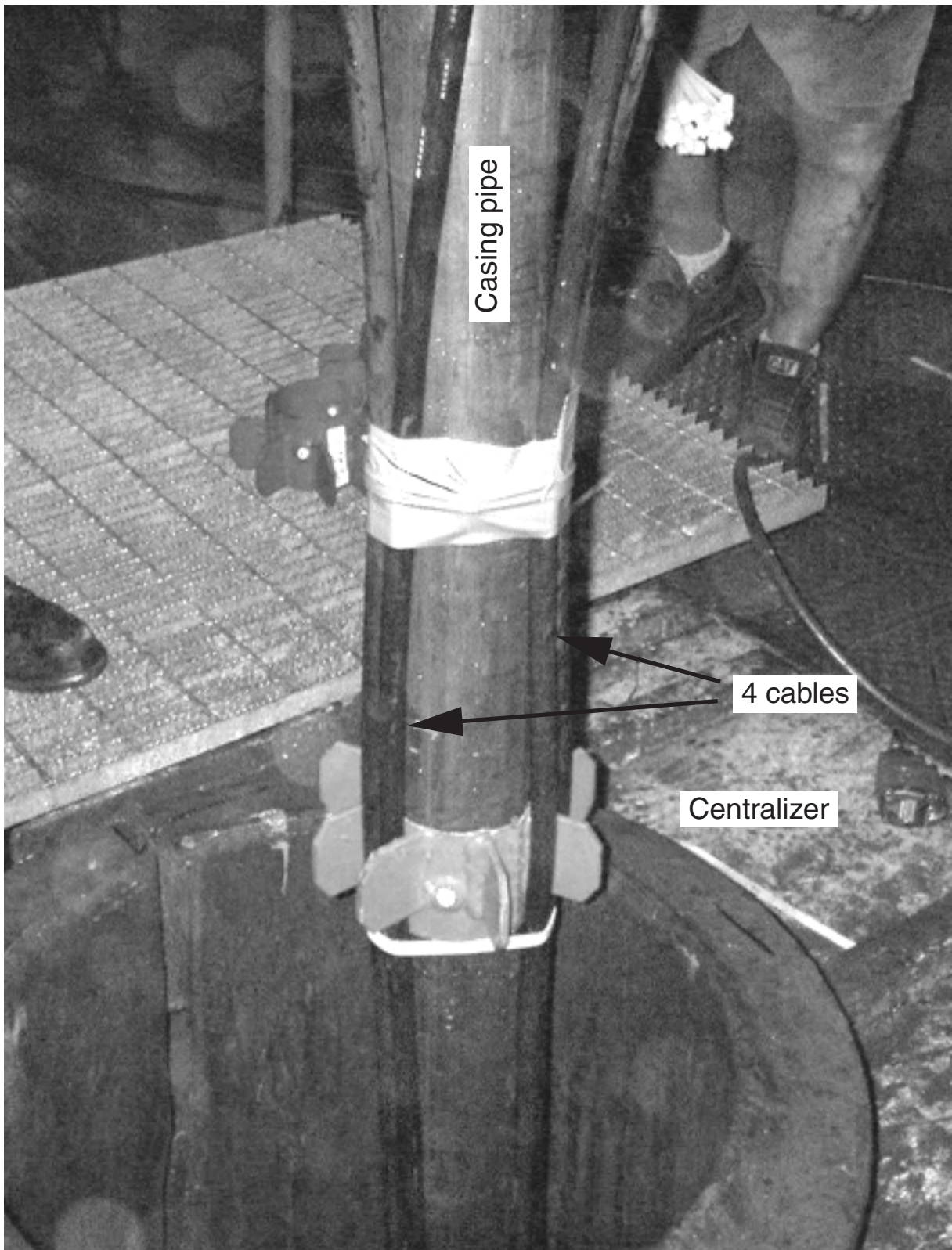


Figure F79. Battery frame bridal assembly. PAT = power access terminal.

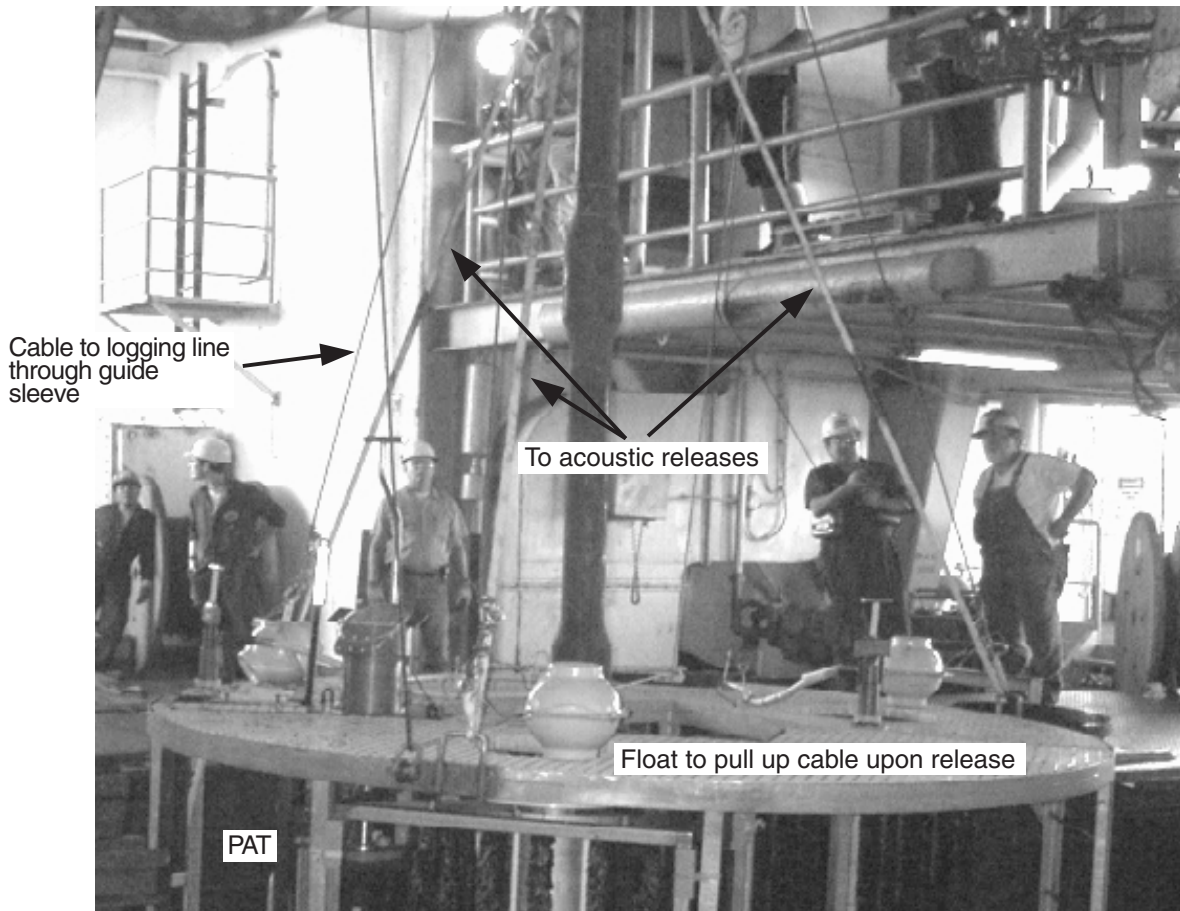


Guide sleeve

Acoustic releases



Acoustic releases



Cable to logging line
through guide
sleeve

To acoustic releases

Float to pull up cable upon release

PAT

Figure F80. The array of emplaced instruments from bottom to top in Hole 1150D consists of the three-component strainmeter, three-component broadband PMD seismometer, two-component tiltmeter, and three-component CMG broadband seismometer.



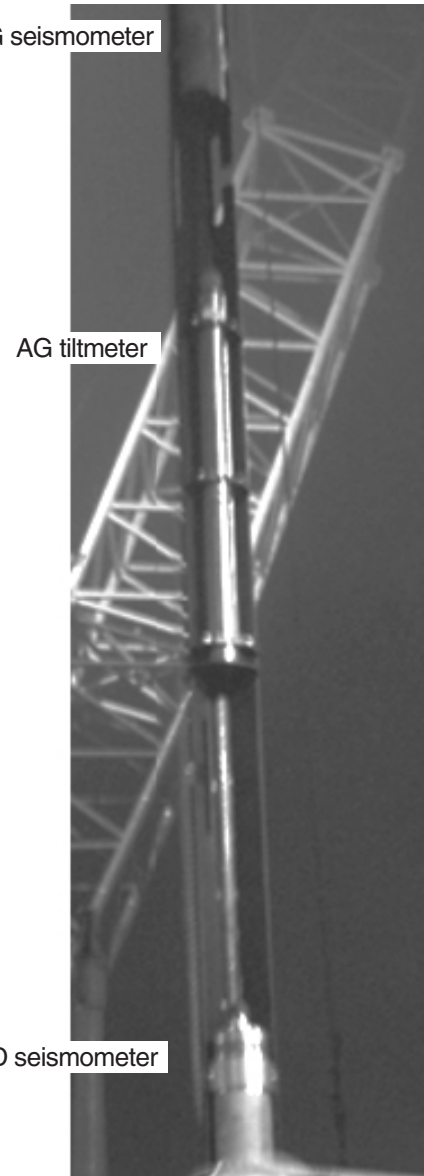
Figure F81. Stinger strainmeter coupling tube assembly.



Stinger-strainmeter assembly



Strainmeter-coupling tube assembly



Sensors on coupling tube

Figure F82. Power access terminal (PAT) and storage acquisition module (SAM). ROV = remotely operated vehicle; UMC = underwater mateable connector.

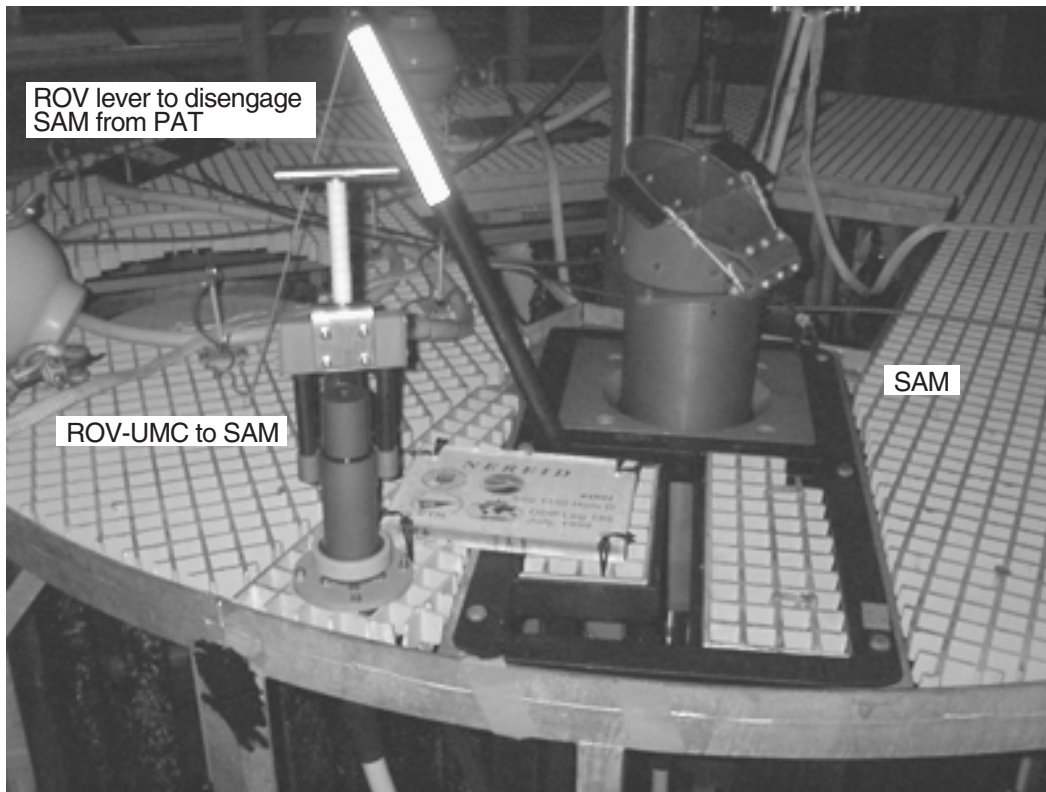


Figure F83. Diagram of location of existing fiber-optic cable linked to the coast, currently terminated near Hole 1150D. This cable may be extended to connect to the borehole observatory in future. ERI = Earthquake Research Institute of the University of Tokyo.

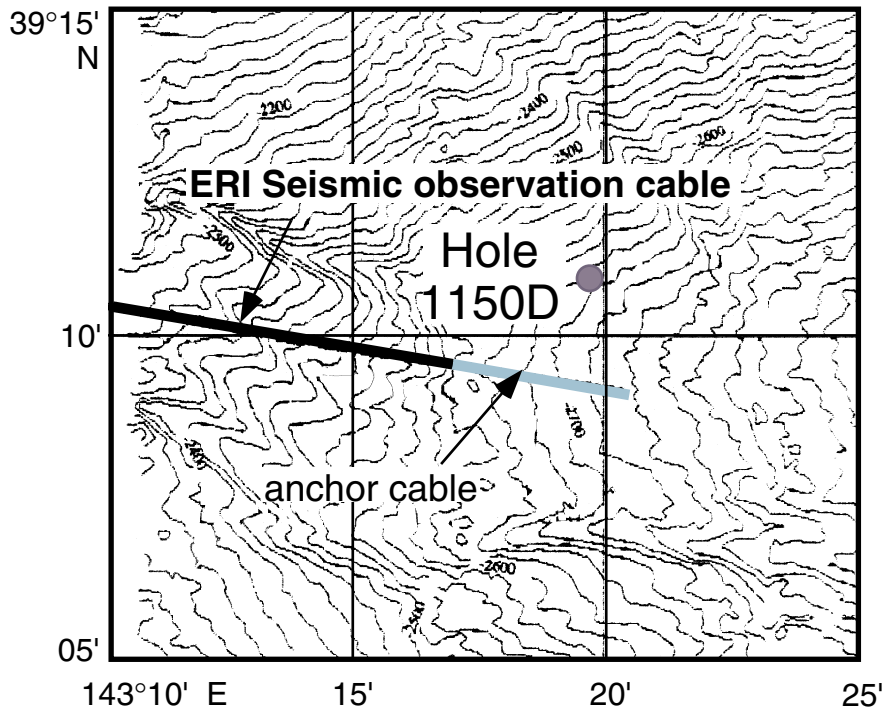


Figure F84. Photograph of a set of steep-dipping, parallel-anastomosing normal faults crosscutting and slightly displacing a moderate- to steep-dipping set of normal faults that formerly displaced an ~3-cm light gray carbonaceous layer (interval 186-1150B-16R-4, 6–26 cm).

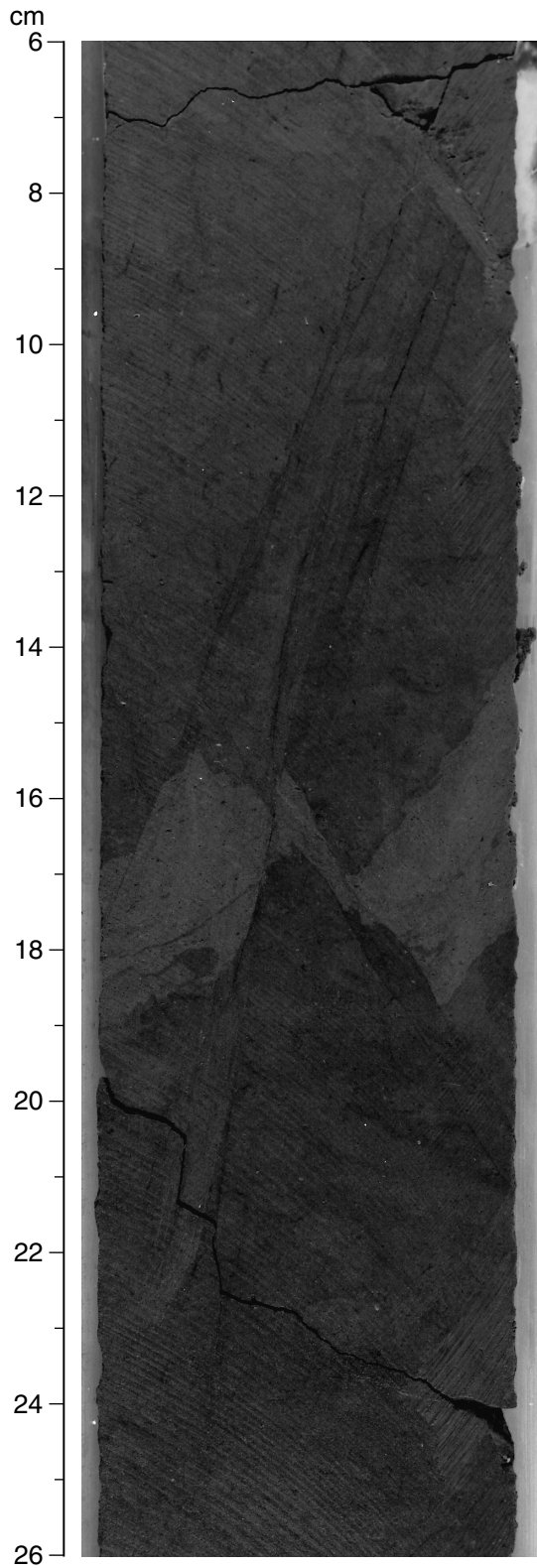


Figure F85. Photograph of thin normal faults (dipping steeply to the right) crosscutting and displacing an anastomosing parallel joint set (dipping steeply to the left) (interval 186-1150B-50R-3, 60–80 cm). Bioturbation gives displacement of minor normal fault in the upper part of the photograph. Abundant small and branching minor joints and faults are visible. At the bottom, an open fracture provides a view of fault surface with dark slickenside striae plunging in dip direction of the fault plane (interval 186-1150B-50R-1, 73–80 cm).

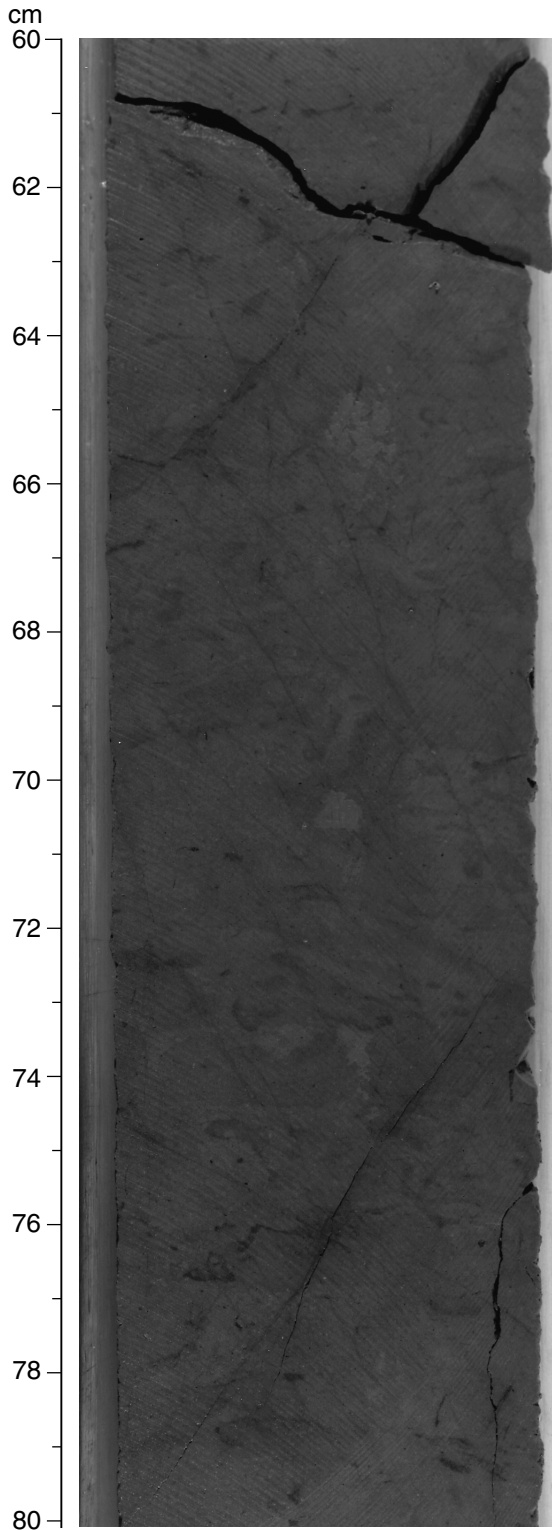


Figure F86. Photograph of a strongly anastomosing, closely spaced parallel joint set that formed under low strain and/or high water content (interval 186-1150B-28R-1, 10–22 cm).

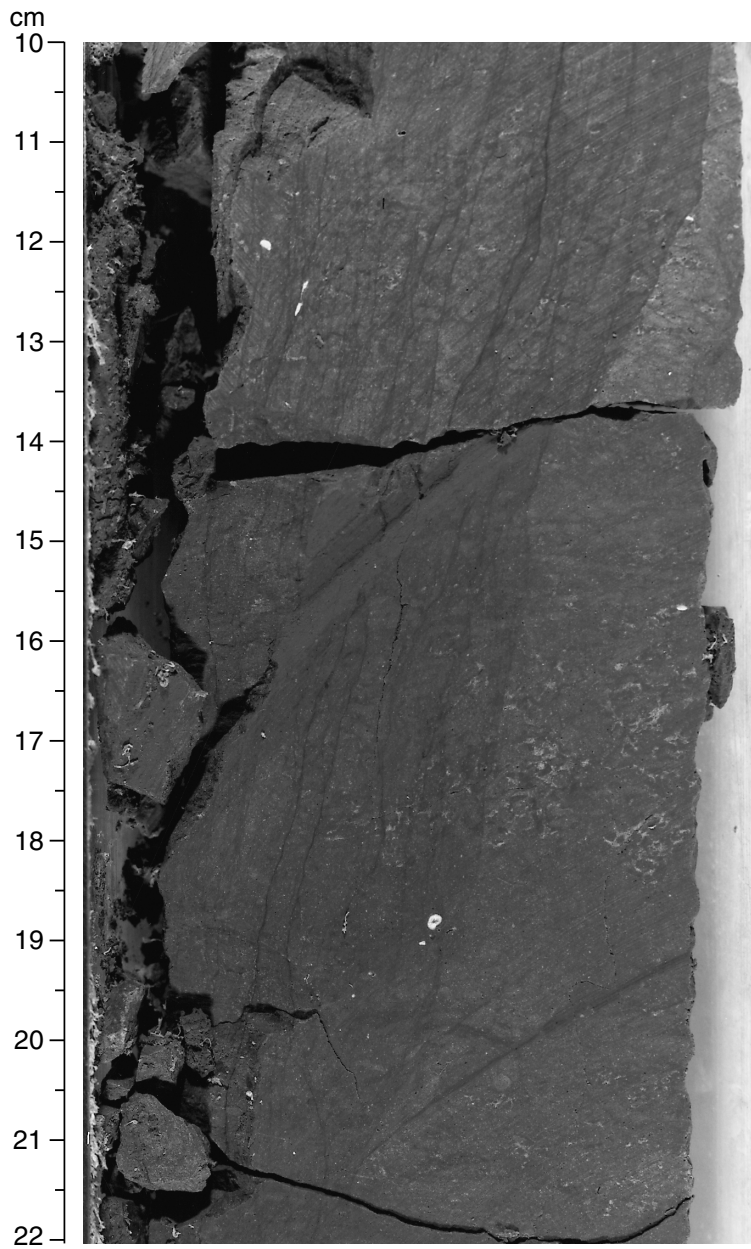


Figure F87. Depth-dependent comparison (A) between the number of open and healed fractures in Hole 1150B, (B) between the number of joints and faults in Hole 1150B, and (C) of healed fractures, sand/silt, and pebbles.

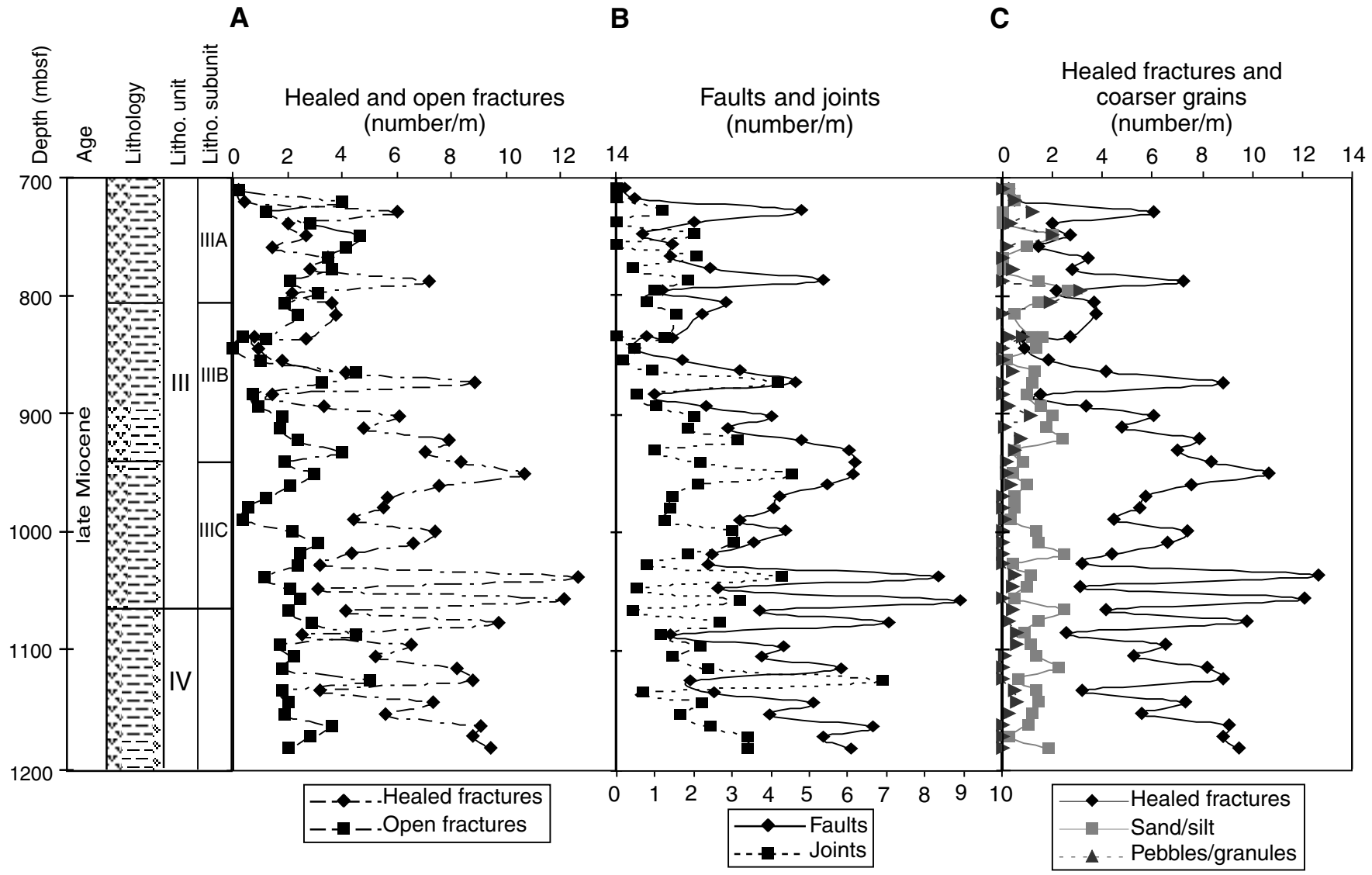


Figure F88. Declination, inclination (after 30 mT demagnetization), and core image of Section 186-1150B-30R-2. The core image shows the surface of the archive half with the dip directions of healed fractures.

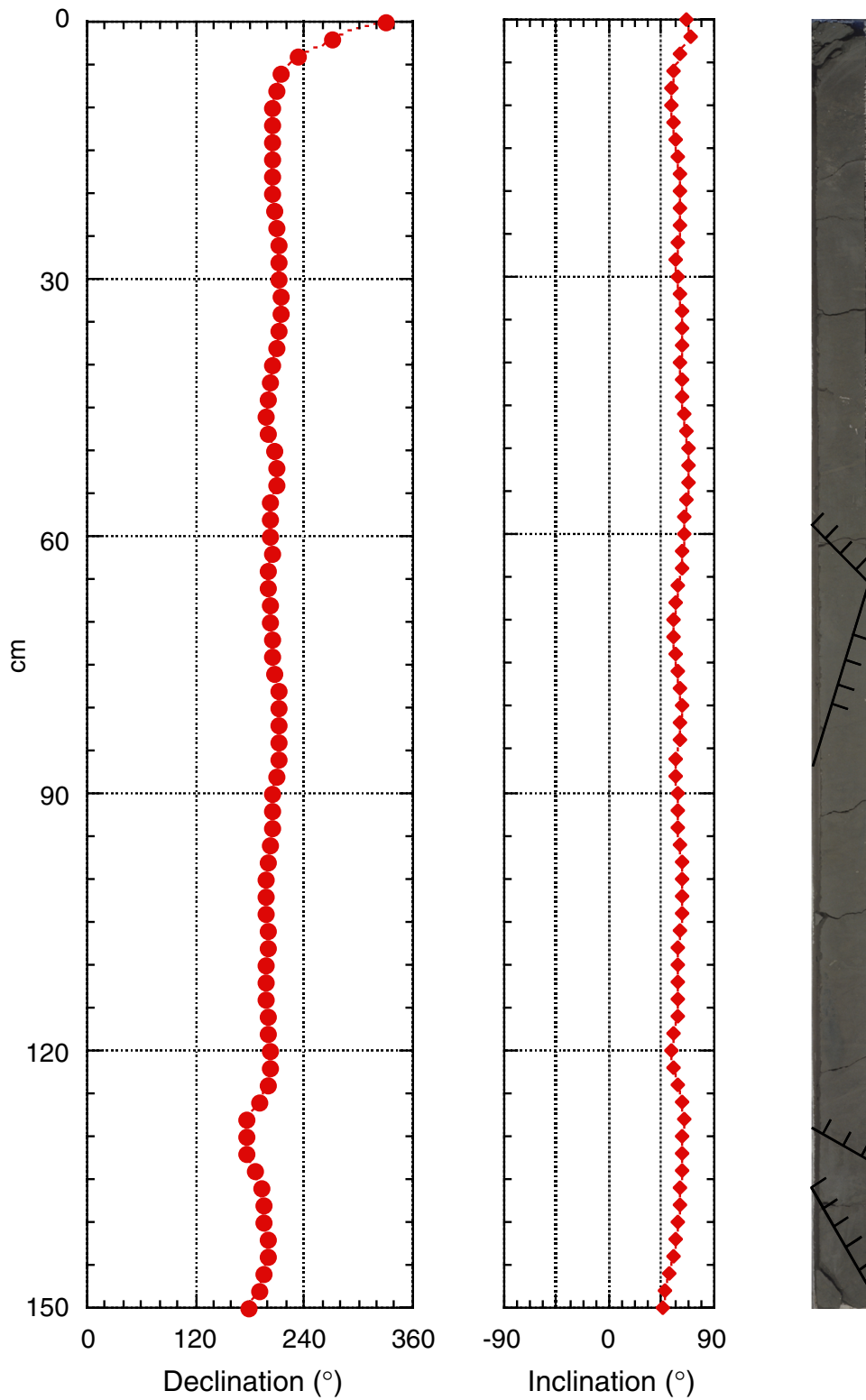


Figure F89. Stereoplot (lower hemisphere and equal-area projection) of planes of healed fractures reoriented using paleomagnetic declination in Cores 186-1150B-23R through 25R. **A.** ODP core reference coordinates. **B.** Geographic coordinates. Solid circles = poles to the planes of healed fractures; solid lines = the planes of healed fractures.

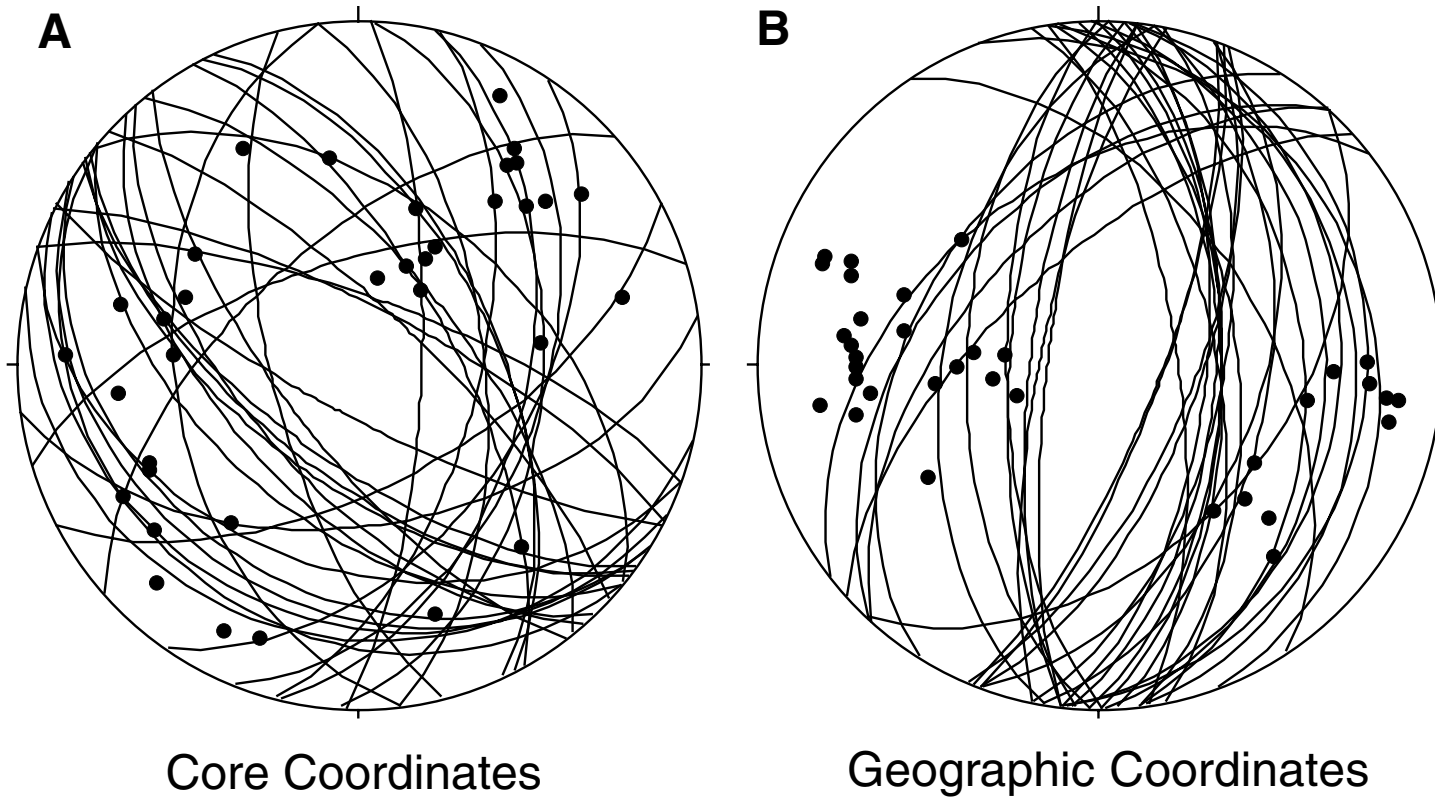


Figure F90. A. Frequency of measured healed fractures through Hole 1150B. B. Distribution of dip azimuth of healed fracture planes after reorientation. C. Distribution of dip angle of healed fracture planes after reorientation.

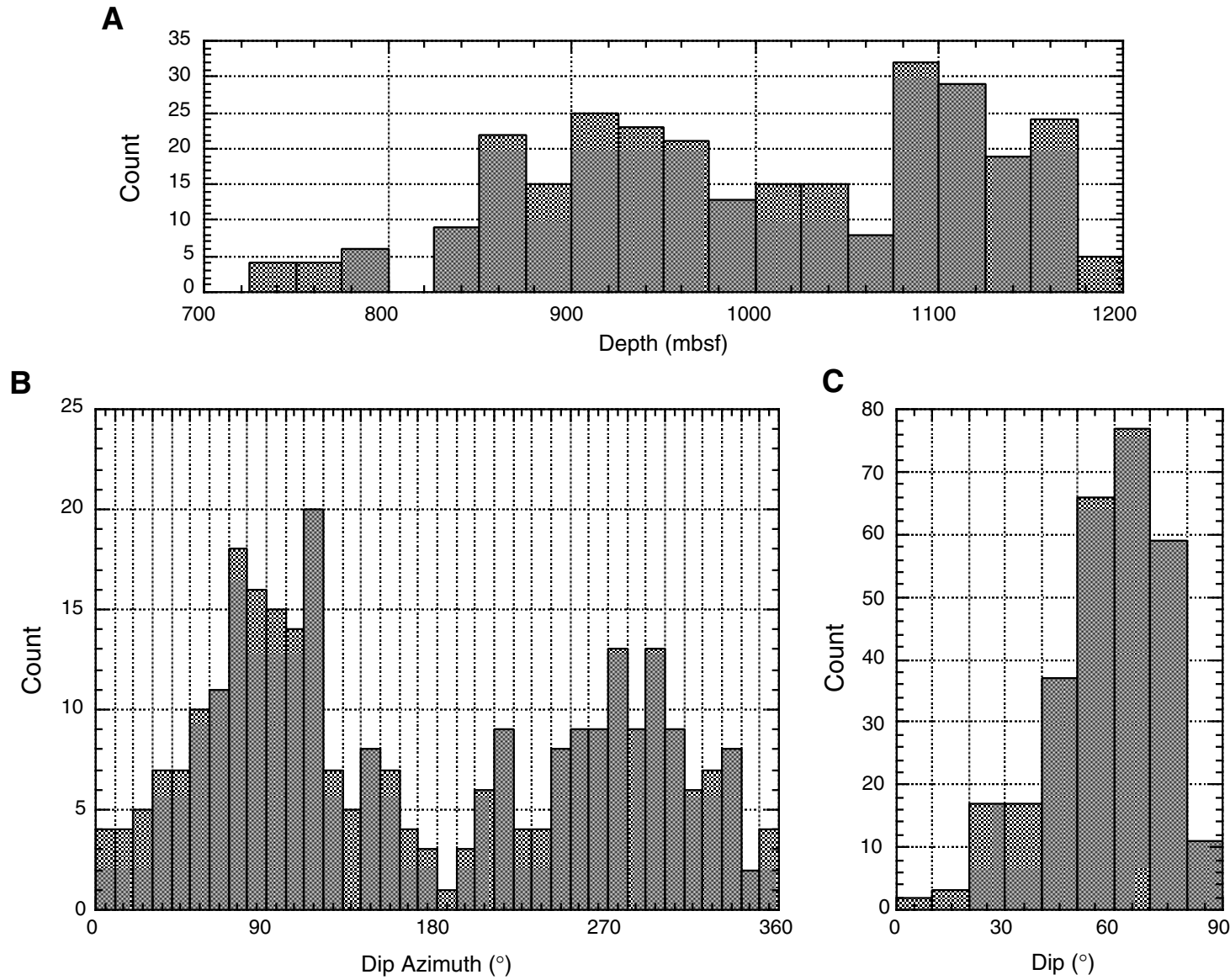


Figure F91. Downhole variation in dip azimuths of healed fracture planes in Hole 1150B, subdivided into domains.

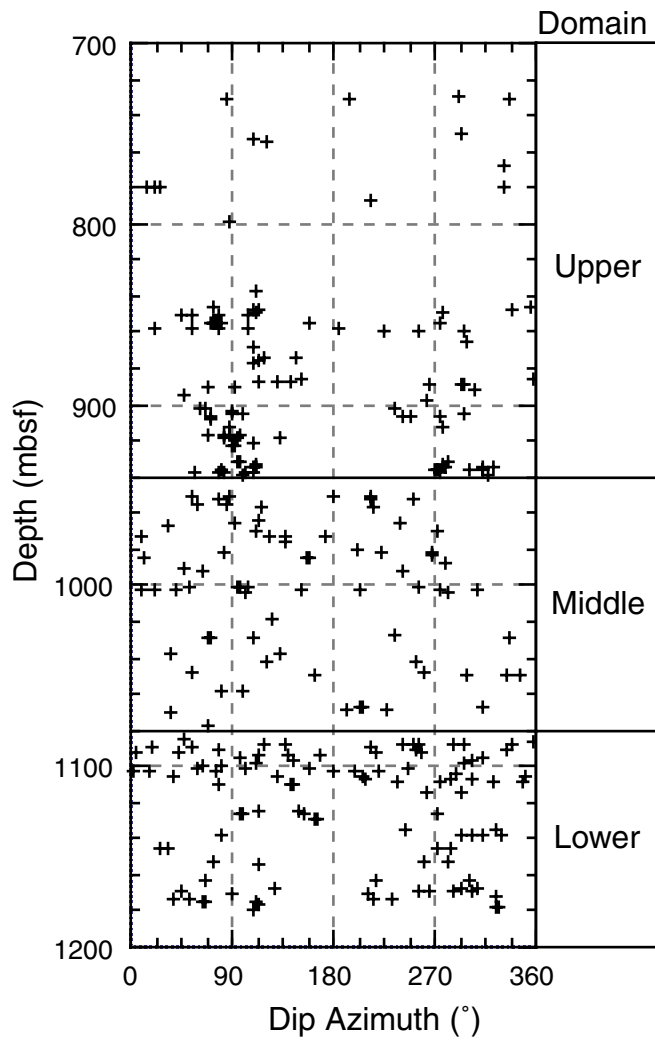


Figure F92. Contour diagram of poles of healed fracture planes in Hole 1150B, subdivided into domains. Contour intervals every 0.5 count, starting at 1.

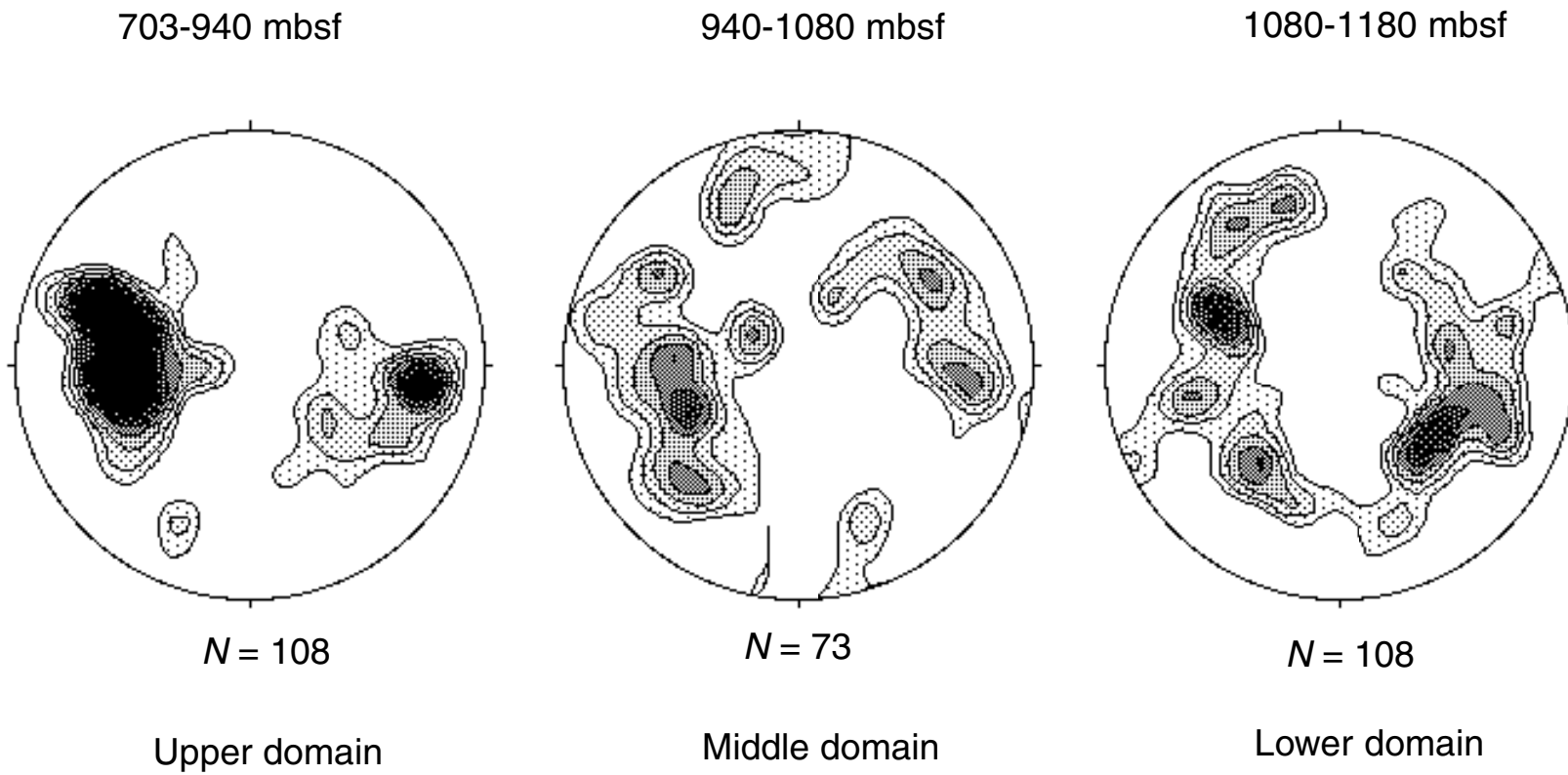


Figure F93. Contour diagram of poles of open fracture planes in Hole 1150B, subdivided into domains. Contour intervals every 0.5 count, starting at 1.

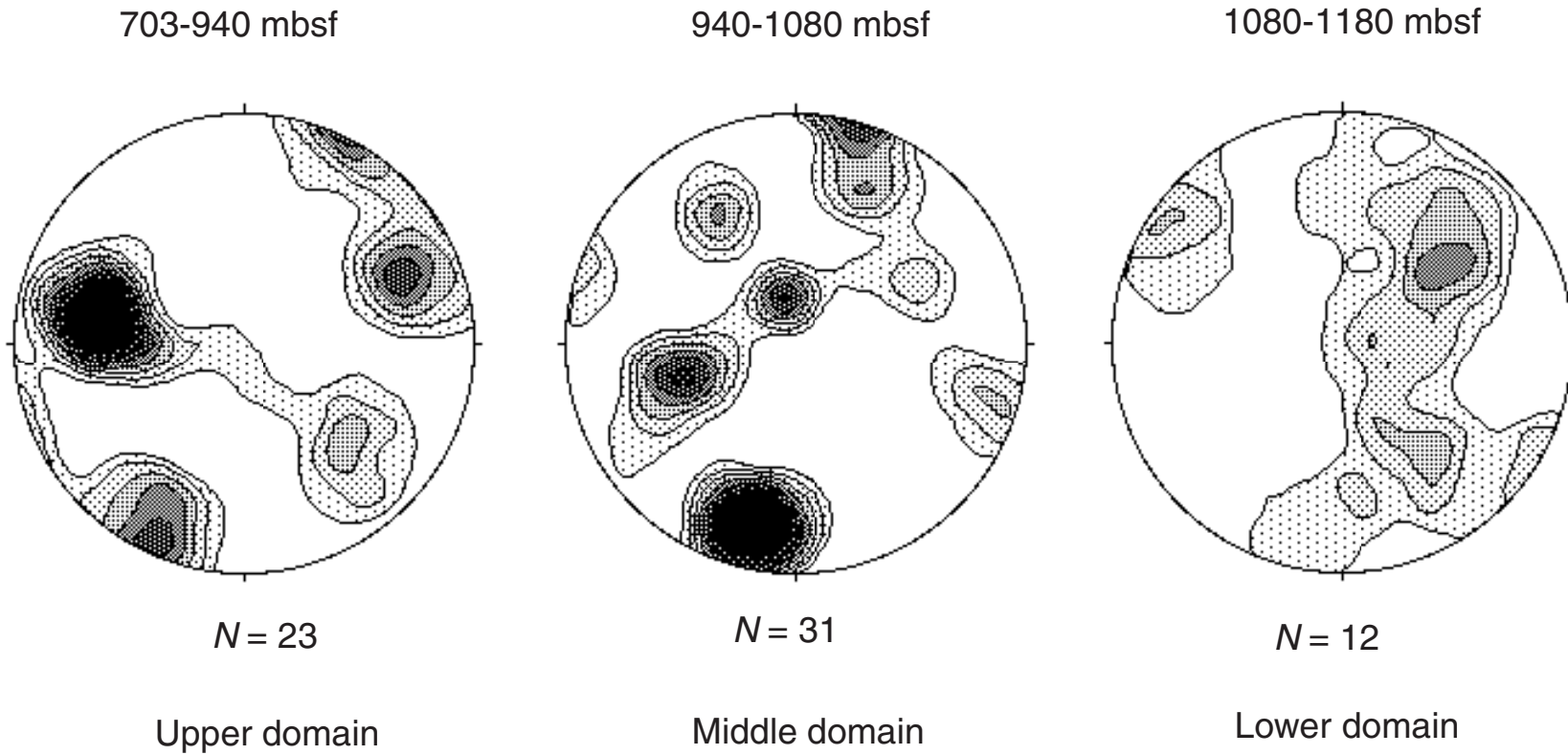


Figure F94. Bedding orientation from Hole 1150B. Solid circles = poles of bedding planes; solid square = mean pole of bedding plane; and thick line = mean bedding plane.

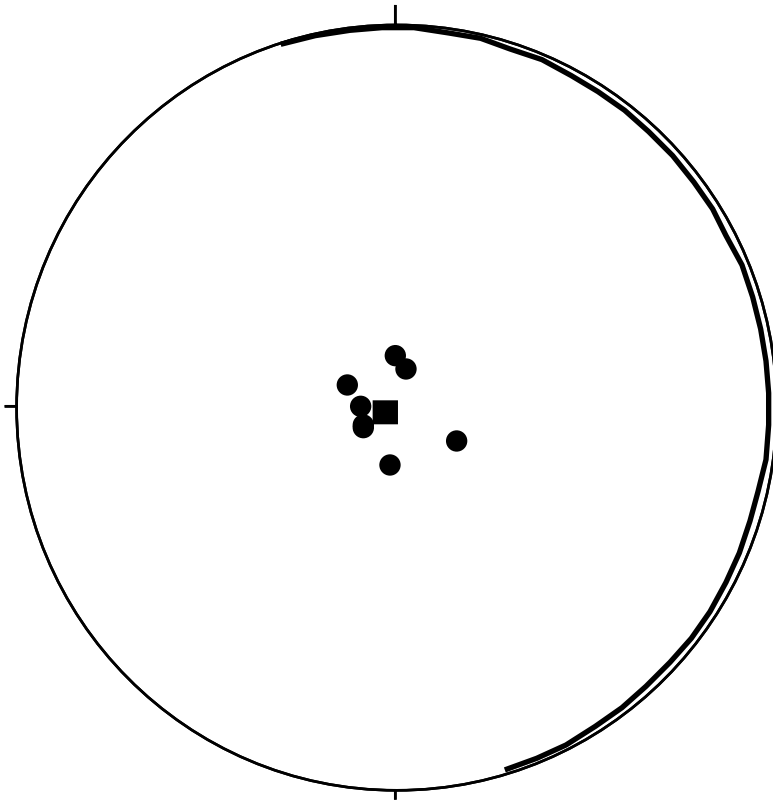


Table T1. Site 1150 coring summary. (See table notes. Continued on next two pages.)

Hole 1150A

Latitude: 39.1819117° (39°10.9147'N)
 Longitude: 143.331925° (143°19.9155'E)
 Time on hole: 99.75 hr (1830 hr, 22 June 1999–2215 hr, 26 June 1999)
 Time on site: 309.5 hr (1830 hr, 22 June 1999–1900 hr, 28 June 1999)
 Seafloor (drill-pipe measurement from rig floor, mbrf): 2692.2
 Distance between rig floor and sea level (m): 11.3
 Water depth (drill-pipe measurement from sea level, m): 2680.9
 Total depth (from rig floor, mbrf): 3414.8
 Total penetration (mbsf): 722.6
 Total length of cored section (m): 722.6
 Total core recovered (m): 566.4
 Core recovery (%): 78.4
 Total number of cores: 76
 Total number of drilled intervals: 0

Hole 1150B

Latitude: 39.1819077° (39°10.91446'N)
 Longitude: 143.3324432° (143°19.94659'E)
 Time on hole: 159.25 hr (2215 hr, June 1999–1330 hr, 3 July 1999)
 Seafloor (drill-pipe measurement from rig floor, mbrf): 2692.2
 Distance between rig floor and sea level (m): 11.4
 Water depth (drill-pipe measurement from sea level, m): 2680.8
 Total depth (from rig floor, mbrf): 3873.8
 Total penetration (mbsf): 1181.6
 Total length of cored section (m): 478.3
 Total length of drilled intervals (m): 703.3
 Total core recovered (m): 269.29
 Core recovery (%): 56.3
 Total number of cores: 50
 Total number of drilled intervals: 1

Hole 1150C

Latitude: 39.181953° (39°10.9172'N)
 Longitude: 143.33157° (143°19.8942'E)
 Time on Hole 1150C1: 207.0 hr (1330 hr, 3 July 1999–0430 hr, 12 July 99)
 Time on Hole 1150C2: 7.0 hr (1530 hr, 22 July 1999–2230 hr, 23 July 1999)
 Seafloor (drill-pipe measurement from rig floor, mbrf): 2692.2
 Distance between rig floor and sea level (m): 11.4
 Water depth (drill-pipe measurement from sea level, m): 2680.8
 Comments: Drilling, casing, and emplacement of downhole instrument. No coring.

Hole 1150D

Latitude: 39.1813383° (39°10.8803'N)
 Longitude: 143.33193° (143°19.9158'E)
 Time on Hole 1150D1: 161.0 hr (0430 hr, 12 July 1999–2130 hr, 18 July 1999)
 Time on Hole 1150D2: 30.5 hr (0700 hr, 22 July 1999–23 July 1999)
 Time on Hole 1150D3: 118.0 hr (2230 hr, 23 July 1999–1900 hr, 28 July 1999)
 Seafloor (drill-pipe measurement from rig floor, mbrf): 2692.2
 Distance between rig floor and sea level (m): 11.5
 Water depth (drill-pipe measurement from sea level, m): 2680.7
 Comments: Drilling, casing, and emplacement of downhole instrument. No coring.

Core	Date (1999)	Time (Local)	Depth (mbsf)		Length (m)		Recovery (%)	Comments
			Top	Bottom	Cored	Recovered		
186-1150A-								
1H	23 June	0550	0.0	7.7	7.7	7.73	100.4	
2H	23 June	0650	7.7	17.2	9.5	10.04	105.7	
3H	23 June	0750	17.2	26.7	9.5	10.30	108.4	Oriented; Adara
4H	23 June	0845	26.7	36.2	9.5	10.00	105.3	Oriented
5H	23 June	0930	36.2	45.7	9.5	10.18	107.2	Oriented
6H	23 June	1020	45.7	55.2	9.5	10.08	106.1	Oriented; Adara
7H	23 June	1105	55.2	64.7	9.5	10.15	106.8	Oriented
8H	23 June	1155	64.7	74.2	9.5	9.80	103.2	Oriented
9H	23 June	1235	74.2	83.7	9.5	10.38	109.3	Oriented; Adara
10H	23 June	1325	83.7	93.2	9.5	10.44	109.9	Oriented, but liner shattered
11H	23 June	1405	93.2	102.7	9.5	9.65	101.6	Oriented, but liner shattered
12H	23 June	1450	102.7	112.2	9.5	9.50	100.0	Oriented
13X	23 June	1555	112.2	116.4	4.2	5.22	124.3	
14X	23 June	1735	116.4	126.0	9.6	8.36	87.1	DVTP
15X	23 June	1820	126.0	135.6	9.6	4.23	44.1	

Table T1 (continued).

Core	Date (1999)	Time (Local)	Depth (mbsf)		Length (m)		Recovery (%)	Comments
			Top	Bottom	Cored	Recovered		
16X	23 June	1905	135.6	145.2	9.6	4.00	41.7	
17X	23 June	1955	145.2	154.8	9.6	9.38	97.7	
18X	23 June	2035	154.8	164.4	9.6	7.36	76.7	
19X	23 June	2215	164.4	174.0	9.6	0.00	0.0	DVTP; no recovery
20X	23 June	2255	174.0	183.6	9.6	0.01	0.1	
21X	23 June	2350	183.6	193.3	9.7	8.46	87.2	
22X	24 June	0025	193.3	202.9	9.6	9.69	100.9	
23X	24 June	0120	202.9	212.5	9.6	9.99	104.1	
24X	24 June	0205	212.5	222.2	9.7	0.77	7.9	
25X	24 June	0300	222.2	231.9	9.7	9.99	103.0	
26X	24 June	0345	231.9	241.5	9.6	7.70	80.2	
27X	24 June	0435	241.5	251.2	9.7	9.71	100.1	
28X	24 June	0525	251.2	260.8	9.6	9.18	95.6	
29X	24 June	0615	260.8	270.4	9.6	8.59	89.5	
30X	24 June	0705	270.4	280.1	9.7	9.76	100.6	
31X	24 June	0755	280.1	289.7	9.6	9.75	101.6	
32X	24 June	0840	289.7	299.4	9.7	9.18	94.6	
33X	24 June	0930	299.4	309.1	9.7	6.22	64.1	
34X	24 June	1025	309.1	318.7	9.6	9.89	103.0	
35X	24 June	1115	318.7	328.4	9.7	10.20	105.2	
36X	24 June	1210	328.4	338.0	9.6	10.09	105.1	
37X	24 June	1300	338.0	347.6	9.6	9.42	98.1	
38X	24 June	1345	347.6	357.2	9.6	9.84	102.5	
39X	24 June	1430	357.2	366.8	9.6	9.83	102.4	
40X	24 June	1520	366.8	376.4	9.6	9.66	100.6	
41X	24 June	1610	376.4	386.0	9.6	2.26	23.5	
42X	24 June	1710	386.0	395.6	9.6	9.67	100.7	
43X	24 June	1805	395.6	405.2	9.6	9.73	101.4	
44X	24 June	1850	405.2	414.8	9.6	9.32	97.1	
45X	24 June	1935	414.8	424.4	9.6	9.56	99.6	
46X	24 June	2025	424.4	434.1	9.7	4.46	46.0	
47X	24 June	2130	434.1	443.7	9.6	9.61	100.1	
48X	24 June	2235	443.7	453.3	9.6	9.68	100.8	
49X	24 June	2345	453.3	462.9	9.6	9.89	103.0	
50X	25 June	0105	462.9	472.6	9.7	0.14	1.4	
51X	25 June	0210	472.6	482.3	9.7	8.03	82.8	
52X	25 June	0310	482.3	492.0	9.7	0.25	2.6	
53X	25 June	0430	492.0	501.7	9.7	0.30	3.1	
54X	25 June	0535	501.7	511.3	9.6	9.79	102.0	
55X	25 June	0640	511.3	520.9	9.6	9.55	99.5	
56X	25 June	0745	520.9	530.6	9.7	6.64	68.5	
57X	25 June	0840	530.6	540.3	9.7	1.12	11.6	
58X	25 June	0945	540.3	549.9	9.6	0.25	2.6	
59X	25 June	1050	549.9	559.5	9.6	0.00	0.0	
60X	25 June	1210	559.5	569.1	9.6	4.27	44.5	
61X	25 June	1310	569.1	578.7	9.6	2.53	26.4	
62X	25 June	1420	578.7	588.4	9.7	9.82	101.2	
63X	25 June	1555	588.4	598.0	9.6	1.54	16.0	
64X	25 June	1725	598.0	607.7	9.7	3.38	34.9	
65X	25 June	1850	607.7	617.3	9.6	2.29	23.9	
66X	25 June	2015	617.3	626.9	9.6	9.80	102.1	
67X	25 June	2150	626.9	636.5	9.6	9.88	102.92	
68X	25 June	2310	636.5	645.8	9.3	9.21	99.0	
69X	26 June	0050	645.8	655.4	9.6	9.74	101.5	
70X	26 June	0225	655.4	664.8	9.4	7.81	83.1	
71X	26 June	0355	664.8	674.4	9.6	9.71	101.2	
72X	26 June	0530	674.4	684.0	9.6	9.88	102.9	
73X	26 June	0650	684.0	693.7	9.7	2.60	26.8	
74X	26 June	0815	693.7	703.3	9.6	9.19	95.7	
75X	26 June	0945	703.3	713.0	9.7	9.87	101.8	
76X	26 June	1130	713.0	722.6	9.6	9.90	103.1	
Totals:					722.6	566.40	78.4	
186-1150B-								
*****Drilled from 0 to 703.3 mbsf*****								
1R	28 June	0420	703.3	709.7	6.4	4.91	76.7	
2R	28 June	0535	709.7	719.3	9.6	2.26	23.5	
3R	28 June	0655	719.3	729.0	9.7	0.83	8.6	
4R	28 June	0810	729.0	738.6	9.6	3.50	36.5	
5R	28 June	0925	738.6	748.3	9.7	1.49	15.4	
6R	28 June	1040	748.3	757.9	9.6	8.26	86.0	

Table T1 (continued).

Core	Date (1999)	Time (Local)	Depth (mbsf)		Length (m)		Recovery (%)	Comments
			Top	Bottom	Cored	Recovered		
7R	28 June	1150	757.9	767.6	9.7	1.45	15.0	
8R	28 June	1300	767.6	777.2	9.6	2.48	25.8	
9R	28 June	1415	777.2	786.9	9.7	4.30	44.3	
10R	28 June	1525	786.9	796.5	9.6	4.14	43.1	
11R	28 June	1640	796.5	806.1	9.6	6.35	66.2	
12R	28 June	1805	806.1	815.7	9.6	5.86	61.0	
13R	28 June	1915	815.7	825.4	9.7	4.11	42.4	
14R	28 June	2040	825.4	835.0	9.6	5.11	53.2	
15R	28 June	2155	835.0	844.6	9.6	2.20	22.9	
16R	28 June	2320	844.6	854.2	9.6	7.65	79.7	
17R	29 June	0050	854.2	863.8	9.6	5.36	55.8	
18R	29 June	0220	863.8	873.5	9.7	4.31	44.4	
19R	29 June	0340	873.5	883.2	9.7	4.05	41.8	
20R	29 June	0505	883.2	892.9	9.7	9.84	101.4	
21R	29 June	0625	892.9	902.1	9.2	5.44	59.1	
22R	29 June	0745	902.1	911.8	9.7	8.59	88.6	
23R	29 June	0855	911.8	921.5	9.7	7.96	82.1	
24R	29 June	1010	921.5	931.1	9.6	1.99	20.7	
25R	29 June	1135	931.1	940.7	9.6	7.98	83.1	
26R	29 June	1250	940.7	950.3	9.6	7.31	76.2	
27R	29 June	1410	950.3	959.9	9.6	7.03	74.3	
28R	29 June	1525	959.9	969.5	9.6	8.96	93.3	
29R	29 June	1650	969.5	979.1	9.6	8.56	89.2	
30R	29 June	1820	979.1	988.7	9.6	8.78	91.5	
31R	29 June	1940	988.7	998.3	9.6	3.66	38.1	
32R	29 June	2050	998.3	1007.9	9.6	9.55	99.5	
33R	29 June	2200	1007.9	1017.5	9.6	1.60	16.7	
34R	29 June	2320	1017.5	1027.1	9.6	2.52	26.3	
35R	30 June	0040	1027.1	1036.7	9.6	4.43	46.2	
36R	30 June	0200	1036.7	1046.5	9.8	8.06	82.2	
37R	30 June	0325	1046.5	1056.3	9.8	4.04	41.2	
38R	30 June	0450	1056.3	1066.0	9.7	2.42	25.0	
39R	30 June	0620	1066.0	1075.7	9.7	4.82	49.7	
40R	30 June	0805	1075.7	1085.3	9.6	3.53	36.8	
41R	30 June	0930	1085.3	1094.9	9.6	9.19	95.7	
42R	30 June	1110	1094.9	1104.6	9.7	8.99	92.7	
43R	30 June	1245	1104.6	1114.2	9.6	6.71	69.9	
44R	30 June	1420	1114.2	1123.9	9.7	1.59	16.4	
45R	30 June	1605	1123.9	1133.5	9.6	5.98	62.3	
46R	30 June	1740	1133.5	1143.1	9.6	5.47	57.0	
47R	30 June	1930	1143.1	1152.8	9.7	4.30	44.3	
48R	30 June	2110	1152.8	1162.4	9.6	4.96	51.7	
49R	30 June	2255	1162.4	1172.0	9.6	8.19	85.3	
50R	01 July	0035	1172.0	1181.6	9.6	8.25	85.9	
Coring totals:					478.3	269.29	56.3	
Drilled total:					703.3			
Total:					1181.6			

Notes: Adara = Adara temperature tool, DVTP = Davis-Villinger temperature probe. This table is also available in [ASCII format](#).

Table T2. X-ray diffraction data, Site 1150.

Leg	Site	Hole	Core	Type	Section	Interval (cm)		Depth top (mbsf)	Janus code	Intensity (cps)							14-Å minerals			
						Top	Bottom			Quartz (100)	Quartz (101)	Feldspar	Hornblende (310)	Clinopyroxene	Calcite (104)	Dolomite (104)	Halite (200)	Peak intensity (cps)	Area intensity (cps)	Relative (%)
186	1150	A	1	H	1	59	61	0.59	1328169	113	544	180	22	28	181	13	306	30	2390	33
186	1150	A	1	H	5	60	62	6.60	1328173	154	1001	342		54	274	19	168	33	2786	32
186	1150	A	2	H	1	60	61	8.30	1328213	171	1014	496		67	249	20	223	33	2283	23
186	1150	A	2	H	4	60	61	12.80	1328214	208	741	347	51	48	163	19	254	29	2440	28
186	1150	A	3	H	1	60	61	17.80	1328247	187	1004	346		54	281	25	273	40	2624	30
186	1150	A	3	H	4	60	62	22.30	1328250	223	1162	393		71	103	21	189	33	2539	26
186	1150	A	4	H	1	60	61	27.30	1328320	232	1163	557	66	74	42		208	31	2148	27
186	1150	A	4	H	4	60	62	31.80	1328323	201	1122	351		67	102	21	199	32	2307	29
186	1150	A	5	H	1	94	95	37.14	1328326	144	825	288		57	177	23	205	20	1942	30
186	1150	A	5	H	3	96	97	40.16	1328328	211	1111	473		59	181	19	190	32	2397	23

Leg	Site	Hole	Core	Type	Section	Interval (cm)		Depth top (mbsf)	Janus code	10-Å minerals			7-Å minerals			Opal-A hump (cps)	Opal-CT area (cps)	CT/A ratio
						Top	Bottom			Peak intensity (cps)	Area intensity (cps)	Relative (%)	Peak intensity (cps)	Area intensity (cps)	Relative (%)			
186	1150	A	1	H	1	59	61	0.59	1328169	20	734	41	31	913	26	132	3187	24.06
186	1150	A	1	H	5	60	62	6.60	1328173	40	999	46	43	969	22	92	2037	22.12
186	1150	A	2	H	1	60	61	8.30	1328213	40	1422	57	46	996	20	90	2072	22.92
186	1150	A	2	H	4	60	61	12.80	1328214	42	1103	51	46	906	21	146	3362	22.99
186	1150	A	3	H	1	60	61	17.80	1328247	55	1017	46	45	1047	24	112	2292	20.43
186	1150	A	3	H	4	60	62	22.30	1328250	45	1126	47	59	1274	27	99	1733	17.44
186	1150	A	4	H	1	60	61	27.30	1328320	42	964	49	50	964	24	102	2150	21.04
186	1150	A	4	H	4	60	62	31.80	1328323	33	907	46	40	947	24	109	1677	15.35
186	1150	A	5	H	1	94	95	37.14	1328326	33	764	48	33	700	22	127	2803	22
186	1150	A	5	H	3	96	97	40.16	1328328	46	1353	53	53	1216	24	106	2297	21.66

Notes: CC = core catcher, PP = physical properties. Only a portion of this table appears here. The entire table is available in [ASCII format](#).

Table T3. Number of primary, reworked, and bioturbated ash layers, Site 1150. (See table notes. Continued on next page.)

Leg	Site	Hole	Type	Core	Depth (mbsf)	Recovered length (m)	Primary and reworked ash		Bioturbated ash patches	
							(Layers/core)	(Layers/m)	(Layers/core)	(Layers/m)
186	1150	A	H	1	0.00	7.73	2	0.3	0	0
186	1150	A	H	2	7.70	10.04	1	0.1	1	0.1
186	1150	A	H	3	17.20	10.30	0	0	0	0
186	1150	A	H	4	26.70	10.00	5	0.5	2	0.2
186	1150	A	H	5	36.20	10.18	0	0	3	0.3
186	1150	A	H	6	45.70	10.08	2	0.2	3	0.3
186	1150	A	H	7	55.20	10.15	10	1.0	4	0.4
186	1150	A	H	8	64.70	9.80	6	0.6	9	0.9
186	1150	A	H	9	74.20	10.38	6	0.6	0	0.0
186	1150	A	H	10	83.70	10.44	3	0.3	7	0.7
186	1150	A	H	11	93.20	9.65	4	0.4	6	0.6
186	1150	A	H	12	102.70	9.50	9	0.9	2	0.2
186	1150	A	H	13	112.20	5.22	0	0	3	0.6
186	1150	A	X	14	116.40	8.36	0	0	1	0.1
186	1150	A	X	15	126.00	4.23	1	0.2	3	0.7
186	1150	A	X	16	135.60	4.00	1	0.3	3	0.8
186	1150	A	X	17	145.20	9.38	3	0.3	11	1.2
186	1150	A	X	18	154.80	7.36	3	0.4	2	0.3
186	1150	A	X	19	164.40	0.00				
186	1150	A	X	20	174.00	0.01				
186	1150	A	X	21	183.60	8.46	1	0.1	4	0.5
186	1150	A	X	22	193.30	9.96	6	0.6	2	0.2
186	1150	A	X	23	202.90	9.99	1	0.1	0	0
186	1150	A	X	24	212.50	0.77	0	0	0	0
186	1150	A	X	25	222.20	9.99	1	0.1	0	0
186	1150	A	X	26	231.90	7.70	0	0	0	0
186	1150	A	X	27	241.50	9.71	1	0.1	1	0.1
186	1150	A	X	28	251.20	9.18	0	0	0	0
186	1150	A	X	29	260.80	8.59	0	0	1	0.1
186	1150	A	X	30	270.40	9.76	0	0	0	0
186	1150	A	X	31	280.10	9.75	0	0	0	0
186	1150	A	X	32	289.70	9.18	1	0.1	4	0.4
186	1150	A	X	33	299.40	6.22	0	0	0	0
186	1150	A	X	34	309.10	9.89	1	0.1	0	0
186	1150	A	X	35	318.70	10.20	2	0.2	0	0
186	1150	A	X	36	328.40	10.09	0	0	0	0
186	1150	A	X	37	338.00	9.42	1	0.1	1	0.1
186	1150	A	X	38	347.60	9.84	1	0.1	1	0.1
186	1150	A	X	39	357.20	9.83	1	0.1	0	0
186	1150	A	X	40	366.80	9.66	1	0.1	0	0
186	1150	A	X	41	376.40	2.26	1	0.4	0	0
186	1150	A	X	42	386.00	9.67	2	0.2	0	0
186	1150	A	X	43	395.60	9.73	0	0	0	0
186	1150	A	X	44	405.20	9.32	0	0	0	0
186	1150	A	X	45	414.80	9.56	0	0	0	0
186	1150	A	X	46	424.40	4.46	0	0	0	0
186	1150	A	X	47	434.10	9.61	0	0	1	0.1
186	1150	A	X	48	443.70	9.68	0	0	1	0.1
186	1150	A	X	49	453.30	9.89	3	0.3	1	0.1
186	1150	A	X	50	462.90	0.14	0	0	0	0
186	1150	A	X	51	472.60	8.03	0	0	0	0
186	1150	A	X	52	482.30	0.25	0	0	0	0
186	1150	A	X	53	492.00	0.30	0	0	0	0
186	1150	A	X	54	501.70	9.79	0	0	0	0
186	1150	A	X	55	511.30	9.55	1	0.1	0	0
186	1150	A	X	56	520.90	6.64	1	0.2	0	0
186	1150	A	X	57	530.60	1.12	0	0	0	0
186	1150	A	X	58	540.30	0.25	0	0	0	0
186	1150	A	X	59	549.90	0.00				
186	1150	A	X	60	559.50	4.27	0	0	0	0
186	1150	A	X	61	569.10	2.53	0	0	0	0
186	1150	A	X	62	578.70	9.82	0	0	0	0
186	1150	A	X	63	588.40	1.54	1	0.6	0	0
186	1150	A	X	64	598.00	3.38	0	0	0	0
186	1150	A	X	65	607.70	2.29	0	0	0	0
186	1150	A	X	66	617.30	9.80	1	0.1	0	0
186	1150	A	X	67	626.90	9.78	0	0	0	0
186	1150	A	X	68	636.50	9.21	0	0	0	0
186	1150	A	X	69	645.80	9.74	2	0.2	0	0

Table T3 (continued).

Leg	Site	Hole	Type	Core	Depth (mbsf)	Recovered length (m)	Primary and reworked ash		Bioturbated ash patches	
							(Layers/core)	(Layers/m)	(Layers/core)	(Layers/m)
186	1150	A	X	70	655.40	7.81	0	0	0	0
186	1150	A	X	71	664.80	9.71	1	0.1	0	0
186	1150	A	X	72	674.40	9.88	6	0.6	1	0.1
186	1150	A	X	73	684.00	2.60	0	0	0	0
186	1150	A	X	74	693.70	9.19	2	0.2	2	0.2
186	1150	A	X	75	703.30	9.87	1	0.1	1	0.1
186	1150	A	X	76	713.00	9.90	4	0.4	0	0
186	1150	B	R	1	703.30	4.91	0	0	0	0
186	1150	B	R	2	709.70	2.26	0	0	0	0
186	1150	B	R	3	719.30	0.83	0	0	0	0
186	1150	B	R	4	729.00	3.50	0	0	0	0
186	1150	B	R	5	738.60	1.50	0	0	1	0.7
186	1150	B	R	6	748.30	8.26	2	0.2	1	0.1
186	1150	B	R	7	757.90	1.45	0	0	0	0
186	1150	B	R	8	767.60	2.48	0	0	0	0
186	1150	B	R	9	777.20	4.30	1	0.2	0	0
186	1150	B	R	10	786.90	4.14	1	0.2	1	0.2
186	1150	B	R	11	796.50	6.35	1	0.2	3	0.5
186	1150	B	R	12	806.10	5.86	1	0.2	0	0
186	1150	B	R	13	815.70	4.11	0	0	0	0
186	1150	B	R	14	835.40	5.11	0	0	0	0
186	1150	B	R	15	835.00	2.20	1	0.5	0	0
186	1150	B	R	16	844.60	7.65	0	0	0	0
186	1150	B	R	17	854.20	5.36	0	0	1	0.2
186	1150	B	R	18	863.80	4.31	0	0	0	0
186	1150	B	R	19	873.50	4.05	1	0.2	0	0
186	1150	B	R	20	883.20	9.84	0	0	1	0.1
186	1150	B	R	21	892.90	5.44	0	0	0	0
186	1150	B	R	22	902.10	8.59	0	0	1	0.1
186	1150	B	R	23	911.80	7.96	1	0.1	2	0.3
186	1150	B	R	24	921.50	1.99	1	0.5	0	0
186	1150	B	R	25	931.10	7.89	1	0.1	0	0
186	1150	B	R	26	940.70	7.31	0	0	0	0
186	1150	B	R	27	950.30	7.13	0	0	0	0
186	1150	B	R	28	959.90	8.96	0	0	1	0.1
186	1150	B	R	29	969.50	8.56	0	0	0	0
186	1150	B	R	30	979.10	8.78	0	0	1	0.1
186	1150	B	R	31	988.70	3.66	0	0	0	0
186	1150	B	R	32	998.30	9.55	0	0	0	0
186	1150	B	R	33	1007.90	1.60	1	0.6	0	0
186	1150	B	R	34	1017.50	2.52	0	0	0	0
186	1150	B	R	35	1027.10	4.43	1	0.2	0	0
186	1150	B	R	36	1036.70	8.06	0	0	3	0.4
186	1150	B	R	37	1046.50	4.04	0	0	0	0
186	1150	B	R	38	1056.30	2.42	0	0	0	0
186	1150	B	R	39	1066.00	4.82	0	0	0	0
186	1150	B	R	40	1075.70	3.53	0	0	0	0
186	1150	B	R	41	1085.30	9.19	0	0	1	0.1
186	1150	B	R	42	1094.90	8.99	0	0	0	0
186	1150	B	R	43	1104.60	6.71	0	0	1	0.1
186	1150	B	R	44	1114.20	1.59	0	0	0	0
186	1150	B	R	45	1123.90	5.98	0	0	0	0
186	1150	B	R	46	1133.50	5.47	1	0.2	0	0
186	1150	B	R	47	1143.10	4.30	0	0	0	0
186	1150	B	R	48	1152.80	4.96	0	0	1	0.2
186	1150	B	R	49	1162.40	8.19	0	0	0	0
186	1150	B	R	50	1172.00	8.25	1	0.1	6	0.7

Notes: Depths are measured at top of interval. Blank = no recovery. This table is also available in [ASCII format](#).

Table T4. Number of pebbles, granules, and sand/silt grains and accumulations, Site 1150. (See table notes. Continued on next page.)

Leg	Site	Hole	Core	Type	Depth (mbsf)	Recovered length (m)	Pebbles and granules		Sand and silt	
							(Layers/ core)	(Layers/ m)	(Layers/ core)	(Layers/ m)
186	1150	A	1	H	0.0	7.73	8	1.0	8	1.0
186	1150	A	2	H	7.70	10.04	1	0.1	5	0.5
186	1150	A	3	H	17.20	10.30	10	1.0	3	0.3
186	1150	A	4	H	26.70	10.00	0	0	9	0.9
186	1150	A	5	H	36.20	10.18	13	1.3	7	0.7
186	1150	A	6	H	45.70	10.08	8	0.8	8	0.8
186	1150	A	7	H	55.20	10.15	4	0.4	23	2.3
186	1150	A	8	H	64.70	9.80	4	0.4	22	2.2
186	1150	A	9	H	74.20	10.38	8	0.8	9	0.9
186	1150	A	10	H	83.70	10.44	7	0.7	8	0.8
186	1150	A	11	H	93.20	9.65	7	0.7	19	2.0
186	1150	A	12	H	102.70	9.50	18	1.9	15	1.6
186	1150	A	13	H	112.20	5.22	6	1.1	8	1.5
186	1150	A	14	X	116.40	8.36	14	1.7	5	0.6
186	1150	A	15	X	126.00	4.23	1	0.2	7	1.7
186	1150	A	16	X	135.60	4.00	2	0.5	7	1.8
186	1150	A	17	X	145.20	9.38	2	0.2	16	1.7
186	1150	A	18	X	154.80	7.36	5	0.7	6	0.8
186	1150	A	19	X	164.40	0.00				
186	1150	A	20	X	174.00	0.01				
186	1150	A	21	X	183.60	8.46	1	0.1	8	0.9
186	1150	A	22	X	193.30	9.96	2	0.2	18	1.8
186	1150	A	23	X	202.90	9.99	2	0.2	8	0.8
186	1150	A	24	X	212.50	0.77	1	1.3	0	0
186	1150	A	25	X	222.20	9.99	2	0.2	6	0.6
186	1150	A	26	X	231.90	7.70	1	0.1	0	0
186	1150	A	27	X	241.50	9.71	1	0.1	5	0.5
186	1150	A	28	X	251.20	9.18	3	0.3	1	0.1
186	1150	A	29	X	260.80	8.59	1	0.1	2	0.2
186	1150	A	30	X	270.40	9.76	3	0.3	1	0.1
186	1150	A	31	X	280.10	9.75	0	0	0	0
186	1150	A	32	X	289.70	9.18	4	0.4	8	0.9
186	1150	A	33	X	299.40	6.22	4	0.6	1	0.2
186	1150	A	34	X	309.10	9.89	1	0.1	1	0.1
186	1150	A	35	X	318.70	10.20	0	0	3	0.3
186	1150	A	36	X	328.40	10.09	0	0	0	0
186	1150	A	37	X	338.00	9.42	2	0.2	2	0.2
186	1150	A	38	X	347.60	9.84	0	0.0	3	0.3
186	1150	A	39	X	357.20	9.83	3	0.3	4	0.4
186	1150	A	40	X	366.80	9.66	0	0	3	0.3
186	1150	A	41	X	376.40	2.26	0	0	2	0.9
186	1150	A	42	X	386.00	9.67	1	0.1	5	0.5
186	1150	A	43	X	395.60	9.73	0	0	3	0.3
186	1150	A	44	X	405.20	9.32	2	0.2	0	0
186	1150	A	45	X	414.80	9.56	2	0.2	5	0.5
186	1150	A	46	X	424.40	4.46	10	2.2	4	0.9
186	1150	A	47	X	434.10	9.61	1	0.1	5	0.5
186	1150	A	48	X	443.70	9.68	0	0	1	0.1
186	1150	A	49	X	453.30	9.89	0	0	5	0.5
186	1150	A	50	X	462.90	0.14	0	0	0	0
186	1150	A	51	X	472.60	8.03	1	0.1	0	0
186	1150	A	52	X	482.30	0.25	0	0	0	0
186	1150	A	53	X	492.00	0.30	0	0	0	0
186	1150	A	54	X	501.70	9.79	1	0.1	5	0.5
186	1150	A	55	X	511.30	9.55	3	0.3	3	0.3
186	1150	A	56	X	520.90	6.64	1	0.2	3	0.5
186	1150	A	57	X	530.60	1.12	0	0	0	0
186	1150	A	58	X	540.30	0.25	1	4.0	0	0
186	1150	A	59	X	549.90	0.00				
186	1150	A	60	X	559.50	4.27	0	0	1	0.2
186	1150	A	61	X	569.10	2.53	1	0.4	2	0.8
186	1150	A	62	X	578.70	9.82	0	0	0	0
186	1150	A	63	X	588.40	1.54	1	0.6	1	0.6
186	1150	A	64	X	598.00	3.38	2	0.6	2	0.6
186	1150	A	65	X	607.70	2.29	1	0.4	0	0
186	1150	A	66	X	617.30	9.80	0	0	3	0.3
186	1150	A	67	X	626.90	9.78	0	0	2	0.2
186	1150	A	68	X	636.50	9.21	0	0	0	0
186	1150	A	69	X	645.80	9.74	0	0	5	0.5

Table 4 (continued).

Leg	Site	Hole	Core	Type	Depth (mbsf)	Recovered length (m)	Pebbles and granules		Sand and silt	
							(Layers/ core)	(Layers/ m)	(Layers/ core)	(Layers/ m)
186	1150	A	70	X	655.40	7.81	1	0.1	5	0.6
186	1150	A	71	X	664.80	9.71	0	0	1	0.1
186	1150	A	72	X	674.40	9.88	1	0.1	6	0.6
186	1150	A	73	X	684.00	2.60	0	0	1	0.4
186	1150	A	74	X	693.70	9.19	0	0	6	0.7
186	1150	A	75	X	703.30	9.87	0	0	4	0.4
186	1150	A	76	X	713.00	9.90	1	0.1	3	0.3
186	1150	B	1	R	703.90	4.91	0	0	1	0.2
186	1150	B	2	R	709.70	2.26	1	0.4	1	0.4
186	1150	B	3	R	719.30	0.83	1	1.2	0	0
186	1150	B	4	R	729.00	3.50	1	0.3	0	0
186	1150	B	5	R	738.60	1.50	3	2.0	3	2.0
186	1150	B	6	R	748.30	8.26	1	0.1	8	1.0
186	1150	B	7	R	757.90	1.45	0	0	0	0
186	1150	B	8	R	767.60	2.48	1	0.4	0	0
186	1150	B	9	R	777.20	4.30	0	0	6	1.4
186	1150	B	10	R	786.90	4.14	13	3.1	11	2.7
186	1150	B	11	R	796.50	6.35	12	1.9	9	1.4
186	1150	B	12	R	806.10	5.86	0	0	3	0.5
186	1150	B	13	R	815.70	4.11	1	0.2	5	1.2
186	1150	B	14	R	835.40	5.11	4	0.8	8	1.6
186	1150	B	15	R	835.00	2.20	0	0	3	1.4
186	1150	B	16	R	844.60	7.65	0	0	1	0.1
186	1150	B	17	R	854.20	5.36	2	0.4	7	1.3
186	1150	B	18	R	863.80	4.31	0	0	5	1.2
186	1150	B	19	R	873.50	4.05	0	0	4	1.0
186	1150	B	20	R	883.20	9.84	2	0.2	15	1.5
186	1150	B	21	R	892.90	5.44	6	1.1	11	2.0
186	1150	B	22	R	902.10	8.59	1	0.1	15	1.7
186	1150	B	23	R	911.80	7.96	6	0.8	19	2.4
186	1150	B	24	R	921.50	1.99	1	0.5	1	0.5
186	1150	B	25	R	931.10	7.89	1	0.1	6	0.8
186	1150	B	26	R	940.70	7.31	1	0.1	3	0.4
186	1150	B	27	R	950.30	7.13	2	0.3	7	1.0
186	1150	B	28	R	959.90	8.96	0	0	4	0.4
186	1150	B	29	R	969.50	8.56	0	0	4	0.5
186	1150	B	30	R	979.10	8.78	1	0.1	3	0.3
186	1150	B	31	R	988.70	3.66	0	0	5	1.4
186	1150	B	32	R	998.30	9.55	0	0	14	1.5
186	1150	B	33	R	1007.90	1.60	0	0	4	2.5
186	1150	B	34	R	1017.50	2.52	0	0	1	0.4
186	1150	B	35	R	1027.10	4.43	2	0.5	5	1.1
186	1150	B	36	R	1036.70	8.06	3	0.4	8	1.0
186	1150	B	37	R	1046.50	4.04	0	0	2	0.5
186	1150	B	38	R	1056.30	2.42	1	0.4	6	2.5
186	1150	B	39	R	1066.00	4.82	1	0.2	7	1.5
186	1150	B	40	R	1075.70	3.53	2	0.6	3	0.8
186	1150	B	41	R	1085.30	9.19	5	0.5	10	1.1
186	1150	B	42	R	1094.90	8.99	1	0.1	12	1.3
186	1150	B	43	R	1104.60	6.71	0	0	15	2.2
186	1150	B	44	R	1114.20	1.59	0	0	1	0.6
186	1150	B	45	R	1123.90	5.98	3	0.5	8	1.3
186	1150	B	46	R	1133.50	5.47	3	0.5	8	1.5
186	1150	B	47	R	1143.10	4.30	1	0.2	5	1.2
186	1150	B	48	R	1152.80	4.96	0	0	5	1.0
186	1150	B	49	R	1162.40	8.19	0	0	2	0.2
186	1150	B	50	R	1172.00	8.25	0	0	15	1.8

Notes: Depths are measured at top of interval. Blank = no recovery. This table is also available in [ASCII format](#).

Table T5. Occurrences of dolomitic layers in recovered core and in the downhole measurements, Site 1150.

Occurrence number	Leg	Site	Hole	Core	Type	Section	Interval (cm)		Depth (mbsf)		Occurrence description	Identification	Hole 1150B logging depth (mbsf)		Identification
							Top	Bottom	Top	Bottom			Top	Bottom	
1150-D-1	186	1150	A	5	H	5	40	41	42.60	42.61	Patches of coarse grains	Recovered core VCD, XRD			In drill pipe
1150-D-2	186	1150	A	9	H	1	93	97	75.13	75.17	Turbiditic layer	Recovered core VCD, XRD			In drill pipe
1150-D-3	186	1150	A	25	X	1	119	120	223.39	223.40	Patches of coarse grains	Recovered core XRD	218.88	219.02	Resistivity (very weak)
1150-D-4	186	1150	A	29	X	1	0	2	260.80	260.82	Fragments (drop in)	Recovered core VCD	260.41	261.10	Resistivity
1150-D-5	186	1150	A	47	X	2	42	59	436.02	436.19	Layer	Recovered core VCD, XRD	440.48	440.69	Resistivity, FMS
1150-D-6a	186	1150	A	52	X	CC	2	6	482.32	482.36	Fragments (drop in)	Recovered core VCD, XRD	471.67	472.41	Resistivity
1150-D-6b	186	1150									No recovery	474.06	474.81	Resistivity	
1150-D-7a	186	1150	A	63	X	CC	22	26	589.85	589.89	Layer	Recovered core VCD, XRD	602.15	602.92	Resistivity
1150-D-7b	186	1150	A	65	X	1	0	5	607.70	607.75	Fragments (drop in)	Recovered core VCD	603.35	604.36	Resistivity
1150-D-8a*	186	1150									No recovery	792.61	792.93	Resistivity, FMS	
1150-D-8b*	186	1150									No recovery	794.24	794.64	Resistivity	
1150-D-9	186	1150	B	12	R	3	127	145	810.15	810.33	Layer	Recovered core VCD, XRD	809.79	810.44	Resistivity, FMS
1150-D-10a	186	1150	B	26	R	3	47	63	944.05	944.21	Layer	Recovered core VCD, XRD	945.06	945.58	Resistivity, FMS
1150-D-10b	186	1150									No recovery	945.70	946.56	Resistivity, FMS	
1150-D-11	186	1150	B	38	R	1	12	40	1056.42	1056.70	Layer	Recovered core VCD	1057.36	1058.09	Resistivity, FMS

Notes: VCD = visual core description, XRD = X-ray diffraction, FMS = Formation MicroScanner, CC = core catcher. * = no positive evidences from core.

Table T6. Stratigraphic occurrence and chronology of datum levels of calcareous nannofossils, Site 1150.

Datum event	Zone (base)	Age (Ma)	Upper sample		Lower sample		
			Core, section, interval (cm)	Depth (mbsf)	Core, section, interval (cm)	Depth (mbsf)	
FO	<i>Emiliana huxleyi</i>	CN 15	0.248	186-1150A- 5H-CC	46.33	186-1150A- 6H-CC	55.73
LO	<i>Pseudoemiliana lacunosa</i>	CN14b	0.408	7H-CC	65.30	8H-CC	74.45
FO	<i>Gephyrocapsa parallela</i>	CN14a	0.94	10H-CC	84.53	11H-CC	94.09
FO	<i>Gephyrocapsa caribbeanica</i>	CN13b	1.71	14X-CC	124.71	15X-CC	130.20
LO	<i>Discoaster brouweri</i>	CN13a	1.95	15X-CC	130.20	16X-CC	139.58
LO	<i>Discoaster pentaradiatus</i>	CN12d	2.36	21X-CC	192.01	22X-CC	202.94
LO	<i>Discoaster tamalis</i>	CN12b	2.51	26X-CC	239.55	27X-CC	251.16
LO	<i>Reticulofenestra pseudumbilicus</i>	CN 11	3.83	37X-CC	357.39	38X-CC	366.98
FO	<i>Ceratolithus rugosus</i>	CN10c	5.089	64X-CC	601.35	65X-CC	609.96
LO	<i>Discoaster quinqueramus</i>	CN10a	5.537	186-1150B- 11R-1, 10 cm	796.60	186-1150B- 11R-3, 10cm	799.48
FO and LO	<i>Amaurolithus amplificus</i>		5.99-6.84	19R-CC	877.53		
FO	<i>Discoaster berggrenii</i>	CN9a	8.28	38R-CC	1058.56	39R-CC	1070.80

Note: FO = first occurrence, LO = last occurrence.

Table T8. Stratigraphic occurrences and chronology of datum levels of diatoms, Site 1150.

Datum event	Zone (base)	Age (Ma)	Upper sample		Lower sample	
			Core, section, interval (cm)	Depth (mbsf)	Core, section, interval (cm)	Depth (mbsf)
LO <i>Proboscia curvirostris</i>	NPD 12	0.30	186-1150A- 6H-CC	55.73	186-1150A- 7H-4, 65-69	60.35
LCO <i>Actinocyclus oculatus</i>	NPD 11	1.01-1.46	11H-CC	102.66	12H-1, 140-144	104.10
LO <i>Neodenticula koizumii</i>	NPD 10	2.0	14H-3, 70-72	120.10	14H-5, 71-73	123.11
LCO <i>Neodenticula kamtschatica</i>	NPD 9	2.61-2.68	21X-CC	192.01	22X-3, 140-144	197.70
FO <i>Neodenticula koizumii</i>	NPD 8	3.53-3.95	28X-CC	260.33	29X-3, 63-67	264.43
FO <i>Thalassiosira latimarginata</i>		5.07	45X-CC	424.33	46X-CC	428.83
FO <i>Thalassiosira oestrupii</i> sensu lato	NPD 7Bb	5.49	56X-CC	527.49	57X-1, 70-74	531.30
LCO <i>Rouxia californica</i>	NPD 7Ba	6.65	186-1150B- 20R-CC	893.02	186-1150B- 21R-3, 70-72	896.44
LO <i>Cavitatus jouseanus</i>		6.7-6.8	23R-CC	919.73	24R-CC	923.46
FO <i>Neodenticula kamtschatica</i>		7.3-7.4	28R-CC	968.83	29R-3, 75-78	972.88
LO <i>Thalassionema schraderi</i>	NPD 7A	7.6	31R-CC	992.31	32R-1, 60-63	998.90
LO <i>Denticulopsis katayamae</i>		8.5	39R-CC	1070.80	40R-CC	1079.21
LCO <i>Denticulopsis simonsenii</i>	NPD 6B	8.6	40R-CC	1079.21	41R-1, 68-71	1085.98
LO <i>Denticulopsis dimorpha</i>	NPD 6A	9.16	43R-1, 69-71	1105.29	43R-3, 71-72	1108.26
FO <i>Denticulopsis katayamae</i>		9.26	45R-CC	1129.85	46R-CC	1138.94
FO <i>Thalassionema schraderi</i>		9.5	46R-CC	1138.94	47R-CC	1147.36
FO <i>Denticulopsis dimorpha</i>	NPD 5D	9.9	50R-CC	1180.23		

Notes: LO = last occurrence, LCO = last common occurrence, FO = first occurrence. NPD = North Pacific diatom zones. This table is also available in [ASCII format](#).

Table T9. Depths of prominent geomagnetic reversals.

Chron	Age (Ma)	Sample identification	Depth (mbsf)
		Core, section, interval	
		186-1150A-	
C1n(o)	0.780	10H-1, 48 cm	84.18
C2An.1n(t)	2.581	17X-5, 80 cm	152
C2An.3n(o)	3.580	~29X	268 ± 10
C3n.1n(t)	4.180	~36X	331 ± 3
C3n.4n(o)	5.230	51X through 54X	490 ± 10
C3An.1n(t)	5.894	~67X	629 ± 10
		186-1150B-	
C3An.2n(o)	6.567	8R through 9R	777 ± 5

Table T10. NRM and ARM results from the NP2 magnetometer before and after AF demagnetization.

Leg	Site	Hole	Core	Section	Interval (cm)	Depth (mbsf)	Ljn (0 mT)	Ljn (10 mT)	Ljn (20 mT)	Inclination (20 mT)	Declination (20 mT)	ErrIC (20 mT)	Ljn (30 mT)	Ljn (40 mT)	MDF (jn)	LjaZ (0 mT)
186	1150	A	1	1	69	0.69	-5.27163	-5.71778	-5.87391	60.6	155.9	1.94	-5.92267	-6.13884	6.75	-5.35371
186	1150	A	1	2	25	1.75	-5.3526	-5.58715	-5.80315	64.5	182.8	2.06	-5.89926	-6.17058	13.08	-5.30375
186	1150	A	1	3	25	3.25	-4.75235	-5.04719	-5.2257	59.8	192.0	2.58	-5.36419	-5.71820	10.35	-4.78480
186	1150	A	1	4	52	5.02	-4.75914	-5.39337	-5.55229	45.2	198.8	8.83	-5.74288	-5.60221	4.75	-4.81262
186	1150	A	1	5	25	6.25	-5.10243	-5.64067	-5.7142	52.7	163.1	6.19	-5.94443	-6.11129	5.59	-5.02411
186	1150	A	2	1	26	7.96	-5.07043	-5.44811	-6.13875	65.5	265.7	18.16	-6.12063	-6.09793	7.97	-4.99993
186	1150	A	2	2	26	9.46	-5.03339	-5.87181	-6.10754	57.5	208.8	19.33	-6.38848	-6.43352	3.59	-5.07527
186	1150	A	2	3	26	10.96	-4.36859	-5.13604	-5.35718	48.3	248.3	1.66	-5.63336	-5.82901	3.92	-4.68980
186	1150	A	2	4	26	12.46	-4.75943	-5.66887	-5.92912	48.8	257.0	22.69	-5.96938	-6.07479	3.31	-4.93331
186	1150	A	2	5	26	13.96	-5.14591	-5.78845	-5.88008	59.7	289.6	9.71	-6.04070	-6.30566	4.69	-5.06006

Leg	Site	Hole	Core	Section	Interval (cm)	Depth (mbsf)	LjaZ (10 mT)	LjaZ (20 mT)	LjaZ (30 mT)	LjaZ (40 mT)	MDF (ja)	Jn/Ja (0 mT)	Jn/Ja (10 mT)	Jn/Ja (20 mT)	Jn/Ja (30 mT)
186	1150	A	1	1	69	0.69	-5.48778	-5.86326	-6.10913	-6.99126	14.4	1.208	0.589	0.976	1.536
186	1150	A	1	2	25	1.75	-5.42883	-5.58736	-5.9811	-7.36188	20.4	0.894	0.695	0.608	1.207
186	1150	A	1	3	25	3.25	-4.86350	-5.05063	-5.41689	-6.46233	21.0	1.078	0.655	0.668	1.129
186	1150	A	1	4	52	5.02	-4.88222	-5.05126	-5.43635	-6.13684	21.6	1.131	0.308	0.315	0.494
186	1150	A	1	5	25	6.25	-5.07436	-5.28411	-5.68165	-6.64444	21.0	0.835	0.271	0.371	0.546
186	1150	A	2	1	26	7.96	-5.07277	-5.27757	-5.72054	-7.42615	20.5	0.850	0.421	0.138	0.398
186	1150	A	2	2	26	9.46	-5.18866	-5.37886	-5.68382	-6.36289	19.9	1.101	0.207	0.187	0.197
186	1150	A	2	3	26	10.96	-4.80832	-5.05677	-5.51300	-6.58895	17.3	2.095	0.470	0.501	0.758
186	1150	A	2	4	26	12.46	-5.04876	-5.22953	-5.51107	-6.26746	20.2	1.492	0.240	0.200	0.348
186	1150	A	2	5	26	13.96	-5.13968	-5.31549	-5.67398	-6.69388	21.3	0.821	0.225	0.273	0.430

Leg	Site	Hole	Core	Section	Interval (cm)	Depth (mbsf)	Lj (sus)	Principal axes of AMS (°)						MST (sus)	
								Max. Inc.	Max. Dec.	Int. Inc.	Int. Dec.	Min. Inc.	Min. Dec.		qn
186	1150	A	1	1	69	0.69	-6.48531	-45.4508	188.6	-9.1800	288.0	-43.0895	26.73	0.145100	10.0
186	1150	A	1	2	25	1.75	-6.60588	-24.4649	68.1	-29.0083	323.5	-50.3789	191.42	-0.487452	8.9
186	1150	A	1	3	25	3.25	-6.33233	-64.5220	300.7	-10.8421	187.0	-22.7591	92.41	1.588700	30.5
186	1150	A	1	4	52	5.02	-6.13014	-29.9896	225.4	-25.9269	331.7	-48.3879	94.88	-0.253054	101.2
186	1150	A	1	5	25	6.25	-6.31022	-22.8991	339.8	-66.9023	151.9	-2.8621	248.63	-1.404190	26.5
186	1150	A	2	1	26	7.96	-6.48425	-46.5301	350.0	-21.2573	104.3	-35.7809	210.54	-0.384398	28.8
186	1150	A	2	2	26	9.46	-6.34414	-36.5065	152.6	-26.0550	41.4	-42.3119	284.97	-0.722941	68.8
186	1150	A	2	3	26	10.96	-6.58756	-36.8074	113.9	-8.6928	17.3	-51.8373	276.10	-1.344530	76.5
186	1150	A	2	4	26	12.46	-6.34205	-19.7073	309.9	-35.0129	54.5	-48.2778	196.25	1.345300	32.5
186	1150	A	2	5	26	13.96	-6.46432	-36.9767	296.2	-24.6468	46.4	-42.9528	161.66	-0.469852	25.8

Notes: Ljn = log of NRM intensity; ErrIC = a measure of uncertainty in the directional measurement; MDF = medium destructive field; LjaZ = log of ARM intensity for the z-axis; Jn = NRM intensity; ja = ARM intensity; Jn/Ja = the ratio of the NRM to the ARM, where the level of demagnetization of both the ARM and NRM is given in parentheses; LJ = log of the susceptibility. AMS = anisotropy of magnetic susceptibility; Inc. = inclination; Dec. = declination; Max. = maximum AMS axis; Int. = intermediate AMS axis; Min. = minimum AMS axis; qn = anisotropy shape factor. All intensities are given as log values in kA/m units. Only a portion of this table appears here. The complete table is available in [ASCII format](#).

Table T11. NRM results from the NP2 magnetometer before and after AF demagnetization.

Leg	Site	Hole	Core	Section	Depth (mbsf)	Ljn (kA/m)	Inclination (°)	Declination (°)	AF demag. (mT)
186	1150	A	35	2	319.92	-5.97231	59.9	1.1	0
186	1150	A	35	2	319.92	-6.24849	6.8	32.6	10
186	1150	A	35	2	319.92	-6.52357	-3.9	9.7	20
186	1150	A	35	3	321.21	-6.17384	64.4	346.0	0
186	1150	A	35	3	321.21	-6.65496	28.8	37.3	10
186	1150	A	35	3	321.21	-6.60130	3.6	89.9	20
186	1150	A	35	4	322.88	-6.15268	60.5	321.7	0
186	1150	A	35	4	322.88	-6.44811	49.6	250.6	10
186	1150	A	35	4	322.88	-6.54524	18.9	341.6	20
186	1150	A	35	5	324.19	-5.64697	78.3	70.7	0
186	1150	A	35	5	324.19	-6.42242	74.5	330.8	10
186	1150	A	35	5	324.19	-6.88131	-30.0	283.9	20
186	1150	A	36	3	331.39	-5.65408	61.5	302.1	0
186	1150	A	36	3	331.39	-5.84238	56.6	301.0	10
186	1150	A	36	3	331.39	-6.00559	52.2	294.4	20
186	1150	A	36	4	332.95	-5.77170	52.5	344.2	0
186	1150	A	36	4	332.95	-5.91566	46.5	329.5	10
186	1150	A	36	4	332.95	-6.05593	46.3	348.3	20
186	1150	A	37	1	338.53	-5.78021	59.0	40.1	0
186	1150	A	37	1	338.53	-5.93883	52.5	27.2	10
186	1150	A	37	1	338.53	-6.05699	49.6	37.2	20
186	1150	A	37	2	340.05	-5.70543	58.5	107.0	0
186	1150	A	37	2	340.05	-5.82073	47.6	104.6	10
186	1150	A	37	2	340.05	-5.99492	50.8	123.7	20
186	1150	A	37	3	341.17	-5.48405	55.5	241.8	0
186	1150	A	37	3	341.17	-5.59851	51.6	241.6	10
186	1150	A	37	3	341.17	-5.74215	47.3	233.7	20
186	1150	A	37	4	343.08	-5.78330	64.3	156.0	0
186	1150	A	37	4	343.08	-5.85819	48.8	167.7	10
186	1150	A	37	4	343.08	-5.90485	47.6	166.7	20
186	1150	A	37	5	344.41	-5.46111	53.1	326.6	0
186	1150	A	37	5	344.41	-5.61613	49.8	326.0	10
186	1150	A	37	5	344.41	-5.71761	43.9	341.1	20
186	1150	A	38	1	348.43	-5.61895	54.2	29.0	0
186	1150	A	38	1	348.43	-5.76659	53.8	38.7	10
186	1150	A	38	1	348.43	-5.95690	41.0	31.5	20
186	1150	A	38	3	350.84	-5.66268	52.2	15.6	0
186	1150	A	38	3	350.84	-5.83632	54.4	9.9	10
186	1150	A	38	3	350.84	-5.96044	53.0	7.7	20
186	1150	A	38	4	352.54	-5.73493	53.1	5.2	0
186	1150	A	38	4	352.54	-5.84245	55.5	17.1	10
186	1150	A	38	4	352.54	-6.04527	41.3	40.4	20
186	1150	A	38	5	353.86	-5.77997	71.9	22.6	0
186	1150	A	38	5	353.86	-6.14718	52.8	55.2	10
186	1150	A	38	5	353.86	-6.26007	48.8	53.1	20
186	1150	A	39	1	357.62	-5.48308	75.1	188.2	0
186	1150	A	39	1	357.62	-5.79664	72.9	227.2	10
186	1150	A	39	1	357.62	-5.96542	60.9	209.7	20
186	1150	A	39	2	358.87	-5.52443	58.6	16.6	0
186	1150	A	39	2	358.87	-5.73887	56.6	10.8	10
186	1150	A	39	2	358.87	-5.85611	63.3	12.6	20
186	1150	A	39	3	360.57	-5.61551	73.5	147.2	0
186	1150	A	39	3	360.57	-5.85491	54.6	186.9	10
186	1150	A	39	3	360.57	-6.00677	58.9	164.5	20
186	1150	A	39	4	361.89	-5.64281	74.5	40.8	0
186	1150	A	39	4	361.89	-5.89793	64.9	49.8	10
186	1150	A	39	4	361.89	-6.23258	62.9	21.9	20
186	1150	A	39	5	363.59	-5.62767	74.0	117.3	0
186	1150	A	39	5	363.59	-5.90265	57.6	161.4	10
186	1150	A	39	5	363.59	-6.14854	47.9	169.7	20
186	1150	A	39	6	364.52	-5.58787	58.8	48.0	0
186	1150	A	39	6	364.52	-6.03686	48.4	42.8	10
186	1150	A	39	6	364.52	-5.97510	49.8	20.0	20
186	1150	A	40	1	367.00	-6.32330	-2.2	177.6	0
186	1150	A	40	1	367.00	-5.86073	64.0	184.9	10
186	1150	A	40	1	367.00	-6.01008	68.7	188.6	20

Notes: AF = alternating field. Only a portion of this table appears here. The complete table is available in [ASCII format](#).

Table T12. Results of chemical treatments.

Core	Depth (mbsf)	Sample number	Treatment	Total intensity						MDF (mT)	
				0 mT	5 mT	10 mT	20 mT	30 mT	40 mT		
186-1150A-21X	192.2	1	Jn0	133	117	103	46	7	5	15.3	
		1	Ja0	159	142	127	71	38	22	17.9	
		2	Jn H ₂ O ₂	57	12						2.3
		2	Jn EDTA	237	140						6.6
		2	Jn HCl	46	17						3.5
		2	Ja HCl	86	86	86	35	26	26		17.2
41X	378.7	1	Jn0	202	166	137	90	41	23	15.3	
		1	Ja0	407	332	271	151	34	25	14.9	
		2	Jn H ₂ O ₂	202	55						2.7
		2	Jn EDTA	255	137						5.6
		2	Jn HCl	34	16						4.6
		2	Ja HCl	106	106	106	50	1	24		16.1
61X	571.6	1	Jn0	135	97	70	23	23	23	10.3	
		1	Ja0	221	211	201	100	21	7	18.6	
		2	Jn H ₂ O ₂	144	51						3.4
		2	Jn EDTA	105	51						4.8
		2	Jn HCl	28	16						6.2
		2	Ja HCl	83	83	83	18	1	12		15.8
186-1150B-28R	968.9	1	Jn0	315	287	261	177	118	50	22.9	
		1	Ja0	346	249	179	53	47	36	10.3	
		2	Jn H ₂ O ₂	303	162						5.5
		2	Jn EDTA	233	92						3.7
		2	Jn HCl	34	34	38					0.0
		2	Ja HCl	113	113	113	65	18	51		17.6
36R	1044.8	1	Jn0	255	240	226	76	49	25	15.3	
		1	Ja0	532	440	364	260	127	48	19.3	
		2	Jn H ₂ O ₂	422	283						8.7
		2	Jn EDTA	468	349						11.8
		2	Jn HCl	24	24	24					0.0
		2	Ja HCl	209	187	168	128	29	31		20.7
40R	1079.2	1	Jn0	55	46	38	15	14	5	13.4	
		1	Ja0	85	74	64	39	17	7	18.4	
		2	Jn H ₂ O ₂	106	106	109					0.0
		2	Jn EDTA	101	101	29					10.1
		2	Jn HCl	2	2	9					0.0
		2	Ja HCl	78	78	78	41	7	16		21.4
48R	1157.76	1	Jn0	51	51	51	20	5	3	21.4	
		1	Ja0	76	70	65	42	20	5	21.3	
		2	Jn H ₂ O ₂	131	108	112					22.1
		2	Jn EDTA	201	62	66					3.1
		2	Jn HCl	21	21	28					0.0
		2	Ja HCl	218	185	157	126	70	17		20.3

Notes: Two specimens were taken from each of the core-catcher samples. Values are in 10⁻⁸ Am²/kg. MDF = median destructive field. This table is also available in [ASCII format](#).

Table T13. Age control points for Site 1150 datum events and sedimentation rates.

Datum number	Datum event	Depth (mbsf)	Age (Ma)	Sedimentation rate (m/m.y.)
	Top	0	0.00	
1	FO <i>Emiliana huxleyi</i>	50.72	0.25	204
2	LO <i>Proboscia curvirostris</i>	58.04	0.30	141
3	LO <i>Pseudoemiliana lacunosa</i>	69.73	0.41	108
4	B C1n (Brunhes)	84.18	0.78	39
5	LCO <i>Actinocyclus oculatus</i>	103.38	1.24	42
6	LO <i>Neodenticula koizumii</i>	121.61	2.00	24
7	FO <i>Neodenticula kamschatica</i>	194.86	2.65	114
8	FO <i>Neodenticula koizumii</i>	262.38	3.53	76
9	B C2An (Gauss)	268	3.58	112
10	B C2Ar (Gilbert)	331.17	4.18	105
11	FO <i>Thalassiosira oestrupii</i> s.l.	529.40	5.49	151
12	T C3An.1n	629	5.89	247
13	B C3An.2n	777	6.57	220
14	FO <i>Neodenticula kamschatica</i>	970.86	7.35	248
15	LO <i>Thalassionema schraderi</i>	995.61	7.60	99
16	LCO <i>Denticulopsis simonsenii</i>	1082.60	8.60	87
17	LO <i>Denticulopsis dimorpha</i>	1106.78	9.16	43
18	FO <i>Denticulopsis dimorpha</i>	>1180.23	9.90	99

Note: FO = first occurrence, LO = last occurrence, LCO = last common occurrence, B = base, T = top.

Table T14. Headspace concentrations of light hydrocarbons, Site 1150.

Leg	Site	Hole	Core	Type	Section	Top (cm)	Bottom (cm)	Depth (mbsf)	C ₁ (%)	C ₂ (ppmv)	C ₁ /C ₂
186	1150	A	1	H	4	0	5	4.50	0.00	0.00	
186	1150	A	2	H	4	0	5	12.20	2.18	0.98	22,230.19
186	1150	A	3	H	4	0	5	21.70	4.43	3.00	14,144.67
186	1150	A	4	H	3	0	5	29.70	2.06	2.00	10,304.75
186	1150	A	6	H	4	0	5	50.20	4.88	6.70	7,290.73
186	1150	A	7	H	4	0	5	59.70	3.74	7.00	5,336.66
186	1150	A	8	H	4	0	5	69.20	1.02	2.40	4,264.58
186	1150	A	9	H	4	0	5	78.68	3.81	8.10	4,702.62
186	1150	A	11	H	3	0	5	96.20	4.41	9.90	4,454.75
186	1150	A	12	H	5	0	5	108.33	5.08	11.40	4,456.55
186	1150	A	13	X	3	0	5	115.20	4.26	9.00	4,730.90
186	1150	A	14	X	4	0	5	120.90	4.50	8.40	5,356.57
186	1150	A	15	X	2	0	5	127.50	2.19	5.10	4,284.45
186	1150	A	16	X	2	0	5	137.10	3.00	6.40	4,689.25
186	1150	A	17	X	6	0	5	152.70	2.87	5.70	5,037.19
186	1150	A	18	X	3	0	5	157.80	1.48	4.00	3,704.25
186	1150	A	21	X	4	0	5	188.10	1.49	3.50	4,251.57
186	1150	A	22	X	4	0	5	197.80	2.34	3.40	6,894.03
186	1150	A	23	X	4	0	5	207.16	1.39	2.90	4,787.69
186	1150	A	25	X	4	0	5	226.70	1.45	3.10	4,669.71
186	1150	A	26	X	4	0	5	236.40	1.19	2.60	4,595.12
186	1150	A	27	X	4	0	5	246.00	1.19	3.00	3,964.50
186	1150	A	28	X	4	0	5	255.59	0.83	1.80	4,587.50
186	1150	A	29	X	4	0	5	265.30	0.83	2.10	3,962.62
186	1150	A	30	X	4	0	5	274.90	0.74	1.90	3,889.89
186	1150	A	31	X	4	0	5	283.77	1.53	3.30	4,641.24
186	1150	A	32	X	3	0	5	292.70	1.14	2.30	4,960.87
186	1150	A	33	X	3	0	5	302.40	1.41	3.20	4,415.31
186	1150	A	34	X	4	0	5	313.60	2.08	3.80	5,485.03
186	1150	A	35	X	4	0	5	322.56	0.62	1.50	4,163.60
186	1150	A	36	X	4	0	5	332.67	1.40	2.60	5,385.31
186	1150	A	37	X	4	0	5	342.50	1.37	2.70	5,089.59
186	1150	A	38	X	4	0	5	352.10	1.59	2.70	5,891.59
186	1150	A	39	X	4	0	5	361.70	2.18	3.80	5,728.82
186	1150	A	40	X	4	0	5	371.30	1.38	3.00	4,594.40
186	1150	A	42	X	4	0	5	390.50	1.58	2.00	7,877.15
186	1150	A	43	X	4	0	5	400.10	0.82	1.40	5,847.00
186	1150	A	44	X	4	0	5	409.70	2.27	3.30	6,889.12
186	1150	A	45	X	4	0	5	419.30	1.13	1.90	5,961.53
186	1150	A	47	X	4	0	5	438.60	1.19	2.20	5,395.41
186	1150	A	48	X	4	0	5	448.20	1.05	2.00	5,225.55
186	1150	A	49	X	4	0	5	457.80	0.86	2.00	4,301.75
186	1150	A	51	X	4	0	5	477.10	4.23	6.20	6,817.31
186	1150	A	51	X	CC	0	5	480.32	0.57	1.30	4,402.23
186	1150	A	52	X	CC	24	25	482.54	0.91	2.30	3,938.00
186	1150	A	53	X	CC	0	2	492.00	5.07	6.20	8,185.21
186	1150	A	54	X	4	0	5	506.22	0.69	1.40	4,927.00
186	1150	A	55	X	3	0	5	514.21	0.18	0.00	
186	1150	A	56	X	4	0	5	525.40	1.53	2.60	5,897.58
186	1150	A	57	X	1	90	92	531.50	1.49	2.90	5,128.21
186	1150	A	58	X	CC	0	2	540.30	0.36	0.00	
186	1150	A	60	X	3	0	5	562.50	1.84	3.90	4,719.36
186	1150	A	61	X	2	0	5	570.60	2.72	4.10	6,642.98
186	1150	A	62	X	4	0	5	583.20	0.85	2.00	4,245.10
186	1150	A	63	X	1	118	123	589.58	2.36	4.70	5,019.17
186	1150	A	64	X	2	0	5	599.50	1.97	4.30	4,578.53
186	1150	A	65	X	2	0	5	609.20	5.06	9.20	5,501.95
186	1150	A	66	X	4	0	5	621.80	4.23	7.10	5,961.39
186	1150	A	67	X	4	0	5	631.40	1.80	5.40	3,339.70
186	1150	A	68	X	4	0	5	640.84	2.57	6.60	3,889.56
186	1150	A	69	X	4	0	5	650.30	2.72	6.70	4,063.06
186	1150	A	70	X	4	0	5	659.90	3.20	6.70	4,777.28
186	1150	A	71	X	4	0	5	669.30	2.94	6.20	4,739.50
186	1150	A	72	X	4	0	5	678.90	3.61	6.90	5,230.29
186	1150	A	73	X	2	0	5	685.50	2.09	4.50	4,634.40
186	1150	A	74	X	3	0	5	696.70	2.08	4.70	4,424.19
186	1150	A	75	X	4	0	5	707.80	5.13	8.90	5,764.82
186	1150	A	76	X	3	0	5	716.00	4.78	9.60	4,981.01

Note: Only a portion of this table appears here. The complete table is available in [ASCII format](#).

Table T15. Results of gas pocket analyses, Hole 1150A.

Core	Type	Section	Depth (mbsf)	C ₁ (%)	C ₂ (ppmv)
186-1150A-					
23	X	4	208	88.4	115
25	X	4	227	90.0	108
26	X	4	237	88.5	104
42	X	4	391	89.2	81
43	X	4	401	89.5	79
66	X	5	624	88.6	111
67	X	4	632	87.2	94
68	X	4	641	88.4	110
69	X	4	651	88.6	7633

Table T16. Results of interstitial water analyses, Site 1150.

Leg	Site	Hole	Core	Type	Section	Top (cm)	Bottom (cm)	Depth (mbsf)	pH	Alkalinity (mM)	Salinity	Cl ⁻ (mM)	Na ⁺ (mM)	K ⁺ (mM)	Mg ²⁺ (mM)	Ca ²⁺ (mM)	SO ₄ ²⁻ (mM)	NH ₄ ⁺ (mM)	Li ⁺ (μM)	Sr ²⁺ (μM)
186	1150	A	1	H	3	145	150	4.45	7.64	23.57	34.00	554.00	461.40	11.16	49.10	5.70	12.30	2.00	19.00	92.00
186	1150	A	2	H	3	145	150	12.15	7.55	44.08	34.00	556.00	457.20	11.20	48.50	4.00	0.44	4.15	15.00	108.00
186	1150	A	3	H	4	145	150	23.15	7.54	49.03	34.00	548.00	462.20	11.69	48.10	3.90	ND	5.06	18.00	115.00
186	1150	A	6	H	3	145	150	50.15	7.61	40.63	32.00	527.00	448.40	10.88	39.80	3.90	ND	5.08	23.00	135.00
186	1150	A	9	H	3	143	148	78.63	7.59	32.08	30.00	513.00	439.90	10.49	31.50	4.40	0.31	6.52	119.00	163.00
186	1150	A	12	H	4	145	150	108.28	7.62	29.91	30.00	503.00	443.60	10.45	26.80	5.60	ND	8.07	266.00	187.00
186	1150	A	15	X	1	145	150	127.45	7.76	29.46	30.00	499.00	438.30	9.90	25.90	6.30	ND	8.88	321.00	183.00
186	1150	A	18	X	2	145	150	157.75	7.70	27.20	30.00	500.00	437.10	9.39	26.20	7.00	0.60	9.46	343.00	179.00
186	1150	A	21	X	3	145	150	188.05	7.73	26.70	30.00	496.00	433.80	8.76	26.50	7.30	0.81	9.64	357.00	191.00
186	1150	A	25	X	3	145	150	226.65	7.34	26.72	30.00	496.00	432.20	8.48	26.80	7.50	0.23	9.62	371.00	198.00
186	1150	A	28	X	3	145	150	255.54	7.29	27.43	30.00	502.00	435.60	8.26	27.80	7.70	0.00	9.54	365.00	198.00
186	1150	A	31	X	3	145	150	283.72	7.38	27.22	30.00	506.00	438.30	8.40	29.20	8.10	0.42	9.49	351.00	187.00
186	1150	A	34	X	3	145	150	313.55	7.31	26.88	30.00	510.00	444.90	8.27	29.70	7.10	0.80	9.00	338.00	176.00
186	1150	A	37	X	3	145	150	342.45	7.38	27.59	30.00	515.00	444.50	8.56	30.10	7.00	0.21	9.12	341.00	177.00
186	1150	A	40	X	3	145	150	371.25	7.33	27.35	30.00	516.00	450.00	8.53	30.60	6.40	0.24	8.72	326.00	164.00
186	1150	A	43	X	3	145	150	400.05	7.44	25.36	30.00	518.00	450.80	8.90	30.70	5.60	1.01	7.96	300.00	144.00
186	1150	A	47	X	3	145	150	438.55	7.75	24.39	30.00	516.00	449.00	8.55	30.60	5.50	0.30	7.95	304.00	147.00
186	1150	A	51	X	3	145	150	477.05	7.79	22.85	29.00	501.00	436.20	8.38	28.90	6.10	0.04	7.69	322.00	156.00
186	1150	A	54	X	3	140	150	506.12	7.46	23.45	29.00	491.00	424.10	8.52	29.50	7.20	1.29	7.33	322.00	146.00
186	1150	A	62	X	3	140	150	583.10	7.41	14.79	27.00	394.00	346.10	7.10	16.40	9.60	0.32	6.35	426.00	188.00
186	1150	A	66	X	3	140	150	621.70	7.70	11.08	22.00	364.00	324.30	6.43	15.10	9.50	1.78	5.62	418.00	153.00
186	1150	A	69	X	3	140	150	650.20	7.52	11.09	20.00	344.00	312.90	6.07	12.70	8.60	0.29	5.42	436.00	166.00
186	1150	A	72	X	3	140	150	678.80	7.65	11.09	20.00	338.00	309.50	6.25	12.50	8.40	0.73	5.40	430.00	160.00
186	1150	A	75	X	3	140	150	707.70	7.74	11.02	20.00	343.00	308.40	6.22	12.80	8.60	0.74	5.08	427.00	158.00
186	1150	B	1	R	2	124	134	706.03	7.79	10.88	20.00	350.00	305.00	6.88	13.30	7.84	0.10	5.35	442.00	163.00
186	1150	B	4	R	1	140	150	730.40	7.76	10.44	20.00	344.00	301.00	6.91	13.20	8.79	0.11	5.17	443.00	166.00
186	1150	B	9	R	1	140	150	778.60	7.73	8.79	20.00	340.00	292.00	6.97	13.20	10.90	0.71	4.77	443.00	185.00
186	1150	B	12	R	2	131	141	808.78	7.75	7.75	20.00	338.00	290.00	6.90	12.40	10.20	0.02	4.67	444.00	186.00
186	1150	B	16	R	3	140	150	849.00	7.67	7.93	19.00	336.00	290.00	6.69	12.30	10.80	0.00	3.87	443.00	191.00
186	1150	B	19	R	1	140	150	874.90	7.60	6.58	19.00	331.00	282.00	6.59	12.40	11.50	0.03	3.45	435.00	196.00
186	1150	B	22	R	4	89	100	906.83	7.75	5.43	18.00	325.00	277.00	6.74	11.20	12.10	ND	3.34	430.00	219.00
186	1150	B	25	R	2	132	142	933.92	7.48	5.51	18.00	325.00	274.00	6.55	11.40	13.40	ND	3.09	408.00	209.00
186	1150	B	28	R	3	123	133	964.08	7.58	6.78	18.00	325.00	271.00	6.43	11.70	15.00	0.02	2.86	393.00	220.00
186	1150	B	31	R	1	122	132	989.92	7.73	5.78	18.00	315.00	259.00	6.16	10.70	16.00	ND	2.58	387.00	241.00
186	1150	B	34	R	1	140	150	1018.90	7.77	5.45	18.00	318.00	263.00	6.22	10.90	16.50	ND	2.63	367.00	249.00
186	1150	B	37	R	1	140	150	1047.90	7.66	3.25	18.00	318.00	258.00	6.09	11.20	17.30	0.02	2.36	352.00	246.00
186	1150	B	41	R	3	140	150	1089.59	7.66	2.29	18.00	307.00	250.00	5.95	10.20	17.20	ND	2.17	332.00	252.00
186	1150	B	45	R	2	140	150	1126.80	7.74	3.11	18.00	310.00	249.00	6.34	10.00	19.70	0.12	2.41	297.00	258.00
186	1150	B	49	R	4	140	150	1168.17	7.55	1.76	19.00	324.00	258.00	6.76	10.30	21.40	0.30	1.94	242.00	257.00

Notes: ND = not detected. This table is also available in [ASCII format](#).

Table T17. Thermal conductivity, Hole 1150A.

Core, section, interval (cm)	Depth (mbsf)	Average thermal conductivity (W/[m·K])
186-1150A-		
1H-3, 75	3.75	0.58
2H-3, 75	11.45	0.89
3H-3, 75	20.95	0.82
4H-3, 70	30.40	0.62
5H-3, 70	39.90	0.64
6H-3, 70	49.40	0.51
7H-3, 75	58.95	0.65
8H-3, 75	68.45	0.89
9H-3, 75	77.95	0.76
10H-1, 34	84.04	0.65
11H-2, 78	95.48	0.90
12H-3, 75	106.08	0.79
13X-3, 75	115.95	0.56
14X-3, 75	120.15	0.74
15X-3, 30	129.30	0.52
16X-2, 75	137.85	0.52
17X-3, 75	148.95	0.62
18X-3, 75	158.55	0.60
21X-3, 75	187.35	0.59
22X-3, 75	197.05	0.76
23X-3, 60	206.26	0.71
24X-1, 33	212.83	0.53
25X-3, 84	226.04	0.63
26X-3, 75	235.65	0.45
27X-3, 75	245.25	0.68
28X-3, 77	254.86	0.68
29X-3, 77	264.57	0.62
30X-3, 75	274.15	0.71
31X-3, 75	283.02	0.67
32X-3, 75	293.45	0.76
33X-3, 75	303.15	0.74
34X-3, 95	313.05	0.63
35X-3, 59	321.65	0.60
36X-3, 86	332.03	0.64
37X-3, 71	341.71	0.65
38X-3, 81	351.41	0.59
39X-3, 70	360.90	0.54
40X-3, 53	370.33	0.72
42X-3, 75	389.75	0.57
43X-3, 75	399.35	0.58
44X-3, 75	408.95	0.57
45X-3, 82	418.62	0.64

Note: This table is also available in [ASCII format](#).

Table T18. *P*-wave velocity and anisotropy, Site 1150.

Leg, hole	Core, section, interval (cm)	Depth (mbsf)	<i>P</i> -wave velocity (m/s)			Anisotropy		
			V _X	V _Y	V _Z	A _{Hh}	A _{Hv}	A _{Hv}
186-1150A	1H-2, 80.3	2.30	—	1524	—	—	—	—
186-1150A	1H-3, 80	3.80	—	1469	1511	—	—	—
186-1150A	1H-4, 80	5.30	—	1447	1524	—	—	—
186-1150A	1H-5, 80	6.80	—	1518	1530	—	—	—
186-1150A	2H-1, 80	8.50	—	—	1505	—	—	—
186-1150A	2H-1, 80.1	8.50	—	1484	—	—	—	—
186-1150A	2H-2, 80	10.00	—	1521	—	—	—	—
186-1150A	2H-3, 80.2	11.50	1544	—	—	—	—	—
186-1150A	2H-4, 80.1	13.00	1547	—	—	—	—	—
186-1150A	2H-5, 80.1	14.50	1540	—	—	—	—	—
186-1150A	2H-6, 47.5	15.68	1529	—	—	—	—	—
186-1150A	2H-7, 34.6	17.05	1532	—	—	—	—	—
186-1150A	3H-1, 80	18.00	1519	—	—	—	—	—
186-1150A	3H-2, 80	19.50	1522	—	—	—	—	—
186-1150A	3H-3, 80	21.00	1526	—	—	—	—	—
186-1150A	3H-4, 65	22.35	1536	—	—	—	—	—
186-1150A	3H-5, 24.6	23.45	1521	—	—	—	—	—
186-1150A	3H-6, 62.2	25.32	1525	—	—	—	—	—
186-1150A	3H-7, 39.1	26.59	1531	—	—	—	—	—
186-1150A	4H-2, 80	29.00	1571	—	—	—	—	—
186-1150A	4H-3, 80	30.50	1570	—	—	—	—	—
186-1150A	4H-4, 80	32.00	1556	—	—	—	—	—
186-1150A	5H-2, 93.6	38.64	1193	—	—	—	—	—
186-1150A	5H-3, 86.3	40.06	1162	—	—	—	—	—
186-1150A	5H-3, 100.4	40.20	1100	—	—	—	—	—
186-1150A	5H-6, 89	44.59	1120	—	—	—	—	—
186-1150A	5H-7, 75.2	45.95	1117	—	—	—	—	—
186-1150A	6H-1, 90.5	46.61	1161	—	—	—	—	—
186-1150A	6H-2, 90.4	48.10	1122	—	—	—	—	—
186-1150A	6H-3, 89.5	49.60	1208	—	—	—	—	—
186-1150A	6H-4, 90	51.10	1212	—	—	—	—	—
186-1150A	6H-5, 88.3	52.58	1193	—	—	—	—	—
186-1150A	6H-6, 88.9	54.09	1202	—	—	—	—	—
186-1150A	7H-1, 111.1	56.31	1520	—	—	—	—	—
186-1150A	7H-2, 92.8	57.63	1502	—	—	—	—	—
186-1150A	7H-4, 96.4	60.66	1426	—	—	—	—	—
186-1150A	7H-6, 78.2	63.48	1291	—	—	—	—	—
186-1150A	33X-3, 115	303.55	1565	—	—	—	—	—
186-1150A	33X-4, 61	304.51	1568	—	—	—	—	—
186-1150A	33X-5, 14	305.04	1564	—	—	—	—	—
186-1150A	34X-3, 139	313.49	1553	—	—	—	—	—
186-1150A	34X-4, 77	314.37	1570	—	—	—	—	—
186-1150A	35X-4, 96	323.52	1567	—	—	—	—	—
186-1150A	35X-6, 94	326.50	1570	—	—	—	—	—
186-1150A	35X-7, 44	327.42	1555	—	—	—	—	—
186-1150A	36X-1, 113	329.53	1543	—	—	—	—	—
186-1150A	36X-2, 123	330.90	1538	—	—	—	—	—
186-1150A	36X-5, 137	335.33	1505	—	—	—	—	—
186-1150A	37X-1, 100	339.00	1540	—	—	—	—	—
186-1150A	37X-2, 82	340.32	1578	—	—	—	—	—
186-1150A	37X-3, 60	341.60	1551	—	—	—	—	—
186-1150A	37X-4, 91	343.41	1543	—	—	—	—	—
186-1150A	37X-5, 90	344.90	1577	—	—	—	—	—
186-1150A	37X-6, 80	346.30	1536	—	—	—	—	—
186-1150A	38X-2, 130	350.40	1577	—	—	—	—	—
186-1150A	38X-3, 53	351.13	1563	—	—	—	—	—
186-1150A	38X-4, 47	352.57	1559	—	—	—	—	—
186-1150A	38X-5, 36	353.96	1561	—	—	—	—	—
186-1150A	38X-6, 49	355.44	1565	—	—	—	—	—
186-1150A	39X-3, 97	361.17	1571	—	—	—	—	—
186-1150A	39X-4, 52	362.22	1578	—	—	—	—	—
186-1150A	39X-5, 62	363.82	1599	—	—	—	—	—

Notes: V_X and V_Y are horizontal velocity; V_Z is vertical velocity; A_{Hh} = anisotropy of maximum vs. minimum horizontal velocity; A_{Hv} = anisotropy of maximum horizontal velocity vs. vertical velocity; A_{Hv} = anisotropy of minimum horizontal velocity vs. vertical velocity. — = not measured. Only a portion of this table appears here. The complete table is available in [ASCII format](#).

Table T19. Undrained shear strength, Hole 1150A.

Core, section, interval (cm)	Depth (mbsf)	Shear strength (kPa)	
		Vane shear	Penetrometer
186-1150A-			
1H-2, 92.1	2.42	17.2	—
1H-3, 86.6	3.87	27.1	—
1H-4, 71.8	5.22	43.6	—
1H-5, 71.8	6.72	69.2	—
2H-1, 87.4	8.57	31.7	—
2H-2, 87.7	10.08	69.2	—
2H-3, 79.6	11.50	48.2	—
2H-4, 82.8	13.03	50.4	—
2H-5, 82.8	14.53	56.5	—
2H-6, 82.8	16.03	64.9	—
2H-7, 60.7	17.31	64.9	—
3H-1, 82.8	18.03	69.2	—
3H-2, 82.8	19.53	42.6	—
3H-3, 87.6	21.08	24.5	—
3H-5, 83.7	24.04	34.2	—
3H-6, 87.7	25.58	46.7	—
3H-7, 66.1	26.86	50.7	—
4H-1, 55	27.25	—	39.2
4H-2, 86.5	29.07	—	61.3
4H-3, 83.3	30.53	—	61.3
4H-4, 85	32.05	—	49.1
4H-5, 70.5	33.41	—	61.3
4H-6, 75	34.95	—	63.8
5H-1, 81	37.01	—	58.9
5H-2, 90.2	38.60	—	36.8
5H-3, 90.9	40.11	—	37.3
5H-4, 77	41.47	—	29.4
5H-5, 90	43.10	—	36.8
5H-6, 80.5	44.51	—	58.9
5H-7, 85.2	46.05	—	56.4
6H-1, 93	46.63	—	49.1
6H-2, 94.1	48.14	—	58.9
6H-3, 95	49.65	—	68.7
6H-4, 93.2	51.13	—	58.9
6H-5, 85	52.55	—	73.6
6H-6, 92.2	54.12	—	54.0
7H-2, 88.5	57.59	—	58.9
7H-3, 90.1	59.10	—	54.0
7H-4, 100.5	60.71	—	73.6
7H-5, 82.8	62.03	—	83.4
7H-6, 64.3	63.34	—	58.9
8H-1, 67.7	65.38	—	62.3
8H-2, 84.7	67.05	—	85.8
8H-3, 86.7	68.57	—	86.3
8H-4, 81.7	70.02	—	61.3
8H-5, 70.2	71.40	—	61.8
8H-6, 67.9	72.88	—	110.4
8H-7, 54.5	74.04	—	110.4
9H-1, 86.2	75.06	—	80.9
9H-2, 79.5	76.50	—	78.5
9H-3, 66.5	77.87	—	79.5
9H-4, 62.7	79.31	—	92.7
9H-5, 74.6	80.93	—	73.6
9H-6, 75.8	82.44	—	98.6
9H-7, 49.8	83.68	—	98.6
10H-1, 40	84.10	—	61.3
10H-2, 57	84.94	—	54.9
10H-4, 65	87.98	—	85.8
10H-5, 70	89.46	—	118.2
10H-6, 70	90.91	—	110.4
10H-7, 70	92.41	—	88.3
10H-8, 60	93.49	—	51.5

Notes: — = not measured. This table is also available in [ASCII format](#).

Table T20. Index properties, Site 1150.

Leg, hole	Core, section, interval (cm)	Depth (mbsf)	Salinity	Pore water density (g/cm ³)	Water content of total mass (%)	Water content of mass of solids (%)	Bulk density (g/cm ³)	Dry density (g/cm ³)	Grain density (g/cm ³)	Porosity (%)	Void ratio
186-1150A	1H-1, 91-93	0.91	0.034	1.024	68	213	1.26	0.40	2.42	83	5.02
186-1150A	1H-2, 89-91	2.39	0.034	1.024	61	157	1.33	0.52	2.50	79	3.82
186-1150A	1H-3, 89-91	3.89	0.034	1.024	49	98	1.47	0.74	2.57	71	2.45
186-1150A	1H-4, 89-91	5.39	0.034	1.024	56	128	1.38	0.60	2.46	75	3.08
186-1150A	1H-5, 89-91	6.89	0.034	1.024	49	96	1.47	0.75	2.51	70	2.36
186-1150A	2H-2, 84-86	10.04	0.034	1.024	49	97	1.46	0.74	2.48	70	2.36
186-1150A	2H-3, 84-86	11.54	0.034	1.024	48	91	1.50	0.79	2.60	70	2.30
186-1150A	2H-4, 84-86	13.04	0.034	1.024	46	84	1.51	0.82	2.52	67	2.06
186-1150A	2H-5, 84-86	14.54	0.034	1.024	49	97	1.47	0.75	2.53	70	2.38
186-1150A	2H-6, 84-86	16.04	0.034	1.024	53	114	1.40	0.65	2.41	73	2.68
186-1150A	2H-7, 57-59	17.27	0.034	1.024	54	119	1.40	0.64	2.51	75	2.93
186-1150A	3H-1, 79-81	17.99	0.034	1.024	55	122	1.41	0.63	2.58	75	3.07
186-1150A	3H-2, 79-81	19.49	0.034	1.024	47	89	1.51	0.80	2.58	69	2.23
186-1150A	3H-3, 79-81	20.99	0.034	1.024	45	81	1.53	0.85	2.56	67	2.01
186-1150A	3H-4, 79-81	22.49	0.034	1.024	47	89	1.50	0.79	2.57	69	2.24
186-1150A	3H-5, 79-81	23.99	0.034	1.024	54	116	1.41	0.65	2.51	74	2.85
186-1150A	3H-6, 79-81	25.49	0.034	1.024	48	92	1.48	0.77	2.52	69	2.26
186-1150A	3H-7, 39-41	26.59	0.034	1.024	46	85	1.51	0.81	2.51	68	2.09
186-1150A	4H-1, 67-69	27.37	0.034	1.024	53	111	1.42	0.67	2.50	73	2.71
186-1150A	4H-2, 67-69	28.87	0.034	1.024	58	136	1.36	0.57	2.42	76	3.22
186-1150A	4H-3, 72-74	30.42	0.033	1.024	55	124	1.38	0.61	2.40	74	2.90
186-1150A	4H-4, 72-74	31.92	0.033	1.024	44	78	1.53	0.86	2.47	65	1.88
186-1150A	4H-5, 63-65	33.33	0.033	1.024	49	98	1.46	0.74	2.51	71	2.40
186-1150A	4H-6, 63-65	34.83	0.033	1.024	51	106	1.43	0.69	2.45	72	2.53
186-1150A	5H-1, 96-98	37.16	0.033	1.024	48	93	1.47	0.76	2.47	69	2.25
186-1150A	5H-2, 97-99	38.67	0.033	1.023	47	88	1.50	0.80	2.52	68	2.17
186-1150A	5H-3, 97-99	40.17	0.033	1.023	48	93	1.49	0.77	2.57	70	2.32
186-1150A	5H-4, 96-98	41.66	0.033	1.023	52	110	1.41	0.68	2.44	72	2.61
186-1150A	5H-5, 91-93	43.11	0.033	1.023	47	88	1.50	0.80	2.55	69	2.19
186-1150A	5H-6, 96-98	44.66	0.032	1.023	50	100	1.45	0.73	2.50	71	2.43
186-1150A	5H-7, 77-79	45.97	0.032	1.023	45	81	1.53	0.84	2.53	67	2.00
186-1150A	6H-1, 94-96	46.64	0.032	1.023	44	79	1.53	0.85	2.55	66	1.98
186-1150A	6H-2, 96-98	48.16	0.032	1.023	51	104	1.44	0.70	2.48	72	2.53
186-1150A	6H-3, 96-98	49.66	0.032	1.023	51	103	1.42	0.70	2.37	70	2.38
186-1150A	6H-4, 84-86	51.04	0.032	1.023	45	83	1.53	0.83	2.60	68	2.11
186-1150A	6H-5, 93-95	52.63	0.032	1.023	46	84	1.53	0.83	2.61	68	2.15
186-1150A	6H-6, 94-96	54.14	0.032	1.023	42	72	1.59	0.92	2.66	65	1.88
186-1150A	7H-1, 90-92	56.10	0.032	1.022	41	70	1.59	0.94	2.63	64	1.81
186-1150A	7H-2, 85-87	57.55	0.031	1.022	47	88	1.50	0.80	2.57	69	2.20
186-1150A	7H-3, 92-94	59.12	0.031	1.022	45	81	1.54	0.85	2.59	67	2.05
186-1150A	7H-4, 80-82	60.50	0.031	1.022	44	80	1.53	0.85	2.56	67	2.00
186-1150A	7H-5, 80-82	62.00	0.031	1.022	49	97	1.46	0.74	2.53	71	2.41
186-1150A	7H-6, 60-62	63.30	0.031	1.022	39	64	1.61	0.98	2.57	62	1.62
186-1150A	8H-2, 70-72	66.90	0.031	1.022	46	84	1.50	0.82	2.50	67	2.05
186-1150A	8H-5, 82-84	71.52	0.030	1.022	36	56	1.67	1.07	2.61	59	1.44
186-1150A	8H-6, 70-72	72.90	0.030	1.022	41	69	1.58	0.93	2.52	63	1.70
186-1150A	9H-1, 96-98	75.16	0.030	1.021	42	73	1.58	0.91	2.63	65	1.87
186-1150A	9H-2, 80-82	76.50	0.030	1.021	48	91	1.47	0.77	2.44	69	2.19
186-1150A	9H-3, 63-65	77.83	0.030	1.021	48	93	1.46	0.76	2.46	69	2.25
186-1150A	9H-4, 59-61	79.27	0.030	1.021	46	84	1.50	0.81	2.48	67	2.05
186-1150A	9H-5, 71-73	80.89	0.030	1.021	42	72	1.55	0.90	2.46	63	1.74
186-1150A	9H-6, 73-75	82.41	0.030	1.021	45	81	1.50	0.83	2.43	66	1.93
186-1150A	9H-7, 47-49	83.65	0.030	1.021	43	76	1.53	0.87	2.48	65	1.85
186-1150A	10H-1, 40-42	84.10	0.030	1.021	43	76	1.55	0.88	2.53	65	1.87
186-1150A	10H-2, 58-60	84.95	0.030	1.021	43	75	1.56	0.89	2.56	65	1.88
186-1150A	10H-3, 66-68	86.53	0.030	1.021	48	93	1.49	0.77	2.57	70	2.33
186-1150A	10H-4, 63-65	87.96	0.030	1.021	42	73	1.56	0.90	2.53	64	1.81
186-1150A	10H-5, 67-69	89.43	0.030	1.021	46	86	1.52	0.82	2.61	69	2.20
186-1150A	10H-6, 67-69	90.88	0.030	1.021	45	82	1.51	0.83	2.51	67	2.02
186-1150A	10H-7, 67-69	92.38	0.030	1.021	44	79	1.55	0.86	2.61	67	2.02
186-1150A	10H-8, 57-59	93.46	0.030	1.021	50	99	1.45	0.73	2.45	70	2.38
186-1150A	11H-1, 96-98	94.16	0.030	1.021	40	67	1.60	0.96	2.55	63	1.67
186-1150A	11H-2, 95-97	95.65	0.030	1.021	44	77	1.54	0.87	2.53	66	1.92
186-1150A	11H-3, 93-95	97.13	0.030	1.021	44	78	1.52	0.86	2.47	65	1.89

Notes: Values shown are corrected for in situ salinity and density of pore water. Only a portion of this table appears here. The complete table is available in [ASCII format](#).

Table T21. Summary of Site 1150 logging operations.

Logging run	Logging string	Time	Date
1	Triple combo + LDEO-TAP	1615-2400	1 July 1999
2	FMS-sonic	0000-0700	2 July 1999
3	Triple combo + LDEO-TAP	0830-1445	2 July 1999
4	FMS-sonic	1445-2100	2 July 1999
5	BHTV	2100-0545	3 July 1999

Notes: See Figure F66, p. 145, for explanation of tool acronyms. Triple combo = triple combination logging tool, LDEO-TAP = Lamont-Doherty Earth Observatory temperature/acceleration/pressure tool, FMS = Formation MicroScanner, BHTV = borehole televiewer.

Table T22. Summary of in situ temperature measurements, Hole 1150A.

Hole, core	Depth (mbsf)	Tool	Equilibrium temperature (°C)	Comments
186-1150A	Mudline	APC	1.76 ± 0.1	
1150A-3H	17.20	APC	2.63 ± 0.1	
1150A-6H	45.70	APC	3.33 ± 0.1	
1150A-9H	74.20	APC	—	Bad data
1150A-14X	116.40	DVTP	5.73 ± 0.1	
1150A-18X	154.80	DVTP	7.34 ± 0.1	

Note: APC = APC (advanced hydraulic piston core) temperature tool, DVTP = Davis-Villinger temperature probe.

Table T23. Instrument package deployment, Site 1150.

Step	Date (July 1999)	Time	Total time	Description
1	23	22:30	0	Install cable reel stands and rig sheaves in moonpool
2	24	00:05	1:35	Move strainmeter/stinger assembly to rig floor
3	24	00:20	1:50	Make up stinger to strainmeter, vertical on rig floor
4	24	00:55	2:25:00	Make up lifting eyes and landing brackets to strainmeter
5	24	01:20	2:50:00	Make up 4.5-in casing joint to seismometer, vertically on deck; install centralizers on casing
6	24	01:25	2:55:00	Make up seismometer to strainmeter; pick up instrument package and remove strainmeter landing brackets
7	24	02:10	3:40:00	Slowly lower to moonpool
8	24	03:20	4:50:00	Make up instrument cable connections in moonpool
9	24	04:15	5:45:00	Begin strapping and wrapping cables
10	24	16:45	18:15:00	Run 93 joints (~1074 m) of 4.5-in casing
11	24	18:15	19:45:00	RIH (33 m); move hanger/riser on to rig floor
12	24	18:30	20:00:00	Assemble hanger/riser to 4.5-in casing
13	24	19:15	20:45:00	Cut cables to length
14	24	19:45	21:15:00	Raise hanger/riser feeding free end of cables into subsea shop
15	25	10:30	36:00:00	Make up cable terminations
16	25	13:45	39:15:00	Install the MEG
17	25	18:00	43:30:00	Deploy VIT
18	26	17:30	67:00:00	RIH/wash to 23 m from TD/POOH-contingency
19	27	09:00	82:30:00	RIH/ream
20	27	16:30	90:00:00	Pick up instrumentation string/test/RIH
20	27	21:30	95:00:00	RIH/wash to TD
21	27	22:00	95:30:00	Land hanger/riser in reentry cone
22	28	01:00	98:30:00	Pump 68 bbl 16 lb/gal (~2000 kg/m ³) cement slurry/drop dart
23	28	05:45	103:15:00	Prep battery frame in moonpool
24	28	08:30	106:00:00	Deploy battery frame
25	28	12:50	110:20:00	Battery frame land in cone
26	28	19:00	116:30:00	J-joint disconnected
				POOH

Notes: Extra time due to contingency on 25 July 1999, 18:00 hr, through 27 July 1999, 16:30 hr = 46.5 hr. RIH = run in hole, VIT = vibration isolated television, TD = total depth, POOH = pull out of hole.

Table T24. Remotely operated vehicle tasks to start the NEREID system.

Step	Task
1	Dive with the BOB unit
2	Locate Holes 1150C and 1150D
3	Check the status of the Hole 1150C reentry cone area
4	Locate the ROV UMC parking position on the PAT
5	Locate the SAM on the PAT
6	Open the top lid of the SAM
7	Insert the BOB to be able to communicate with the SAM via infrared link
8	Locate, pull out, and retrieve the ROV UMC dummy receptacle from the top of the MEG
9	Pull out pins binding oil-fill cable on the PAT top surface
10	Pull out the ROV UMC and bring over to the furthest side to face the MEG
11	Insert the ROV UMC to automatically start the system
12	Wait 20 min after completion of connection
13	Check the LED status on the BOB
If successful	
14a	Surface and wait 1-2 days for the BOB to recover data
15a	Dive and retrieve the BOB
16a	Close lid on the SAM
17a	Surface
If unsuccessful	
14b	Retrieve the BOB
15b	Surface
16b	Recover the SAM Cut the string attached to the SAM release lever Remove the hat (BOB holder) on the SAM Move the lever to release the SAM connector Pull out the SAM with 20 kg force
17b	Surface and check the SAM
18b	Refurbish the SAM
19b	Dive with the SAM and BOB
20b	Insert the SAM using the guide on the PAT
21b	Place the BOB on top of the SAM
22b	Go to Step 12

Note: BOB = back from ocean bottom module, ROV = remotely operated vehicle, UMC = underwater mateable ROV connector, SAM = storage acquisition module, PAT = power supply access terminal, LED = light emitting diode.

Table T25. Number of deformational structures, Hole 1150B.

Leg	Site	Hole	Type	Core	Depth (mbsf)	Recovered length (m)	Healed fractures						Open fractures	
							Total (faults + joints)		Faults		Joints		(Number/ core)	(Number/ m)
							(Number/ core)	(Number/ m)	(Number/ core)	(Number/ m)	(Number/ core)	(Number/ m)		
186	1150	B	R	1	703.30	4.91	1	0.20	1	0.20	0	0.00	1	0.20
186	1150	B	R	2	709.70	2.26	1	0.44	1	0.44	0	0.00	9	3.98
186	1150	B	R	3	719.30	0.83	5	6.02	4	4.82	1	1.20	1	1.20
186	1150	B	R	4	729.00	3.50	7	2.00	7	2.00	0	0.00	10	2.86
186	1150	B	R	5	738.60	1.50	4	2.67	1	0.67	3	2.00	7	4.67
186	1150	B	R	6	748.30	8.26	12	1.45	12	1.45	0	0.00	34	4.12
186	1150	B	R	7	757.90	1.45	5	3.45	2	1.38	3	2.07	5	3.45
186	1150	B	R	8	767.60	2.48	7	2.82	6	2.42	1	0.40	9	3.63
186	1150	B	R	9	777.20	4.30	31	7.21	23	5.35	8	1.86	9	2.09
186	1150	B	R	10	786.90	4.14	9	2.17	5	1.21	4	0.97	13	3.14
186	1150	B	R	11	796.50	6.35	23	3.62	18	2.83	5	0.79	12	1.89
186	1150	B	R	12	806.10	5.86	22	3.75	13	2.22	9	1.54	14	2.39
186	1150	B	R	13	815.70	4.11	11	2.68	6	1.46	5	1.22	5	1.22
186	1150	B	R	14	835.40	5.11	4	0.78	4	0.78	0	0.00	2	0.39
186	1150	B	R	15	835.00	2.20	2	0.91	1	0.45	1	0.45	0	0.00
186	1150	B	R	16	844.60	7.65	14	1.83	13	1.70	1	0.13	8	1.05
186	1150	B	R	17	854.20	5.36	22	4.10	17	3.17	5	0.93	24	4.48
186	1150	B	R	18	863.80	4.31	38	8.82	20	4.64	18	4.18	14	3.25
186	1150	B	R	19	873.50	4.05	6	1.48	4	0.99	2	0.49	3	0.74
186	1150	B	R	20	883.20	9.84	33	3.35	23	2.34	10	1.02	9	0.91
186	1150	B	R	21	892.90	5.44	33	6.07	22	4.04	11	2.02	10	1.84
186	1150	B	R	22	902.10	8.59	41	4.77	25	2.91	16	1.86	15	1.75
186	1150	B	R	23	911.80	7.96	63	7.91	38	4.77	25	3.14	19	2.39
186	1150	B	R	24	921.50	1.99	14	7.04	12	6.03	2	1.01	8	4.02
186	1150	B	R	25	931.10	7.89	66	8.37	49	6.21	17	2.15	15	1.90
186	1150	B	R	26	940.70	7.31	78	10.67	45	6.16	33	4.51	22	3.01
186	1150	B	R	27	950.30	7.13	54	7.57	39	5.47	15	2.10	15	2.10
186	1150	B	R	28	959.90	8.96	51	5.69	38	4.24	13	1.45	11	1.23
186	1150	B	R	29	969.50	8.56	47	5.49	35	4.09	12	1.40	5	0.58
186	1150	B	R	30	979.10	8.78	39	4.44	28	3.19	11	1.25	3	0.34
186	1150	B	R	31	988.70	3.66	27	7.38	16	4.37	11	3.01	8	2.19
186	1150	B	R	32	998.30	9.55	63	6.60	34	3.56	29	3.04	30	3.14
186	1150	B	R	33	1007.90	1.60	7	4.38	4	2.50	3	1.88	4	2.50
186	1150	B	R	34	1017.50	2.52	8	3.17	6	2.38	2	0.79	6	2.38
186	1150	B	R	35	1027.10	4.43	56	12.64	37	8.35	19	4.29	5	1.13
186	1150	B	R	36	1036.70	8.06	25	3.10	21	2.61	4	0.50	17	2.11
186	1150	B	R	37	1046.50	4.04	49	12.13	36	8.91	13	3.22	10	2.48
186	1150	B	R	38	1056.30	2.42	10	4.13	9	3.72	1	0.41	5	2.07
186	1150	B	R	39	1066.00	4.82	47	9.75	34	7.05	13	2.70	14	2.90
186	1150	B	R	40	1075.70	3.53	9	2.55	5	1.42	4	1.13	16	4.53
186	1150	B	R	41	1085.30	9.19	60	6.53	40	4.35	20	2.18	16	1.74
186	1150	B	R	42	1094.90	8.99	47	5.23	34	3.78	13	1.45	20	2.22
186	1150	B	R	43	1104.60	6.71	55	8.20	39	5.81	16	2.38	12	1.79
186	1150	B	R	44	1114.20	1.59	14	8.81	3	1.89	11	6.92	8	5.03
186	1150	B	R	45	1123.90	5.98	19	3.18	15	2.51	4	0.67	11	1.84
186	1150	B	R	46	1133.50	5.47	40	7.31	28	5.12	12	2.19	11	2.01
186	1150	B	R	47	1143.10	4.30	24	5.58	17	3.95	7	1.63	8	1.86
186	1150	B	R	48	1152.80	4.96	45	9.07	33	6.65	12	2.42	18	3.63
186	1150	B	R	49	1162.40	8.19	72	8.79	44	5.37	28	3.42	23	2.81
186	1150	B	R	50	1172.00	8.25	78	9.45	50	6.06	28	3.39	17	2.06

Notes: Depth is measured at top of interval. This table is also available in [ASCII format](#).

Table T26. Orientations of healed fractures, Hole 1150B.

Core, section	Interval (cm)	Depth (mbsf)	Paleomagnetic direction		Core coordinates		Geographic coordinates	
			Dec. (°)	Inc. (°)	Dip Azimuth (°)	Dip Azimuth (°)	Dip Azimuth (°)	Dip Angle (°)
186-1150B-								
1R-3	66	706.66	—	—	100	74	—	—
2R-1	110	711.10	—	—	9	67	—	—
2R-2	75	711.75	—	—	114	40	—	—
3R-1	28	719.28	—	—	5	50	—	—
4R-1	48	729.48	154	43	84	62	290	62
4R-2	75	731.25	94	54	180	15	86	15
4R-2	81	731.31	94	54	71	52	337	52
4R-2	50	731.00	94	54	287	61	193	61
6R-2	35	750.15	177	54	111	71	294	71
6R-4	50	752.53	135	54	245	53	110	53
6R-5	130	754.83	176	55	297	67	121	68
7R-1	134	759.24	—	—	265	70	—	—
8R-1	83	768.43	294	20	265	70	331	70
9R-1	30	777.50	—	—	290	81	—	—
9R-2	18	778.95	—	—	85	80	—	—
9R-2	57	779.27	233	—52	75	80	22	80
9R-2	80	779.50	233	—52	67	42	14	42
9R-2	90	779.60	233	—52	26	22	333	22
9R-2	110	779.80	233	—52	79	70	26	70
10R-1	55	787.45	84	—58	117	67	213	68
10R-1	66	787.56	—	—	134	67	—	—
11R-1	20	796.70	—	—	261	34	—	—
11R-2	92	798.83	162	52	249	73	87	73
13R-3	66	819.31	—	—	129	52	—	—
14R-2	44	827.27	—	—	115	53	—	—
14R-4	40	830.22	—	—	50	57	—	—
15R-2	15	836.65	197	19	309	52	112	52
16R-2	50	846.60	155	61	229	62	75	62
16R-2	140	847.50	155	61	135	55	340	55
16R-2	50	846.60	155	61	150	55	355	55
16R-2	90	847.00	155	61	264	65	110	65
16R-3	10	847.70	128	64	243	67	115	68
16R-4	10	849.20	152	58	69	74	277	74
16R-4	10	849.20	152	58	264	55	112	55
16R-4	75	849.85	152	58	255	61	103	61
16R-4	95	850.05	152	58	198	70	46	70
16R-4	95	850.05	152	58	207	69	55	69
16R-5	45	851.05	181	63	259	46	78	46
17R-1	130	855.50	221	59	302	59	81	59
17R-1	130	855.50	221	59	292	44	71	44
17R-1	140	855.60	221	59	20	74	159	74
17R-2	60	854.80	230	56	303	45	73	45
17R-2	70	854.90	230	56	144	71	274	71
17R-2	130	855.50	230	56	304	64	74	64
17R-2	105	855.25	230	56	305	48	75	48
17R-3	50	857.70	253	60	357	45	104	45
17R-3	80	858.00	253	60	275	70	22	70
17R-3	80	858.00	253	60	77	51	184	51
17R-3	100	858.20	253	60	332	61	79	61
17R-3	110	858.30	253	60	307	56	54	56
17R-4	10	858.80	38	62	264	55	226	55
17R-4	60	859.30	38	62	335	68	297	68
17R-4	80	859.50	38	62	293	52	255	52
18R-1	120	865.00	134	55	73	64	299	64
18R-2	20	865.50	—	—	316	63	—	—

Notes: — = not determined. Only a portion of this table appears here. The complete table is available in [ASCII format](#).

Table T27. Orientations of open fractures, Hole 1150B.

Core, section	Interval (cm)	Depth (mbsf)	Paleomagnetic direction		Core coordinates		Geographic coordinates	
			Dec. (°)	Inc. (°)	Dip Azimuth (°)	Dip angle (°)	Dip Azimuth (°)	Dip angle (°)
186-1150B-								
4R-1	44	729.44	154	43	109	52	315	52
4R-2	10	730.60	94	54	64	72	330	72
4R-2	30	730.80	94	54	28	61	294	61
4R-2	40	730.90	94	54	222	61	128	61
4R-2	88	731.38	94	54	177	2	83	2
6R-2	35	750.15	177	54	67	62	250	62
6R-4	30	752.33	135	54	244	72	109	72
10R-2	65	789.01	—	—	244	45	—	—
10R-2	111	789.47	—	—	249	52	—	—
12R-3	20	809.08	—	—	293	52	—	—
12R-3	33	809.21	—	—	307	44	—	—
12R-3	43	809.31	—	—	296	28	—	—
12R-4	93	811.31	—	—	238	45	—	—
12R-4	100	811.38	—	—	251	50	—	—
20R-1	55	883.75	338	55	224	82	247	82
20R-2	120	885.90	66	59	96	80	30	80
20R-4	80	888.38	252	57	288	80	36	81
20R-5	100	890.08	21	54	38	76	17	76
21R-1	50	893.40	269	60	143	74	234	74
21R-2	80	895.10	312	59	263	74	311	74
21R-4	20	897.39	170	64	261	58	91	58
21R-4	30	897.49	170	64	268	62	98	62
22R-1	110	903.20	209	63	105	78	256	78
22R-3	70	905.14	216	68	319	69	103	69
22R-5	80	907.74	241	73	82	80	201	80
22R-6	50	908.92	160	68	258	59	98	59
22R-6	120	909.62	160	68	244	45	84	45
23R-1	75	912.55	291	54	25	73	94	73
23R-4	15	916.45	124	56	104	26	340	26
23R-4	140	917.70	339	57	61	28	82	28
26R-1	40	941.10	—	—	342	43	—	—
26R-1	80	941.50	—	—	156	55	—	—
26R-2	140	943.52	—	—	156	57	—	—
26R-4	10	945.18	—	—	67	26	—	—
26R-4	15	945.23	—	—	313	72	—	—
26R-4	20	945.28	—	—	141	6	—	—
26R-4	90	945.98	—	—	274	70	—	—
26R-4	130	946.38	—	—	25	51	—	—
26R-5	20	946.74	—	—	204	57	—	—
26R-5	110	947.64	—	—	27	60	—	—
26R-5	130	947.84	—	—	272	88	—	—
27R-2	100	952.80	44	72	282	57	238	57
27R-4	125	956.06	—	—	102	75	—	—
27R-5	40	956.41	39	72	255	74	216	74
27R-5	60	956.61	39	72	255	41	216	41
27R-5	120	957.21	39	72	241	76	202	76
28R-1	110	961.00	—	—	3	20	—	—
28R-1	110	961.00	—	—	290	65	—	—
28R-3	100	963.85	—	—	261	58	—	—
28R-5	60	966.28	—	—	112	28	—	—
28R-5	110	966.78	—	—	95	53	—	—
28R-6	110	968.28	—	—	281	70	—	—
31R-2	90	990.92	38	60	109	64	71	64
31R-3	40	991.92	34	68	44	79	10	80
32R-4	130	1003.85	102	62	103	69	1	70

Notes: — = not determined. Only a portion of this table appears here. The complete table is available in [ASCII format](#).